

UC Berkeley

UC Berkeley Electronic Theses and Dissertations

Title

Black Hole Masses in Nearby Brightest Cluster Galaxies

Permalink

<https://escholarship.org/uc/item/2nb831v6>

Author

McConnell, Nicholas James

Publication Date

2012

Peer reviewed|Thesis/dissertation

Black Hole Masses in Nearby Brightest Cluster Galaxies

by

Nicholas James McConnell

A dissertation submitted in partial satisfaction of the
requirements for the degree of
Doctor of Philosophy

in

Astrophysics

in the

Graduate Division
of the
University of California, Berkeley

Committee in charge:
Professor Chung-Pei Ma, Co-chair
Professor James Graham, Co-chair
Professor Leo Blitz
Professor Bernard Sadoulet

Fall 2012

Black Hole Masses in Nearby Brightest Cluster Galaxies

Copyright 2012
by
Nicholas James McConnell

Abstract

Black Hole Masses in Nearby Brightest Cluster Galaxies

by

Nicholas James McConnell
 Doctor of Philosophy in Astrophysics

University of California, Berkeley

Professor Chung-Pei Ma, Co-chair
 Professor James Graham, Co-chair

The most massive galaxies in the Universe live at the centers of galaxy clusters and exhibit a number of extreme properties. Although their evolution broadly resembles that of normal elliptical galaxies, with early gas quenching and gradual assembly from smaller stellar systems, their unique cosmic environments may have offered additional pathways for growth. The extreme stellar mass growth of BCGs is clearly demonstrated by their overall luminosities, but the growth histories and present-day masses of their central black holes are not well known. A key body of evidence for the evolutionary connections between galaxies and supermassive black holes is the set of scaling relations between black hole masses (M_{\bullet}) and the stellar velocity dispersions (σ), luminosities (L), or bulge masses (M_{bulge}) of their host galaxies. However, these scaling relations are poorly sampled for BCGs. Populating the relations with direct measurements of M_{\bullet} could offer new insights to the growth of black holes and stellar systems at the hearts of galaxy clusters.

Along with collaborators, I have undertaken a series of observations of the centers of BCGs, using integral-field spectrographs on the Keck, Gemini, and Harlan J. Smith telescopes. In this dissertation, I describe the measurement and analysis of stellar kinematics at the centers of five BCGs, and measurements of their black hole masses using stellar orbit models. The most notable result is the measurement of black holes with approximately 10 billion solar masses in NGC 3842 and NGC 4889. These are the largest black hole masses ever directly measured, and they significantly exceed predictions from both the $M_{\bullet} - \sigma$ and $M_{\bullet} - L$ relations. Their masses are comparable to the biggest black holes powering high-redshift quasars, suggesting a tantalizing link between early sites of prolific black hole growth and rich galaxy clusters today. In contrast, I find that NGC 6086 and NGC 7768 host black holes with only a few billion solar masses. These measurements, as well as my upper limit for M_{\bullet} in NGC 2832, are more consistent with the existing black hole scaling relations.

Recent measurements by my team and others have reshaped the sample of well-measured black hole masses, introducing significant updates to previous compilations. I present a sample of 65 dynamical black hole mass measurements, compiled from published literature through May 2012. In addition to previously reported values of σ and L , I have compiled

an updated sample of bulge masses for 34 galaxies. The updated sample yields a steeper $M_{\bullet} - \sigma$ relation than previous versions, while the $M_{\bullet} - L$ and $M_{\bullet} - M_{\text{bulge}}$ relations experience relatively small changes. I have examined the black hole scaling relations for a variety of galaxy subsamples and find noteworthy variations in the $M_{\bullet} - \sigma$ relation for early- versus late-type galaxies and core-profile versus power-law galaxies.

Using the new sample, I have measured the empirical scatter in M_{\bullet} and have attempted to measure the intrinsic scatter for multiple intervals in σ , L , and M_{bulge} . This is an important step forward from previous studies, which have only measured the intrinsic scatter over the full range of a given host galaxy property. Several models of black hole growth over cosmic time have predicted decreasing scatter in M_{\bullet} as galaxy mass increases, reflecting the influence of hierarchical mergers driving galaxies and black holes toward an average $M_{\bullet}/M_{\text{bulge}}$ ratio. In contrast, I find nearly constant scatter in M_{\bullet} over a wide range of galaxy luminosities and bulge masses.

My investigations thus far have contributed to a gradual change in astronomers' understanding of the black hole scaling relations. The present-day relations are not as tight as previously reported versions, and evidence is mounting against a universal process for co-evolution between black holes and galaxies. I will use observations of a larger sample of BCGs and massive group galaxies to explore the effects of environment on the growth of individual black holes and on cosmic scatter in M_{\bullet} .

To anyone who has failed and stood back up.

Contents

| | |
|-------------------------------------------------------------------------------------|-------------|
| List of Figures | v |
| List of Tables | vii |
| Acknowledgments | viii |
| 1 Introduction | 1 |
| 1.1 Galaxies Past and Present | 1 |
| 1.1.1 Brightest Cluster Galaxies | 3 |
| 1.2 Supermassive Black Holes | 5 |
| 1.3 Scaling Relations between Black Holes and Host Galaxies | 7 |
| 1.4 Measuring Black Hole Masses | 11 |
| 1.4.1 Dynamical Modeling Methods | 12 |
| 1.4.2 Observations | 13 |
| 1.5 This Dissertation | 14 |
| 2 The Black Hole Mass in the Brightest Cluster Galaxy NGC 6086 | 15 |
| 2.1 Introduction | 16 |
| 2.2 Observations | 18 |
| 2.2.1 Photometry | 18 |
| 2.2.2 Spectroscopy | 20 |
| 2.3 Kinematics | 26 |
| 2.3.1 Extracting Kinematics from IFS Data | 26 |
| 2.3.2 Two-Dimensional Kinematics in NGC 6086 | 31 |
| 2.4 Stellar Orbit Models and Black Hole Mass | 32 |
| 2.4.1 Stellar Orbits | 32 |
| 2.4.2 Black Hole Mass and Mass-to-Light Ratio | 35 |
| 2.4.3 Determining Errors | 43 |
| 2.5 Conclusions and Discussion | 47 |
| 2.6 Appendix A: Uncertainties in the PSF and Stellar Templates for OSIRIS | 51 |
| 2.7 Appendix B: Non-Parametric LOSVDs | 55 |

| | | |
|----------|----------------------------------------------------------------------------------------------------|------------|
| 3 | Two Ten-Billion-Solar-Mass Black Holes at the Centers of Giant Elliptical Galaxies | 62 |
| 3.1 | Introduction | 62 |
| 3.2 | Stellar Kinematics and Black Hole Masses | 63 |
| 3.3 | Predictions from Black Hole Scaling Relations | 64 |
| 3.4 | Connection to High-Redshift Quasars | 68 |
| 3.5 | Appendix A: Spectroscopic Data and LOSVD Extraction | 69 |
| 3.6 | Appendix B: Photometric Data | 75 |
| 3.7 | Appendix C: Kinematic Data from Different Instruments | 75 |
| 3.8 | Appendix D: Stellar Orbit Models and Statistical Analysis | 77 |
| 3.9 | Appendix E: Models of NGC 4889 | 79 |
| 3.10 | Appendix F: Power-Law Fits to the $M_{\bullet} - \sigma$ and $M_{\bullet} - L$ Relations | 83 |
| 4 | Dynamical Measurements of Black Hole Masses in Four Brightest Cluster Galaxies at 100 Mpc | 90 |
| 4.1 | Introduction | 91 |
| 4.2 | Observations | 93 |
| 4.2.1 | Global Galaxy Properties | 93 |
| 4.2.2 | Photometry | 93 |
| 4.2.3 | Integral-field Spectroscopy | 95 |
| 4.3 | Extracting Stellar Kinematics | 103 |
| 4.4 | Two-Dimensional Kinematics | 104 |
| 4.4.1 | NGC 4889 | 104 |
| 4.4.2 | NGC 3842 | 108 |
| 4.4.3 | NGC 7768 | 109 |
| 4.4.4 | NGC 2832 | 112 |
| 4.5 | Stellar Orbit Models and Black Hole Masses | 114 |
| 4.5.1 | Axisymmetric Orbit Models | 114 |
| 4.5.2 | Black Hole Masses and Mass-to-Light Ratios | 115 |
| 4.5.3 | Tangentially Biased Orbits | 126 |
| 4.5.4 | Possible Systematic Errors | 129 |
| 4.6 | Conclusion and Discussion | 130 |
| 5 | Revisiting the Black Hole Scaling Relations | 135 |
| 5.1 | Introduction | 135 |
| 5.2 | An Updated Black Hole and Galaxy Sample | 137 |
| 5.3 | Subsamples and Power-law Fits | 143 |
| 5.3.1 | $M_{\bullet} - \sigma$ | 144 |
| 5.3.2 | $M_{\bullet} - L$ and $M_{\bullet} - M_{\text{bulge}}$ | 144 |
| 5.3.3 | Comparison to Previous Studies | 148 |
| 5.4 | Scatter in $\log(M_{\bullet})$ | 150 |
| 5.5 | Discussion | 152 |

| | |
|--------------------------------------|------------|
| 6 Conclusions and Future Work | 155 |
| Bibliography | 157 |

List of Figures

| | | |
|------|-----------------------------------------------------------------------------------------------------------------|----|
| 1.1 | Wide-field image of a Brightest Cluster Galaxy | 4 |
| 1.2 | $M_{\bullet} - \sigma$ correlation | 8 |
| 1.3 | $M_{\bullet} - L$ and $M_{\bullet} - M_{\text{bulge}}$ correlations | 9 |
| 2.1 | Stellar luminosity density vs. radius in NGC 6086 | 19 |
| 2.2 | Collapsed OSIRIS image of NGC 6086 | 22 |
| 2.3 | OSIRIS spectra of NGC 6086 and template star | 24 |
| 2.4 | GMOS spectra of NGC 6086 and template star | 25 |
| 2.5 | Central LOSVDs in NGC 6086 | 28 |
| 2.6 | Maps of kinematic moments in NGC 6086 | 29 |
| 2.7 | Gaussian vs. non-parametric kinematics for NGC 6086 | 30 |
| 2.8 | Major-axis kinematics in NGC 6086 | 33 |
| 2.9 | χ^2 vs. M_{\star}/L_R and M_{\bullet} , from models of NGC 6086 with OSIRIS and GMOS data | 36 |
| 2.10 | Dark matter fraction vs. radius in models of NGC 6086 | 39 |
| 2.11 | Best-fit M_{\bullet} and M_{\star}/L_R vs. model dark matter halo mass in NGC 6086 | 40 |
| 2.12 | χ^2 vs. M_{\star}/L_R and M_{\bullet} , using integral-field data from different instruments | 42 |
| 2.13 | Marginalized likelihood functions for M_{\bullet} and M_{\star}/L_R in NGC 6086 | 45 |
| 2.14 | $M_{\bullet} - \sigma$ relation, including NGC 6086 | 49 |
| 2.15 | PSF models for OSIRIS observations of NGC 6086 | 54 |
| 2.16 | H -band equivalent widths of NGC 6086 and template stars | 56 |
| 2.17 | LOSVDs in NGC 6086 from OSIRIS spectra | 57 |
| 2.18 | LOSVDs in NGC 6086 from GMOS spectra | 58 |
| 2.19 | LOSVDs in NGC 6086 from long-slit data | 60 |
| 3.1 | Two-dimensional maps of velocity dispersions in NGC 3842 and NGC 4889 | 65 |
| 3.2 | One-dimensional velocity dispersion profiles in NGC 3842 and NGC 4889 | 66 |
| 3.3 | $M_{\bullet} - \sigma$ and $M_{\bullet} - L$ correlations | 67 |
| 3.4 | GMOS spectra of NGC 3842 and NGC 4889 | 71 |
| 3.5 | OSIRIS spectrum of the central region of NGC 3842 | 72 |
| 3.6 | VIRUS-P spectrum of NGC 3842 | 73 |
| 3.7 | Radial velocity and dispersion in NGC 4889, from GMOS and long-slit data | 76 |
| 3.8 | χ^2 versus M_{\bullet} and M_{\star}/L_R for stellar orbit models of NGC 3842 | 78 |

| | | |
|------|-----------------------------------------------------------------------------------------------------------|-----|
| 3.9 | χ^2 vs. M_\bullet for NGC 4889, after marginalizing over M_\star/L | 80 |
| 3.10 | Orbital anisotropy in models of NGC 3842 and NGC 4889 | 82 |
| 4.1 | Stellar luminosity density vs. radius in four BCGs | 96 |
| 4.2 | GMOS spectra of NGC 4889, NGC 3842, and NGC 2832 | 100 |
| 4.3 | OSIRIS spectra of NGC 3842 and NGC 7768 | 101 |
| 4.4 | Mitchell Spectrograph spectra of NGC 3842, NGC 7768, and NGC 2832 | 102 |
| 4.5 | Stellar kinematics in NGC 4889 | 105 |
| 4.6 | LOSVD near the velocity dispersion peak in NGC 4889 | 107 |
| 4.7 | Residual image of NGC 4889, after subtracting elliptical isophotes | 108 |
| 4.8 | Stellar kinematics in NGC 3842 | 110 |
| 4.9 | Stellar kinematics in NGC 7768 | 111 |
| 4.10 | Stellar kinematics in NGC 2832 | 113 |
| 4.11 | χ^2 vs. M_\star/L_R and M_\bullet for models of NGC 4889 | 118 |
| 4.12 | χ^2 vs. M_\star/L_R and M_\bullet for models of NGC 3842 | 119 |
| 4.13 | χ^2 vs. M_\star/L_R and M_\bullet for models of NGC 7768 | 121 |
| 4.14 | χ^2 vs. M_\star/L_R and M_\bullet for models of NGC 2832 | 123 |
| 4.15 | Marginalized likelihood function for M_\bullet in NGC 2832 | 125 |
| 4.16 | Orbital anisotropy vs. radius in four BCGs | 127 |
| 4.17 | Three-dimensional velocity dispersion vs. radius in NGC 4889 | 128 |
| 4.18 | Measured black hole masses in four BCGs vs. predictions from scaling relations | 131 |
| 5.1 | Three black hole scaling relations | 146 |
| 5.2 | Power-law fits to $M_\bullet(\sigma)$, using different cuts in σ | 147 |
| 5.3 | Scatter in $\log(M_\bullet)$ for different intervals in σ , L , and M_{bulge} | 151 |
| 6.1 | The $M_\bullet - \sigma$ relation from 2000 to 2012 | 156 |

List of Tables

| | | |
|-----|-----------------------------------------------------------------------------------|-----|
| 2.1 | Spectroscopic observations of NGC 6086 | 21 |
| 2.2 | Results from stellar orbit models of NGC 6086 | 37 |
| 2.3 | PSF and Template Star Trials for NGC 6086 | 52 |
| 3.1 | Spectroscopic observations of NGC 3842 and NGC 4889 | 74 |
| 3.2 | Models of NGC 4889 | 81 |
| 3.3 | Fits to $M_{\bullet}(\sigma)$ and $M_{\bullet}(L)$ | 84 |
| 3.4 | Galaxies with dynamical measurements of M_{\bullet} through July 2011 | 85 |
| 4.1 | Global properties of target galaxies | 94 |
| 4.2 | Spectroscopic observations | 97 |
| 4.3 | Axisymmetric models of NGC 4889 | 117 |
| 4.4 | Axisymmetric models of NGC 3842 | 120 |
| 4.5 | Axisymmetric models of NGC 7768 | 122 |
| 4.6 | Axisymmetric models of NGC 2832 | 124 |
| 5.1 | Galaxies with dynamical measurements of M_{\bullet} through May 2012 | 139 |
| 5.2 | Galaxies with multiple definitions of σ | 143 |
| 5.3 | Power-law fits to $M_{\bullet}(\sigma)$ | 145 |
| 5.4 | Power-law fits to $M_{\bullet}(L)$ | 149 |
| 5.5 | Power-law fits to $M_{\bullet}(M_{\text{bulge}})$ | 149 |

Acknowledgments

Mom, I cannot thank you enough for all you have given me. You have worked tirelessly and passionately to instill your children with integrity and curiosity, and everything I accomplish builds upon the foundation you laid. Joanna and Cameron, you have been my partners in crime since the days you were born. Your opinions and support mean the world to me. Thank you for all you have let me get away with, and all you have refused to.

Concerning astronomy, I owe enormous thanks to my advisors, James Graham and Chung-Pei Ma. James, you demonstrated scientific inquiry by example, provided scaffolding when I needed it, and gave encouragement when I felt progress was slow. Chung-Pei, you kept me pointed toward the finish line, opened doors to numerous collaborations, and provided invaluable perspectives on astronomy as a career. Both of you have nurtured my emerging independence as a scientist and have supported my goals outside the field. I thank Leo Blitz and Bernard Sadoulet for serving on my thesis committee. My academic advisor, Geoff Marcy, was a source of affirmation and enthusiasm on several occasions.

The hunt for massive black holes has been a team effort from day one, and I am grateful for several collaborators' contributions toward this work. Shelley Wright, Karl Gebhardt, Tod Lauer, Jeremy Murphy, and Doug Richstone have provided technical expertise and training, vital intellectual debate, and access to valuable resources. I am excited to continue our work together.

I could not wish for a more exciting group of colleagues than the astronomy community at Berkeley. Every day here has been an opportunity to hear (or overhear) something hilarious and to learn something unexpected. In particular, I want to thank my MONSTER classmates for bringing humor, insight, and companionship to our journey through grad school, and for enforcing full class attendance at grad student parties. Thank you, Linda Strubbe, for hundreds of sincere conversations and for unflagging encouragement. Additional thanks to all the members of the ISEE PDP community, for brightening my outlook and expanding my abilities as a teacher and researcher.

My early path toward inquiry and discovery was nurtured by several exceptional teachers, some of whom hold informal namesakes for the black holes discussed herein: Mr. Bruss (NGC 4889), Mr. Gasper (NGC 3842), Mrs. Wilson (NGC 6086), and Mr. Brame (NGC 7768). Other teachers deserving special recognition (and future black holes to be discovered) are Mrs. Lampert, Professors Hall and Ribner, and Coaches Beaumont and Kauffman. My first steps toward professional science were guided by numerous role models within the

Physics and Astronomy departments at Boston University, especially Professors Chakrabarti, Spence, Brainerd, Carey, Clarke, and Clemens, and Dr. Tim Cook.

It is a great privilege to study worlds millions of light years away while inhabiting a diverse and welcoming one. I am very grateful for the friends who have brought me joy during my first twenty-eight orbits of the Sun. Thank you, Katrine, Cody, Eric, and Tommy, for giving me a place to call home during my last six. Finally, I salute the lifetime members of the Deerfield Distance Crew, my second nuclear family. If it's raining, we're training!

Chapter 1

Introduction

1.1 Galaxies Past and Present

Galaxy evolution is a saga spanning 13 billion years, from the ignition of the very first stars to the astounding diversity of galaxies seen today. In a Universe composed primarily of dark energy (Λ) and cold dark matter (CDM), the battle between gravity and cosmic expansion gave rise to the early collapse of small systems, followed by hierarchical, “bottom-up” merging to form increasingly large structures. Luminous galaxies assembled within the structural web of dark matter halos and subhalos, yet their evolution has been subject to additional processes: interactions between light and atomic matter; gas heating and cooling; star formation, stellar explosions, and chemical enrichment of the cosmos. The combined influences of Λ CDM and baryonic physics have endowed the present-day Universe with a colorful and intriguing mosaic of galaxies: large and small; round, disk, and irregular; passively aging and actively forming new stars.

Galaxies grow by accumulating material from external reservoirs and by merging with other galaxies. Following Recombination – when universal expansion first allowed light and matter to become thermally decoupled – gas collapsed onto regions of high dark matter density. The first galaxies formed when dark matter halos grew massive enough to overcome thermal feedback from early generations of star formation, retaining gas to build long-lived stellar systems (e.g., Bromm & Yoshida 2011, and references therein). Gas falling onto the most massive galaxies first was shock-heated and then cooled to form star-forming disks (e.g., White & Rees 1978; Mo et al. 1998), while streams of cool gas may have flowed along filaments and deposited matter near the centers of high- and low-mass galaxies (e.g., Kereš et al. 2005; Dekel & Birnboim 2006; Brooks et al. 2009). Observed high-redshift galaxies are clearly clumpy, exhibiting localized regions of very high star formation. Still, approximately one third of high-redshift galaxies appear to have rotation-dominated kinematics (e.g., Shapiro et al. 2008; Förster Schreiber et al. 2009).

Galaxy mergers occurred frequently in the early Universe and declined with time as cosmic expansion pushed galaxies further apart. In large Λ CDM simulations of cosmic

structure, major mergers between dark matter halos are found to occur at similar rates across a broad range of halo masses (Fakhouri & Ma 2008; Genel et al. 2010). Major and minor mergers both occur more frequently in dense environments (Fakhouri & Ma 2009). On average, each massive galaxy has experienced one major merger in the past eight billion years, since redshift $z \sim 1$ (e.g., van Dokkum 2005; Bell et al. 2006). Major mergers are efficient at redistributing stellar mass, transforming disks to bulges via violent relaxation (e.g., Toomre 1977). They also provoke gas instabilities and provoke widespread star formation in gas-rich systems. The asymmetric and evolving gravitational potential of a major merger remnant exerts torques on gas originally in circular rotation, depleting its angular momentum and driving inflows toward the nucleus of the remnant. Smaller scale torques – possibly from newly formed stars – are required to channel gas into the inner few parsecs where a black hole may reside (Hopkins & Quataert 2010a,b). The rate of star formation, bulge-to-disk ratio, and photometric and kinematic structure of a major merger remnant depends on the mass ratio, gas fractions, and initial trajectories of the progenitor galaxies (e.g., Barnes 1992; Hernquist et al. 1993; Mihos & Hernquist 1996; Boylan-Kolchin et al. 2005; Boylan-Kolchin et al. 2006; Cox et al. 2006; Burkert et al. 2008). In contrast to the violent consequences of major mergers, minor mergers are more likely to add stellar material at large radii, as the smaller galaxy will become tidally stripped before reaching the nucleus of the primary (e.g., Colpi et al. 1999; Hilz et al. 2012). During a minor merger, gas in the smaller galaxy is prone to ram pressure stripping and often does not survive to form stars (e.g., Sofue 1994; Marcolini et al. 2003).

Galaxies in the present-day Universe can be classified into a few broad categories, albeit with inevitable crossovers and grey areas. Massive galaxies contain star-forming disks with spiral arms, and “red and dead” bulges with old stars. While spiral galaxies exhibit a range of disk-to-bulge mass ratios, massive elliptical galaxies are entirely dominated by an old stellar spheroid. Lenticular or S0 galaxies have a disk and bulge, but little ongoing star formation. Their previous gas supplies may have been heated or stripped by hot intergalactic gas (e.g., Dressler et al. 1997), exhausted by star formation or galaxy winds (e.g., van den Bergh 2009), or preserved in a stable disk (Martig et al. 2009). At lower masses, galaxies have irregular morphologies and ongoing star formation, or are undisturbed dwarf ellipticals. The puniest known galaxies – “ultra-faint” dwarfs – may have lived through a single episode of star formation before supernovae permanently expelled their weakly bound gas reserves.

Elliptical galaxies across a broad mass range lie on a common “fundamental plane” relating their stellar velocity dispersions (σ), effective radii, and average surface brightnesses (e.g., Djorgovski & Davis 1987; Jorgensen et al. 1996). The fundamental plane resembles a “tilted” version of the relationships expected from Virial equilibrium, indicating that the total mass-to-light ratio varies smoothly across the sequence of elliptical galaxies. Observations of galaxies over multiple redshifts demonstrate that the most massive elliptical galaxies stopped forming stars eight to ten billion years ago ($z \sim 1 - 2$), yet have steadily grown in size and mass over a similar interval (e.g., Cowie et al. 1996; Bundy et al. 2006; Trujillo et al. 2006; van Dokkum et al. 2010; Bell et al. 2012). These galaxies were subject to early dissipation, which built a compact bulge and expelled the remaining gas via a combination of

supernovae, stellar winds, and black hole accretion feedback (e.g., Barnes & Hernquist 1996; Khochfar & Silk 2006; Hopkins et al. 2009c; cf. Bruce et al. 2012). It remains unclear which of these mechanisms dominated the quenching of massive ellipticals. The galaxies’ observed evolution from compact bulges to extended spheroids is consistent with the assembly of a stellar envelope from gas-poor major and minor mergers (e.g., Hopkins et al. 2009b, 2010).

1.1.1 Brightest Cluster Galaxies

The most massive galaxies in the present-day Universe are giant ellipticals near the centers of galaxy clusters. These objects are known as central cluster galaxies or Brightest Cluster Galaxies (BCGs), and have typical luminosities (L) of a few times $10^{11} L_{\odot}$ (V -band) or $\sim 10^{12} L_{\odot}$ (K -band). The canonical BCG occupies the very center of its host galaxy cluster and has a “cD” halo of stars, extending well beyond the normal stellar profile for elliptical galaxies. In reality, only $\sim 20\%$ of BCGs have cD halos, and the “central” and “Brightest” galaxy designations do not perfectly overlap (e.g., Oegerle & Hill 2001; von der Linden et al. 2007). In some clusters, the most luminous galaxy does not occupy the center of the cluster’s dark matter halo, and a few clusters feature two central galaxies with nearly equal luminosities. Still, the properties of BCGs warrant attention as an extreme consequence of hierarchical structure formation and galaxy evolution.

Like most giant elliptical galaxies, BCGs typically have old stellar populations and low quantities of cool gas. However, their central regions boast super-solar metallicities and extreme alpha-element enrichment (von der Linden et al. 2007; Loubser et al. 2009; Coccato et al. 2010). Although BCGs tend to have larger effective radii and lower average surface brightnesses than other ellipticals, they have been claimed to occupy the same fundamental plane (Oegerle & Hoessel 1991). It is possible that their cD halos lie off the fundamental plane, if they are fit as a separate component (Gonzalez et al. 2005). They have a higher probability of being prolate or triaxial than lower-mass elliptical galaxies (Porter et al. 1991; Ryden et al. 1993), and very few are rotationally supported (Loubser et al. 2008). Near their centers, many BCGs have flat stellar surface brightness profiles or even central minima (Lauer et al. 2002; Laine et al. 2003), representing extreme versions of the stellar cores commonly found in massive ellipticals. BCGs’ overall luminosities are not just extreme; they are anomalous, lying above the exponential tail of the galaxy luminosity function (e.g., Smith et al. 2009, and references therein).

Competing theories have been proposed for the growth of BCGs, including early-time major mergers (e.g., Merritt 1985; Tremaine 1990; Dubinski 1998), gradual assembly through the merging of smaller sub-halos (e.g., De Lucia & Blaizot 2007), and “cannibalism” of smaller galaxies brought to the cluster center by dynamical friction (e.g., Ostriker & Tremaine 1975; Ostriker & Hausman 1977). These ideas parallel the compact bulge formation and subsequent envelope growth of other massive elliptical galaxies. However, BCGs’ exceptional luminosities and intrinsic shapes suggest that their evolution is not merely a scaled-up version of normal ellipticals’. The major axis of a BCG is often aligned with the overall mass distribution of its host cluster (e.g., Sastry 1968; Carter & Metcalfe 1980; Porter et al. 1991),

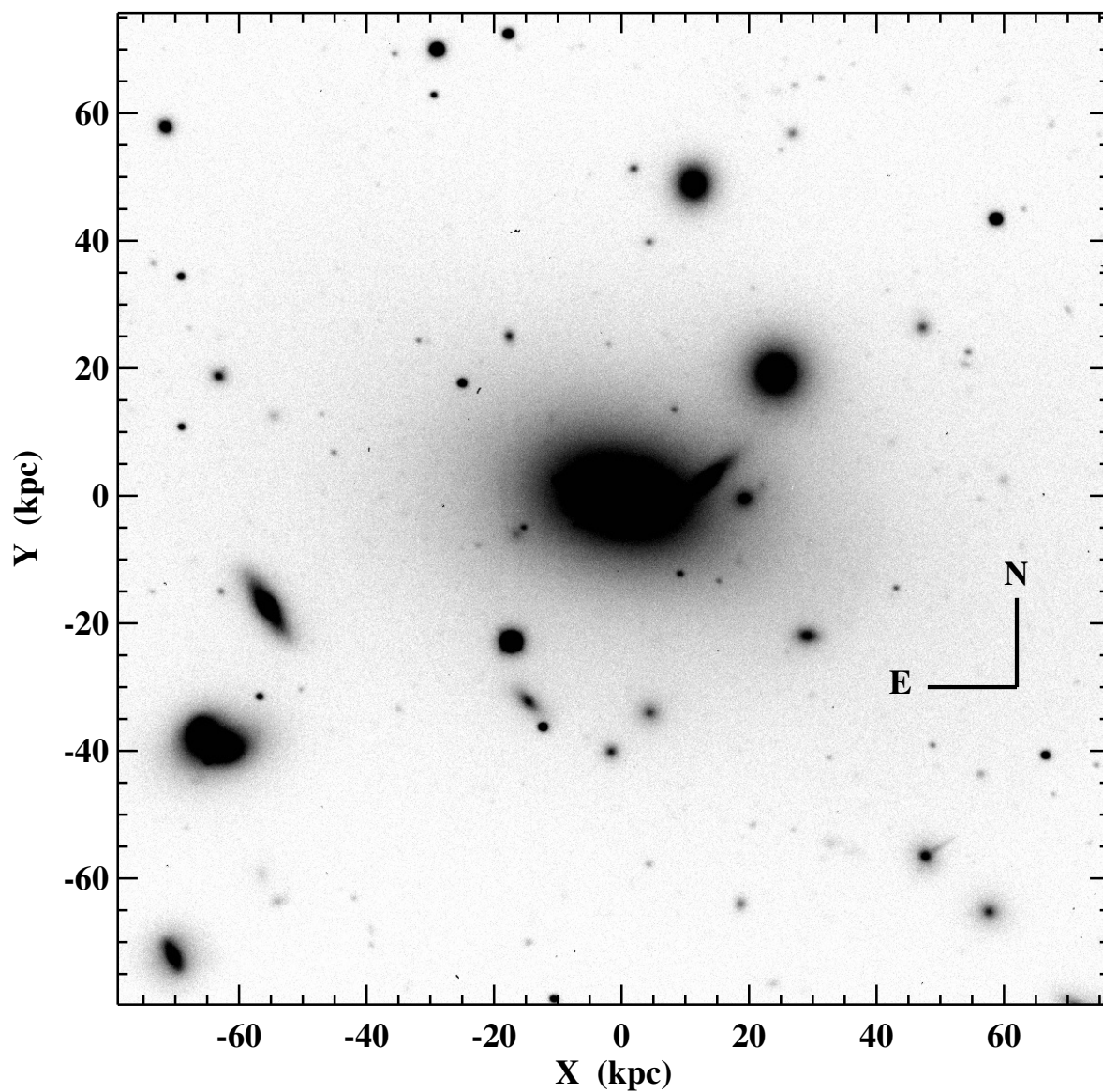


Figure 1.1: Wide-field image of the Brightest Cluster Galaxy NGC 4889 and surrounding galaxies in the Coma galaxy cluster. This image was recorded at Kitt Peak National Observatory and kindly provided by T. R. Lauer.

and in some cases the cD halo is indistinguishable from the intra-cluster light (ICL), the sea of stars bound only to the cluster halo (e.g., Gonzalez et al. 2005). Observations by Burke et al. (2012) indicate that the ICL typically has outgrown the BCG during the past eight billion years ($z < 1$). The combined evidence suggests that a BCG's formation is coupled to the assembly of the cluster halo, and galaxy disruption later populates a physically distinct ICL component. Yet this scenario does not explain the origin of cD halos in BCGs offset from the centers of their host clusters (e.g., Postman & Lauer 1995; Laine et al. 2003). It is unclear whether BCGs possess extreme properties because they formed in particularly massive halos, experienced a particularly large number of hierarchical mergers, or were shaped by special conditions deep inside galaxy clusters.

1.2 Supermassive Black Holes

Supermassive black holes are monstrous objects, whose prominence in popular science and science fiction is well-deserved. The most massive ones weigh billions of solar masses and permanently trap all light and matter approaching within tens to hundreds of astronomical units (AU) – similar to the orbits of our Solar System's outer planets. Unfortunate stars deflected onto chance trajectories toward a supermassive black hole are torn apart or swallowed whole. During collisions between galaxies, black holes tear destructive paths through the wreckage, consuming a few stars and slinging many more into the galaxies' outer reaches. Yet despite their potential for havoc, these beasts spend most of their time slumbering peacefully. Individual stars near a galaxy's center can orbit a supermassive black hole for billions of years without harassment or peril, while stars in the galaxy's outskirts are wholly unaffected by the black hole's presence.

Broadly speaking, every massive galaxy hosts a central supermassive black hole. The general case for their existence is anchored by unambiguous examples in the Milky Way (Schödel et al. 2002; Ghez et al. 2005), the Andromeda Galaxy (Bender et al. 2005), and the maser disk of NGC 4258 (Herrnstein et al. 2005). For each of these cases, the central density required to produce the observed orbits of stars or masers is high enough to rule out a stable cluster of dark objects. At the center of the Milky Way, the only stable alternative to a supermassive black hole is a ball of neutral bosons or fermions, the latter with required particle masses $\sim 10^5$ times larger than the upper limit for neutrino masses (Ghez et al. 2005). A few dozen other galaxies – in particular, elliptical galaxies and spiral or lenticular galaxies with classical bulges – have been found to host massive central objects, which are assumed but not proven to be black holes. Although only a fraction of the nearest elliptical galaxies and bulges can be probed for dynamical evidence of central supermassive objects, the high detection rate suggests that they are ubiquitous in massive spheroidal systems (Gültekin et al. 2011a). Their masses, M_\bullet , range from $\sim 10^6 M_\odot$ (e.g., Greenhill et al. 2003; Kormendy et al. 2011) to over $10^{10} M_\odot$ (McConnell et al. 2011b).

The seeds for present-day supermassive black holes likely formed in the first 300 million years after the Big Bang ($z \sim 15 - 50$), either from the cores of gigantic population III stars

(e.g., Bond et al. 1984; Fryer et al. 2001; Madau & Rees 2001) or from the direct collapse of pure hydrogen clouds with extremely low angular momentum (e.g., Koushiappas et al. 2004; Begelman et al. 2006). Clouds with non-zero initial angular momentum could have collapsed to form massive black holes if pristine conditions in the early Universe suppressed the formation of molecular hydrogen and subsequent cooling below $T \sim 4000$ K (Lodato & Natarajan 2006). The seed black holes may have had initial masses of $10^2 M_\odot$ to $10^6 M_\odot$, depending on the formation mechanism.

Whatever their origins, supermassive black holes grew prolifically to attain their present-day masses. Before the Universe was a billion years old ($z > 6$), black holes with $M_\bullet > 10^9 M_\odot$ shone as quasars, whose light is observed today across enormous distances (e.g., Fan et al. 2001; Mortlock et al. 2011). Over the past eight billion years ($z < 1$) the most massive quasars have gone silent, and present-day quasar activity is dominated by black holes with $M_\bullet < 10^8 M_\odot$ (e.g., Netzer 2003; Vestergaard et al. 2008).

In the early Universe, black holes grew primarily by accreting gas. Cataclysmic events such as mergers between spiral galaxies occur less frequently today, but can still trigger episodes of rapid growth (e.g., Sanders et al. 1988; Hernquist 1989). In individual galaxies, secular processes such as stellar winds or disk instabilities can fuel modest amounts of black hole growth (e.g., Ciotti & Ostriker 2007; Cisternas et al. 2011; Schawinski et al. 2011). Black holes are tremendous sources of gravitational potential energy, which is imparted to infalling matter and converted to kinetic energy or radiation. Such feedback from black holes could have profound effects on their host galaxies. During violent, “quasar-mode” accretion of dense gas, radiation pressure and/or thermal pressure repels inflowing material and drives winds outwards from the galaxy center. These outflows could have sufficient energy and momentum to clear out gas on galactic scales, quenching star formation (Silk & Rees 1998; Di Matteo et al. 2005; Springel et al. 2005; Somerville et al. 2008; cf. Debuhr et al. 2010; Gabor et al. 2011). Low-density gas trickling onto a black hole can produce energetic jets, which shock-heat the interstellar or intergalactic medium (e.g., Binney & Tabor 1995; Churazov et al. 2002). This “radio-mode” feedback may suppress late-time star formation in the most massive galaxies, which hold vast reservoirs of hot gas that would otherwise cool and collapse (e.g., Bower et al. 2006; Croton et al. 2006). Buoyant cavities in X-ray images of galaxies and clusters mark the interactions between black hole jets and hot gas halos (e.g., Fabian et al. 2006).

A third channel for black hole growth occurs during galaxy mergers, even when no gas is present. Dynamical friction causes massive black holes at the centers of the progenitor galaxies to sink to the center of the merger remnant, where they coalesce into a single black hole with the same total mass. This mechanism may be particularly important for black holes in the most massive galaxies, which experience relatively early gas depletion. Cosmological simulations of galaxy assembly and black hole growth indicate that the most massive present-day black holes have acquired at least half of their mass through black hole-black hole merging, which surpassed gas accretion sometime in the past 10 billion years ($z < 2$). In different simulations, the threshold mass where black hole-black hole merging becomes dominant varies from $M_\bullet \sim 10^8 M_\odot$ to $M_\bullet \sim 10^9 M_\odot$ (e.g., Malbon et al. 2007; Yoo

et al. 2007; Fanidakis et al. 2011).

1.3 Scaling Relations between Black Holes and Host Galaxies

Even the largest black holes are dwarfed by their host galaxies, whose stars alone hold hundreds of times as much mass. Consequently, a black hole’s gravitational dominance is confined to a small realm at the very center of the galaxy. Yet M_{\bullet} has been shown to correlate with multiple large-scale galaxy properties, suggesting that black holes still manage to play a role in the evolution of their hosts.

Dressler (1989) was the first to formally assert a proportional scaling relation between black holes and their host galaxies, based on estimates of M_{\bullet} and bulge mass (M_{bulge}) in only five galaxies. In the following decade, the *Hubble Space Telescope* (*HST*) supplied new measurements of M_{\bullet} in over a dozen galaxies, paving the way for the $M_{\bullet} - L$ relation (e.g., Kormendy & Richstone 1995), $M_{\bullet} - \sigma$ relation (Ferrarese & Merritt 2000; Gebhardt et al. 2000a), and an improved $M_{\bullet} - M_{\text{bulge}}$ relation (Magorrian et al. 1998). The 2000’s saw the floodgates burst open, with more measurements from *HST* and the emergence of adaptive optics on ground-based telescopes. The ever-growing sample of black hole masses has fueled astronomers’ ambitions to discover which host galaxy property bears the tightest, “fundamental” relation with the central black hole, resulting in a proliferation of proposed scaling relations. Multiple revisions have been made to the $M_{\bullet} - \sigma$ relation (e.g., Merritt & Ferrarese 2001; Tremaine et al. 2002; Wyithe 2006a,b; Hu 2008; Graham et al. 2011; Gültekin et al. 2009a; Schulze & Gebhardt 2011; McConnell et al. 2011b; Beifiori et al. 2012), $M_{\bullet} - M_{\text{bulge}}$ relation (e.g., Häring & Rix 2004; Hu 2009; Sani et al. 2011; Beifiori et al. 2012), and the $M_{\bullet} - L$ relation in a variety of photometric bandpasses (e.g., Kormendy & Gebhardt 2001; Marconi & Hunt 2003; McLure & Dunlop 2002, 2004; Graham 2007; Hu 2009; Gültekin et al. 2009a; Sani et al. 2011; Schulze & Gebhardt 2011; McConnell et al. 2011b; Beifiori et al. 2012). Recent versions of these correlations are illustrated in Figures 1.2 and 1.3.

Additionally, several authors have explored relations between M_{\bullet} and total galaxy luminosity (e.g., Kormendy & Gebhardt 2001; Kormendy et al. 2011; Beifiori et al. 2012), bulge concentration or Sérsic index (e.g., Graham et al. 2001; Graham & Driver 2007; Beifiori et al. 2012), and the mass or corresponding circular velocity of galaxies’ dark matter halos (e.g., Ferrarese 2002; Baes et al. 2003; Zasov et al. 2005; Kormendy & Bender 2011; Volonteri et al. 2011; Beifiori et al. 2012). Some recent investigations have attempted to link black hole masses with the central stellar cores of some elliptical galaxies (e.g., Lauer et al. 2007a; Kormendy & Bender 2009), or with galaxies’ globular cluster systems (e.g., Burkert & Tremaine 2010; Harris & Harris 2011; Sadoun & Colin 2012).

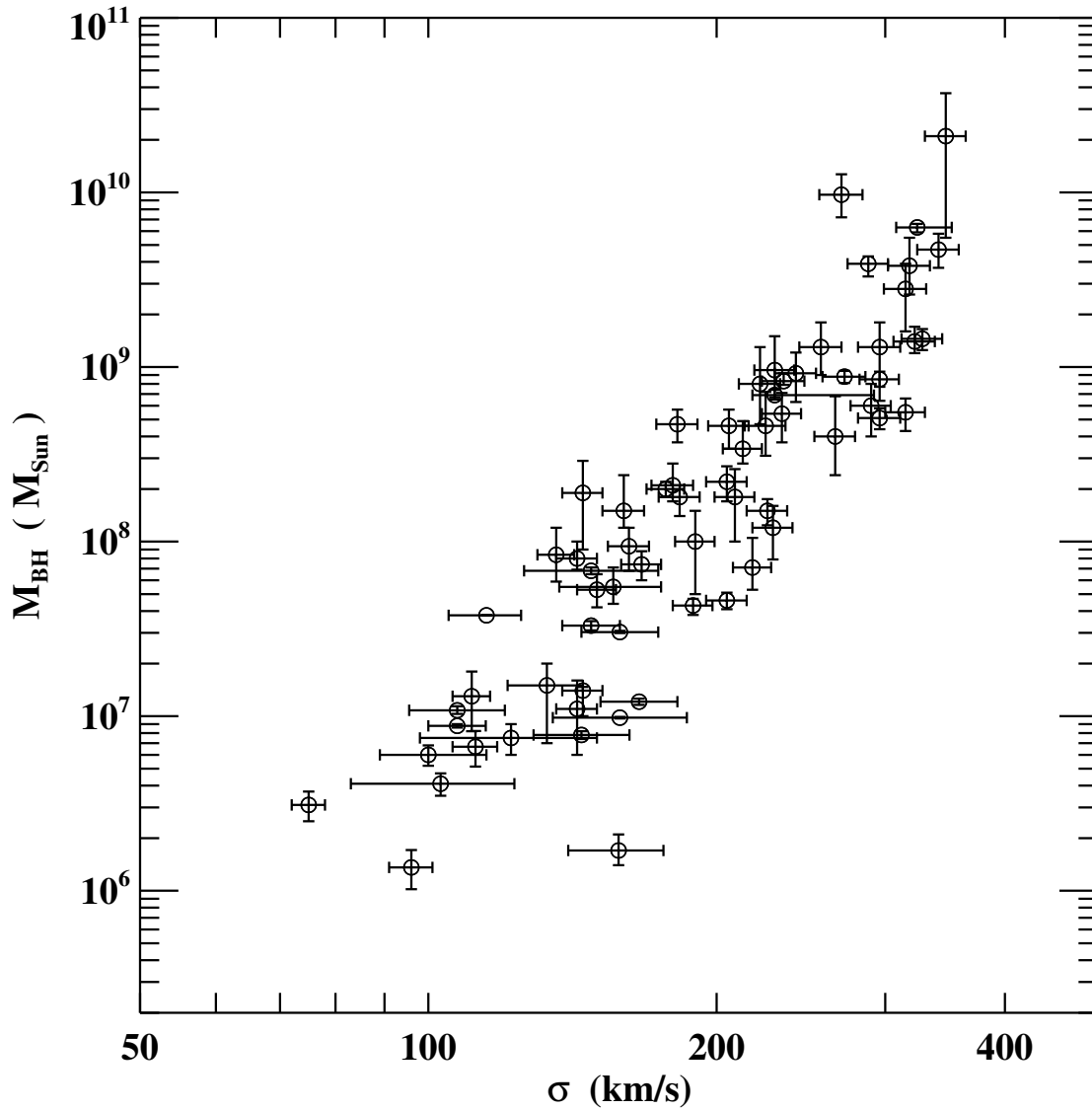


Figure 1.2: Correlation between black hole mass (M_{\bullet}) and host galaxy stellar velocity dispersion (σ), for 65 galaxies with dynamical measurements of M_{\bullet} . This galaxy sample and the best-fit $M_{\bullet}(\sigma)$ relation is discussed in Chapter 5.

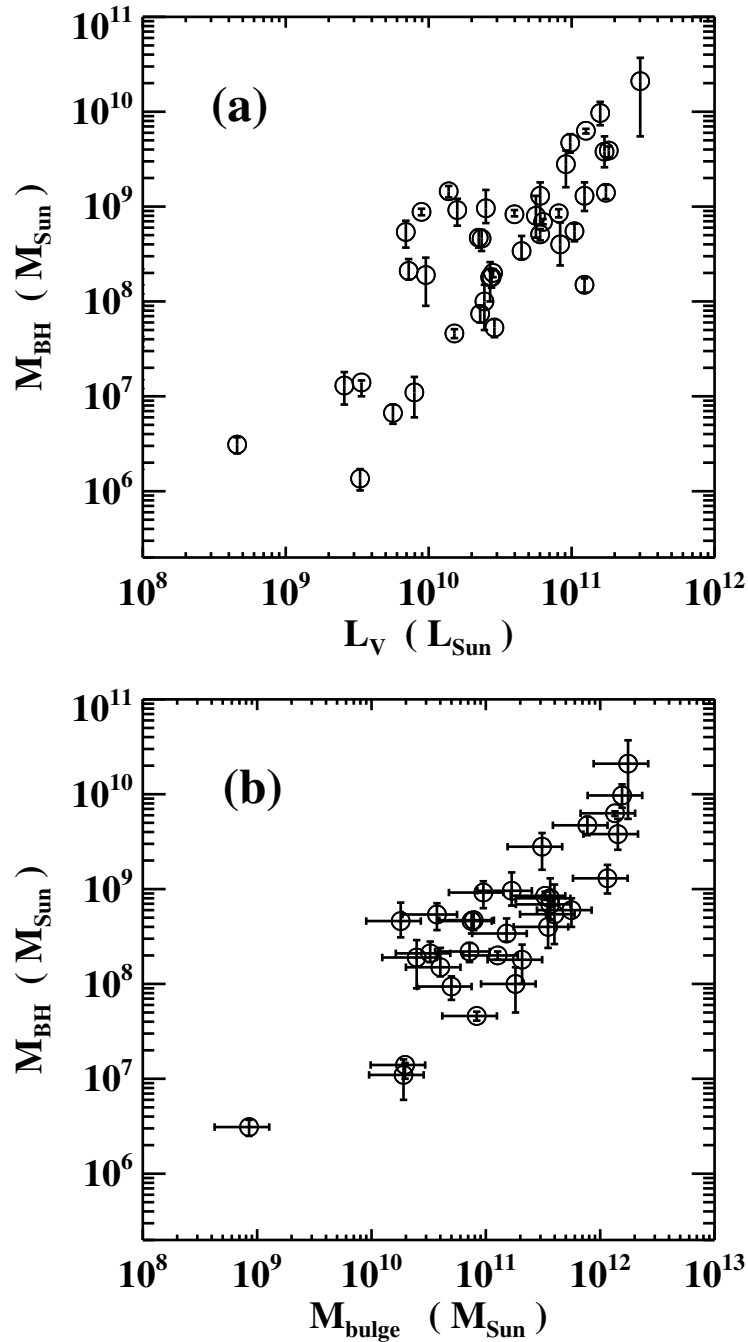


Figure 1.3: (a) Correlation between black hole mass (M_{\bullet}) and host galaxy V -band luminosity (L_V), for 40 galaxies with dynamical measurements of M_{\bullet} . (b) Correlation between black hole mass (M_{\bullet}) and host galaxy bulge mass (M_{bulge}), for 34 galaxies with dynamical measurements of M_{\bullet} . These galaxy samples and the best-fit $M_{\bullet}(L_V)$ and $M_{\bullet}(M_{\text{bulge}})$ relations are discussed in Chapter 5.

Black hole masses appear to correlate most tightly with the bulge component of their host galaxies, with no apparent correlation between M_{\bullet} and disk mass (e.g., Kormendy & Gebhardt 2001). Black holes only correlate weakly with galaxy “pseudobulges,” compact central components with disk-like photometric and kinematic properties (e.g., Kormendy et al. 2011). The special link between black holes and classical bulges suggests that the majority of past black hole growth has been driven by galaxy mergers, rather than secular processes.

In spite of the tremendous efforts invested in establishing and updating the black hole scaling relations, the present set of galaxies with well-measured black hole masses is limited. Some of the most interesting questions about black hole and galaxy growth are best probed at the extreme ends of the galaxy mass function, where direct measurements of M_{\bullet} are sparse. For instance, competing models for the cosmic abundance and initial mass of super-massive black hole seeds predict notably different trends in M_{\bullet} for present-day galaxies with $\sigma < 100 \text{ km s}^{-1}$ (e.g., Volonteri et al. 2008; Volonteri & Natarajan 2009). Unfortunately, these galaxies are predicted to host black holes with $M_{\bullet} < 10^7 M_{\odot}$, whose gravitational influence on surrounding stars is undetectable at distances beyond a few Mpc. At the opposite end, accurate estimates of the black hole mass function out to $M_{\bullet} \sim 10^9 - 10^{10} M_{\odot}$ are needed to determine the space densities and duty cycles of the most energetic quasars and radio galaxies. Yet the large distances and faint centers of extremely luminous galaxies present observational challenges for directly measuring M_{\bullet} . Additionally, the galaxy velocity dispersion function saturates, such that galaxies with $\sigma \approx 350 \text{ km s}^{-1}$ span more than an order of magnitude in L (Bernardi et al. 2007; Lauer et al. 2007a). For the most luminous elliptical galaxies, black hole masses predicted from the $M_{\bullet} - L$ relation can exceed the σ -based predictions by factors $\sim 2 - 10$ (Lauer et al. 2007a).

The steep $L - \sigma$ relation in BCGs and other massive elliptical galaxies could arise from gas-poor mergers under a variety of mass ratios and initial orbits (e.g., Boylan-Kolchin et al. 2005; Boylan-Kolchin et al. 2006; Hopkins et al. 2010). This is broadly consistent with expectations that black holes in massive galaxies grow via black hole-black hole mergers at late times (e.g., Malbon et al. 2007; Yoo et al. 2007), and one would therefore expect today’s most massive ellipticals to follow the $M_{\bullet} - L$ and $M_{\bullet} - M_{\text{bulge}}$ relations. However, numerous investigations of quasar hosts at $z \sim 0.5 - 2$ have produced evidence that galaxies’ $M_{\bullet}/M_{\text{bulge}}$ ratios were greater in the past (e.g., McLure et al. 2006; Peng et al. 2006a,b; Merloni et al. 2010; Bennert et al. 2011). It is possible that σ and M_{\bullet} were both set by an early phase of gas-rich growth, which may be reflected by the present-day $M_{\bullet} - \sigma$ relation.

Estimates of M_{\bullet} in high-redshift quasars suggest that black holes with $M_{\bullet} > 10^{10} M_{\odot}$ existed as early as 1.5 billion years after the Big Bang (Netzer 2003; Shemmer et al. 2004; Netzer et al. 2007; Vestergaard et al. 2008). Few galaxies have sufficiently large σ or L to place these enormous black holes on the present-day scaling relations. Their current whereabouts may correspond to extreme systems such as BCGs, or they may indicate a large degree of cosmic scatter in M_{\bullet} . BCGs and non-BCGs have not been systematically surveyed for extremely massive black holes, and discrepant predictions from the $M_{\bullet} - \sigma$ and $M_{\bullet} - L$ relations have not been resolved empirically. The work presented in this dissertation

is an early step toward addressing these issues.

1.4 Measuring Black Hole Masses

Even when they are not accreting, black holes betray their presence gravitationally, and their masses can be determined from careful observations of the surrounding stars and/or gas. The most reliable measurements use observations with very high spatial resolution, revealing the geometric configuration of orbiting objects and distinguishing the spatial region where the black hole’s gravity dominates other sources of mass. Stars serve as excellent tracers, as they are only subject to gravitational forces. However, stellar motions are typically measured from spectroscopic absorption features, requiring high-quality data and careful template modeling. In some galaxies, bright emission lines trace the kinematics of an extended gas disk surrounding the black hole. Orbiting gas could be subject to non-gravitational effects such as turbulence or thermal or magnetic pressure, but many of these nuclear disks show evidence of Keplerian rotation. A few galaxies exhibit maser emission from multiple points in a disk very close to the black hole. Long-baseline radio interferometry can measure the positions and velocities of maser sources to deliver extremely precise measurements of M_{\bullet} (e.g., Herrnstein et al. 2005; Kuo et al. 2011). Interestingly, only a handful of galaxies have had M_{\bullet} measured using multiple tracers. The independent measurements are broadly consistent for NGC 3379 (Shapiro et al. 2006), NGC 5128 (Neumayer et al. 2007; Cappellari et al. 2009), and NGC 4258 (Siopis et al. 2009), whereas there are significant discrepancies for M87 (Macchetto et al. 1997; Gebhardt & Thomas 2009), IC 1459 (Cappellari et al. 2002), and NGC 3998 (Walsh et al. 2012).

Other techniques for estimating M_{\bullet} do not spatially resolve the black hole’s gravitation influence, but remain useful for quasars and active galactic nuclei (AGN) across a large redshift range. Reverberation mapping tracks the time-varying luminosity of the AGN continuum and broad emission lines, uses time lags to measure the orbital distance of line-emitting clouds, and computes M_{\bullet} from the velocity broadening of AGN emission features and the corresponding orbital radii. These measurements of M_{\bullet} invoke assumptions about the geometry and equilibrium state of the orbiting gas, which can be calibrated by normalizing large reverberation mapping samples to the $M_{\bullet} - \sigma$ relation for galaxies with dynamical black hole mass measurements (Onken et al. 2004; Woo et al. 2010). Reverberation mapping studies have also established tight correlations between the optical or X-ray luminosity of AGN and the characteristic orbital radii of various broad-line emission regions (e.g., Kaspi et al. 2000; McLure & Jarvis 2002; Greene et al. 2010b). In quasars and AGN with single-epoch spectra, M_{\bullet} can be estimated by combining these relations with broad-line velocities, under similar geometric assumptions. The typical uncertainty of these “Virial” estimates of M_{\bullet} is ~ 0.5 dex, and some measurements may be subject to additional systematic biases (e.g., Vestergaard & Peterson 2006; Marconi et al. 2008; Shen et al. 2008; Fine et al. 2010).

1.4.1 Dynamical Modeling Methods

Stellar dynamical measurements of M_{\bullet} use simple physics, but rely upon sophisticated estimates of a galaxy's internal structure. The center of the Milky Way is a special case, whose nearby proximity allows us to monitor the full orbits of individual stars passing within 100 AU of the supermassive black hole (e.g., Ghez et al. 2005). Present technology does not allow us to resolve individual stars in galaxy nuclei beyond the Milky Way, so we must rely on spectroscopy to measure statistical velocity distributions from the broadening of stellar absorption features. Given these statistical measurements, we must turn to numerical models to learn about the underlying mass distribution. The most powerful models employ the concept introduced by Schwarzschild (1979), which computes time-averaged orbits in a smooth, static gravitational potential, and compares a weighted sum of orbits to observational data. While Schwarzschild's original motivation was to fit models to photometric data and recover the intrinsic shape of a galaxy, multiple groups have developed the models further to fit galaxy kinematics (Richstone & Tremaine 1984; Rix et al. 1997; van der Marel et al. 1998; Cretton et al. 1999b; Gebhardt et al. 2000b; Valluri et al. 2004; Thomas et al. 2004, 2005; van den Bosch et al. 2008). These newer models can be used to determine mass-to-light ratios, dark matter halo profiles, and black hole masses.

There are a few notable differences between families of stellar orbit models. Two-integral or Jeans models sample only the energy and angular momentum distributions of orbiting stars, and yield analytic predictions for the second moment of the stellar velocity profile at each spatial location. Three-integral or Schwarzschild models propagate orbits numerically and can accommodate a greater variety of orbital configurations and velocity distributions. All models must make assumptions about the overall shape of the gravitational potential. Most existing measurements of M_{\bullet} have employed axisymmetric models (e.g., Cretton et al. 1999b; Gebhardt et al. 2000b; Valluri et al. 2004), but one model has been developed recently for triaxial potentials (van den Bosch et al. 2008). Finally, a common assumption in stellar orbit models is that the mass distribution of the galaxy follows the light distribution. This assumption becomes invalid at large orbital radii, where dark matter makes a significant contribution to the total enclosed mass. Recent models have incorporated a spherical dark matter halo in addition to the stellar mass component (e.g., Gebhardt & Thomas 2009; Schulze & Gebhardt 2011). In some cases, stellar bulge and disk components are modeled with separate mass-to-light ratios (e.g. Nowak et al. 2007, 2010).

Black hole mass measurements based on gas or maser emission rely on relatively simple models of a thin disk in Keplerian rotation. The enclosed mass is modeled as a black hole plus the galaxy's inner stellar mass profile, and a grid of models are run to determine the best-fit ranges for M_{\bullet} , the stellar mass-to-light ratio, and the disk inclination. To better fit the observed kinematics, these models often include prescriptions for warps in the disk and for enhanced gas velocity dispersions (see, e.g., Shapiro et al. 2006; Dalla Bontà et al. 2009).

1.4.2 Observations

A number of telescopes and instruments are capable of performing spectroscopy with sub-arcsecond spatial resolution. However, we must overcome exceptional observational challenges in order to measure black hole masses in BCGs. First, BCGs and similarly luminous galaxies are extremely rare. Assessing a significant sample requires observations at distances ~ 100 Mpc, with corresponding angular scales of ~ 50 pc per $0.1''$. At these scales, the gravitational influence of a $5 \times 10^9 M_\odot$ black hole is barely resolvable under seeing-limited conditions. Spectrographs aboard *HST* can attain angular resolution $\sim 0.1''$, and have had tremendous success measuring black holes in high-surface-brightness galaxies. However, BCGs have low effective surface brightnesses and extreme stellar cores, and large-aperture telescopes are required to measure their kinematics from stellar absorption spectra. In recent years, the development of adaptive optics has equipped ground-based telescopes with near-diffraction-limited resolution at near-infrared wavelengths. For 8- to 10-meter telescopes, this rivals the angular resolution of *HST* and finally allows for observations with sufficient sensitivity and spatial resolution to measure M_\bullet in BCGs. Ground-based telescopes gain further advantages from integral-field spectrographs, which probe stellar kinematics in a two-dimensional grid instead of a narrow slit.

We have begun an extended campaign to measure stellar kinematics and black hole masses at the centers of BCGs. The outcome will be a dramatic extension of the existing sample of BCGs with well-measured M_\bullet . Prior to our work, stellar dynamical measurements of M_\bullet existed for only three BCG-like galaxies: IC 1459 (Cappellari et al. 2002), NGC 1399 (Houghton et al. 2006; Gebhardt et al. 2007), and M87 (Gebhardt & Thomas 2009). These galaxies all anchor groups or weak clusters within ~ 30 Mpc. Moving to larger distances, Dalla Bontà et al. (2009) have used *HST* to study three BCGs with nuclear gas disks. They report two measurements of M_\bullet and one upper limit, but find few other examples of BCGs with gas emission suitable for measuring M_\bullet .

With large ground-based telescopes, we can measure stellar kinematics in a dozen or more BCGs. Our limiting distance is approximately 150 Mpc, beyond which we struggle to resolve the gravitational influence of all but the most massive black holes. Many BCGs' centers are too faint to observe even with 8-meter class telescopes, so our sample is selected for central surface brightness ($\mu_I < 16$ mag arcsec $^{-1}$). For our initial investigation, we have chosen galaxies with high-resolution photometry from *HST* (Laine et al. 2003) and noteworthy predictions for M_\bullet . We are particularly interested in galaxies predicted to host black holes with $M_\bullet > 3 \times 10^9 M_\odot$, or galaxies with a large discrepancy between the σ - and L -based predictions for M_\bullet . A few of the galaxies in our initial sample reside in rich galaxy clusters, in contrast to the weaker clusters and groups examined at smaller distances.

1.5 This Dissertation

Herein, we probe the relations between the most massive galaxies and their black holes by describing dynamical black hole mass measurements in five BCGs. Our measurements are based on observations with several integral-field spectrographs, with which we measure stellar kinematics at both large and small radii in each BCG. We have measured M_{\bullet} by pairing the kinematics with orbit superposition models.

In Chapter 2 (McConnell et al. 2011a) we describe our observational techniques, analysis of stellar kinematics, stellar orbit modeling, and statistical analysis methods, as applied to the BCG NGC 6086. In Chapter 3 (McConnell et al. 2011b) we announce the measurement of two black holes with $M_{\bullet} \sim 10^{10} M_{\odot}$, in the BCGs NGC 3842 and NGC 4889. These are the most massive black holes ever measured directly, and we discuss their importance with respect to an updated compilation of black hole mass measurements and the resulting $M_{\bullet} - \sigma$ and $M_{\bullet} - L$ relations. Chapter 4 (McConnell et al. 2012) provides a detailed description of our observations and analysis for NGC 3842 and NGC 4889, plus two additional BCGs. We report a secure measurement of M_{\bullet} in NGC 7768 and an upper limit for M_{\bullet} in NGC 2832. In Chapter 5 we describe a compilation of black hole mass measurements for 65 galaxies, including the five BCGs we have analyzed. We compare the $M_{\bullet} - \sigma$, $M_{\bullet} - L$, and $M_{\bullet} - M_{\text{bulge}}$ relations for several subsamples of galaxies and discuss the scatter in M_{\bullet} over different galaxy mass ranges. Considering different galaxy subsamples and their corresponding scaling relations could provide more stringent constraints for galaxy evolution models and improve predictions for M_{\bullet} in individual galaxies. In Chapter 6, we briefly reflect on the present state of the black hole scaling relations and note future prospects for our observing campaign and related investigations.

Chapter 2

The Black Hole Mass in the Brightest Cluster Galaxy NGC 6086

Abstract

We present the first direct measurement of the central black hole mass, M_\bullet , in NGC 6086, the Brightest Cluster Galaxy (BCG) in Abell 2162. Our investigation demonstrates for the first time that stellar dynamical measurements of M_\bullet in BCGs are possible beyond the nearest few galaxy clusters. We observed NGC 6086 with laser guide star adaptive optics and the integral-field spectrograph (IFS) OSIRIS at the W.M. Keck Observatory, and with the seeing-limited IFS GMOS-N at Gemini Observatory North. We combined the IFS data sets with existing major-axis kinematics, and used axisymmetric stellar orbit models to determine M_\bullet and the R -band stellar mass-to-light ratio, M_\star/L_R . We find $M_\bullet = 3.6_{-1.1}^{+1.7} \times 10^9 M_\odot$ and $M_\star/L_R = 4.6_{-0.7}^{+0.3} M_\odot L_{\odot,R}^{-1}$ (68% confidence), from models using the most massive dark matter halo allowed within the gravitational potential of the host cluster. Models fitting only IFS data confirm $M_\bullet \sim 3 \times 10^9 M_\odot$ and $M_\star/L_R \sim 4 M_\odot L_{\odot,R}^{-1}$, with weak dependence on the assumed dark matter halo structure. When data out to 19 kpc are included, the unrealistic omission of dark matter causes the best-fit black hole mass to decrease dramatically, to $0.6 \times 10^9 M_\odot$, and the best-fit stellar mass-to-light ratio to increase to $6.7 M_\odot L_{\odot,R}^{-1}$. The latter value is at further odds with stellar population studies favoring $M_\star/L_R \sim 2 M_\odot L_{\odot,R}^{-1}$. Biases from dark matter omission could extend to dynamical models of other galaxies with stellar cores, and revised measurements of M_\bullet could steepen the empirical scaling relationships between black holes and their host galaxies. This chapter has been published in the *Astrophysical Journal* (McConnell et al. 2011a).

2.1 Introduction

It is increasingly accepted, both observationally and theoretically, that supermassive black holes are ubiquitous at the centers of elliptical galaxies (Magorrian et al. 1998). The black hole mass, M_\bullet , correlates with various host properties, including bulge luminosity, L (e.g., Kormendy & Richstone 1995; Marconi & Hunt 2003), and stellar velocity dispersion, σ (e.g., Ferrarese & Merritt 2000; Gebhardt et al. 2000a). These empirical correlations have been established from approximately 50 galaxies in which M_\bullet has been determined from motions of stars, gas, or masers under the direct gravitational influence of the central black hole. Although galaxies with $L_V \sim 10^9 - 10^{11} L_{\odot,V}$ are well-represented in this sample (e.g., Häring & Rix 2004; Gültekin et al. 2009a), there are very few measurements of M_\bullet in the most luminous galaxies.

Brightest Cluster Galaxies (BCGs) are the most luminous galaxies in the present-day universe ($L_V \sim 10^{10.5} - 10^{11.5} L_{\odot,V}$). Direct measurements of M_\bullet in these galaxies have been lacking because very few kinematic studies spatially resolve the black hole radius of influence, $r_{\text{inf}} = GM_\bullet/\sigma^2$. The $M_\bullet - \sigma$ relation predicts typical values of $r_{\text{inf}} \sim 30$ pc in BCGs; predictions from the $M_\bullet - L$ relation are a few times larger. BCGs' low central surface brightnesses exacerbate the challenge of obtaining high-quality stellar absorption spectra at angular scales comparable to r_{inf} . To date, stellar dynamical measurements of M_\bullet in BCGs have been limited to the nearest groups and clusters: M87 in Virgo (e.g., Sargent et al. 1978; Gebhardt & Thomas 2009) and NGC 1399 in Fornax (Houghton et al. 2006; Gebhardt et al. 2007). In a small number of BCGs, M_\bullet can be measured from emission line kinematics in a resolved disk of ionized gas. Dalla Bontà et al. (2009) have used STIS on the *Hubble Space Telescope* (*HST*) to examine disks at the centers of three BCGs beyond 50 Mpc, reporting two measurements of M_\bullet and one upper limit.

BCGs are distinct from other giant elliptical galaxies in several respects. Two such distinctions are particularly intriguing with regards to the evolutionary connections between galaxies and their central black holes. First, BCGs are preferentially found near the gravitational centers of galaxy clusters, where cosmological dark matter filaments intersect. Second, BCG luminosities vary more steeply with σ than the canonical $L \propto \sigma^4$ relationship for elliptical galaxies (Oegerle & Hoessel 1991); Lauer et al. (2007a) have found $L \propto \sigma^7$ for BCGs and other core-profile galaxies. The steep relationship between L and σ in very massive galaxies requires one or both of the $M_\bullet - \sigma$ and $M_\bullet - L$ relationships to differ from the correlations observed in lower-mass galaxies. Direct measurements of M_\bullet in a statistically significant sample of BCGs will reveal the forms of these relationships for the most massive galaxies, and will help discriminate different evolutionary scenarios for BCGs. For instance, Boylan-Kolchin et al. (2006) have demonstrated that gas-poor galaxies merging on radial orbits could produce the steep relation between L and σ . With little gas available for star formation or black hole accretion, the remnant galaxy and black hole would remain on the same $M_\bullet - L$ relation as the progenitors. These radial mergers could occur at the intersection of cosmological filaments. In one counterexample, Ruszkowski & Springel (2009) performed a zoom-in resimulation of a single $10^{15} M_\odot$ galaxy cluster selected from a cosmological N -

body simulation, and produced a BCG that remained on nearly the same $L - \sigma$ relation as the fainter galaxies. A larger sample of resimulated clusters would help assess the relative frequency of radial orbits and their impact on the scaling relations of BCGs. Alternative scenarios for BCG growth, such as early-time major mergers (e.g., Merritt 1985; Tremaine 1990) or “cannibalism” of smaller galaxies (e.g., Ostriker & Tremaine 1975; Ostriker & Hausman 1977), potentially could produce lower values of M_\bullet , matching predictions from the $M_\bullet - \sigma$ relationship. In these scenarios, the final black hole mass could depend upon a number of factors, such as the orbits, gas fractions and disk-to-bulge ratios of merging galaxies.

In addition to providing clues toward BCG evolution, empirically establishing the high-mass forms of the $M_\bullet - \sigma$ and $M_\bullet - L$ relationships will provide new constraints for the number density of the Universe’s most massive black holes. The most luminous high-redshift quasars are inferred to host black holes exceeding $10^{10} M_\odot$ (e.g., Bechtold et al. 2003; Netzer 2003; Vestergaard 2004), but thus far no such objects have been detected in the local Universe. BCGs in nearby Abell clusters potentially could host black holes with $M_\bullet > 10^{9.5} M_\odot$ (Lauer et al. 2007a).

Another motivation for measuring M_\bullet in BCGs is that the faint centers of these galaxies likely arise from “core-scouring,” whereby stars are ejected from the galactic centers by an inspiraling pair of supermassive black holes after a major merger (e.g., Ebisuzaki et al. 1991). Given theoretical expectations for the efficiency of core scouring, a galaxy’s past merger history can be estimated by comparing M_\bullet to the total luminosity deficit in the core (Lauer et al. 2007a; Kormendy & Bender 2009).

In this chapter, we report measurements of M_\bullet and the R -band stellar mass-to-light ratio, M_\star/L_R , in NGC 6086, the BCG of Abell cluster 2162. Our investigation marks the first attempt to measure M_\bullet using stellar dynamics in a BCG beyond Virgo. Future papers will describe measurements of M_\bullet in a larger sample of BCGs. For BCGs at ~ 100 Mpc, 8- to 10-meter telescopes with adaptive optics (AO) are required to obtain good spectra on $\sim 0.1''$ spatial scales. Laser guide star adaptive optics (LGS-AO) enables the study of targets without a bright nearby guide star. We use integral-field spectrographs (IFS) to obtain full two-dimensional spatial coverage, which places tighter constraints on stellar orbits. Our orbit models include a dark matter component in the gravitational potential, as described in Gebhardt & Thomas (2009). In this chapter, we emphasize methods for pairing IFS data with axisymmetric orbit models, and for assessing errors in M_\bullet and M_\star/L_R .

NGC 6086 is a cD galaxy at the center of Abell 2162. Like many BCGs, it exhibits radio emission (Ledlow & Owen 1995), likely from low-level accretion onto the central black hole. We have derived an effective stellar velocity dispersion of 318 km s^{-1} in NGC 6086, using measurements from Carter et al. (1999). This would correspond to a black hole mass of $9 \times 10^8 M_\odot$, if NGC 6086 were to follow the mean $M_\bullet - \sigma$ relation of Gültekin et al. (2009a). The V -band luminosity of NGC 6086 is $1.4 \times 10^{11} L_{\odot,V}$, from $M_V = -23.11$ in Lauer et al. (2007a); the corresponding black hole mass predicted from the mean $M_\bullet - L$ relation of Gültekin et al. (2009a) is $1.3 \times 10^9 M_\odot$. Abell 2162 is a relatively small galaxy cluster at redshift $z = 0.032$, with a richness class of 0 based on 37 members (Abell et al. 1989), and a line-of-sight velocity dispersion of $302_{-58}^{+132} \text{ km s}^{-1}$ (Zabludoff et al. 1993). NGC

6086 is offset from the average radial velocity of Abell 2162, by 82 km s^{-1} (Laine et al. 2003).

This chapter is organized as follows. In Section 2.2, we describe our photometric data of NGC 6086, our IFS observations at Keck and Gemini observatories, and the subsequent data reduction procedures. In Section 2.3, we describe our procedures for extracting two-dimensional kinematics from IFS data, and compare our resulting measurements in NGC 6086 with other studies. In Section 2.4 we review the stellar orbit modeling procedure. We also report our measurements of M_\bullet and M_\star/L_R , and describe how these measurements depend on the assumed dark matter halo profile. We estimate confidence intervals for M_\bullet and M_\star/L_R , and discuss both tested and un-tested systematic errors. In Section 2.5 we compare our results to predictions from the $M_\bullet - \sigma$ and $M_\bullet - L$ relationships, and discuss whether the effect of dark matter on stellar orbit models of NGC 6086 can be generalized to reveal biases in measurements of M_\bullet in other galaxies. Section 2.6 contains a detailed description of systematic errors from stellar template mismatch and uncertain PSFs. Section 2.7 contains our full set of measured line-of-sight velocity distributions (LOSVDs).

Throughout this chapter, we assume $H_0 = 70 \text{ km s}^{-1}$, $\Omega_m = 0.27$, $\Omega_\Lambda = 0.73$, and an angular-diameter distance of 133 Mpc to NGC 6086. One arc sec corresponds to 0.64 kpc at this distance; for $\sigma = 318 \text{ km s}^{-1}$, $r_{\text{inf}} = 0.066'' \times (M_\bullet/10^9 M_\odot)$.

2.2 Observations

2.2.1 Photometry

We use a combination of R -band ($0.6 \mu\text{m}$) and I -band ($0.8 \mu\text{m}$) photometry to constrain the stellar mass profile of NGC 6086. For radii out to $10''$ we adopt the high-resolution surface brightness profile presented in Laine et al. (2003), obtained with WFPC2 on the *Hubble Space Telescope*. This surface brightness profile has been corrected for the WFPC2 point-spread function (PSF) by applying the Lucy-Richardson deconvolution method (Richardson 1972; Lucy 1974); specific details of the implementation are described in Laine et al. (2003).

At larger radii out to $86''$ we use R -band data from Lauer, Postman & Strauss (private communication), obtained with the 2.1-m telescope at Kitt Peak National Observatory (KPNO). The KPNO data have a field-of-view (FOV) of $5.2' \times 5.2'$, which enables accurate sky subtraction. To create a single surface brightness profile, we assessed the individual profiles from WFPC2 and KPNO data at overlapping radii between $5''$ and $10''$. We measured the average $R - I$ color for these radii and added it to the WFPC2 profile. The two profiles were then stitched together such that their respective weights varied linearly with radius between $5''$ and $10''$: the WFPC2 data contribute 100% to the combined profile for $r \leq 5''$ and the KPNO data contribute 100% for $r \geq 10''$. PSF deconvolution was not necessary for the KPNO data, as they contribute to the combined surface brightness profile at radii well beyond the seeing full-width at half-maximum (FWHM). Our translation of the WFPC2 profile to R -band assumes no $R - I$ color gradient; Lauer et al. (2005) find a median color gradient, $\frac{\Delta(V-I)}{\Delta \log(r)}$, of -0.03 magnitudes for BCGs and other core profile galaxies.

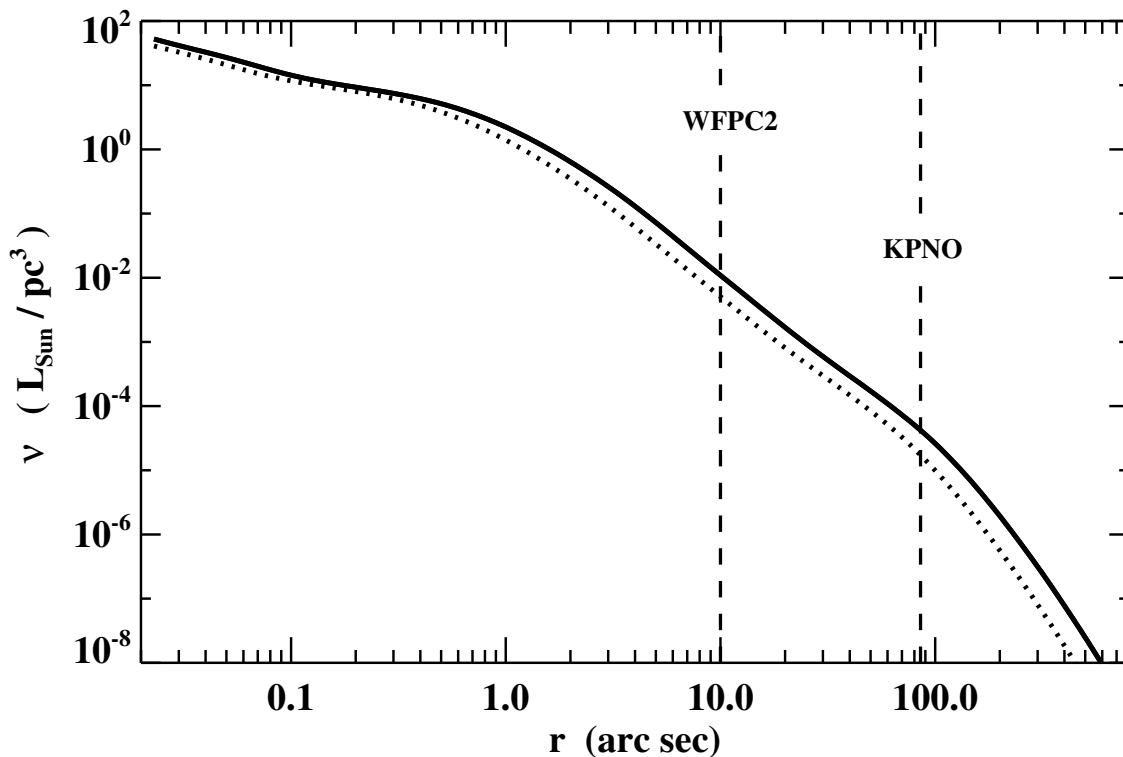


Figure 2.1: De-projected R -band stellar luminosity density *vs.* radius along the major axis (solid line) and minor axis (dotted line) of NGC 6086. The dashed vertical lines mark the outermost extents of photometric data from *HST*/WFPC2 and KPNO. Luminosity densities beyond $86''$ are derived from a de Vaucouleurs surface brightness profile. The R -band surface brightness at $86''$ is $24.3 \text{ mag arcsec}^{-2}$ on the major axis.

At radii beyond $1''$, isophotes of NGC 6086 all have major-axis position angles within 5° of true north, with an average apparent axis ratio of 0.7. We adopt 0° east of north as the major-axis position angle of NGC 6086, and we assume edge-on inclination. We deprojected the surface brightness using the procedure of Gebhardt et al. (1996), which assumes spheroidal isodensity contours. The resulting major- and minor-axis luminosity density profiles are shown in Figure 2.1.

2.2.2 Spectroscopy

We performed integral-field spectroscopic observations of NGC 6086 with OSIRIS (Larkin et al. 2006) on the 10-m W. M. Keck II telescope and GMOS-North (Allington-Smith et al. 2002; Hook et al. 2004) on the 8-m Gemini Observatory North telescope. The instrument properties and our observations are summarized in Table 2.1. Our observations with OSIRIS used the W. M. Keck Observatory laser guide star adaptive optics (LGS-AO) system (van Dam et al. 2006; Wizinowich et al. 2006); the inner component of the resulting H -band ($1.6 \mu\text{m}$) PSF has an FWHM value of $\approx 0.1''$. The GMOS data were collected under excellent seeing conditions; images of point sources from the Gemini North Acquisition Camera¹ indicate an I -band FWHM of $0.4''$.

In Figure 2.2 we display the reduced mosaic of NGC 6086 from OSIRIS, summed over all spectral channels. Usable data from OSIRIS and GMOS extend to radii of $0.84''$ and $4.9''$, respectively. For radii out to $30''$ we use major-axis kinematics from Carter et al. (1999), obtained with the Intermediate Dispersion Spectrograph (IDS)² on the 2.5-m Isaac Newton Telescope.

2.2.2.1 OSIRIS

OSIRIS is a near-infrared (NIR), integral-field spectrograph built for use with the Keck AO system. It features two-dimensional spatial sampling at four scales between $0.02''$ and $0.1''$. We observed NGC 6086 with the $0.05''$ spatial scale, which provided adequate signal-to-noise and placed several pixels within the radius of influence. To minimize noise in individual spectra, we used the broad H -band filter, which covered several $\Delta\nu = 3$, ^{12}CO bandheads at observed wavelengths from $1.54 \mu\text{m}$ to $1.71 \mu\text{m}$ (at $z \approx 0.032$). We chose to detect H -band features instead of the more prominent $\nu = 0-2$ ^{12}CO bandhead in K -band, which suffered from higher thermal background at an observed wavelength of $2.37 \mu\text{m}$.

We recorded 9 science exposures of the galaxy center and 5 sky exposures of a blank field $50''$ away, for total integration times of 2.25 hr and 1.25 hr, respectively. Our dithers repeated an “object-sky-object,” sequence, such that every science frame was immediately preceded or followed by a sky frame. We also recorded spectra of 9 spectral template stars, using the same filter and spatial scale as for NGC 6086. To measure telluric absorption,

¹<http://www.gemini.edu/sciops/telescopes-and-sites/acquisition-hardware-and-techniques/acquisition-cameras>

²<http://www.ing.iac.es/Astronomy/instruments/ids/>

Table 2.1: Spectroscopic observations of NGC 6086

| Instrument | UT Date | λ Range (nm) | $\Delta\lambda$ (nm) | Δx (arc sec) | t_{int} (s) | PA ($^{\circ}$) | FWHM (arc sec) |
|------------|----------------|-------------------------|-------------------------|-------------------------|------------------|----------------------|-------------------|
| (1) | (2) | (3) | (4) | (5) | (6) | (7) | (8) |
| OSIRIS | 2008 May 13-14 | 1473-1803 | 0.2 | 0.05 | 9×900 | -45 | 0.10 |
| GMOS | 2003 Apr 25 | 744-948 | 0.1377 | 0.2 | 5×1200 | 0 | 0.4 |
| IDS | 1996 Jun 10-16 | 493-573 | 0.2 | 0.4×3.0 | 22,800 | 0 | 1.3 |

Notes: Column 1: instrument. OSIRIS (OH-Suppressing Infra-Red Imaging Spectrograph) was used on Keck II with LGS-AO. GMOS (Gemini Multi-Object Spectrograph) was used on Gemini North. IDS (Intermediate Dispersion Spectrograph) was used on the Isaac Newton Telescope; here we summarize the observations published by Carter et al. (1999). Column 2: date(s) of observations. Column 3: observed wavelength range. Column 4: spectral pixel scale in 3-d data cubes, for OSIRIS and GMOS data. FWHM spectral resolution, for IDS data. Column 5: angular spacing of lenslets, for OSIRIS and GMOS data. Pixel scale along slit \times slit width, for IDS data. Column 6: number of science exposures \times integration time per exposure. For IDS data, the total integration time of 6.33 hours is reported from Carter et al. (1999). Column 7: position angle of the long axis for OSIRIS and GMOS, or the slit for IDS, in degrees east of north. Column 8: PSF FWHM at science wavelengths.

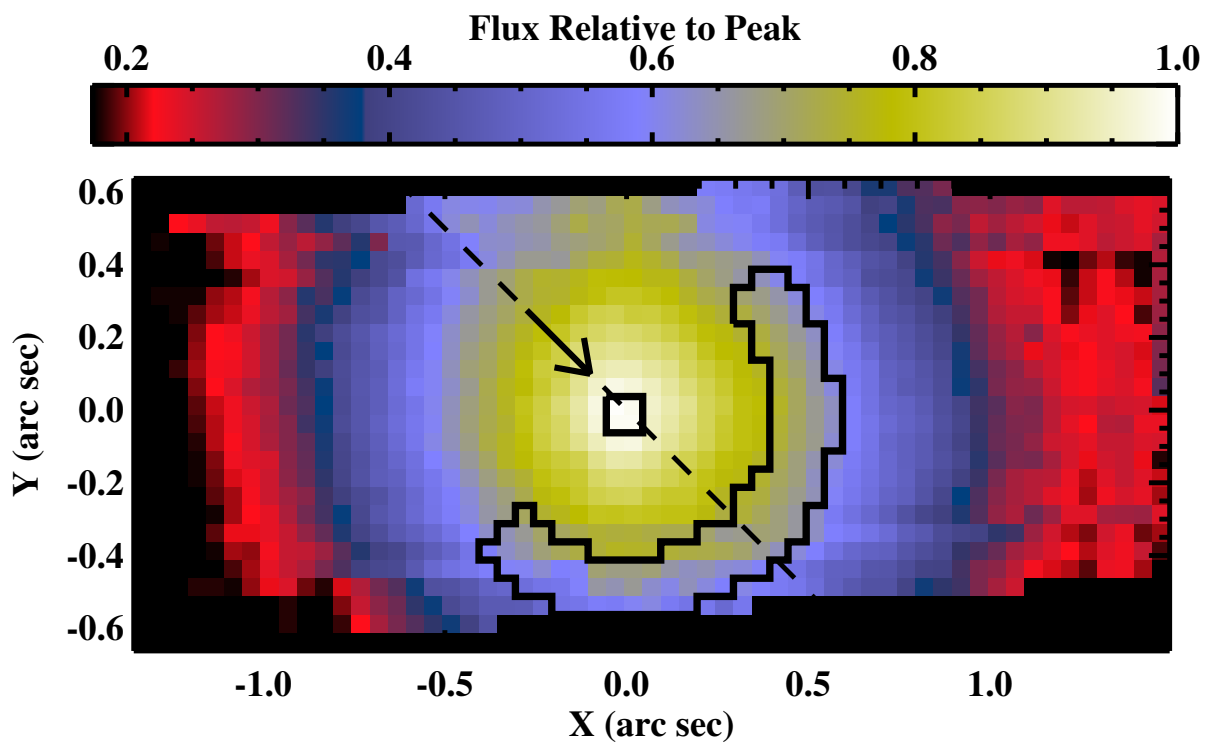


Figure 2.2: Total H -band flux for NGC 6086, using collapsed spectra from OSIRIS. The dashed line traces the major axis of the galaxy, with the arrow pointing north. Thick black lines enclose the spatial bins corresponding to the spectra displayed in Figure 2.3.

we recorded spectra of several A0V stars, covering a range of airmasses similar to those for NGC 6086 and template stars.

We used version 2.2 of the OSIRIS data reduction pipeline³ to subtract sky frames, correct detector artifacts, perform spatial flat-fielding, calibrate wavelengths, generate data cubes with two spatial dimensions (x, y) and one spectral dimension (λ), and construct a mosaic of NGC 6086 from multiple data cubes. The pipeline uses an archived calibration file to perform spectral extraction of the raw spectra across the detector and assemble a data cube; the calibration file was generated by illuminating individual columns of the OSIRIS lenslet array with a white light source. We used custom routines to remove additional bad pixels from detector images, extract one-dimensional stellar spectra from three-dimensional data cubes, and calibrate galaxy and template spectra for telluric absorption. Although one-dimensional stellar spectra from OSIRIS comprise an average over many spatial pixels, spatial variations in instrumental resolution are negligible relative to the velocity broadening in NGC 6086: $(\Delta\sigma_{\text{inst}})^2 \sim 5 \times 10^{-3} \sigma^2$.

Contamination from telluric OH emission presents a severe challenge for observing faint, extended objects with OSIRIS. The small field of view ($0.8'' \times 3.2''$ for broadband observations at $0.05''$ per spatial pixel) does not allow for in-field sky subtraction, and subtracting consecutive science and sky frames only provides partial correction, as the relative flux from different vibrational transitions in OH varies on timescales of a few minutes. After subtracting a sky frame from each science frame, we are forced to discard the spectral channels with strong residual signals from OH, which compose approximately 15% of our spectral range. In Figure 2.3, we illustrate representative spectra from OSIRIS and distinguish kinematic fitting regions from residual telluric features. At both ends of the H -band spectrum, atmospheric water vapor acts as an additional contaminant. We have restricted our kinematic analysis to observed wavelengths between 1.48 and 1.73 μm .

A second challenge for studying the centers of galaxies with OSIRIS is accurate determination of the PSF. We must construct an average PSF for mosaicked data from several hours of observations over multiple nights, during which seeing conditions and the quality of AO correction can change significantly. To estimate the PSF, we recorded a one-time sequence of exposures of the LGS-AO tip/tilt star for NGC 6086, using the OSIRIS spectrograph with the same filter and spatial scale settings as for our science frames. Data cubes were then collapsed along the spectral dimension to produce images of the star. In Section 2.6, we discuss different methods for estimating the PSF, and how PSF uncertainty influences our modeling results.

2.2.2.2 GMOS

GMOS-N is a multi-purpose spectrograph on Gemini North. GMOS includes an IFS mode, in which hexagonal lenslets divide the focal plane and fibers map the two-dimensional field to a one-dimensional slit configuration. A second set of lenslets samples a field $\sim 60''$

³available from the UCLA Infrared Laboratory, at <http://irlab.astro.ucla.edu/osiris/pipeline.html>

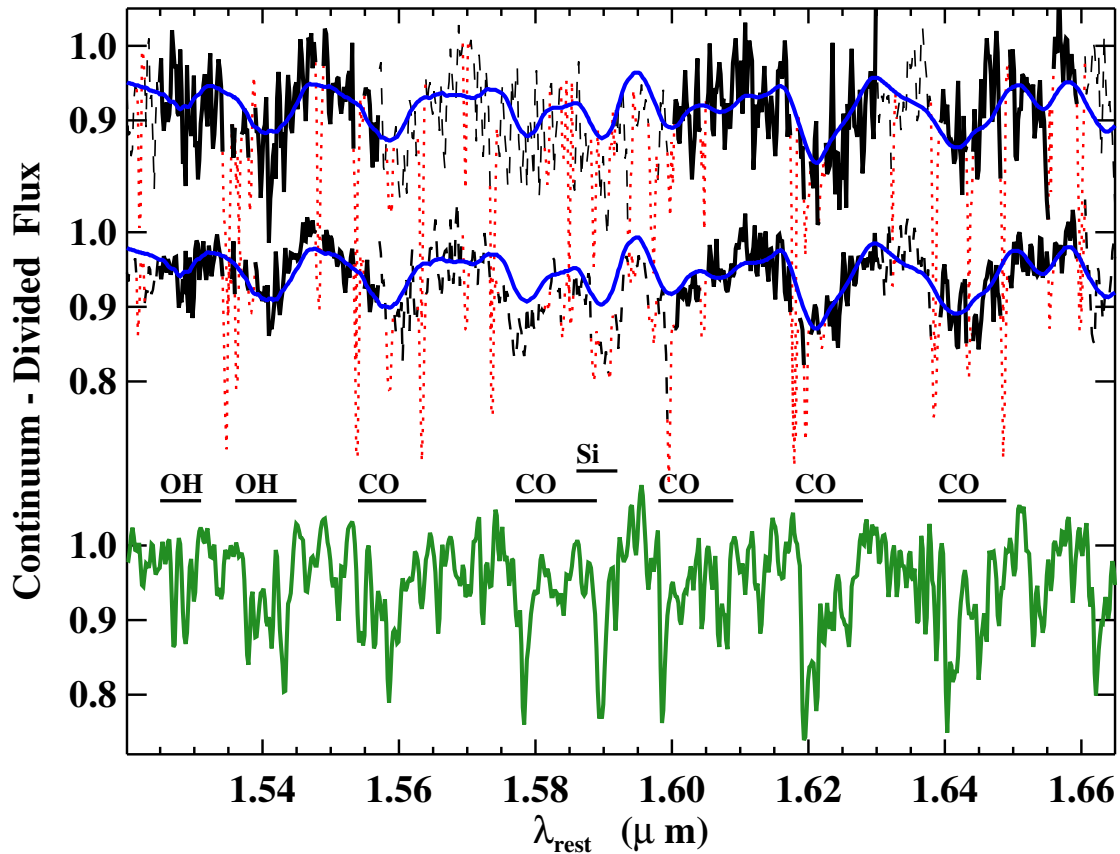


Figure 2.3: OSIRIS spectra of NGC 6086 and template star. *Top*: OSIRIS spectrum of the center of NGC 6086 (0.01 arcsec^2 ; $S/N = 21$). *Middle*: OSIRIS spectrum $0.49''$ from the center of NGC 6086 (0.28 arcsec^2 ; $S/N = 39$). The dashed and dotted portions of OSIRIS spectra are excluded from the kinematic fitting, with red dotted portions specifically indicating regions of telluric OH contamination. Each thick blue line is the M4III template spectrum from OSIRIS, convolved with the best-fit LOSVD for the respective galaxy spectrum. *Bottom*: Spectrum of template star HD 110964 (M4III), from observations with OSIRIS. This is the only star used in our final extraction of kinematics from OSIRIS data.

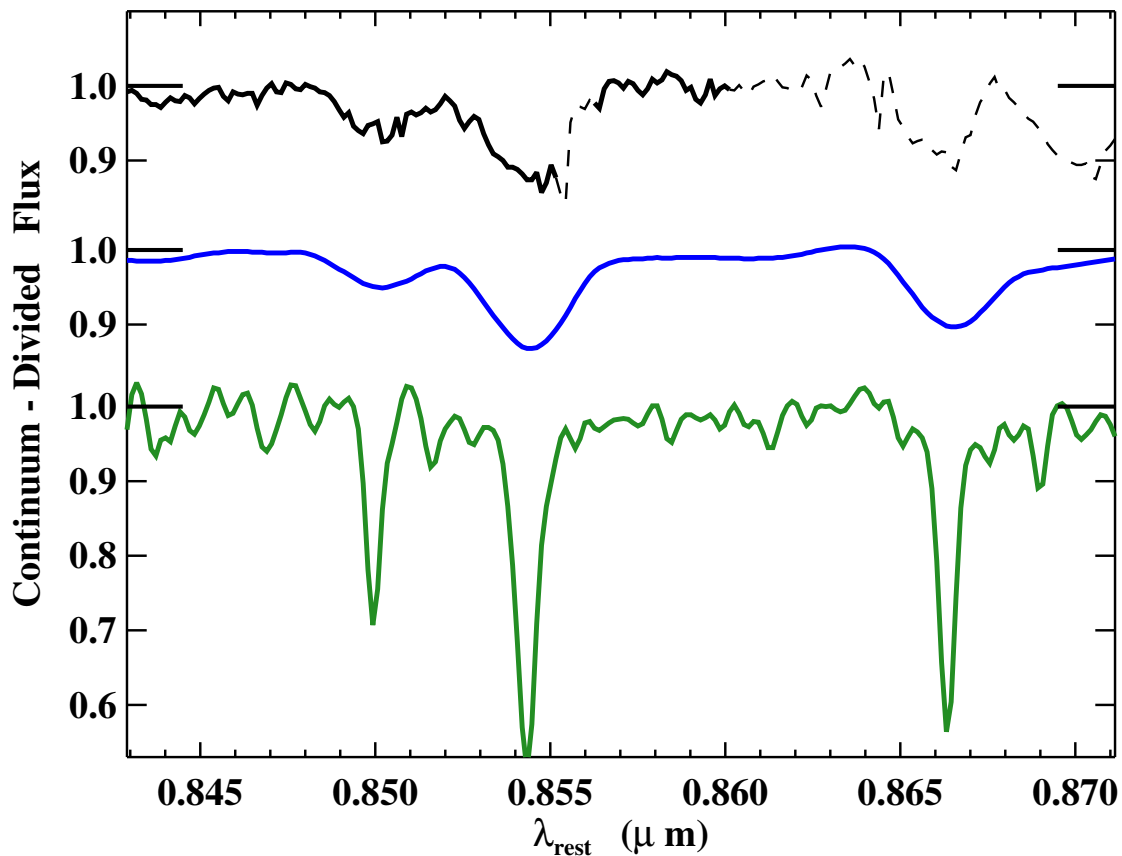


Figure 2.4: GMOS spectra of NGC 6086 and template star. *Top*: GMOS spectrum of the center of NGC 6086 (0.24 arcsec^2 ; $S/N = 91$). Dashed portions are excluded from the kinematic fitting. *Middle*: G9III template spectrum from GMOS, convolved with the best-fit LOSVD. *Bottom*: Spectrum of template star HD 73710 (G9III), from observations with GMOS. This is the only star used in our final extraction of kinematics from GMOS data.

from the science target, allowing for simultaneous sky subtraction. We observed the center of NGC 6086 in IFS mode with the detector’s *CaT* filter, detecting the infra-red Ca II triplet at observed wavelengths between 0.87 and 0.90 μm . A representative spectrum from the center of NGC 6086 is shown in Figure 2.4. GMOS data were reduced using version 1.4 of the Gemini IRAF software package⁴. This standard pipeline subtracts bias and overscan signals, removes cosmic rays, mosaics data from three CCDs, extracts spectra, corrects throughput variations across fibers and within individual spectra, calibrates wavelengths using arc lamp exposures, computes an average sky spectrum, and performs sky subtraction. We stored individual spectra from each GMOS exposure, along with their spatial positions relative to the center of NGC 6086, for eventual spatial binning.

With seeing-limited spatial resolution, GMOS poorly resolves the black hole sphere of influence. Nonetheless, kinematics derived from GMOS provide a good complement to those from OSIRIS. The Ca II triplet region in GMOS spectra has a more clearly-defined continuum than *H*-band spectra, and with less telluric contamination, as is evident from comparing Figures 2.3 and 2.4. As a result, line-of-sight velocity distributions (LOSVDs) extracted from GMOS spectra have lower systematic errors than LOSVDs extracted from OSIRIS spectra. Additionally, the angular region yielding high signal-to-noise spectra from GMOS is four times larger than that for OSIRIS.

2.3 Kinematics

Our dynamical models fit weighted and superposed stellar orbits to LOSVDs extracted from spectroscopic data. For both OSIRIS and GMOS data, we extract LOSVDs with a Maximum Penalized Likelihood (MPL) technique, which fits an LOSVD-convolved stellar template to each galaxy spectrum. The LOSVDs are non-parametric, defined at 15 radial velocity bins in our orbit models. Representative LOSVDs from the central OSIRIS and GMOS bins are shown in Figure 2.5, and the full sets of LOSVDs extracted from OSIRIS and GMOS spectra are presented in Section 2.7. The MPL fitting method is described in detail in Gebhardt et al. (2000b), Pinkney et al. (2003), and Nowak et al. (2008). Here we describe the specific adjustments made for IFS data of NGC 6086.

2.3.1 Extracting Kinematics from IFS Data

In order to attain sufficient signal-to-noise (S/N) for effective kinematic extraction, we perform spatial binning on our two-dimensional grids of spectra from OSIRIS and GMOS. For the mean-normalized galaxy spectrum Y , mean-normalized stellar template T , and LOSVD

⁴available from Gemini Observatory, at <http://www.gemini.edu/sciops/data-and-results/processing-software>

\mathcal{L} from the best fit over N_c spectral channels, we define:

$$S/N \equiv \left(\sum_{i=1}^{N_c} [Y_i - (T * \mathcal{L})_i]^2 / N_c \right)^{-1/2} \quad (2.1)$$

At the very center of NGC 6086, we spatially bin spectra until $S/N > 20$ is achieved. This requires binning 2×2 spatial pixels from OSIRIS; consequently our kinematic data have a central spatial resolution of $0.1''$, similar to the PSF FWHM. At the center of the GMOS mosaic, we bin 7 hexagonal pixels, corresponding to an approximate diameter of $0.55''$. The remaining spectra from each dataset are grouped to match angular and radial bins defined within the orbit models, and to maintain S/N between 25 and 40. Our resulting binning schemes for both OSIRIS and GMOS use only two angular bins on each of the positive (north) and negative (south) sides of the major axis. The angular bins span $0 - 36.9^\circ$ and $36.9 - 90^\circ$ from the major axis. Axisymmetric models perform LOSVD fitting in one quadrant of the projected galaxy. Symmetry about the major axis is enforced by co-adding spectra from the positive and negative (east and west) sides of the minor axis, before LOSVD extraction. LOSVDs extracted from the negative (south) side of the major axis are inverted before being input to the models. We define systemic velocity relative to the template star separately for OSIRIS and GMOS data.

Additionally, a spectral binning factor is necessary to smooth over channel-to-channel noise in spectra of NGC 6086. Our final kinematic extraction uses smoothing factors of 30 and 12 spectral pixels for OSIRIS and GMOS spectra, respectively. These values are chosen by comparing the best-fit LOSVDs from a large range of smoothing factors, and identifying the minimum factor above which LOSVDs in each dataset are stable between -500 km s^{-1} and 500 km s^{-1} . Our smoothing values are consistent with the range of optimal values determined by Nowak et al. (2008) for near-infrared spectra with $S/N \sim 25 - 50$.

H -band spectra from OSIRIS contain several absorption features that are potentially useful for kinematic extraction, but some are compromised by incompletely subtracted telluric OH emission lines, which are masked from the fit. Three broad features are relatively insensitive to the narrow OH lines: the $\nu = 3-6$ ^{12}CO bandhead at $1.6189 \mu\text{m}$ rest, the $\nu = 4-7$ ^{12}CO bandhead at $1.6401 \mu\text{m}$ rest, and the $\Delta\nu = 2$ band of OH between 1.537 and $1.545 \mu\text{m}$ rest. Additionally, the $\Delta\nu = 2$ OH band between 1.526 and $1.529 \mu\text{m}$ rest does not intersect any strong telluric emission features. We have verified that these four spectral features offer a robust comparison between stellar and galaxy spectra by repeating the fits with a large range of spectral smoothing factors. When we add other features to the fit, the root-mean-squared residual (RMS, essentially S/N^{-1}) becomes unstable to small changes in spectral smoothing.

To extract LOSVDs from GMOS spectra, we analyzed the $\lambda 8498$ and $\lambda 8542$ lines of Ca II. The third line in the well-known calcium triplet, $\lambda 8662$, is compromised by a flat-field artifact and discarded from kinematic analysis. The thick black lines in Figure 2.3 and Figure 2.4 indicate the spectral channels used in our final extraction of LOSVDs from OSIRIS and GMOS, respectively.

Uncertainties for each LOSVD are determined by 100 Monte-Carlo trials. In each trial, random noise is added to the galaxy spectrum, according to the RMS value of the original fit, and the LOSVD fitting process is repeated. At each velocity bin, the uncertainties $\sigma_{\mathcal{L}+}$ and $\sigma_{\mathcal{L}-}$ are computed from the distribution of trial LOSVD values. We then adjust the uncertainties in the wings of each LOSVD, so that $\mathcal{L} - \sigma_{\mathcal{L}-} = 0$.

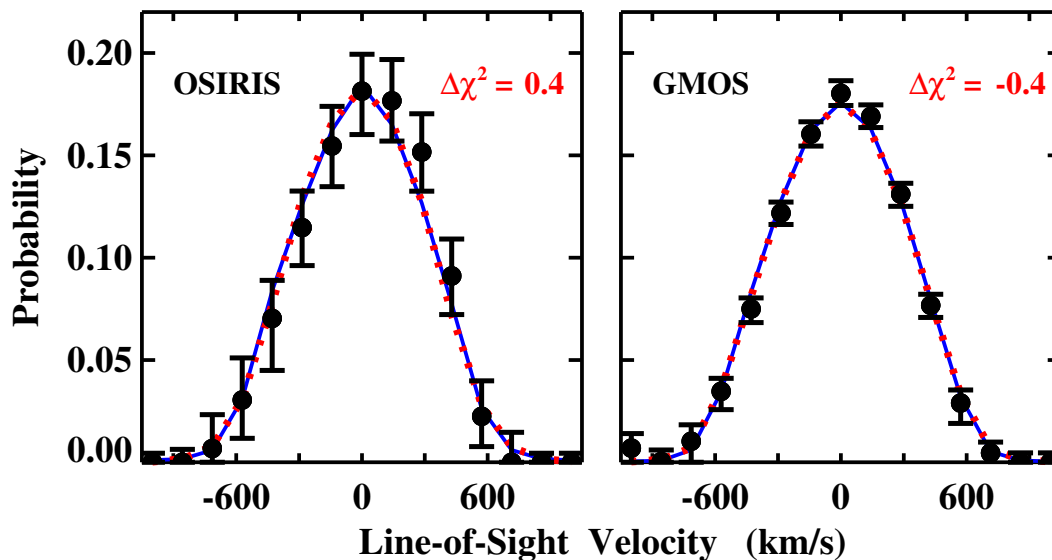


Figure 2.5: Sample LOSVDs for NGC 6086. *Left*: LOSVD extracted from the central spatial region, measured with OSIRIS ($0.1'' \times 0.1''$). *Right*: LOSVD extracted from the central spatial region measured with GMOS ($\approx 0.55''$ diameter). The solid blue line in each figure is the corresponding LOSVD generated by the best-fitting orbit model with the maximum-mass LOG dark matter halo ($M_*/L_R = 4.7 M_\odot L_{\odot,R}^{-1}$; $M_\bullet = 3.5 \times 10^9 M_\odot$; $v_c = 500$ kpc; $r_c = 8.0$ kpc). The dotted red line in each figure is from the best-fitting orbit model with no dark matter halo ($M_*/L_R = 6.8 M_\odot L_{\odot,R}^{-1}$; $M_\bullet = 3.2 \times 10^8 M_\odot$). For each LOSVD, $\Delta\chi^2$ is the difference in the χ^2 statistic for the two models: $\Delta\chi^2 > 0$ indicates that the model including dark matter (solid blue line) is a better fit. The full sets of LOSVDs from OSIRIS, GMOS, and Carter et al. (1999) are shown in Figures 2.17 through 2.19.

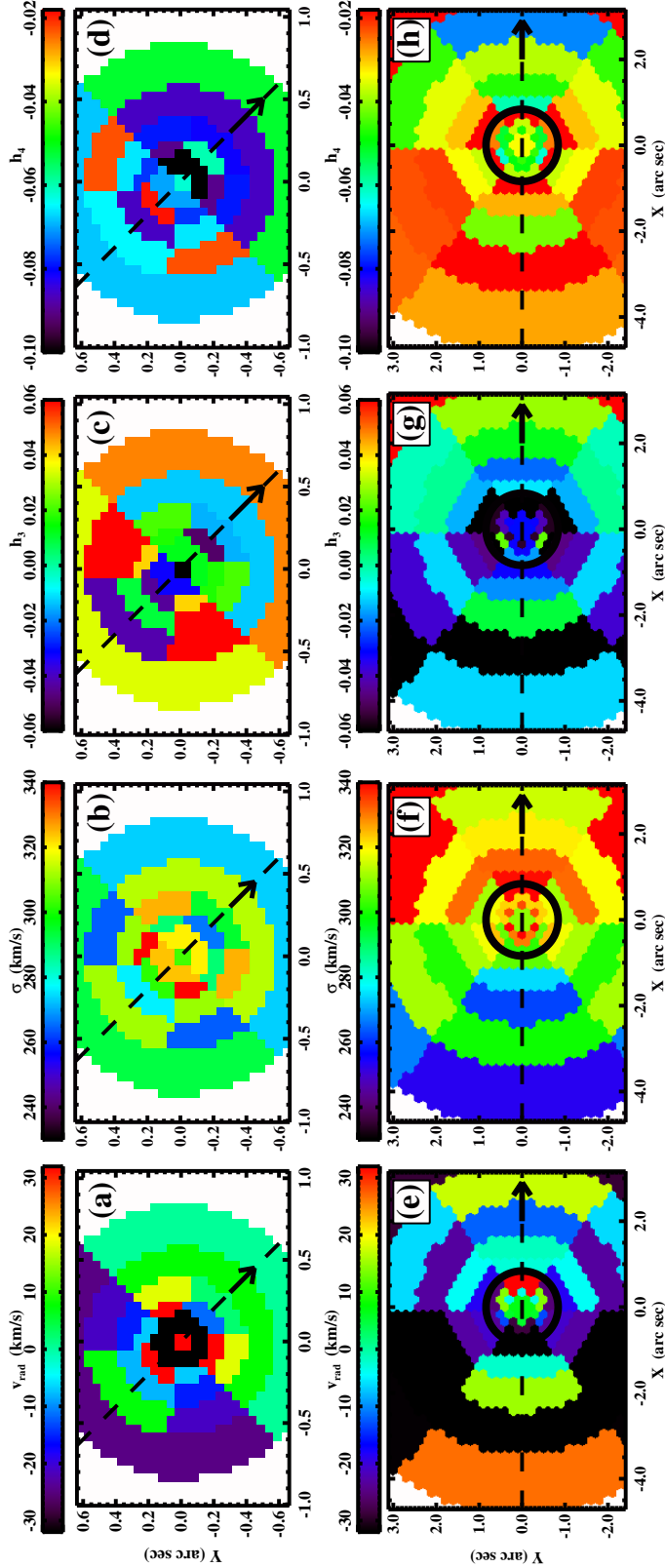


Figure 2.6: Two-dimensional kinematics in NGC 6086. (a) Radial velocity map from OSIRIS. (b) Velocity dispersion map from OSIRIS. (c) Map of h_3 from OSIRIS. (d) Map of h_4 from OSIRIS. (e) Radial velocity map from GMOS. (f) Velocity dispersion map from GMOS. (g) Map of h_3 from GMOS. (h) Map of h_4 from GMOS. All maps are derived by fitting fourth-order Gauss-Hermite polynomials to non-parametric LOSVDs. The dashed line in each figure represents the major axis of the galaxy, with the arrow pointing north. The solid circles in (e) through (h) represent the outermost extent of kinematics from OSIRIS. The median error values are (a) 41 km s^{-1} ; (b) 26 km s^{-1} ; (c) 0.042 ; (d) 0.024 ; (e) 20 km s^{-1} ; (f) 16 km s^{-1} ; (g) 0.035 ; and (h) 0.021 .

Stellar template mismatch can be a major source of systematic error in determining LOSVDs (e.g., Carter et al. 1999; Silge & Gebhardt 2003; Emsellem et al. 2004). To address this issue, we have directly observed a diverse set of late-type template stars. Our nine templates from OSIRIS are giant, supergiant, and dwarf stars with spectral types from G8 to M4. We have found the most appropriate template for OSIRIS spectra of NGC 6086

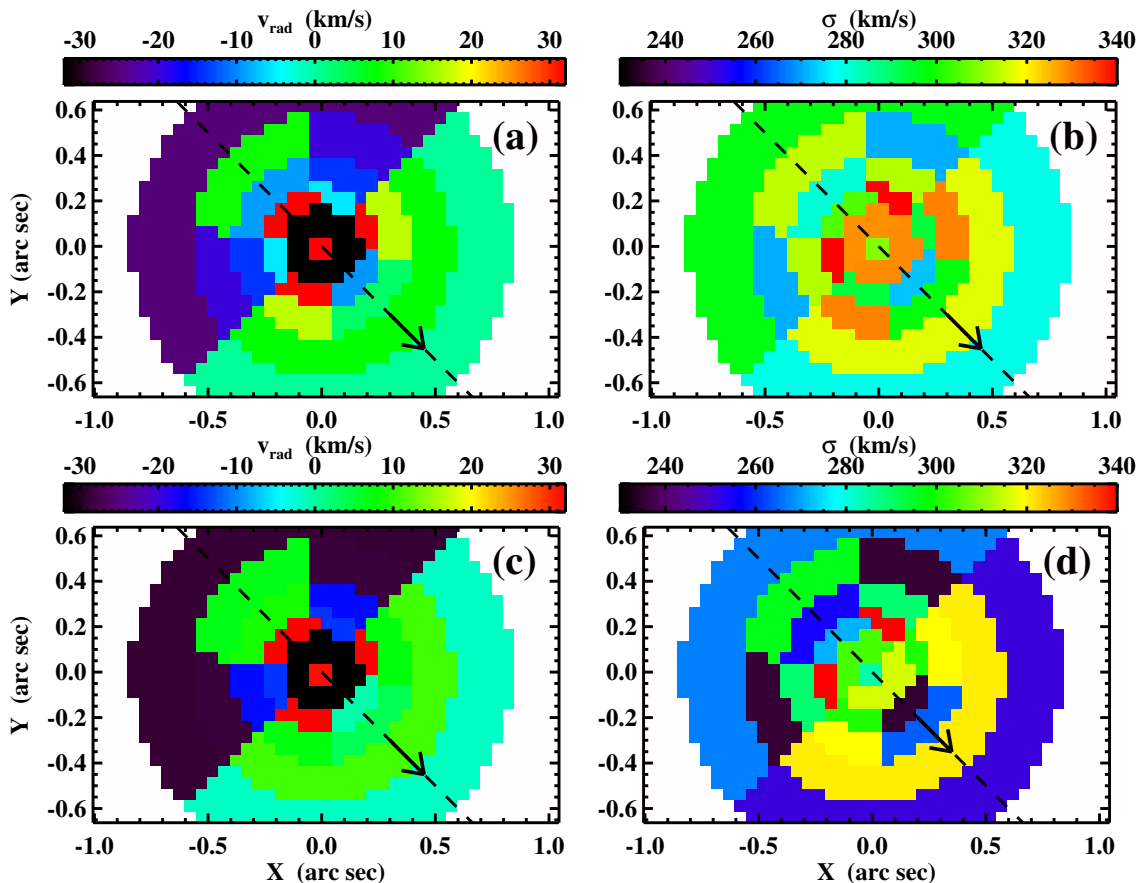


Figure 2.7: Comparison of Gaussian and non-parametric LOSVD extraction methods. (a) Radial velocity map of NGC 6086 from OSIRIS, derived by fitting Gaussian profiles to non-parametric LOSVDs. (b) Velocity dispersion map from fitting Gaussian profiles to non-parametric LOSVDs. (c) Radial velocity map, derived by fitting Gaussian LOSVDs to OSIRIS spectra. (d) Velocity dispersion map from fitting Gaussian LOSVDs to OSIRIS spectra. The dashed line in each figure represents the major axis of the galaxy, with the arrow pointing north. The median error values are (a) 41 km s^{-1} ; (b) 26 km s^{-1} ; (c) 35 km s^{-1} ; and (d) 32 km s^{-1} . Radial velocities and dispersions from the two extraction methods are consistent within errors.

to be HD 110964, an M4III star. In Section 2.6, we describe our method for choosing the optimal template star, and how fitting LOSVDs with different template stars influences measurements of M_\bullet and M_\star/L_R . We fit GMOS spectra of NGC 6086 with a single G9III template star, HD 73710, which we observed with GMOS. The calcium triplet region is less sensitive to template mismatch than other optical and near-infrared regions used to measure kinematics (Barth et al. 2002).

2.3.2 Two-Dimensional Kinematics in NGC 6086

Our integral-field observations uncover complex kinematic structures within the central 3.1 kpc (4.9'') of NGC 6086. In Figure 2.6, we display two-dimensional maps of kinematic moments from OSIRIS and GMOS data; we have computed v_{rad} , σ , h_3 , and h_4 by fitting a fourth-order Gauss-Hermite polynomial to each non-parametric LOSVD. For data with modest signal-to-noise, non-parametric LOSVDs must be used with caution, as noise may falsely introduce strong non-Gaussian components to the fit. In Figure 2.7, we compare two estimates of v_{rad} and σ from OSIRIS spectra. One estimate is obtained by fitting Gaussian profiles to non-parametric LOSVDs (Figures 7a and 7b), and the other is obtained by forcing a Gaussian LOSVD to fit the original spectra (Figures 7c and 7d). In every spatial region, v_{rad} and σ from the two fitting options are consistent within errors, and so we can trust the non-parametric LOSVDs. GMOS data show similar agreement between the two estimates.

The stellar velocity dispersions measured by OSIRIS and GMOS each peak within 250 pc of the galaxy center, but not at the central spatial bin. Central decreases in velocity dispersion have been observed in several other early-type galaxies with known black holes (e.g., van der Marel 1994; Pinkney et al. 2003; Gebhardt et al. 2007; Nowak et al. 2008). Possible physical explanations include an unresolved stellar disk or a localized population of young stars. No dust features are present in photometry of NGC 6086, nor is there any evidence of an active galactic nucleus. The radial velocities are highly disturbed within the central 200 pc, which are only resolved by OSIRIS: at maximum, $\Delta v_{\text{rad}} = 194 \pm 52 \text{ km s}^{-1}$. Gebhardt et al. (2007) found similar patterns in v_{rad} and σ in the central 100 pc of NGC 1399, which were reproduced by models with a high prevalence of tangential orbits. Likewise, our best-fitting model of NGC 6086 is tangentially biased in the central 200 pc; the average value of σ_r/σ_t is 0.55. However, the two-dimensional structure of v_{rad} is not consistent with a resolved stellar disk. Axisymmetric modeling of elliptical galaxies by Gebhardt et al. (2003), Shapiro et al. (2006), and Shen & Gebhardt (2010) suggests that tangential bias is common within the black hole sphere of influence.

Figures 6c, 6d, 6g, and 6h illustrate the two-dimensional behavior of the third- and fourth-order Gauss-Hermite moments, h_3 and h_4 . Within errors, our measurements are largely consistent with $h_3 = 0$, while h_4 is significantly negative, corresponding to LOSVDs with ‘‘boxy’’ shapes and truncated wings.

We use major-axis kinematics from Carter et al. (1999) to constrain stellar orbit models at radii out to 18.9 kpc (29.3''), several times the extent of our IFS data. To incorporate these data into our models, we have adopted higher uncertainties than the values quoted in Carter

et al. (1999); our treatment attempts to account for additional systematic errors, which are described by Carter et al. (1999) but excluded from their published measurements for NGC 6086. In Figure 2.8, we compare kinematic moments from Carter et al. (1999) to the moments derived from OSIRIS and GMOS, selecting the spatial bins along the galaxy’s major axis. We invert the sign of v_{rad} and h_3 for bins on the southern half of the galaxy. Values of v_{rad} , σ , and h_3 measured from the three data sets largely agree, although the OSIRIS data yield somewhat smaller values of σ . At radii between $0.6''$ and $4.9''$, GMOS spectra from the southern half of the galaxy yield significantly lower values of σ than spectra from the northern half. The average asymmetry is 35 km s^{-1} ; our median error for individual GMOS measurements is 16 km s^{-1} . The asymmetry is not seen in long-slit data, which more consistently agree with GMOS along the north side of the major axis. In spatial bins corresponding to the minor axis, v_{rad} and σ behave similarly to the major-axis trends depicted in Figure 2.8, and agree with minor-axis kinematics from Loubser et al. (2008). Beyond the central 200 pc, we find no convincing signs of kinematically distinct stellar populations dominating galaxy spectra at 0.5 , 0.9 , and $1.6 \mu\text{m}$.

The most significant discrepancy in the major-axis kinematics is between the negative values of h_4 derived from IFS data and the positive values of h_4 measured by Carter et al. (1999) (Figure 8d). Given the uniformity of the positive and negative values over many radial bins, we attribute this discrepancy to systematic errors in at least one set of measurements. As noted by Carter et al. (1999; and references therein), stellar template mismatch can bias h_4 ; however, this study and Carter et al. (1999) both perform careful analysis with multiple stellar templates (9 and 28 stars, respectively). Nowak et al. (2008) demonstrated that large spectral smoothing factors can also bias h_4 to negative values. Still, a smoothing factor > 100 would be necessary to produce the full discrepancy between our values and those from Carter et al. (1999). Another source of error could be adjustments to the equivalent widths of absorption features in galaxy and template spectra; we address this issue in Section 2.6. Regardless of the cause, including discrepant data in stellar orbit models can influence the best-fit solutions. We discuss the effects on measurements of M_\bullet and M_\star/L_R in Section 2.4.3.

2.4 Stellar Orbit Models and Black Hole Mass

2.4.1 Stellar Orbits

We generate stellar orbit models of NGC 6086, using the static potential method introduced by Schwarzschild (1979). We use the axisymmetric modeling algorithm described in detail in Gebhardt et al. (2000b, 2003), Thomas et al. (2004, 2005), and Siopis et al. (2009). Here we provide a summary of the procedure. Similar models are presented in Richstone & Tremaine (1984), Rix et al. (1997), Cretton et al. (1999b), and Valluri et al. (2004).

We assume that the central region of NGC 6086 consists of three mass components – stars, a central black hole, and an extended dark matter halo – described by the radial

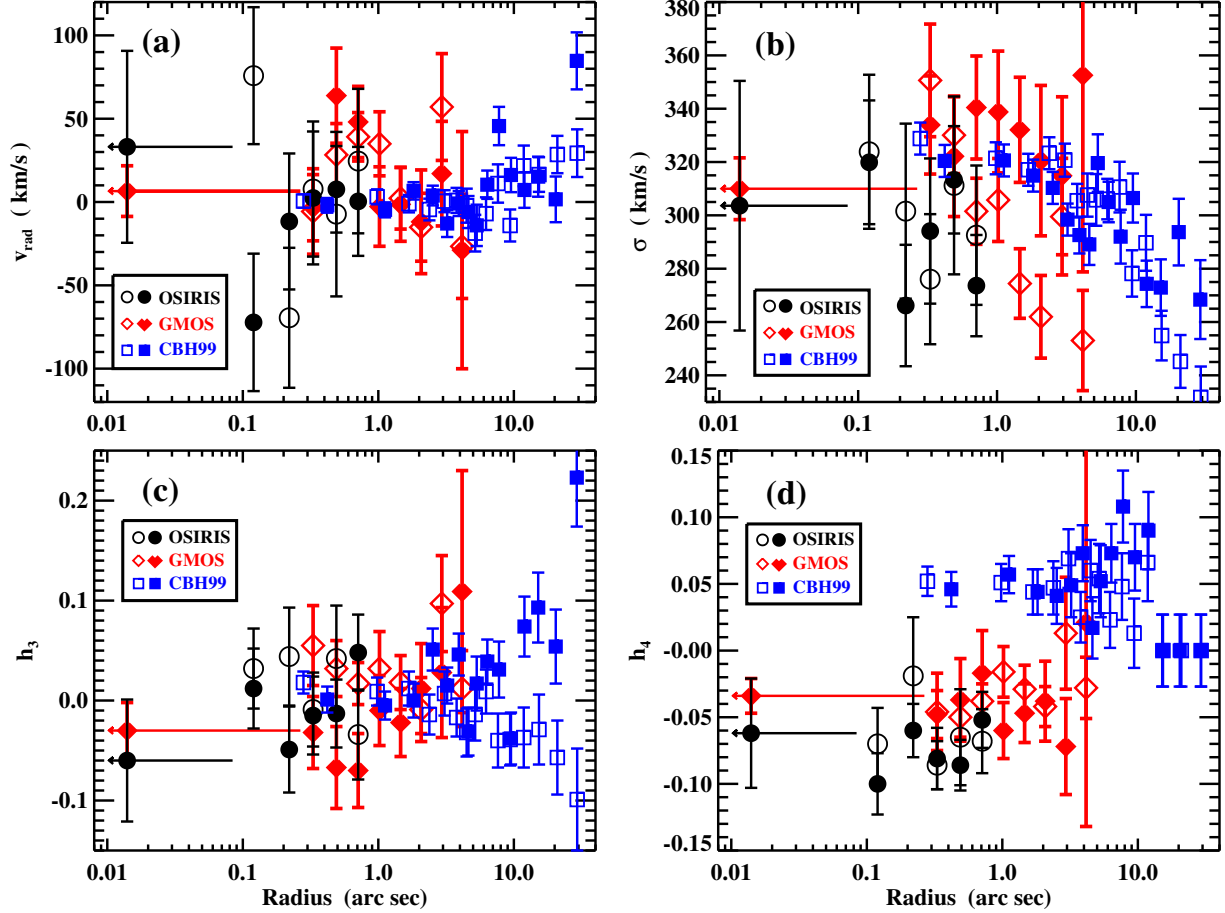


Figure 2.8: Extracted kinematics along the major axis of NGC 6086. Black circles are OSIRIS measurements, red diamonds are GMOS measurements, and blue squares are measurements from Carter et al. (1999). Filled symbols represent points from the positive (north) side of the major axis, and open symbols represent points from the negative (south) side. For OSIRIS and GMOS data, the kinematic moments are computed from non-parametric LOSVDs. (a) Radial velocity, relative to the central velocity of NGC 6086. The central velocity is defined separately for each dataset, such that the spatial averages to either side of the major axis are symmetric about $v_{\text{rad}} = 0$. Velocities from the negative (south) side of the major axis have been inverted. (b) Line-of-sight velocity dispersion. (c) Gauss-Hermite h_3 , with values from the negative (south) side of the major axis inverted. (d) Gauss-Hermite h_4 .

density profile

$$\rho(r) = \frac{M_\star}{L_R} \nu(r) + M_\bullet \delta(r) + \rho_{\text{halo}}(r). \quad (2.2)$$

The stellar distribution is assumed to follow the observed (deprojected) luminosity density $\nu(r)$ (see Figure 2.1) with a constant stellar mass-to-light ratio M_\star/L_R . For the dark matter halo, we compare two density profiles: the commonly used NFW form (Navarro et al. 1996), and a logarithmic (LOG) profile⁵:

$$\rho_{\text{halo}}(r) = \frac{v_c^2}{4\pi G} \frac{3r_c^2 + r^2}{(r_c^2 + r^2)^2}. \quad (2.3)$$

The free parameters in the LOG profile are the asymptotic circular speed v_c and the core radius r_c , within which the density is approximately constant. The enclosed halo mass for this profile,

$$M_{\text{halo}}(< r) = \frac{v_c^2 r}{G} \left(1 - \frac{r_c^2}{r_c^2 + r^2} \right), \quad (2.4)$$

is predominantly set by v_c . The difference between the NFW and LOG profiles is greatest at small radii, where the NFW profile yields higher densities, $\rho_{\text{halo}} \propto r^{-1}$. However, each profile is greatly exceeded by the stellar mass density in the inner regions of NGC 6086. As described below, we have compared LOG and NFW profiles in a subset of models, and find no significant differences in the best-fit values of M_\bullet .

For a given set of input parameters M_\bullet , M_\star/L_R , and ρ_{halo} , we compute a continuous, static gravitational potential from Equation (2.2). Azimuthal symmetry about the z -axis (corresponding to the projected minor axis) is imposed, as well as symmetry about the equatorial plane ($z = 0$). We then generate stellar orbits by propagating test particles through the potential. Orbits are tracked in a finely spaced polar grid, (r, θ) , where θ is the polar angle from the z -axis. Our models of NGC 6086 use 96 radial and 20 polar bins per quadrant. Each orbit is sampled at a random set of azimuthal angles, ϕ .

The initial phase space coordinates of test particles are chosen to sample thoroughly three integrals of motion: energy E , angular momentum component L_z , and the third, non-classical integral, I_3 . Computational noise and finite propagation steps introduce noise into test particle trajectories; this is mitigated by allowing each particle to complete 200 circuits of the potential and then determining its average orbit. Orbits that escape the potential are not included in subsequent fitting. For a given potential, our model of NGC 6086 includes approximately 16,000 to 19,000 bound orbits. Identical counterparts with the opposite sign of L_z raise the total to 32,000 - 38,000 orbits. Each orbit in the model is assigned a scalar weight; initially, all bound orbits are given equal weights.

The set of best-fit orbital weights is determined by comparing projected LOSVDs from the orbits to the observed LOSVDs for the galaxy. Our models use non-parametric LOSVDs, defined in 15 velocity bins between -1000 and 1000 km s^{-1} . Each observed LOSVD spatially

⁵The gravitational potential is logarithmic: $\Phi = \frac{1}{2}v_c^2 \ln(r^2 + r_c^2)$.

maps to a linear combination of bins within the model, according to the spatial boundaries of the corresponding spectrum, and to the instrument-specific PSF. A corresponding model LOSVD is computed from the projected velocity distributions of individual orbits in each spatial bin, the appropriate combination of spatial bins, and the orbital weights. Only the orbital weights are varied to determine the best-fit solution.

The best-fit solution is determined by the method of maximum entropy, as in Richstone & Tremaine (1988). This method maximizes the function $f \equiv S - \alpha\chi^2$, where

$$\chi^2 = \sum_i^{N_b} \sum_j \frac{[\mathcal{L}_{i,\text{data}}(v_j) - \mathcal{L}_{i,\text{model}}(v_j)]^2}{\sigma_i^2(v_j)} \quad (2.5)$$

and

$$S = - \sum_k w_k \ln \left(\frac{w_k}{V_k} \right) \quad (2.6)$$

Here, $\mathcal{L}_{i,\text{data}}$ and $\mathcal{L}_{i,\text{model}}$ are LOSVDs in each of the $i = 1, \dots, N_b$ spatial bins, $\sigma_i^2(v_j)$ is the squared uncertainty in $\mathcal{L}_{i,\text{data}}$ at velocity bin v_j , w_k is the orbital weight for the k th orbit, and V_k is the phase volume of the k th orbit. The parameter α is initially small so as to distribute orbital weights broadly over phase space, and is increased over successive iterations so that the final optimization steps exclusively minimize χ^2 . A further constraint for all solutions is that the summed spatial distribution of all weighted orbits must match the observed luminosity density profile.

2.4.2 Black Hole Mass and Mass-to-Light Ratio

Our combination of IFS and long-slit data within $30''$ is not sufficient to measure directly the dark matter halo profile or enclosed mass. We therefore consider different halo masses and profiles in our analysis. For a given dark matter halo profile, we generate a set of 32,000–38,000 stellar orbits for an input M_\bullet and M_\star/L_R , and obtain χ^2 for the best-fit orbital weights using the method described in the previous subsection. This process is repeated over a finely sampled grid in M_\bullet and M_\star/L_R . We have completed all trials for NGC 6086 on supercomputers at the Texas Advanced Computing Center (TACC), totaling $\sim 10,000$ CPU hours. Our results are summarized in Table 2.2.

In Figure 2.9, we illustrate how χ^2 in the orbit models varies with M_\bullet and M_\star/L_R . Three dark matter halo masses are shown: no dark matter (left panel), an intermediate LOG halo with $v_c = 300 \text{ km s}^{-1}$ (middle), and a maximal LOG halo with $v_c = 500 \text{ km s}^{-1}$ (right). The latter is chosen to approximate the measured line-of-sight velocity dispersion of 302 km s^{-1} for NGC 6086’s host cluster (Zabludoff et al. 1993), which corresponds to a full three-dimensional velocity dispersion of 523 km s^{-1} . We set the core radius in Equation (2.3) to be $r_c = 8.0 \text{ kpc}$, reflecting the value of 8.2 kpc determined by Thomas et al. (2007) for NGC 4889, the Coma BCG. Our dynamical models are constrained within a radius of 18.9 kpc , corresponding to outermost radius of $29.3''$ for long-slit data in Carter et al. (1999).

We also have run models with a single NFW dark matter profile, constructed to contain the same enclosed mass within 18.9 kpc as our most massive LOG halo. In cosmological N -body simulations, the NFW scaling parameters c and r_s are correlated according to the relationship

$$r_s^3 = \left(\frac{3 \times 10^{13} M_\odot}{200 \frac{4\pi}{3} \rho_{\text{crit}} c^3} \right) 10^{\frac{1}{0.15}(1.05 - \log_{10} c)} \quad (2.7)$$

(Navarro et al. 1996; Rix et al. 1997)⁶, where $\rho_{\text{crit}} = 3H_0^2/8\pi G$. Combining this relationship with our enclosed mass constraint, we obtain $c = 9.6$ and $r_s = 94.0$ kpc.

⁶Note the erratum in Equation (B3) of Rix et al. (1997); the correct equation is $\log_{10} c = 1.05 - 0.15 \log_{10} (M_{200}/3 \times 10^{13} M_\odot)$.

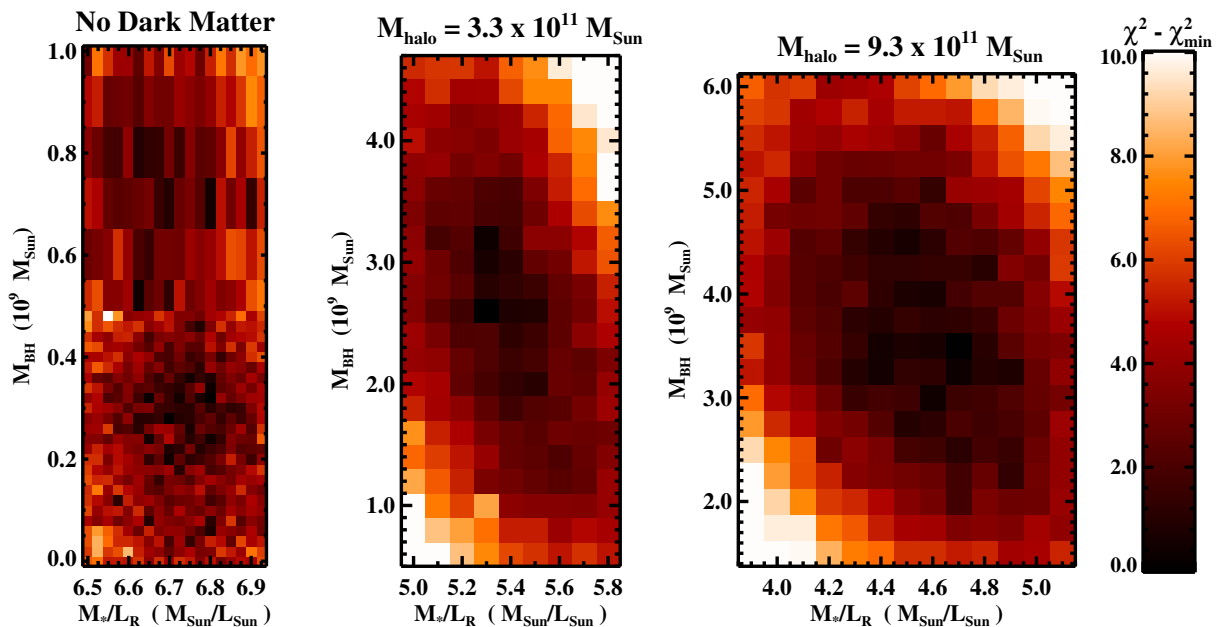


Figure 2.9: Surface plots of χ^2 vs. M_\star/L_R and M_\bullet , for models of NGC 6086 fitting both OSIRIS and GMOS data. *Left:* Models with no dark matter halo. Long vertical pixels represent regions with coarser sampling in M_\bullet . *Middle:* $v_c = 300 \text{ km s}^{-1}$ and $r_c = 8.0$ kpc, for $M_{\text{halo}} = 3.3 \times 10^{11} M_\odot$ within 18.9 kpc. *Right:* $v_c = 500 \text{ km s}^{-1}$ and $r_c = 8.0$ kpc, for $M_{\text{halo}} = 9.3 \times 10^{11} M_\odot$ within 18.9 kpc. For each dark matter halo, additional models were run outside the range of M_\star/L_R and M_\bullet depicted here. These models all yield higher values of χ^2 .

Table 2.2: Results from stellar orbit models of NGC 6086

| Data | v_c (km s^{-1}) | r_c (kpc) | c | r_s (kpc) | M_{halo} ($10^{11} M_{\odot}$) | M_{\bullet} ($10^9 M_{\odot}$) | M_{\star}/L_R ($M_{\odot} L_{\odot}^{-1}$) | χ^2_{min} | N_{dof} |
|---------------|---------------------------------|----------------|-----|----------------|----------------------------------------------|---------------------------------------|---------------------------------------------------|-----------------------|------------------|
| (1) | (2) | (3) | (4) | (5) | (6) | (7) | (8) | (9) | (10) |
| O + G + CBH99 | 0.01 | 20.0 | | | ≈ 0 | $0.6^{+0.4}_{-0.4}$ | $6.68^{+0.15}_{-0.17}$ | 1114.4 | 795 |
| O + G + CBH99 | 300 | 8.0 | | | 3.34 | $2.6^{+1.0}_{-1.0}$ | $5.4^{+0.3}_{-0.3}$ | 1019.4 | 795 |
| O + G + CBH99 | 500 | 8.0 | | | 9.28 | $3.6^{+1.2}_{-1.1}$ | $4.6^{+0.3}_{-0.4}$ | 1010.2 | 795 |
| O + G + CBH99 | | | 9.6 | 94.0 | 9.05 | $3.6^{+1.1}_{-1.2}$ | $4.3^{+0.3}_{-0.4}$ | 1009.4 | 795 |
| O + G | 0.01 | 20.0 | | | ≈ 0 | $3.2^{+1.5}_{-1.3}$ | $4.4^{+0.4}_{-0.3}$ | 622.9 | 345 |
| O + G | 500 | 8.0 | | | 9.28 | $3.5^{+1.4}_{-1.5}$ | $4.1^{+0.4}_{-0.5}$ | 623.8 | 345 |
| O + CBH99 | 500 | 8.0 | | | 9.28 | $1.9^{+1.4}_{-1.1}$ | $4.6^{+0.7}_{-0.7}$ | 412.7 | 570 |
| G + CBH99 | 500 | 8.0 | | | 9.28 | 7^{+2}_{-3} | $4.5^{+0.5}_{-0.5}$ | 725.5 | 675 |

Notes: Column 1: Data sets included in trial. “O” refers to OSIRIS, “G” to GMOS, and “CBH99” to long-slit kinematics from Carter et al. (1999). Column 2: circular velocity of LOG dark matter halo (Eq. 2.3). Column 3: core radius of LOG dark matter halo (Eq. 2.3). Column 4: concentration parameter for NFW dark matter halo. Column 5: scale radius for NFW dark matter halo. Column 6: enclosed halo mass, defined at the outermost long-slit data point. The corresponding radius is 18.9 kpc. The “no dark matter” case has $v_c = 0.01 \text{ km s}^{-1}$, $r_c = 20.0$ kpc, and $M_{\text{halo}} \sim 200 M_{\odot}$. Column 7: best-fit black hole mass. Quoted errors correspond to 68% confidence intervals. Values in parentheses include all systematic errors. Column 8: best-fit R -band stellar mass-to-light ratio. Quoted errors correspond to 68% confidence intervals. Values in parentheses include all systematic errors. Column 9: minimum χ^2 value for all models. Column 10: degrees of freedom in model fits to LOSVDs. Computed values include a smoothing factor of 1 degree of freedom per 2 velocity bins for non-parametric LOSVDs from OSIRIS and GMOS.

Dark matter is ubiquitous in galaxies, thus motivating its inclusion in stellar orbit models. Furthermore, models with dark matter produce better fits to our full set of kinematics: when the dark matter component is removed, χ_{min}^2 increases by ~ 100 (Table 2.2). In Section 2.7 we compare our full sets of observed LOSVDs to the best-fitting models with and without dark matter. The largest discrepancies between the two models occur at radii beyond $15''$, where we only have a few data points from Carter et al. (1999). Without thorough radial coverage or multiple long-slit position angles, we cannot fully untangle degeneracies between M_\star/L_R , v_c , and r_c (or M_\star/L_R , c , and r_s in the case of an NFW profile).

In Figure 2.10 we display the dark matter fraction as a function of radius, for each of the halos described above. In each case, we use the best-fit values of M_\bullet and M_\star/L_R , described below, to compute the total enclosed mass. Using our surface brightness profile from *HST*/KPNO we compute an effective radius, r_{eff} , of $31.7''$ (20.4 kpc), defined as the semi-major axis of the elliptical isophote containing half of the total luminosity. We assume a total luminosity of $1.82 \times 10^{11} L_{\odot,R}$, from $M_V = -23.11$ in Lauer et al. (2007a) and $V - R = 0.64$. Within r_{eff} , dark matter composes 44% to 74% of the total mass (for the intermediate-mass LOG halo and the NFW halo, respectively). This range agrees with dynamical models of other cD galaxies with LOG and NFW halos: Thomas et al. (2007) found $\sim 50 - 75\%$ dark matter within r_{eff} for NGC 4889 and NGC 4874, and Gebhardt & Thomas (2009) found $\sim 40\%$ dark matter within r_{eff} for M87. Within the $4.9''$ outer radius of GMOS data, the maximum dark matter fraction in our models is 20%.

In Figure 2.11 we illustrate the variation of M_\bullet and M_\star/L_R with enclosed halo mass. We compute best-fit values for M_\bullet and M_\star/L_R by integrating the two-dimensional likelihood function from each χ^2 surface; we describe this method and our determination of errors in Section 2.4.3. Figures 2.9 and 2.11 show that the best-fit values of M_\bullet and M_\star/L_R are substantially influenced by the presence of dark matter in the stellar orbit models. This occurs because our innermost kinematics sample the nucleus of the galaxy, where orbits are dominated by the enclosed mass of stars and the central black hole, whereas enclosed stellar and dark halo masses are both important at larger radii. The significant presence of dark matter at large radii drives the best-fit models to lower values of M_\star/L_R . In turn, the decreased stellar mass requires a higher black hole mass to reproduce the kinematics in the nucleus. This trend was initially demonstrated by Gebhardt & Thomas (2009), for M87. Negative covariance between M_\bullet and M_\star/L_R is also visible in χ^2 contours for individual dark matter halo models (Figure 2.9). In Section 2.5, we compare our best-fit values of M_\bullet from different dark matter halo models to the predictions from the $M_\bullet - \sigma$ and $M_\bullet - L$ relationships.

Using an NFW profile yields a 7% decrease in the best-fit value of M_\star/L_R , relative to the LOG profile with the same enclosed mass at 18.9 kpc. This is because the majority of our kinematic measurements occur at $r \leq 5$ kpc, where the more centrally-concentrated NFW profile yields higher dark matter densities. In the central 100 pc, the stellar core of NGC 6086 varies nearly as r^{-1} in luminosity density, mimicking the slope of the NFW profile. Near the black hole, the lower stellar mass density balances the higher density in dark matter, and so the best-fit values of M_\bullet are identical for the NFW and LOG profiles.

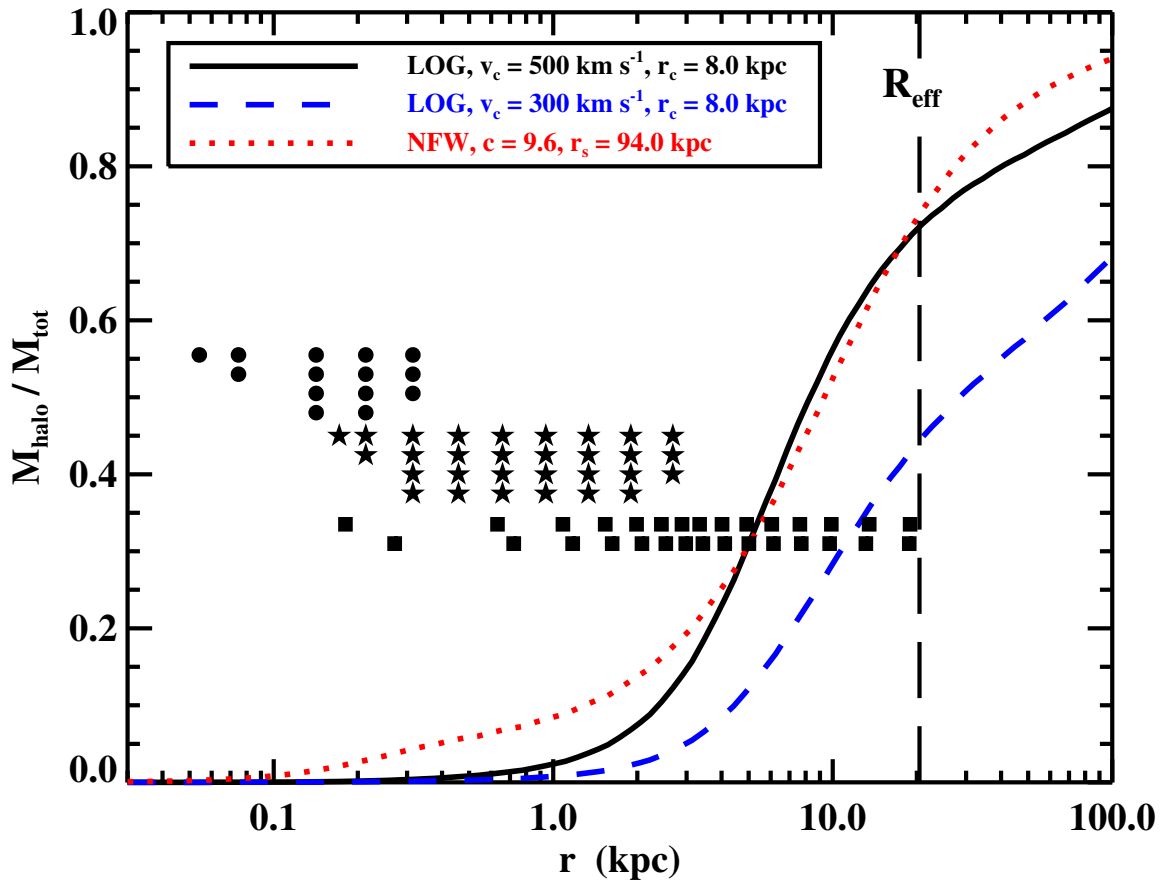


Figure 2.10: Dark matter fraction of total enclosed mass, for the model dark matter halos presented in Table 2.2. For each halo, the total enclosed mass includes the best-fit black hole mass and best-fit stellar mass-to-light ratio, derived using OSIRIS, GMOS, and long-slit data. The dashed vertical line marks the effective radius derived from our photometric data. Filled symbols represent the radial positions of spectra from OSIRIS (circles), GMOS (stars), and Carter et al. (1999) (squares); the vertical positions of the symbols have no physical meaning.

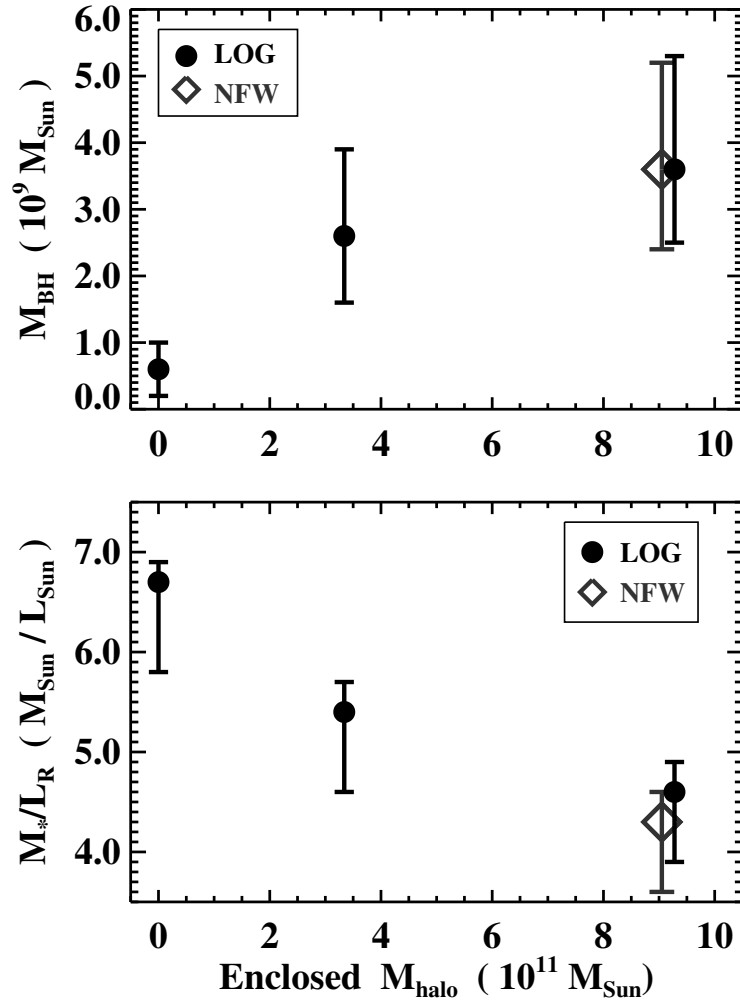


Figure 2.11: Best-fit M_{\bullet} and M_{\star}/L_R vs. model dark matter halo mass in NGC 6086. *Top:* Best-fit black hole mass for different assumed dark matter halos. *Bottom:* Best-fit stellar mass-to-light ratio. Black circles represent LOG halos, and grey diamonds represent the NFW halo. Each measurement comes from fitting the full set of LOSVDs from OSIRIS, GMOS, and Carter et al. (1999). The enclosed halo mass is defined at 18.9 kpc, the radius of the outermost data point from Carter et al. (1999). Error bars indicate 68% confidence, and include systematic errors.

We find $\chi_{\min, \text{LOG}}^2 - \chi_{\min, \text{NFW}}^2 = 0.8$, indicating no significant difference in the goodness of fit. Thomas et al. (2005, 2007) and Gebhardt & Thomas (2009) have found similar difficulties in distinguishing between NFW and LOG profiles.

A second way to address the influences of dark matter on M_\star/L_R and M_\bullet is to fit the orbit models only at radii where dark matter composes a small fraction of the enclosed mass. For NGC 6086, we have run two trials in which we only fit LOSVDs from OSIRIS and GMOS: one trial with the maximum-mass LOG dark matter halo described above, and one trial with no dark matter. In both of these trials, the best-fit values of M_\bullet and M_\star/L_R agree with our results from fitting IFS and long-slit data with the maximum-mass LOG halo (see Table 2.2). This agreement provides strong evidence that $M_\bullet \sim 3 \times 10^9 M_\odot$, regardless of our insensitivity to the exact structure of the dark matter halo in NGC 6086. In contrast, forcing models without dark matter to fit long-slit data biases the best-fit black hole mass to a substantially lower value, $\sim 6 \times 10^8 M_\odot$, and increases the best-fit stellar mass-to-light ratio to $6.7 M_\odot L_{\odot, R}^{-1}$. This mass-to-light ratio is highly inconsistent with stellar population estimates, as we discuss in Section 2.5. Even though excluding long-slit data results in consistency between models with and without dark matter, these models are not as thoroughly constrained, and we obtain slightly larger confidence intervals in M_\bullet and M_\star/L_R for each trial.

Our data from OSIRIS, GMOS, and Carter et al. (1999) play complementary roles in constraining the gravitational potential of NGC 6086. In Figure 2.12, we compare model results for one dark matter halo (LOG; $v_c = 500 \text{ km s}^{-1}$), using data only from GMOS and Carter et al. (1999), versus only from OSIRIS and Carter et al. (1999). The GMOS data are sufficient to detect a black hole, in part because of excellent seeing. Yet the strong diagonal contours in the left panel of Figure 2.12 indicate that the black hole mass derived from GMOS is degenerate with the enclosed stellar mass. LOSVDs from OSIRIS have large statistical errors and by themselves cannot place strong constraints on the black hole mass. However, the OSIRIS data help separate the respective influences of the stars and the black hole. Using GMOS and OSIRIS data together reduces covariance between M_\bullet and M_\star/L_R and lowers the statistical uncertainties of both quantities. Long-slit data from Carter et al. (1999) confirm the presence of dark matter and tighten constraints on M_\star/L_R and M_\bullet for individual dark matter halo models.

It is not clear how to interpret the significant increase in the best-fit value of M_\bullet , from $1.9_{-1.1}^{+1.5} \times 10^9 M_\odot$ with OSIRIS and long-slit data only, to $7_{-3}^{+3} \times 10^9 M_\odot$ with GMOS and long-slit data only. Using central $\sigma = 329 \text{ km s}^{-1}$ from Loubser et al. (2008), and $M_\bullet = 3.6 \times 10^9 M_\odot$ from our combined-data trial, we compute $r_{\text{inf}} = 0.22''$. In this case, GMOS marginally resolves the sphere of influence, with a seeing FWHM $\sim 2 r_{\text{inf}}$. At small radii, LOSVDs from GMOS yield slightly higher velocity dispersions than overlapping LOSVDs from OSIRIS (Figure 8b), which could contribute to the increase in M_\bullet . With no obvious way to assess independently the accuracy of data from OSIRIS versus GMOS, we favor including both sets of LOSVDs. The corresponding black hole mass is $3.6_{-1.1}^{+1.7} \times 10^9 M_\odot$, which lies between the two partial-data values and has the narrowest confidence interval. The confidence interval in M_\star/L_R is also minimized by including all data, though the best-

fit value of $4.6_{-0.7}^{+0.3}$ does not change significantly upon exclusion of OSIRIS or GMOS data.

None of the χ^2 surfaces in Figures 2.9 and 2.12 are completely smooth. In particular, the models without any dark matter show large variations in χ^2 over small changes in M_\bullet and M_\star/L_R (Figure 2.9). We suspect that these variations arise from numerical noise in propagating test particles through different potentials: each small change in the potential may send a given test particle through a different set of spatial regions. The cumulative effect is that each model creates a different set of test-particle LOSVDs, and χ^2 can change abruptly in spite of the freedom to adjust orbital weights. When the models include a constant dark matter component, the relative changes in the potential are smaller, and the noise in χ^2 is less pronounced. Still, the χ^2 surface for each dark matter halo exhibits a noise floor at the level of $\Delta\chi^2 \sim 1$. In Section 2.4.3, we describe how this noise influences our measurements of confidence intervals.

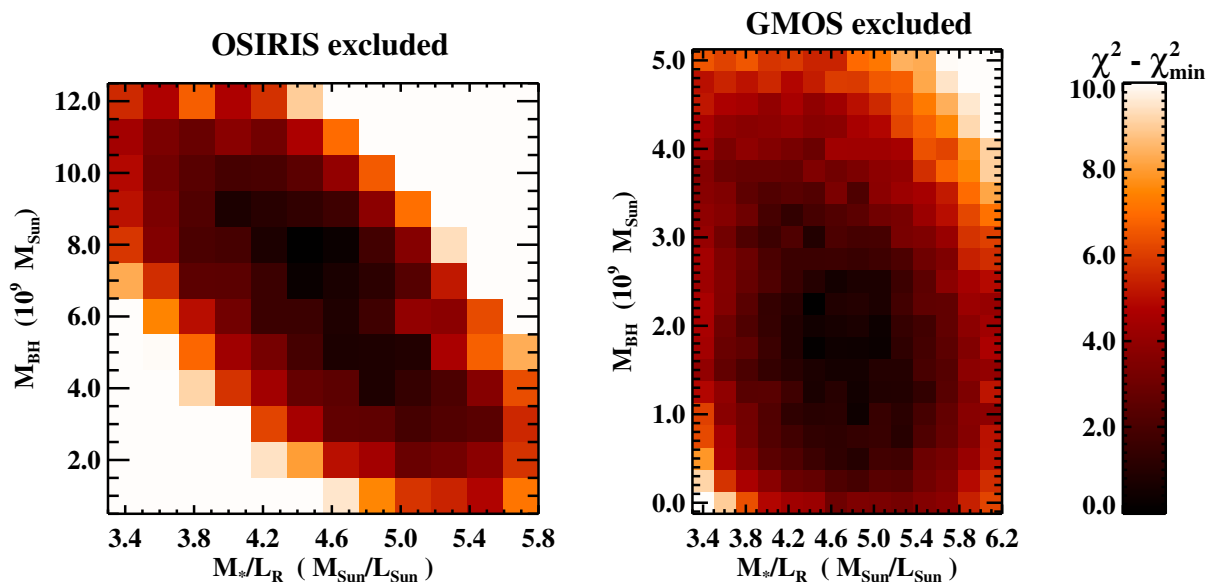


Figure 2.12: χ^2 vs. M_\star/L_R and M_\bullet , using integral-field data from different instruments. *Left*: GMOS data plus long-slit data from Carter et al. (1999). *Right*: OSIRIS data plus long-slit data from Carter et al. (1999). All models include a LOG dark matter halo with $v_c = 500 \text{ km s}^{-1}$ and $r_c = 8.0 \text{ kpc}$, yielding $M_{\text{halo}} = 9.3 \times 10^{11} M_\odot$ within 18.9 kpc. In each case, additional models were run outside the range of M_\star/L_R and M_\bullet depicted here. These models all yield higher values of χ^2 .

2.4.3 Determining Errors

The figure of merit for evaluating confidence intervals in M_\bullet and M_\star/L_R is $\Delta\chi^2 \equiv \chi^2 - \chi_{\min}^2$, where χ_{\min}^2 is the lowest output value among all models. For NGC 6086, we determined confidence intervals by integrating the relative likelihood function, $P \propto e^{-\frac{1}{2}\Delta\chi^2}$. Although $\Delta\chi^2$ is a better statistical indicator than χ^2 per degree of freedom (e.g., van der Marel et al. 1998; Gebhardt et al. 2003), the latter is useful for crudely indicating the level of agreement between the data and the model with the best fit. For each model, the number of degrees of freedom, N_{dof} , depends on the number of observed LOSVDs and the number of velocity bins evaluated per LOSVD. Because we used a spectral smoothing factor in determining LOSVDs for OSIRIS and GMOS, the velocity bins are not entirely independent. We estimate that each LOSVD from OSIRIS or GMOS has 1 degree of freedom per 2 velocity bins, whereas long-slit data from Carter et al. (1999) has 1 degree of freedom per velocity bin. For all experiments with NGC 6086, we find $\chi_{\min}^2/N_{\text{dof}}$ between 0.7 and 1.8, indicating reasonable agreement.

2.4.3.1 Confidence Intervals

We determine confidence intervals by using $\Delta\chi^2$ as an empirical measure of relative likelihood between models with different M_\bullet and M_\star/L_R , and by numerically integrating this likelihood with respect to M_\bullet and M_\star/L_R . In contrast to the majority of previous studies (e.g., Gebhardt et al. 2000b; 2003; 2007; Nowak et al. 2007; 2008; Gebhardt & Thomas 2009; Gültekin et al. 2009b; Siopis et al. 2009; Shen & Gebhardt 2010; cf. van der Marel et al. 1998), we do not use fixed values of $\Delta\chi^2$ to define confidence intervals. The fixed $\Delta\chi^2$ method is appropriate only if the orbit models cleanly sample a well-defined likelihood function of M_\bullet and M_\star/L_R ; other studies typically assume a two-dimensional Gaussian likelihood function. Our models of NGC 6086 produce noisy χ^2 contours (Figure 2.9), in which case the fixed $\Delta\chi^2$ method is sensitive to noise in individual models. This effect is especially pronounced for models without a dark matter halo.

We define likelihood P such that two models with χ_1^2 and χ_2^2 have relative likelihood

$$\frac{P_1}{P_2} = e^{-\frac{1}{2}(\chi_1^2 - \chi_2^2)} \quad (2.8)$$

This form of P is valid, provided that χ^2 is measured from independent, Gaussian-distributed data points (Cowan 1998); in our case, these are the observed LOSVDs. To evaluate likelihood with respect to a single variable (i.e. $x \equiv M_\bullet$), we marginalize the two-dimensional surface with respect to the other variable ($y \equiv M_\star/L_R$), such that:

$$P(x) \propto \sum_{y_{\min}}^{y_{\max}} e^{-\frac{1}{2}\chi^2(x,y)} \delta y, \quad (2.9)$$

where δy is the interval between sampled values of y . Confidence intervals in x are determined

by evaluating the cumulative distribution:

$$C(x) = \frac{\int_{x_{\min}}^x P(x') dx'}{\int_{x_{\min}}^{x_{\max}} P(x') dx'} \quad (2.10)$$

In practice, we define $[x_{\min}, x_{\max}]$ and $[y_{\min}, y_{\max}]$ by expanding our range of models until the marginalized likelihood functions $P(M_{\bullet})$ and $P(M_{\star}/L_R)$ are nearly zero at the minimum and maximum modeled values of M_{\bullet} and M_{\star}/L_R . The physical limit $M_{\bullet} = 0$ is included in all trials. For confidence level k , we define confidence limits at $C = \frac{1}{2}(1 \pm k)$. For example, the 68% confidence interval comprises all x for which $0.16 \leq C \leq 0.84$. For each trial, we define the best-fit values of M_{\bullet} and M_{\star}/L_R as the median values from $P(M_{\bullet})$ and $P(M_{\star}/L_R)$, corresponding to $C = \frac{1}{2}$. In Figure 2.13, we show $P(M_{\bullet})$ and $P(M_{\star}/L_R)$ for each dark halo setting, along with cumulative distributions, median values, and confidence intervals. To estimate precise confidence limits, we linearly interpolate C between discretely sampled values of M_{\bullet} and M_{\star}/L_R .

Our empirical treatment yields wider 68% confidence intervals than those derived from fixed $\Delta\chi^2$ and a Gaussian likelihood function. Our intervals for confidence levels $\geq 90\%$ typically fall near those derived from fixed $\Delta\chi^2$. By construction, our confidence intervals do not include $M_{\bullet} = 0$. For the maximum-mass LOG dark matter halo in NGC 6086, the marginalized likelihood corresponding to $M_{\bullet} = 0$, $P(M_{\bullet} = 0)$, is 0.06% of the maximum marginalized likelihood value. For a Gaussian likelihood function, this likelihood ratio would indicate $> 99.98\%$ confidence for a black hole detection. For models without dark matter, $P(M_{\bullet} = 0)$ is 23.2% of the maximum value, and the detection falls to 91% confidence.

An alternative way to determine confidence intervals from noisy χ^2 is the method of van der Marel et al. (1998), in which random noise is added to the LOSVDs output by each orbit model, the χ^2 surface is re-computed, and confidence limits are determined using fixed $\Delta\chi^2$. This process is repeated in a Monte Carlo fashion, and the extrema of the confidence limits from all trials are adopted. This treatment assumes that numeric noise in orbit models produces fluctuations about an intrinsically Gaussian likelihood distribution. The global likelihood function of our models, however, is visibly non-Gaussian (see Figure 2.13, top, in particular).

2.4.3.2 Systematic Errors

The confidence intervals measured from χ^2 surfaces account for statistical errors in the observed LOSVDs and random noise within the stellar orbit models. Systematic errors must be addressed separately. We have directly tested several systematic effects.

Our largest systematic error arises from discrepancies between LOSVD shapes derived from IFS versus long-slit data, as indicated by the parameter h_4 (Figure 8d). To test how this discrepancy biases M_{\bullet} and M_{\star}/L_R , we fit Gaussian profiles to the original LOSVDs from Carter et al. (1999), constructing an alternative set of LOSVDs with $h_3 = 0$ and $h_4 = 0$. Using these new LOSVDs in combination with the OSIRIS and GMOS data, we repeated the

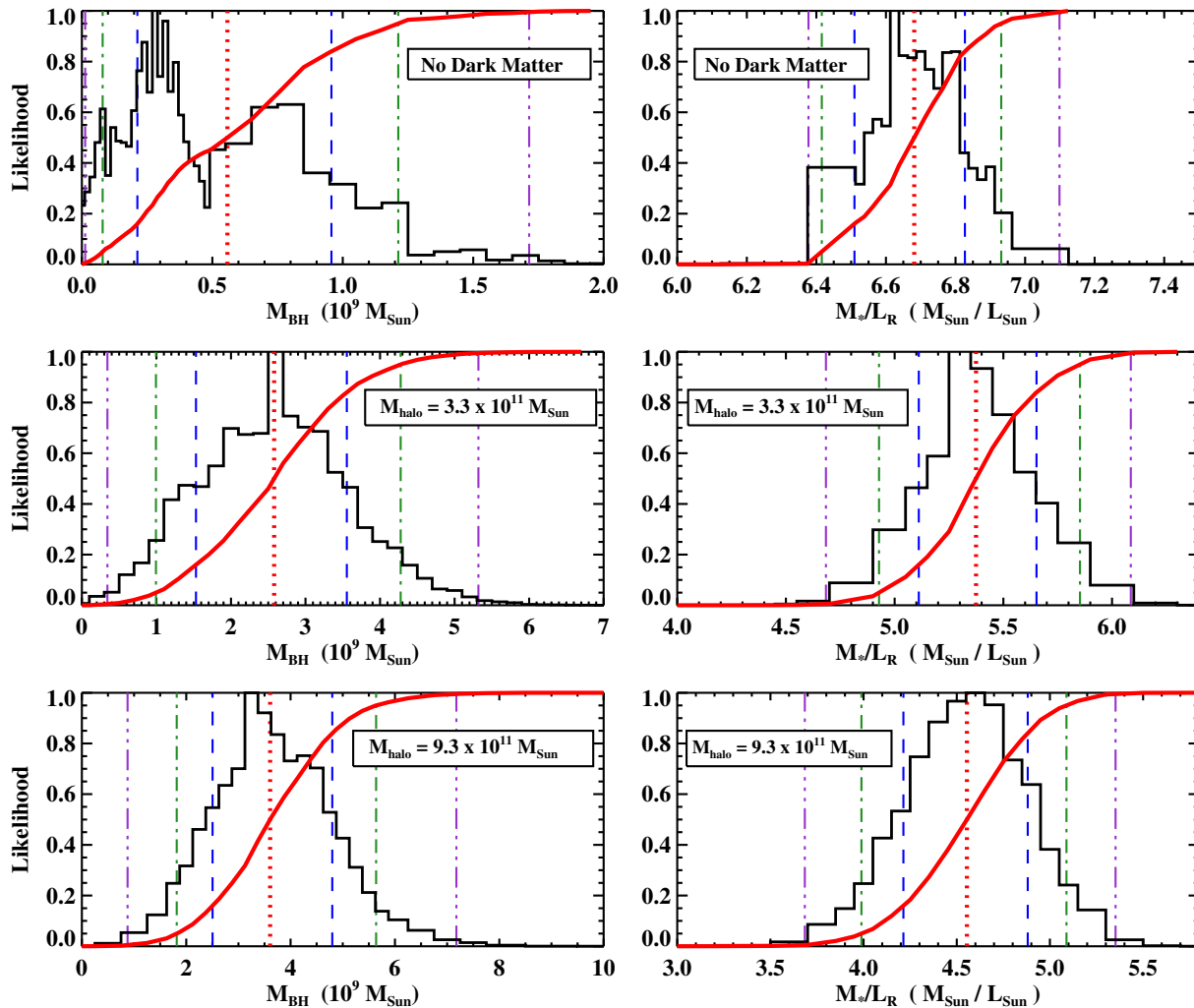


Figure 2.13: Likelihood functions $P(M_\bullet)$ and $P(M_\star/L_R)$, after marginalizing over one variable (M_\star/L_R and M_\bullet , respectively) and re-normalizing. The solid red line in each plot is the cumulative distribution. Vertical lines in each figure represent the median value (dotted red line) and intervals for 68%, 90%, and 99% confidence (dashed lines). *Top*: Models with no dark matter halo. *Middle*: $v_c = 300 \text{ km s}^{-1}$ and $r_c = 8.0 \text{ kpc}$, for $M_{\text{halo}} = 3.3 \times 10^{11} M_\odot$ within 18.9 kpc. *Bottom*: $v_c = 500 \text{ km s}^{-1}$ and $r_c = 8.0 \text{ kpc}$, for $M_{\text{halo}} = 9.3 \times 10^{11} M_\odot$ within 18.9 kpc.

stellar orbit models for the maximum dark matter halo, and found $M_\bullet = 4.5_{-1.1}^{+1.4} \times 10^9 M_\odot$, and $M_\star/L_R = 4.2_{-0.3}^{+0.3} M_\odot L_{\odot,R}^{-1}$. This is a 22% increase in M_\bullet and a 9% decrease in M_\star/L_R , relative to the corresponding trial with original LOSVDs from Carter et al. (1999). The direction of the bias indicates that more enclosed mass is required to produce LOSVDs with extended wings ($h_4 > 0$) at $\sim 3 - 19$ kpc. Since the additional mass is obtained by increasing M_\star/L_R , the innermost LOSVDs drive the best fit toward a smaller value of M_\bullet .

Two additional sources of systematic error are the uncertainties of the optimal stellar template for fitting LOSVDs, and the average PSF for OSIRIS. We find that both effects yield small errors. Trials with 3 PSFs yield a standard deviation of 8% in M_\bullet and 1% in M_\star/L_R . Trials with 2 stellar templates differ by 5% in M_\bullet (corresponding to 3.6% standard deviation) and 2% in M_\star/L_R (1.6% standard deviation). We describe these tests in detail in Section 2.6.

We use the following prescription to compute the total error in M_\bullet for a given dark halo:

$$\sigma_{+,tot} = \left(\sigma_{+,\chi^2}^2 + \sigma_{\text{PSF}}^2 + \sigma_{\text{temp}}^2 + 2\delta_{h_4}^2 \right)^{\frac{1}{2}} \quad (2.11)$$

and

$$\sigma_{-,tot} = \left(\sigma_{-,\chi^2}^2 + \sigma_{\text{PSF}}^2 + \sigma_{\text{temp}}^2 \right)^{\frac{1}{2}}. \quad (2.12)$$

Here, $\sigma_{+,tot}$ and $\sigma_{-,tot}$ are the upper and lower portions of the 68% confidence interval, including all errors; σ_{+,χ^2} and σ_{-,χ^2} are the contributions from integrating the empirical likelihood function as in Section 2.4.3, and represent statistical errors; σ_{PSF} is the standard deviation in best-fit M_\bullet from trials with different OSIRIS PSFs; σ_{temp} is the standard deviation from trials with different template stars; and δ_{h_4} is the difference in best-fit M_\bullet from using re-fit versus original LOSVDs from Carter et al. (1999). As excluding h_3 and h_4 from these LOSVDs introduces a bias toward higher M_\bullet , we assign this effect solely to $\sigma_{+,tot}$, with a magnitude of $2 \times \frac{1}{\sqrt{2}} \delta_{h_4}$. Our equations defining $\sigma_{+,tot}$ and $\sigma_{-,tot}$ for M_\star/L_R are similar to (2.11) and (2.12), except we apply δ_{h_4} entirely to $\sigma_{-,tot}$. To apply our results to different dark matter halo settings, we define the systematic errors as percentages, such that δ_{h_4} , σ_{PSF} and σ_{temp} scale with M_\bullet and M_\star/L_R . We list the 68% confidence intervals, including all errors, inside parentheses in Table 2.2. The confidence intervals outside parentheses in Table 2.2 only include σ_{\pm,χ^2}^2 .

By adding in quadrature, we have assumed zero correlation between different sources of systematic error; this is the most conservative approximation. δ_{h_4} and σ_{temp} are likely correlated (see, e.g., Carter et al. 1999), but the contributions from σ_{temp} are small, and we have not run extensive tests to measure covariance between stellar templates and overall trends in h_4 . There is no obvious reason to suspect covariance between other terms.

2.4.3.3 Other Potential Sources of Error

The shapes and depths of CO bandheads depend on luminosity class as well as spectral type (e.g., Silge & Gebhardt 2003). Although we have extensively examined stars of multiple spectral types, our library of template stars from OSIRIS lacks an M-dwarf template; it is

uncertain whether dwarf stars contribute significantly to spectra of NGC 6086. Our sample of templates is also limited by the range of elemental abundances found in bright stars in the solar neighborhood. Loubser et al. (2009) determine stellar metallicity at the center of NGC 6086 to be ~ 2 times solar ($[Z/H] = 0.28 \pm 0.07$), with an α -enhancement ratio, $[E/Fe]$, of 0.39 ± 0.04 . Other BCGs are similarly metal- and α -rich (Brough et al. 2007; Loubser et al. 2009). If LOSVDs derived from Ca II, CO, and OH absorption features are sensitive to template star metallicities and α ratios, then our systematic error could be higher than estimated above.

Another issue is the possibility of significant spatial variations in the stellar mass-to-light ratio, contradicting the uniformity imposed upon stellar orbit models. Radial gradients in age, metallicity, and α -enhancement have been measured in individual BCGs (Brough et al. 2007; Coccato et al. 2010); further modeling is necessary to quantify corresponding gradients in M_*/L .

An untested source of systematic error for NGC 6086 is the assumed shape and inclination of the galaxy. Our orbit models use an oblate, axisymmetric potential and assume edge-on inclination. Previous studies have indicated that uncertain inclination can bias M_\bullet by 30 – 50% in elliptical galaxies (Verolme et al. 2002; Gebhardt et al. 2003; Shapiro et al. 2006). Moreover, isophotal evidence and simulations of galaxy mergers suggest that many BCGs are prolate or triaxial (Porter et al. 1991; Ryden et al. 1993; Boylan-Kolchin et al. 2006). Although the orbit superposition method was originally developed for a triaxial potential (Schwarzschild 1979), triaxial orbit models with the spatial and velocity resolutions necessary to measure M_\bullet are a very recent development (van den Bosch et al. 2008). In an early comparison of triaxial and axisymmetric models, van den Bosch & de Zeeuw (2010) found that M_\bullet was unchanged in M32, whereas triaxial models of NGC 3379 increased M_\bullet by a factor of 2.

2.5 Conclusions and Discussion

We have reported the first stellar dynamical measurement of the central black hole mass in a BCG beyond the Virgo Cluster. Our results are based on two-dimensional stellar kinematics in the central region of NGC 6086 (the BCG in Abell 2162): the inner $0.9''$ (580 pc) from the IFS OSIRIS with LGS-AO at Keck, the inner $4.9''$ from the IFS GMOS-N at Gemini North, and long-slit data out to $30''$ from Carter et al. (1999). The individual datasets play complementary roles in constraining the gravitational potential of NGC 6086. Used together, GMOS and OSIRIS data reduce degeneracy between the black hole mass and enclosed stellar mass near the center, decreasing the uncertainties of both quantities. The long-slit data confirm the presence of dark matter and constrain the total enclosed mass, but they are insensitive to the precise form of the dark matter halo profile.

We have used axisymmetric stellar orbit models including a dark matter halo to determine M_\bullet and the R -band stellar mass-to-light ratio. We have tested several dark matter halo profiles with our full set of kinematic measurements; in each case, the best-fit black hole is

at least 4 times as massive as the best fit without dark matter. Including dark matter in the models decreases the best-fit value of M_*/L_R by 20 – 40%. For the most massive halo allowed within the gravitational potential of the host cluster, we find $M_\bullet = 3.6_{-1.1}^{+1.7} \times 10^9 M_\odot$ and $M_*/L_R = 4.6_{-0.7}^{+0.3} M_\odot L_{\odot,R}^{-1}$. We obtain similar values of M_\bullet and M_*/L_R when we exclude long-slit data, for models with and without dark matter.

In Figure 2.14, we add our measurement of M_\bullet in NGC 6086 to the $M_\bullet - \sigma$ relationship of Gültekin et al. (2009a). Our plotted measurement corresponds to the most massive dark matter halo used in our models. We derive an effective velocity dispersion of $318 \pm 2 \text{ km s}^{-1}$ within 1 effective radius, by weighting the kinematic measurements from Carter et al. (1999) with respect to our measured surface brightness profile. The $M_\bullet - \sigma$ relation and intrinsic scatter from Gültekin et al. (2009a) yield a σ -predicted black hole mass of $0.9_{-0.6}^{+1.7} \times 10^9 M_\odot$. Our measurement of $M_\bullet = 3.6_{-1.1}^{+1.7} \times 10^9 M_\odot$ with a maximum-mass dark matter halo is marginally consistent with this prediction, while our measurement of $M_\bullet = 2.6_{-1.0}^{+1.3} \times 10^9 M_\odot$ for an intermediate-mass halo is closer to the predicted value. Our measurement of $M_\bullet = (0.6 \pm 0.4) \times 10^9 M_\odot$ without dark matter also agrees with the predicted value. However, the unrealistic omission of dark matter at radii covered by long-slit data biases M_\bullet toward low values. The V -band luminosity of NGC 6068 is $1.4 \times 10^{11} L_{\odot,V}$, using $M_V = -23.11$ from Lauer et al. (2007a). The $M_\bullet - L$ relation and intrinsic scatter from Gültekin et al. (2009a) yield a prediction of $M_\bullet = 1.3_{-0.7}^{+1.9} \times 10^9 M_\odot$, which is consistent with our measurements with and without dark matter.

Of the existing sample of ~ 30 galaxies with M_\bullet measured from stellar dynamics, this study of NGC 6086 is only the third to consider dark matter. Like NGC 6086, measurements of M_\bullet and M_*/L in M87 depend strongly on the inclusion of a dark matter halo (Gebhardt & Thomas 2009). However, Shen & Gebhardt (2010) found that introducing dark matter to models of M60 produced minimal changes in M_\bullet and M_*/L . Several factors contribute to the greater importance of dark matter in models of NGC 6086 and M87. First, the quality and spatial resolution of the kinematics are insufficient to distinguish thoroughly the black hole from the central stellar mass profile. Neither NGC 6086 nor M87 have good spectra from *HST*, and the potential advantage of AO IFS data for NGC 6086 was compromised by low S/N and coarse spatial binning. In principle, very high-quality data could reveal unambiguously a compact mass at the center of the gravitational potential, permitting robust measurements of M_\bullet in spite of biased M_*/L_R values. Second, shallow stellar mass profiles in NGC 6086 and M87 limit the range of radii where stars dominate the gravitational potential, especially in the presence of a relatively massive and concentrated dark matter halo. In contrast, models of M60 can exclude dark matter and still accurately constrain M_*/L by removing only the few outermost data points. Third, shallow stellar light profiles affect kinematic measurements near the centers of NGC 6086 and M87: there is more contamination along the line of sight from stars at larger radii, where dark matter is influential. The latter two factors suggest that existing stellar dynamical measurements of M_\bullet are most likely biased in galaxies with large stellar cores. New and revised measurements using models with dark matter could raise or steepen the upper end of the black hole scaling relations, as stellar core size increases with galaxy mass (Lauer et al. 2007a).

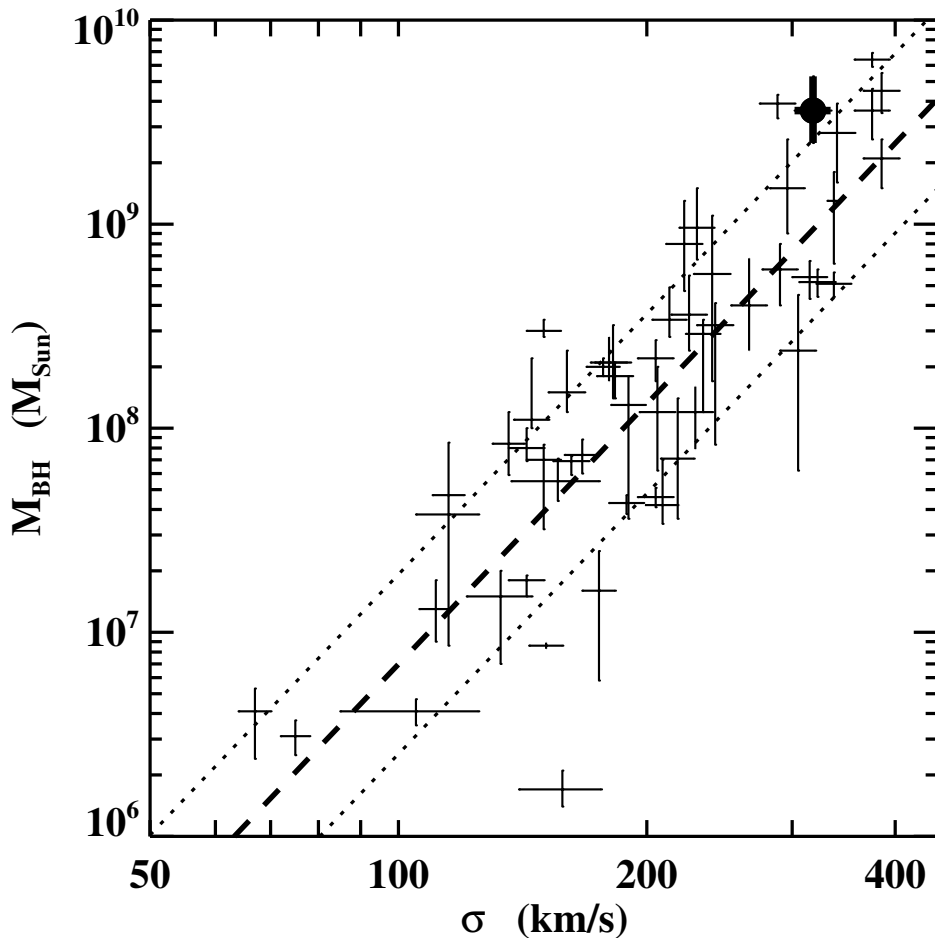


Figure 2.14: $M_{\bullet} - \sigma$ relation, including NGC 6086. The filled circle is our measurement of $M_{\bullet} = 3.6_{-1.1}^{+1.7} \times 10^9 M_{\odot}$ in NGC 6086, using the maximum-mass LOG dark matter halo ($v_c = 500 \text{ km s}^{-1}$) and our full set of data from OSIRIS, GMOS, and Carter et al. (1999). Without dark matter, we measure $M_{\bullet} = 0.6_{-0.4}^{+0.4} \times 10^9 M_{\odot}$. The remaining data points are the measurements compiled in Gültekin et al. (2009a), plus updated measurements for M87 and M60 (Gebhardt & Thomas 2009; Shen & Gebhardt 2010). The thick dashed line is the fit $\log(M_{\bullet}) = 8.12 + 4.24 \log(\sigma/200 \text{ km s}^{-1})$, and the dotted lines enclose a scatter of 0.44 dex, from Gültekin et al. (2009a).

Stellar population modeling can yield an independent measurement of the stellar mass-to-light ratio. To compare existing stellar population studies to our dynamical results, we translate M_*/L_V and M_*/L_I to R band by using the $(g - r)$ and $(r - i)$ colors of NGC 6086 from the Sloan Digital Sky Survey (SDSS). Applying the filter translations of Blanton & Roweis (2007), we find $V - R = 0.64$ and $R - I = 0.68$; the resulting adjustments in solar units are $M_*/L_R = 0.76M_*/L_V$, and $M_*/L_R = 1.33M_*/L_I$. For the maximum-mass dark matter halo, our dynamical measurement of $M_*/L_R = 4.6^{+0.3}_{-0.7} M_\odot L_{\odot,R}^{-1}$ agrees with population-based measurements from Cappellari et al. (2006), who find $M_*/L_I \approx 3 M_\odot L_{\odot,I}^{-1}$ ($M_*/L_R \approx 4 M_\odot L_{\odot,R}^{-1}$) for M87 and several other early-type galaxies observed with SAURON. However, a different range of stellar mass-to-light ratios is suggested by the study of von der Linden et al. (2007), who model the stellar masses of 625 BCGs from SDSS. The peak values of their mass and luminosity distribution functions yield a ratio of $M_*/L_V = 3.1 M_\odot L_{\odot,V}^{-1}$ ($M_*/L_R = 2.4 M_\odot L_{\odot,R}^{-1}$). Additionally, Graves & Faber (2010) have compiled various estimates of M_*/L for a sample of $\sim 16,000$ early-type galaxies from SDSS, finding that M_*/L increases with σ , and $M_*/L_V \approx 2 - 3 M_\odot L_{\odot,V}^{-1}$ ($M_*/L_R \approx 1.5 - 2.3 M_\odot L_{\odot,R}^{-1}$) for the highest-dispersion objects in their sample ($\sigma \sim 250 \text{ km s}^{-1}$). Both of these results fall significantly below our dynamical values of M_*/L_R for NGC 6086. The discrepancy is most severe for orbit models without dark matter ($M_*/L_R = 6.7^{+0.2}_{-0.9} M_\odot L_{\odot,R}^{-1}$).

To test whether any model of the gravitational potential for NGC 6086 can hold lower values of M_*/L_R and still fit our data, we have run a series of orbit models with M_*/L_R fixed at $2.5 M_\odot L_{\odot,R}^{-1}$. We sampled the LOG dark matter halo parameters v_c and r_c over a wide range of values and marginalized χ^2 over trials with $M_\bullet = 3.5 \times 10^9 M_\odot$ and $M_\bullet = 7.0 \times 10^9 M_\odot$. The resulting best-fit parameter values are $v_c = 420 \text{ km s}^{-1}$ and $r_c = 2.0 \text{ kpc}$. Fixing v_c and r_c at these values and finely sampling M_\bullet yields $M_\bullet = 5.5^{+2.0}_{-0.9} \times 10^9 M_\odot$, including systematic errors, with $\chi^2_{min} = 1018.6$. In comparison, $\chi^2_{min} = 1010.2$ for our maximum-mass LOG halo ($v_c = 500 \text{ km s}^{-1}$; $r_c = 8.0 \text{ kpc}$). We conclude that the lower values of M_*/L_R motivated by stellar population modeling can produce a reasonable fit to our kinematics, given a more centrally concentrated dark matter halo. Nonetheless, our original assumptions about the dark matter halo profile of NGC 6086 produce a better fit than the assumption of low M_*/L_R . Decreasing the enclosed stellar mass leads to a larger best-fit black hole mass, matching the trend from our other trials.

For each individual dark matter halo, the dominant systematic effect in our results is a discrepancy in the wings of LOSVDs from IFS versus long-slit data, illustrated by a jump in h_4 from negative to positive values. The magnitude of the resulting error is 22% in M_\bullet and 9% in M_*/L_R . Uncertainties in determining an optimal template star and AO PSF yield smaller errors, totaling $\sim 9\%$ in M_\bullet and $\sim 2\%$ in M_*/L_R . Additional, unmeasured systematic errors may arise from our assumptions of axisymmetry and edge-on inclination.

Our investigation of NGC 6086 has established that stellar-dynamical measurements of M_\bullet in BCGs are possible with existing facilities; this dramatically expands the sample volume of viable targets. We plan to follow this work with similar measurements from an ongoing survey of several additional BCGs. This survey is a critical step toward a statistically robust

census of black holes in the Universe’s most massive galaxies, and will eventually shed new light on the histories of galaxies and black holes at the hearts of galaxy clusters.

Acknowledgments

We are grateful for insightful discussions with many colleagues during this investigation: particularly, Genevieve Graves, Kayhan Gültekin, Anne Medling, Kristen Shapiro, Remco van den Bosch, and Jong-Hak Woo. We also thank Sandra Faber and Scott Tremaine for their contributions to our OSIRIS observing proposal. Support astronomers Randy Campbell, Al Conrad, and Jim Lyke played crucial roles in conducting observations with OSIRIS. We thank David Carter and George Hau for providing long-slit data of NGC 6086. We thank the anonymous referee for many helpful suggestions.

This work was supported by NSF AST-1009663. Work by N.J.M. and J.R.G. was supported in part by the NSF Center for Adaptive Optics, managed by the University of California at Santa Cruz under cooperative agreement AST 98-76783. Support for C.-P.M. is provided in part by the Miller Institute for Basic Research in Science, University of California, Berkeley. KG acknowledges support from NSF-0908639. This investigation would not have been possible without the facilities at the Texas Advanced Computing Center at The University of Texas at Austin, which has allowed access to over 5000 node computers where we ran all of the models. The W. M. Keck Observatory is operated as a scientific partnership among the California Institute of Technology, the University of California, and the National Aeronautics and Space Administration. The Observatory was made possible by the generous financial support of the W. M. Keck Foundation. The Gemini Observatory is operated by the Association of Universities for Research in Astronomy, Inc., under a cooperative agreement with the NSF on behalf of the Gemini partnership: the National Science Foundation (United States), the Science and Technology Facilities Council (United Kingdom), the National Research Council (Canada), CONICYT (Chile), the Australian Research Council (Australia), Ministério da Ciência e Tecnologia (Brazil) and Ministerio de Ciencia, Tecnología e Innovación Productiva (Argentina). GMOS data of NGC 6086 were obtained under Program GN-2003A-Q-11.

In addition, the authors wish to recognize and acknowledge the very significant cultural role and reverence that the summit of Mauna Kea has always had within the indigenous Hawaiian community. We are most fortunate to have the opportunity to conduct observations from this mountain.

2.6 Appendix A: Uncertainties in the PSF and Stellar Templates for OSIRIS

We ran additional series of orbit models to assess the effects of stellar template mismatch and PSF uncertainty on the best-fit values of M_{\bullet} and M_{\star}/L_R . We expect these systematic effects to be largest for OSIRIS data. Lower signal-to-noise spectra have larger uncertainties

in template matching, and the crowded series of atomic and molecular features in H -band is more sensitive to template choice than the Ca II features at $0.85 \mu\text{m}$. The structure of the LGS-AO PSF is sensitive to atmospheric turbulence, laser power, the density and thickness of the ionospheric sodium layer, performance of the wavefront sensor and deformable mirror, and the brightness and position of the tip/tilt star. Because several of these factors change over time, delays between observations of an extended science target and a point source can induce errors the estimated PSF. Uncertainties in seeing-limited PSFs arise predominantly from changes in atmospheric turbulence. In order to highlight the effect of template and PSF errors for OSIRIS, we excluded the more stable GMOS data from our trials below. Each trial included our maximum mass dark matter halo. We summarize the trials in Table 2.3.

Table 2.3: PSF and Template Star Trials for NGC 6086

| Data | PSF | Template | v_c (km s^{-1}) | r_c (kpc) | M_\bullet ($10^9 M_\odot$) | M_\star/L_R ($M_\odot L_\odot^{-1}$) | χ^2_{min} | N_{dof} |
|-----------|-----|----------|---------------------------------|----------------|-----------------------------------|---------------------------------------------|-----------------------|------------------|
| (1) | (2) | (3) | (4) | (5) | (6) | (7) | (8) | (9) |
| O + CBH99 | A | M4III | 500 | 8.0 | $1.8^{+1.3}_{-1.0}$ | $4.5^{+0.7}_{-0.6}$ | 419.0 | 570 |
| O + CBH99 | B | M4III | 500 | 8.0 | $1.9^{+1.4}_{-1.1}$ | $4.6^{+0.7}_{-0.7}$ | 412.7 | 570 |
| O + CBH99 | B | M0III | 500 | 8.0 | $2.0^{+1.3}_{-1.0}$ | $4.5^{+0.7}_{-0.7}$ | 415.6 | 570 |
| O + CBH99 | C | M4III | 500 | 8.0 | $2.1^{+1.4}_{-1.1}$ | $4.5^{+0.7}_{-0.6}$ | 414.6 | 570 |

Notes: Column 1: Data sets included in trial. “O” refers to OSIRIS, and “CBH99” refers to long-slit kinematics from Carter et al. (1999). Column 2: estimated PSF for OSIRIS data. A: original PSF measured from tip/tilt star with OSIRIS, folded over major and minor axes of NGC 6086 (Figure 2.15, top right). B: tapered and folded PSF (Figure 2.15, bottom left). C: core-halo PSF, with 25% Strehl ratio (Figure 2.15, bottom right). Column 3: spectral type of template star for OSIRIS data. We used spectra from HD 110964 (M4III) and HD 108629 (M0III). Column 4: circular velocity of LOG dark matter halo (Eq. 2.3). Column 5: core radius of dark matter halo (Eq. 2.3). Column 6: best-fit black hole mass. Column 7: best-fit R -band stellar mass-to-light ratio. Column 8: minimum χ^2 value for all models. Column 9: degrees of freedom in model fits to LOSVDs. Computed values include a smoothing factor of 1 degree of freedom per 2 velocity bins for non-parametric LOSVDs from OSIRIS. Quoted errors in M_\bullet and M_\star/L_R correspond to 68% confidence intervals. All trials in Section 2.4 used PSF B and template star HD 110964 (M4III).

In Figure 2.15, we display various estimates of the average PSF for OSIRIS observations of NGC 6086. Our initial estimate, displayed at the top middle, was constructed from a one-time sequence of exposures of the LGS-AO tip/tilt star. We have characterized the two-component structure of this PSF by fitting a narrow Gaussian profile plus a broad Moffat profile. The resulting FWHM values are $0.10''$ and $0.42''$. The narrow component contains 44% of the total flux. However, we cannot directly compute a Strehl ratio from this percentage, because the $0.05''$ pixels in our collapsed OSIRIS images undersample the H -band diffraction limit ($\lambda/D = 0.033''$). Our trials use PSFs derived from the original tip/tilt images, rather than the Gaussian plus Moffat model. The PSFs used in our trials (A, B, and C) were all symmetrized with respect to the major- and minor-axis position angles of NGC 6086, in order to match the spatial folding of kinematic data for axisymmetric models.

PSF A (Figure 2.15, top right) symmetrizes the estimate from the tip/tilt star, but contains no further changes. This estimate has two primary limitations. It only captures the PSF at a single moment in time, and it does not account for the $42''$ separation between the tip/tilt star and the center of NGC 6086. A complementary method for estimating the PSF is to compare the collapsed OSIRIS mosaic of the galaxy center to an image from *HST*/WFPC2. We convolved this mosaic with an appropriate WFPC2 PSF and convolved the WFPC2 image with a trial PSF, so that both images would have the same total smoothing kernel. Using our original PSF estimate from the tip/tilt star, we found that the brightness profile of the convolved WFPC2 image was shallower than the collapsed OSIRIS mosaic. Therefore, we tested a series of PSFs that multiplied this original estimate by tapering functions with various inner and outer radii. We found the lowest root-mean-squared residual for PSF B, depicted in Figure 2.15 (bottom left), which suppresses power at radii beyond $0.3''$. In order to probe the effect of a Nyquist-sampled, diffraction-limited core, we constructed a third estimate, PSF C (Figure 2.15, bottom right). We interpolated the original tip/tilt-based PSF from $0.05''/\text{pixel}$ to $0.01''/\text{pixel}$, and replaced the central $0.1'' \times 0.1''$ with a two-dimensional Airy profile ($\lambda/D = 0.033''$). The amplitude of the core was scaled relative to the outer profile to yield a Strehl ratio of 25%.

PSFs A, B, and C incorporate a variety of methods for PSF estimation, and the range of variation in their structures is comparable to the uncertainty in any particular method. We find a standard deviation of 8% in M_\bullet and 1% in M_\star/L_R among trials using each of these three PSFs. Similarly, Nowak et al. (2008) found little variation in M_\bullet and M_\star/L_{K_s} from different estimates of the PSF for AO data of Fornax A. For all of our primary trials to measure M_\bullet and M_\star/L_R in NGC 6086 (Section 2.4), we matched OSIRIS data to PSF B. For data from GMOS and Carter et al. (1999), we use Gaussian PSFs. The GMOS PSF has a FWHM of $0.4''$, based on acquisition camera images. Carter et al. (1999) report a FWHM of $1.3''$. Uncertainties in these seeing-limited PSFs should have smaller effects on measurements of M_\bullet , due to poorer spatial resolution.

Our stellar template library for OSIRIS contains stars with spectral types from G8 through M4. In principle, we can determine a best-fit weighted combination of library templates for each spectrum of NGC 6086, while simultaneously fitting for the LOSVD. However, noise in our OSIRIS spectra renders this method unstable: when we include a

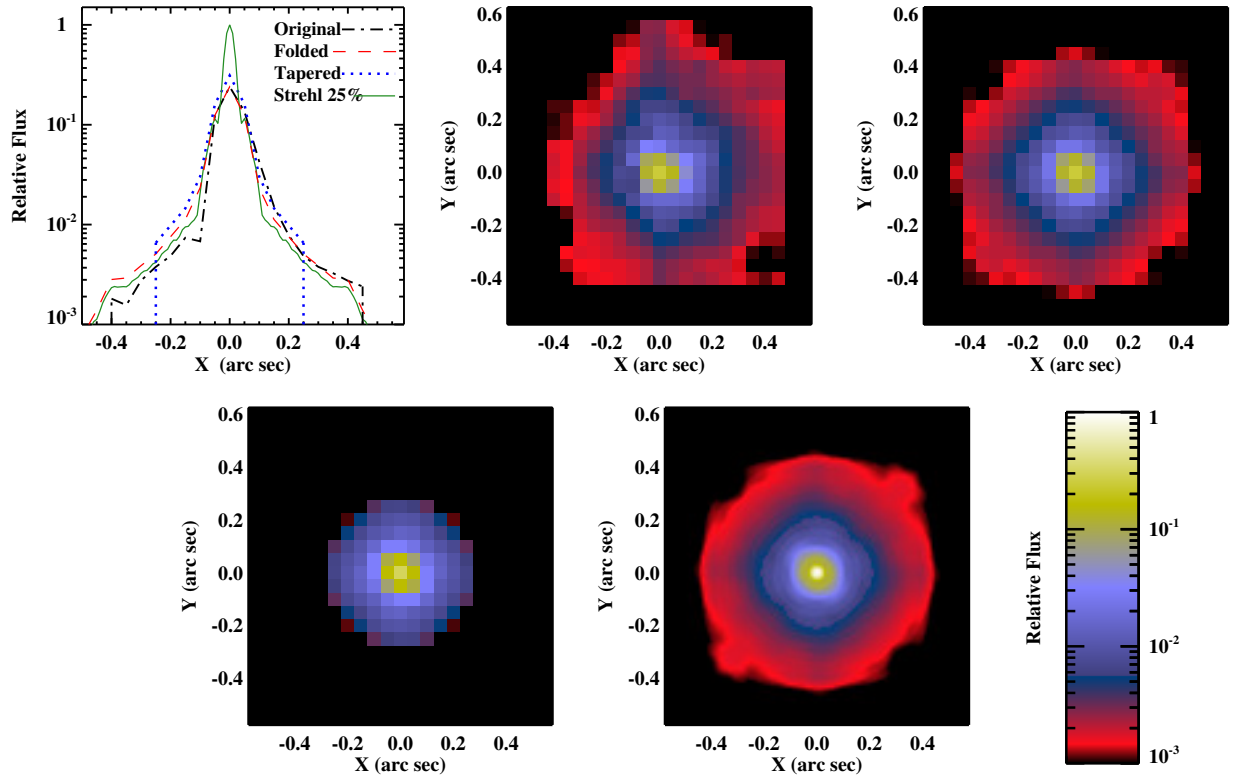


Figure 2.15: PSF models for OSIRIS observations of NGC 6086. *Top left*: horizontal slice through the center of each PSF. *Top middle*: Original estimate from the LGS-AO tip/tilt star. *Top right*: PSF A, folded for axisymmetry. *Bottom left*: PSF B, folded and tapered. *Bottom right*: PSF C, interpolated for a diffraction-limited core and 25% Strehl ratio. The major and minor axes of NGC 6086 are oriented 45° from the plotted X- and Y-axes. Relative flux is defined with respect to the peak value of PSF C. All of our orbit models used PSF B with OSIRIS data, with the exception of trials to test model dependence on PSF structure.

large number of templates, the weights vary dramatically between adjacent spatial regions. To narrow our sample, we compared the equivalent widths (EWs) of H -band absorption features in NGC 6086 to each library template, as illustrated in Figure 2.16. EWs for NGC 6086 were measured from a high- S/N spectrum covering a large portion of the OSIRIS field-of-view. Our kinematic fitting is dominated by high-EW features at $1.54 \mu\text{m}$, $1.55 \mu\text{m}$, $1.62 \mu\text{m}$, and $1.64 \mu\text{m}$. For these features, the three M-giant stars provide much closer EW matches than other stars in our library. Trial kinematic fits using only M-giant stars weighted HD 110964 (M4III) by nearly 100%; for simplicity, we adopted this star as our only template for the final kinematic extraction from OSIRIS spectra.

To test template mismatch, we extracted a second set of LOSVDs from OSIRIS spectra, this time using HD 108629 (M0III) as the template star. The difference between spectral types M0III and M4III is a reasonable estimate for template mismatch in our kinematic fitting, as indicated by our equivalent width measurements. In particular, our fits exclude the Mg/Fe absorption feature near $1.50 \mu\text{m}$ rest, which is a better match to our K-dwarf template. Orbit model trials with M4III-based LOSVDs versus M0III-based LOSVDs differ by 5% in M_\bullet and 2% in M_\star/L_R .

Even though HD 110964 compares favorably to other template stars, its average equivalent width over the spectral features used to extract LOSVDs is $\approx 13\%$ higher than the average equivalent width of NGC 6086. To improve the EW agreement, we artificially decreased the line strengths of the template spectrum, by a constant factor $f_{EW} = 0.83$. We did not allow f_{EW} to vary over different spatial regions in NGC 6086. Optimizing the value of f_{EW} produces smoother LOSVDs, which are also more stable to small changes in spectral smoothing. However, we have found a positive correlation between f_{EW} and the value of h_4 derived from the resulting fit. In non-parametric terms, the wings of the best-fit LOSVD become truncated as absorption features in the template star are artificially made shallower. This effect may contribute partially to the differences between our computed values of h_4 and those from Carter et al. (1999).

2.7 Appendix B: Non-Parametric LOSVDs

We present our final extracted LOSVDs from OSIRIS (Figure 2.17) and GMOS (Figure 2.18), and LOSVDs derived from the measurements of Carter et al. (1999) (Figure 2.19). The LOSVDs from OSIRIS use template star HD 110964 (M4III). We compare each LOSVD to the best-fitting orbit model with our maximum-mass LOG halo, and the best-fitting orbit model with no dark matter. Including dark matter gives a better fit to the total set of LOSVDs, with a cumulative difference $\Delta\chi^2 = 104.2$. Similarities between the LOSVDs generated by each model occur in part because $\sim 30,000$ orbits give the models a high degree of flexibility to optimally fit the data. The models inability to perfectly match the data arises in part from constraints such as axisymmetry and uniformity in M_\star/L_R .

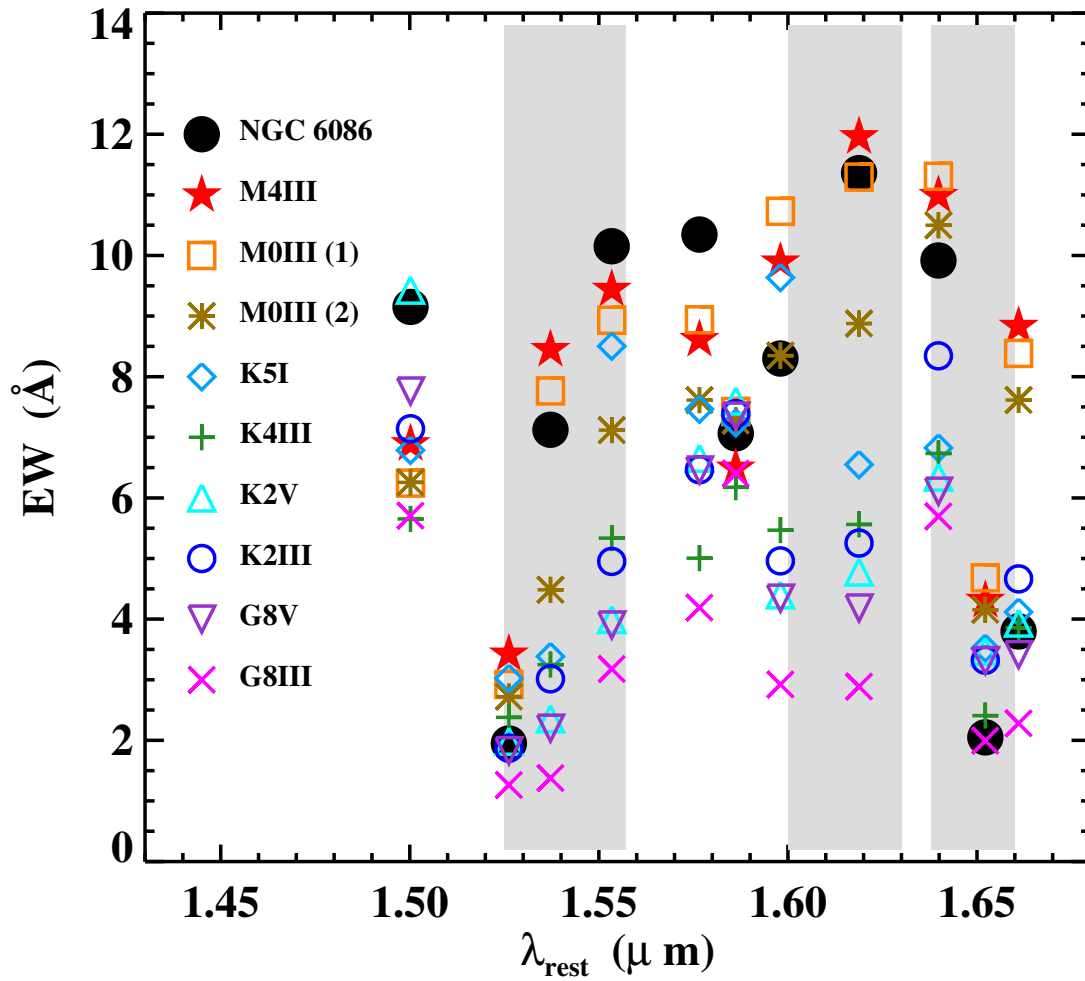


Figure 2.16: *H*-band equivalent widths of NGC 6086 and template stars. The shaded areas mark the spectral range used for kinematic extraction from OSIRIS spectra. Template stars are: HD 110964 (M4III); HD 108629 (M0III 1); HD 63348 (M0III 2); HD 44537 (K5I); 15 Lib (K4III); HD 99492 (K2V); HD 94386 (K2III); 55 Cnc (G8V); HD 89638 (G8III).

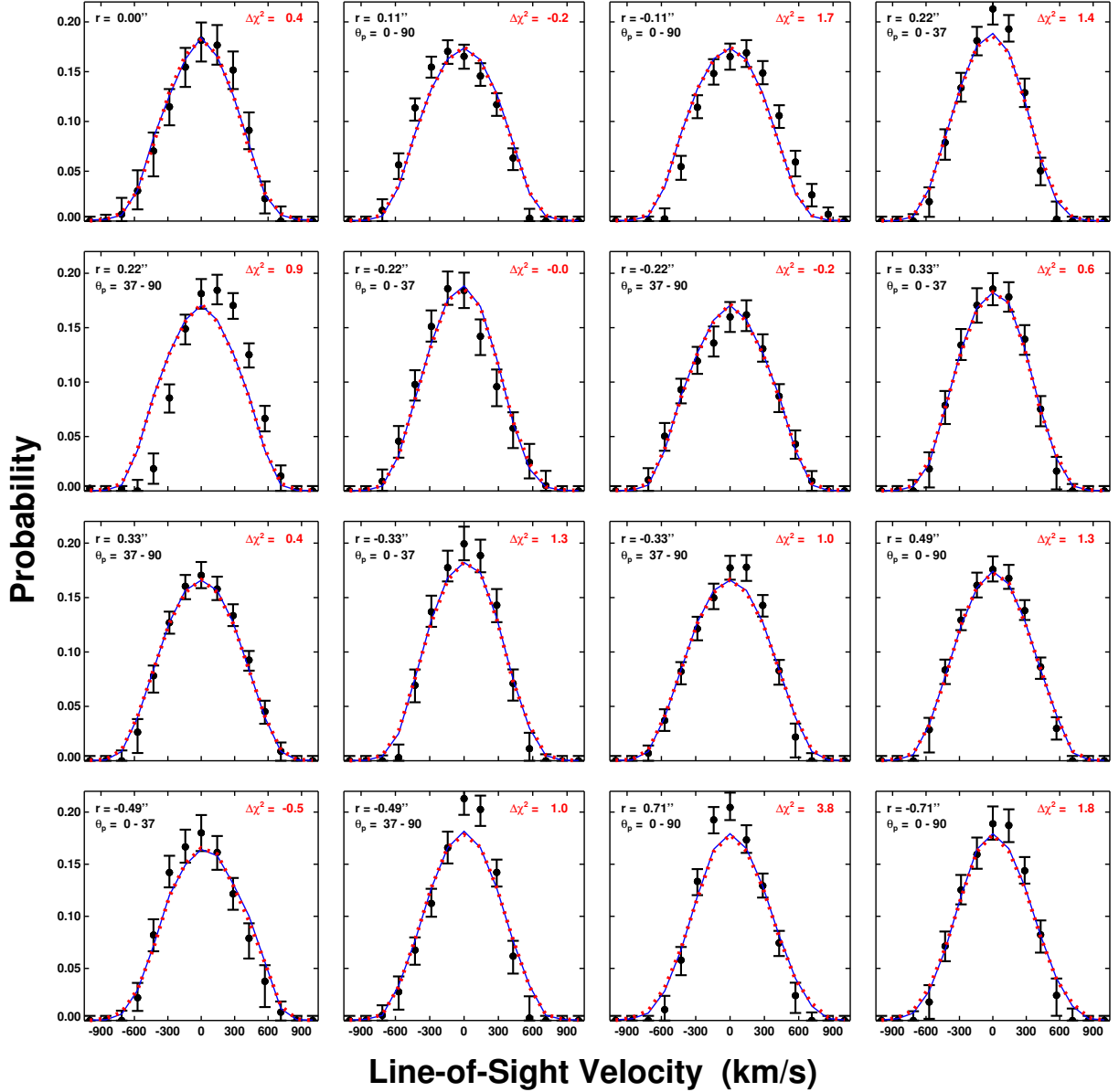


Figure 2.17: LOSVDs in NGC 6086 from OSIRIS spectra. Solid blue lines are corresponding LOSVDs generated by the best-fitting orbit model with the maximum-mass LOG dark matter halo ($M_*/L_R = 4.7 M_\odot L_{\odot,R}^{-1}$, $M_\bullet = 3.5 \times 10^9 M_\odot$, $v_c = 500$ kpc, $r_c = 8.0$ kpc). Dotted red lines are generated by the best-fitting orbit model with no dark halo ($M_*/L_R = 6.8 M_\odot L_{\odot,R}^{-1}$, $M_\bullet = 3.2 \times 10^8 M_\odot$). In each sub-plot, r is the distance from the center of NGC 6086, and θ_p is the range of angles with respect to the major axis. Negative values of r indicate spectra from the south side of NGC 6086. For each LOSVD, $\Delta\chi^2$ is the difference in the χ^2 statistic for the two models: $\Delta\chi^2 > 0$ indicates that the model including dark matter (solid blue line) is a better fit.

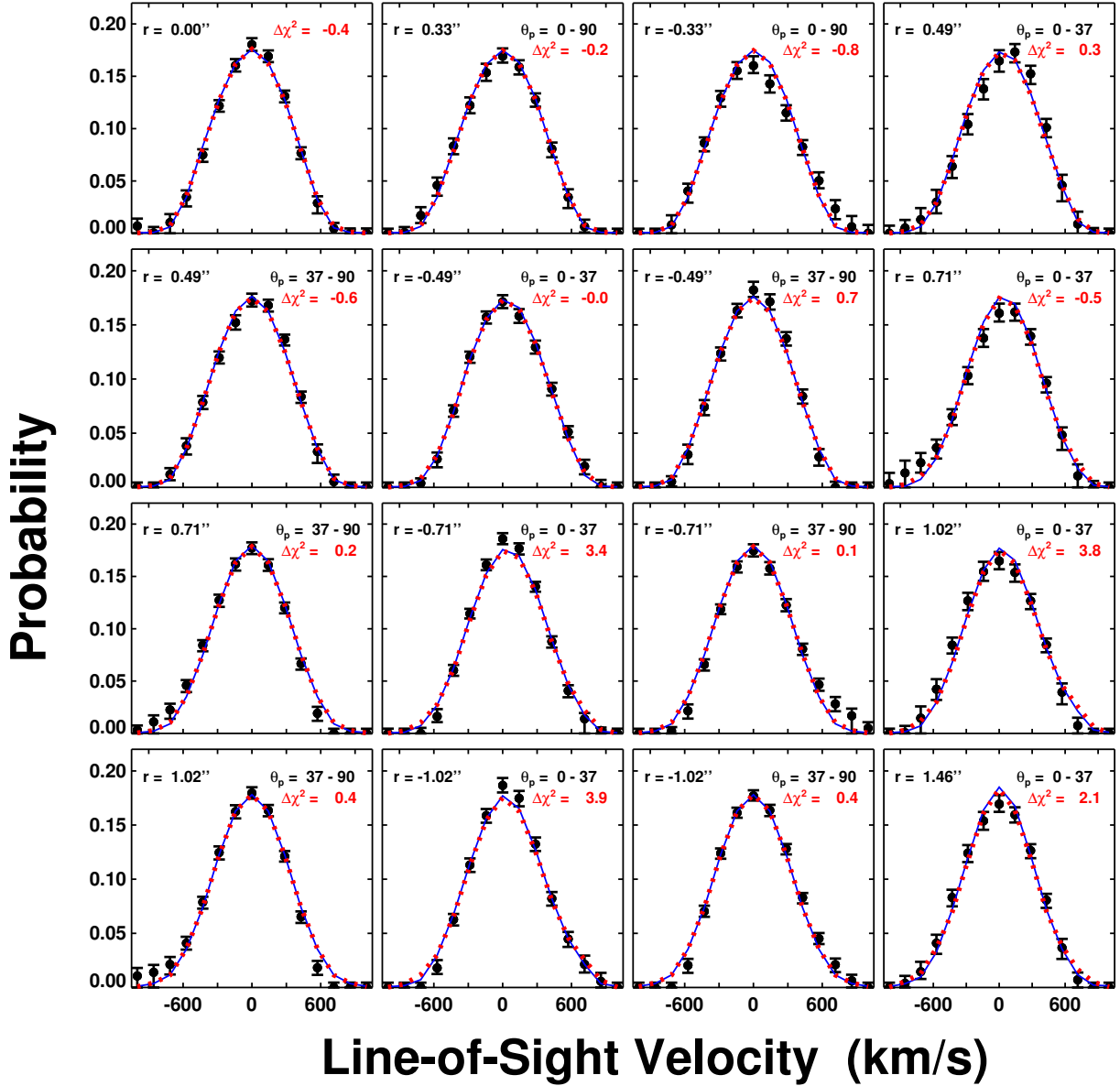


Figure 2.18: LOSVDs in NGC 6086 from GMOS spectra. Solid blue lines are corresponding LOSVDs generated by the best-fitting orbit model with the maximum-mass LOG dark matter halo ($M_*/L_R = 4.7 M_\odot L_{\odot,R}^{-1}$, $M_\bullet = 3.5 \times 10^9 M_\odot$, $v_c = 500$ kpc, $r_c = 8.0$ kpc). Dotted red lines are generated by the best-fitting orbit model with no dark halo ($M_*/L_R = 6.8 M_\odot L_{\odot,R}^{-1}$, $M_\bullet = 3.2 \times 10^8 M_\odot$). In each sub-plot, r is the distance from the center of NGC 6086, and θ_p is the range of angles with respect to the major axis. Negative values of r indicate spectra from the south side of NGC 6086. For each LOSVD, $\Delta\chi^2$ is the difference in the χ^2 statistic for the two models: $\Delta\chi^2 > 0$ indicates that the model including dark matter (solid blue line) is a better fit.

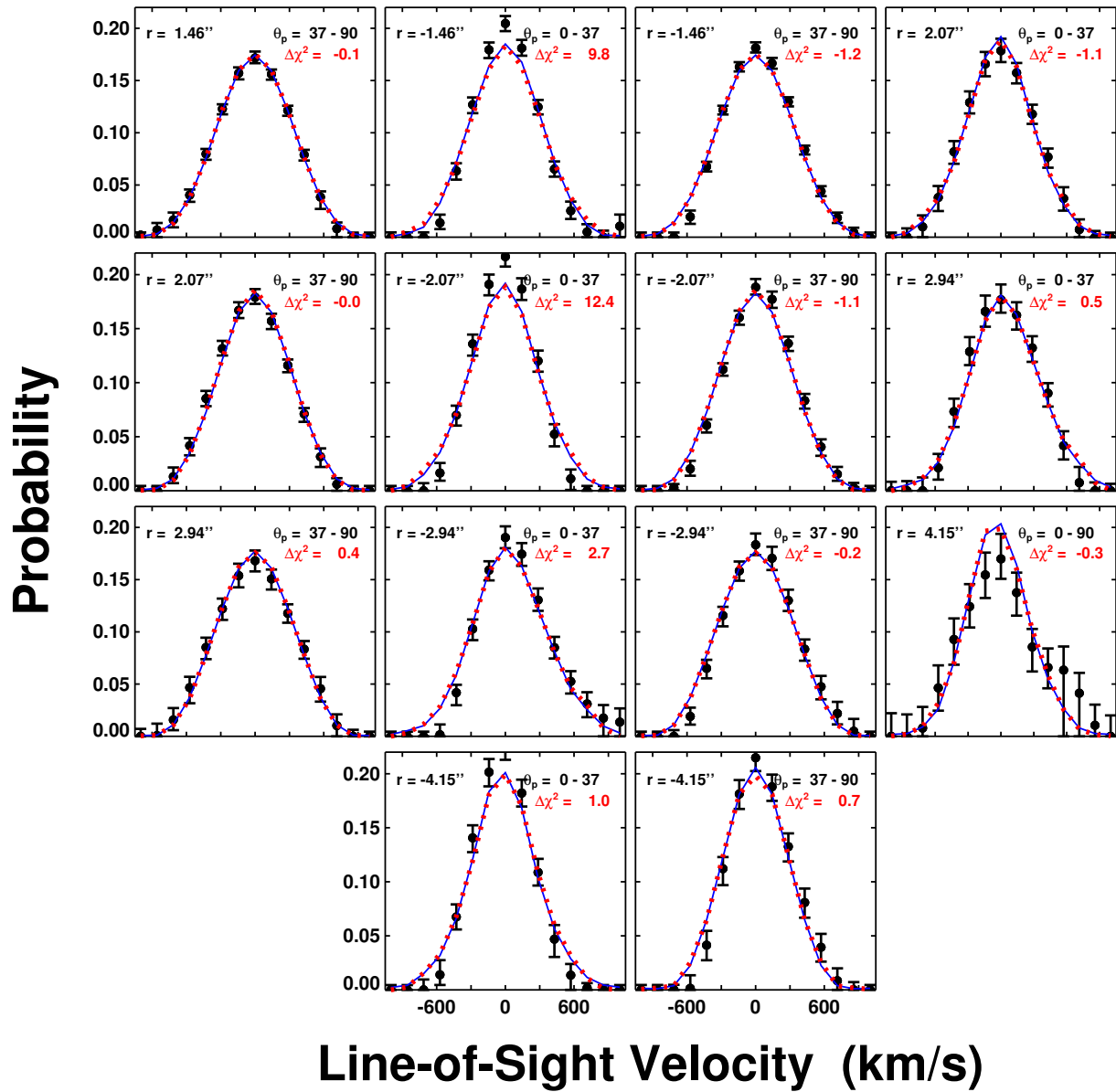


Figure 2.18, continued

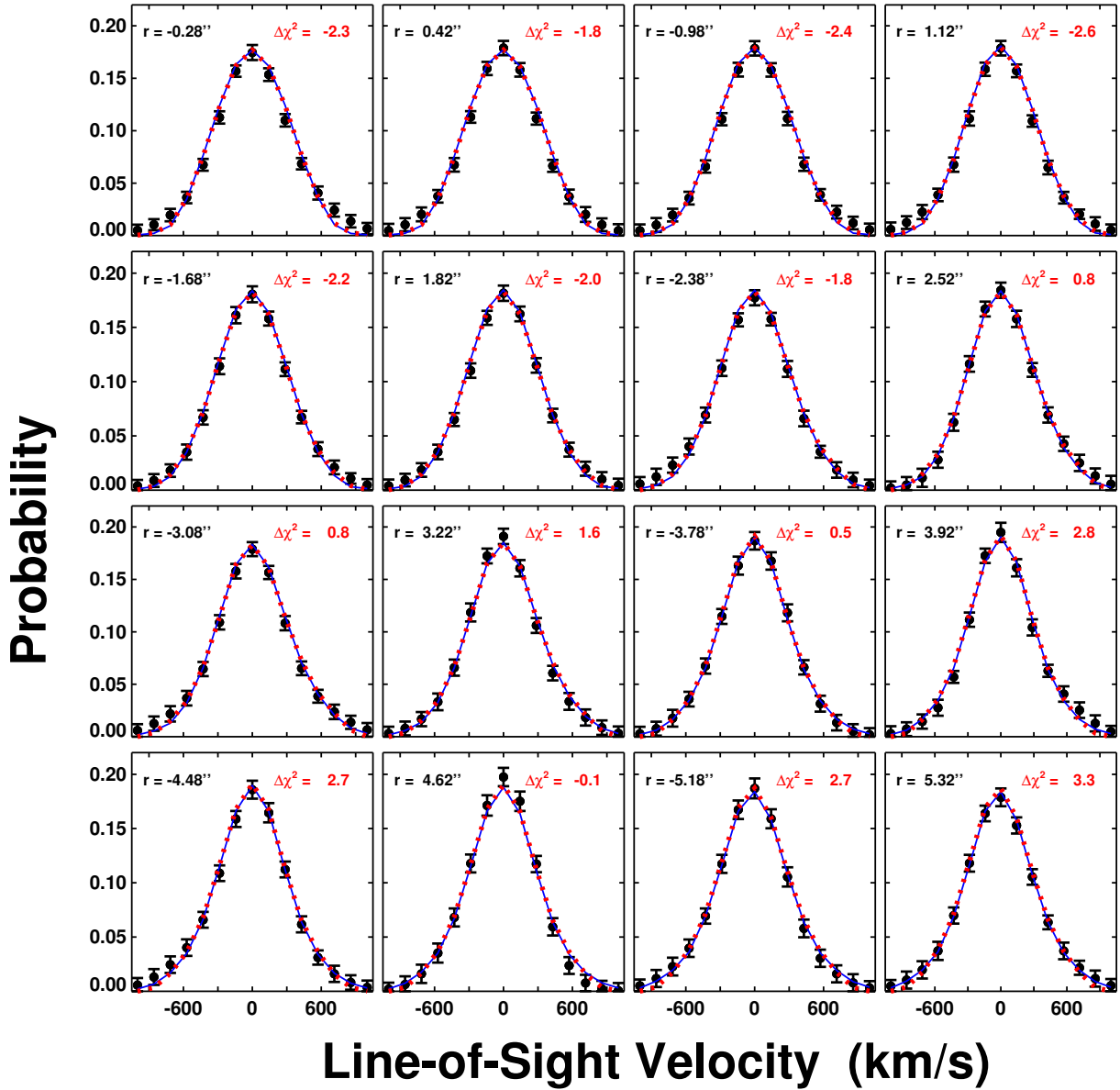


Figure 2.19: LOSVDs in NGC 6086 from long-slit data. LOSVDs were generated from the kinematic moments measured by Carter et al. (1999). Solid blue lines are corresponding LOSVDs generated by the best-fitting orbit model with the maximum-mass LOG dark matter halo ($M_{\star}/L_R = 4.7 M_{\odot} L_{\odot,R}^{-1}$, $M_{\bullet} = 3.5 \times 10^9 M_{\odot}$, $v_c = 500$ kpc, $r_c = 8.0$ kpc). Dotted red lines are generated by the best-fitting orbit model with no dark halo ($M_{\star}/L_R = 6.8 M_{\odot} L_{\odot,R}^{-1}$, $M_{\bullet} = 3.2 \times 10^8 M_{\odot}$). In each sub-plot, r is the distance from the center of NGC 6086, along the major axis. Negative values of r indicate spectra from the south side of NGC 6086. For each LOSVD, $\Delta\chi^2$ is the difference in the χ^2 statistic for the two models: $\Delta\chi^2 > 0$ indicates that the model including dark matter (solid blue line) is a better fit.

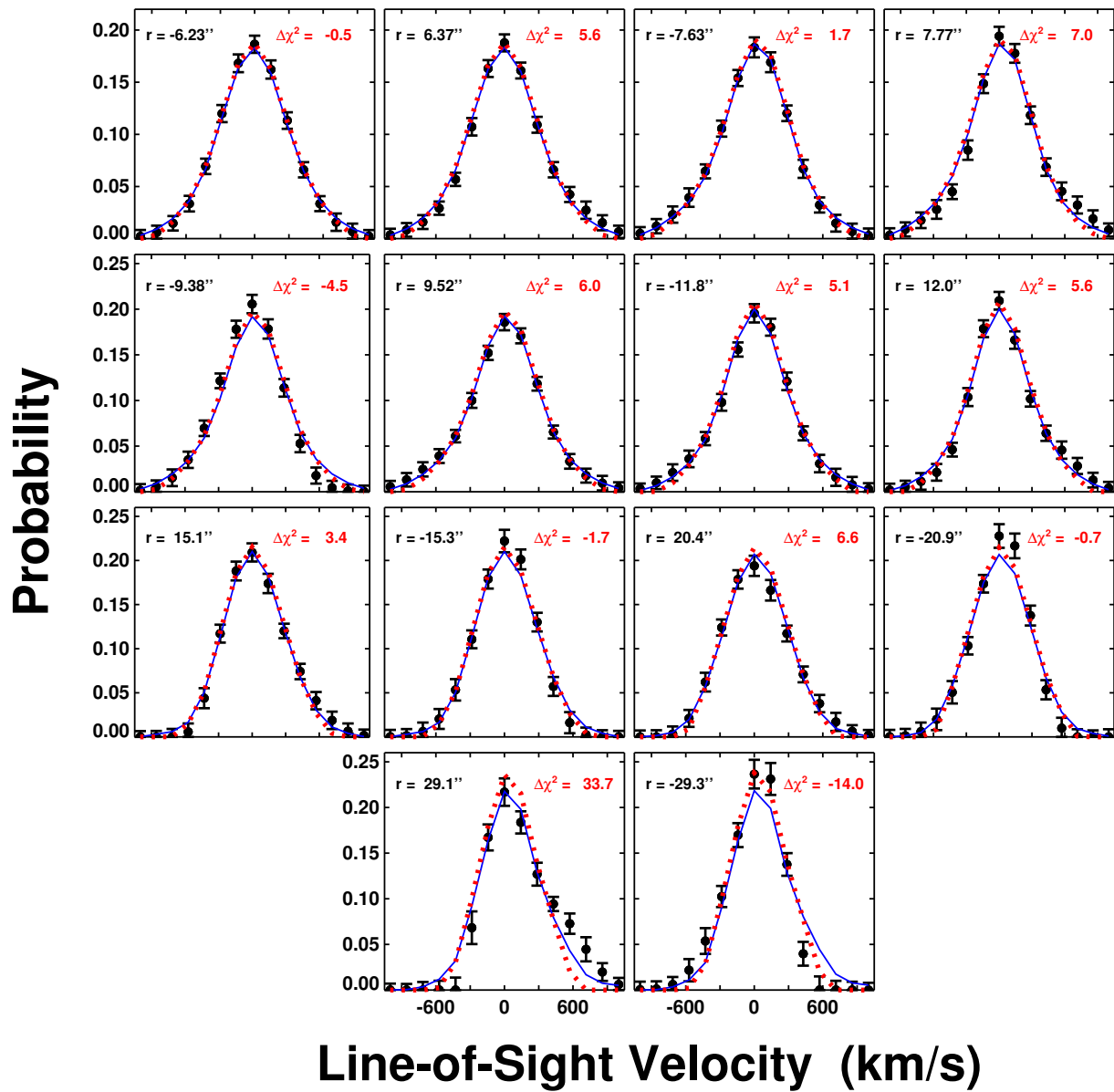


Figure 2.19, continued

Chapter 3

Two Ten-Billion-Solar-Mass Black Holes at the Centers of Giant Elliptical Galaxies

Abstract

We report that the Brightest Cluster Galaxy NGC 3842 hosts a central black hole with a mass, M_{\bullet} , of 9.7 billion solar masses (M_{\odot}), and that the Brightest Cluster Galaxy NGC 4889 hosts a black hole of comparable or greater mass. We have measured M_{\bullet} by comparing the line-of-sight stellar velocities in the central regions of NGC 3842 and NGC 4889 to orbit superposition models. Stellar kinematic measurements were obtained using integral field spectrographs at the Gemini North and Keck 2 telescopes. The black holes are significantly more massive than predicted by linearly extrapolating the widely-used correlations between black hole mass and the stellar velocity dispersion or bulge luminosity of the host galaxy. Black holes with $M_{\bullet} \sim 10^{10} M_{\odot}$ in NGC 3842 and NGC 4889 are comparable in mass to the most extreme quasars observed in the early Universe, providing circumstantial evidence that BCGs host the remnants of extremely luminous quasars. This chapter has been published in Nature (McConnell et al. 2011b).

3.1 Introduction

Observational work conducted over the last few decades indicates that all massive galaxies have supermassive black holes at their centers. Although the luminosities and brightness fluctuations of quasars in the early Universe suggest that some are powered by black holes with masses greater than 10 billion solar masses (e.g., Netzer 2003; Vestergaard et al. 2008), the remnants of these objects have not been found in the nearby Universe. The giant elliptical galaxy Messier 87 hosts the hitherto most massive known black hole, which has a

mass of 6.3 billion solar masses (Sargent et al. 1978; Gebhardt et al. 2011). Here we report that NGC 3842, the brightest galaxy in a cluster at a distance from Earth of 98 megaparsecs (Mpc), has a central black hole with a mass of 9.7 billion solar masses, and that a black hole of comparable or greater mass is present in NGC 4889, the brightest galaxy in the Coma cluster (at a distance of 103 Mpc). These two black holes are significantly more massive than predicted by linearly extrapolating the widely-used correlations between black hole mass and the stellar velocity dispersion or bulge luminosity of the host galaxy (e.g., Dressler 1989; Kormendy & Richstone 1995; Ferrarese & Merritt 2000; Gebhardt et al. 2000a; Gültekin et al. 2009a). Although these correlations remain useful for predicting black hole masses in less massive elliptical galaxies, our measurements suggest that different evolutionary processes influence the growth of the largest galaxies and their black holes.

Empirical scaling relations between black hole mass (M_\bullet), galaxy bulge velocity dispersion (σ), and luminosity (L) are commonly used to estimate black hole masses, because for most galaxies we are unable to make a direct measurement. Estimates of the number density of black holes in a given mass range thus depend upon the empirically determined $M_\bullet - \sigma$ and $M_\bullet - L$ relations over an appropriate range of galaxy masses. Directly measuring M_\bullet from the kinematics of stars or gas in the vicinity of the black hole is particularly difficult at the highest galaxy masses, because massive galaxies are rare, their typical distances from Earth are large, and their central stellar densities are relatively low. The most massive galaxies are typically Brightest Cluster Galaxies (BCGs), that is, giant ellipticals that reside near the centers of galaxy clusters.

We have obtained high-resolution, two-dimensional data of the line-of-sight stellar velocities in the central regions of NGC 3842 and NGC 4889 using integral field spectrographs at the Gemini North and Keck 2 telescopes, in Hawaii. The stellar luminosity distribution of each galaxy is provided by surface photometry from NASA’s Hubble Space Telescope and ground-based telescopes (Laine et al. 2003; Postman & Lauer 1995). NGC 3842 is the BCG of Abell 1367, a moderately rich galaxy cluster. NGC 4889 is the BCG of the Coma cluster (Abell 1656), one of the richest nearby galaxy clusters. We targeted these two galaxies because they have relatively high central surface brightnesses and lie at an accessible distance for direct measurements of M_\bullet .

3.2 Stellar Kinematics and Black Hole Masses

We measured the distribution of stellar velocities at 82 different locations in NGC 3842. The line-of-sight velocity dispersion in NGC 3842 is between 270 and 300 km s^{-1} at large galactocentric radii (r) and rises in the central 0.7 arcsec ($r < 330$ pc), peaking at 326 km s^{-1} (Figs 3.1-3.2). We determined the mass of the central black hole by constructing a series of orbit superposition models, based on the method developed by Schwarzschild (1979). Each model assumes a black hole mass, stellar mass-to-light ratio (M_\star/L) and dark matter profile, and generates a library of time-averaged stellar orbits in the resulting gravitational potential. The model then fits a weighted combination of orbital line-of-sight velocities to the set of

measured stellar velocity distributions. The goodness-of-fit statistic χ^2 is computed as a function of the assumed values of M_\bullet and the stellar mass-to-light ratio. Using our best-fitting model dark matter halo, we measure a black hole mass of 9.7×10^9 solar masses (M_\odot), with a 68% confidence interval of $(7.2 - 12.7) \times 10^9 M_\odot$. Models with no black hole are ruled out at the 99.996% confidence level ($\Delta\chi^2 = 17.1$). We find the stellar mass-to-light ratio to equal $5.1 M_\odot/L_\odot$ in R band (L_\odot , solar luminosity), with a 68% confidence interval of $4.4 M_\odot/L_\odot - 5.8 M_\odot/L_\odot$.

We measured stellar velocity distributions at 63 locations in NGC 4889 and combined our measurements with published long-slit kinematics at larger radii (Loubser et al. 2008). The largest velocity dispersions in NGC 4889 are located across an extended region on the east side of the galaxy. The stellar orbits in our models are defined to be symmetric about the galaxy center, so we constrain M_\bullet by running separate trials with velocity profiles from four quadrants of the galaxy. The best-fitting black hole masses from the four quadrants range from $9.8 \times 10^9 M_\odot$ to $2.7 \times 10^{10} M_\odot$. All quadrants favor tangential orbits near the galaxy center, which cause the line-of-sight velocity dispersion to decrease even as the internal three-dimensional velocity dispersion increases toward the black hole. Although no single model is consistent with all of the observed kinematic features in NGC 4889, we can define a confidence interval for M_\bullet by considering the most extreme confidence limits from the cumulative set of models. The corresponding 68% confidence interval is $(0.6 - 3.7) \times 10^{10} M_\odot$. We adopt a black hole mass of $2.1 \times 10^{10} M_\odot$, corresponding to the midpoint of this interval.

3.3 Predictions from Black Hole Scaling Relations

Figure 3.3 shows the $M_\bullet - \sigma$ and $M_\bullet - L$ relations, using data compiled from studies published before August 2011, plus our measurements of NGC 3842 and NGC 4889. Tabulated data with references are provided in Table 3.4. Straight lines in Fig. 3.3 show our fits to $M_\bullet(\sigma)$ and $M_\bullet(L)$. For the $M_\bullet - \sigma$ relation, we find $\log_{10}(M_\bullet/M_\odot) = 8.29 + 5.12 \log_{10}[\sigma/(200 \text{ km s}^{-1})]$. When early-type and late-type galaxies are fit separately, the resulting power laws are $\log_{10}(M_\bullet/M_\odot) = 8.38 + 4.53 \log_{10}[\sigma/(200 \text{ km s}^{-1})]$ for elliptical and S0 galaxies, and $\log_{10}(M_\bullet/M_\odot) = 7.97 + 4.58 \log_{10}[\sigma/(200 \text{ km s}^{-1})]$ for spiral galaxies. The best-fitting $M_\bullet - L$ relation is $\log_{10}(M_\bullet/M_\odot) = 9.16 + 1.16 \log_{10}(L_V/10^{11} L_\odot)$.

The most widely used form for the $M_\bullet - \sigma$ or $M_\bullet - L$ relation is a power law with a constant exponent. The relationship between σ and L , however, flattens at high galaxy masses, and constant-exponent power laws for the $M_\bullet - \sigma$ and $M_\bullet - L$ relations produce contradictory predictions for M_\bullet in this mass range (Lauer et al. 2007a). Direct measurements of M_\bullet in higher mass galaxies will compel the revision of one or both of the $M_\bullet - \sigma$ and $M_\bullet - L$ relations.

The average velocity dispersion in NGC 3842 is 270 km s^{-1} , measured outside the black hole radius of influence (1.2 arcsec or 570 pc) and inside the two-dimensional half-light radius (38 arcsec or 18 kpc). Although NGC 3842 hosts a black hole more massive than any previously detected, its average dispersion ranks only fourteenth among 65 galaxies with

direct measurements of M_{\bullet} . Its luminosity ranks fifth in this sample of galaxies and is exceeded only by other BCGs. On the basis of σ and L for NGC 3842, our revised $M_{\bullet} - \sigma$ and $M_{\bullet} - L$ relations predict $M_{\bullet} = 9.1 \times 10^8 M_{\odot}$ and $2.5 \times 10^9 M_{\odot}$, respectively. Similarly, for NGC 4889 the respective predictions are $3.3 \times 10^9 M_{\odot}$ and $4.5 \times 10^9 M_{\odot}$. These predictions are smaller than our direct measurements of M_{\bullet} , by 1.6-4.6 times the 1-standard-deviation scatter in the $M_{\bullet} - \sigma$ and $M_{\bullet} - L$ relations, as estimated by Gültekin et al. (2009a). Four measurements of M_{\bullet} in BCGs existed before this work. Two measurements based on gas

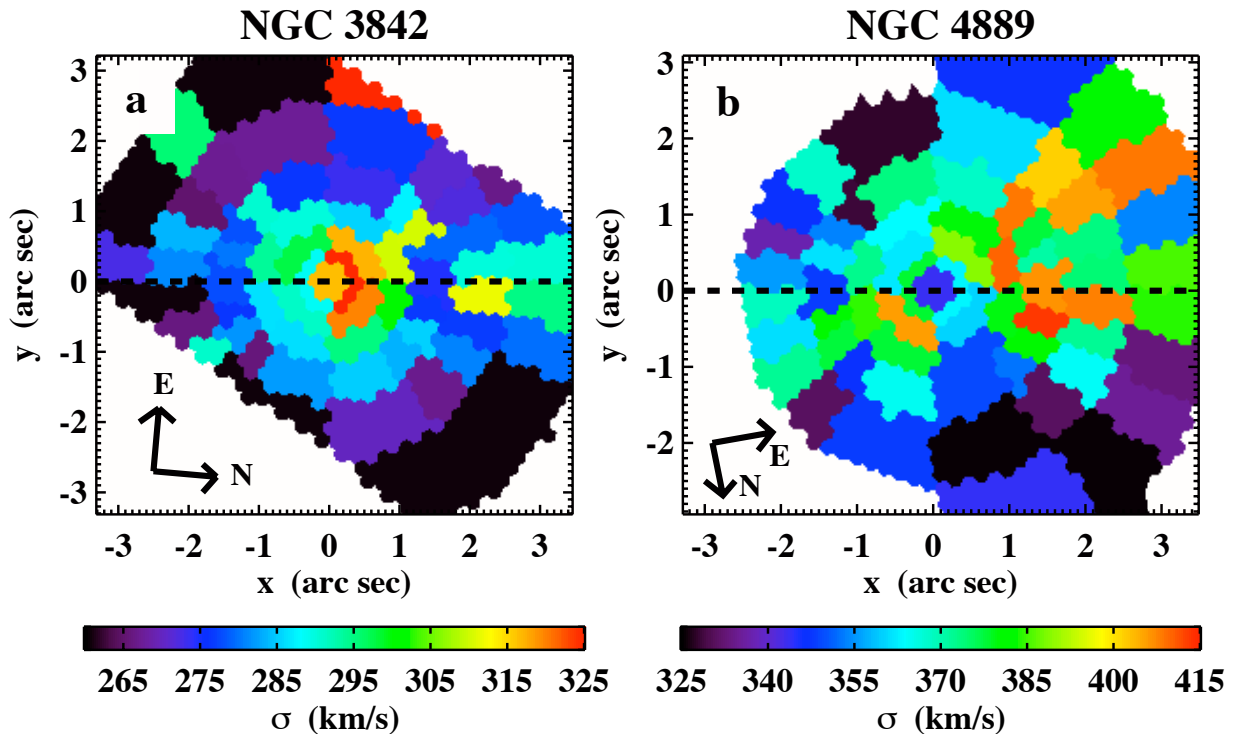


Figure 3.1: Two-dimensional maps of velocity dispersions in NGC 3842 and NGC 4889. The maps show the central regions of NGC 3842 (a) and NGC 4889 (b) observed using the GMOS spectrograph (Allington-Smith et al. 2002) on the 8-m Gemini North telescope. Additional kinematics at large radii were measured using the VIRUS-P spectrograph (Hill et al. 2008) at the 2.7-m Harlan J. Smith telescope, and additional high-resolution data were acquired with the OSIRIS spectrograph (Larkin et al. 2006) at the 10-m Keck 2 telescope. GMOS, OSIRIS, and VIRUS-P are all integral field spectrographs, which record spectra at multiple positions in a two-dimensional spatial array. The horizontal dashed line in each panel traces the major axis of the galaxy. The median errors in velocity dispersion are 12 km s^{-1} and 20 km s^{-1} for NGC 3842 and NGC 4889, respectively. In NGC 4889 the highest velocity dispersions, near 410 km s^{-1} , are located on the east side of the galaxy, at least 1.1 arcsec from the center.

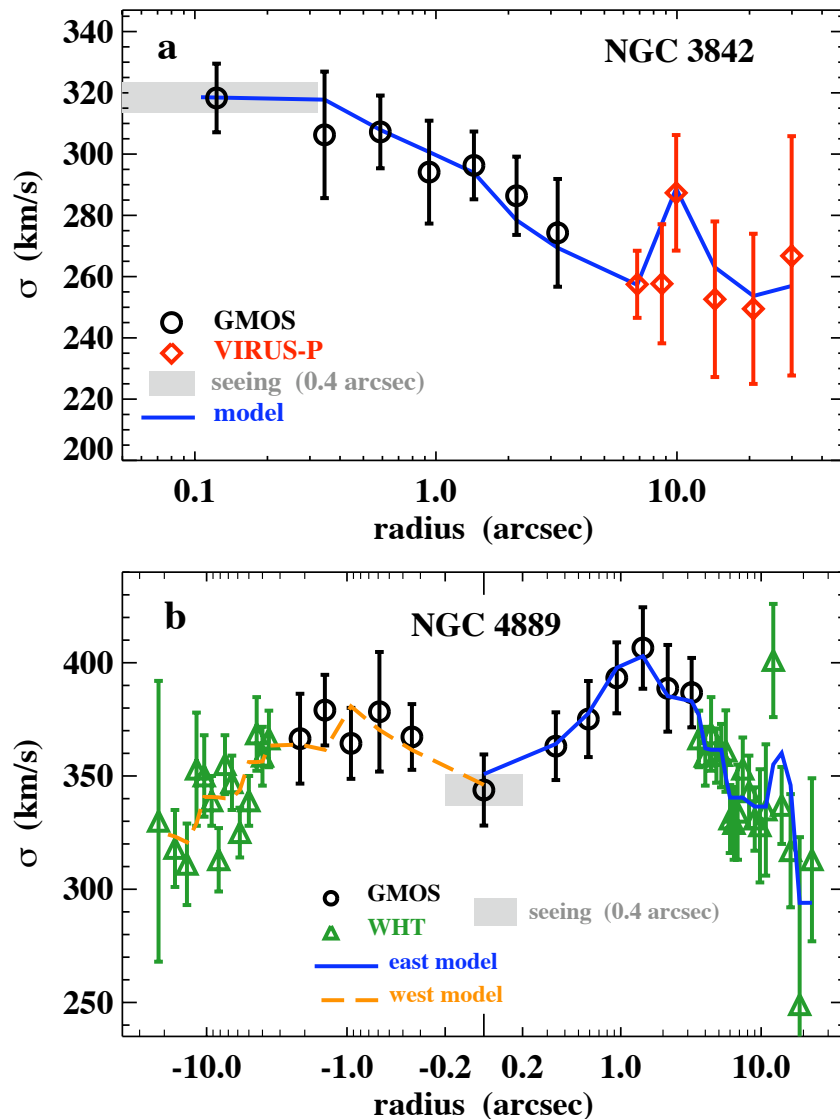


Figure 3.2: One-dimensional velocity dispersion profiles in NGC 3842 and NGC 4889. (a) Dispersion versus radius in NGC 3842, after averaging data at a given radius, based on measurements with GMOS (black circles) and VIRUS-P (red diamonds). The solid blue line is the projected line-of-sight dispersion from our best-fitting stellar orbit model of NGC 3842. (b) Dispersion versus radius along the major axis of NGC 4889, measured from GMOS (black circles) and by Loubser et al. (2008) using the William Herschel Telescope (green diamonds). The maximum velocity dispersion occurs at $r = 1.4$ arcsec. The solid blue line is the projected line-of-sight dispersion from our best-fitting orbit model using data from the east side of NGC 4889 ($r > 0$). The dashed orange line is from our best-fitting orbit model using data from the west side of NGC 4889 ($r < 0$). Error bars are one standard deviation.

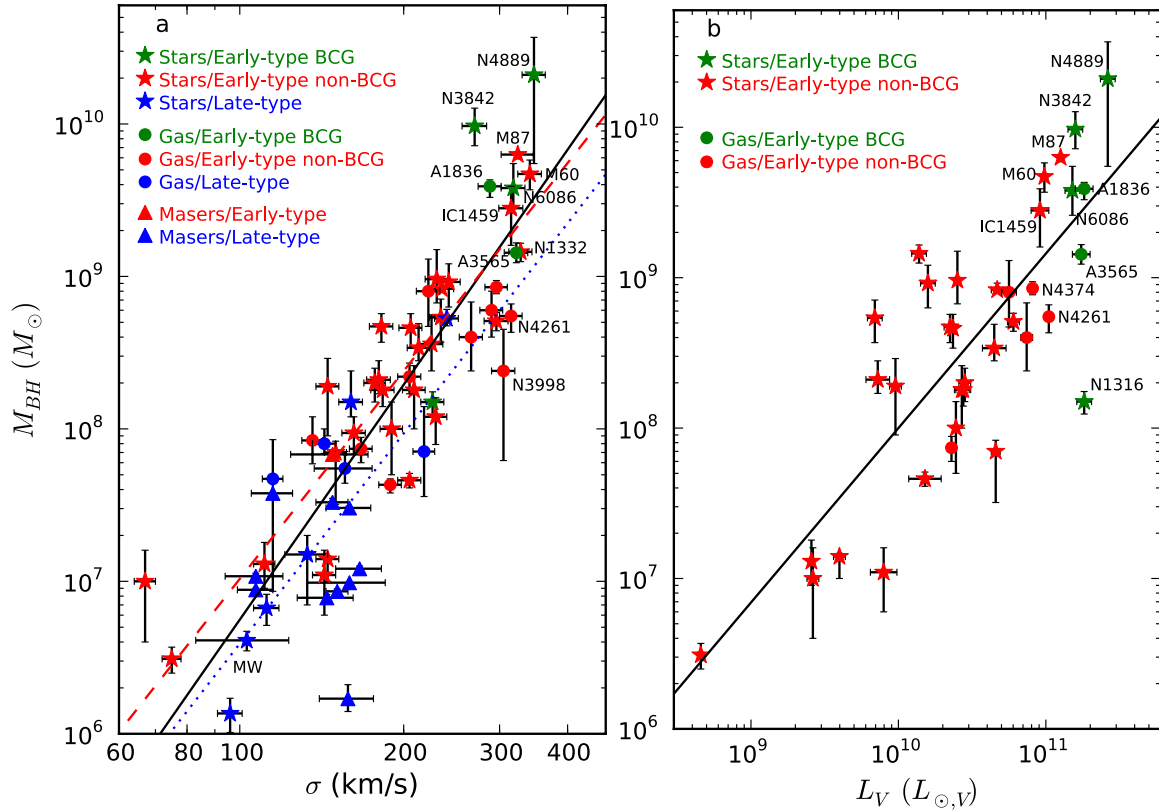


Figure 3.3: $M_{\bullet} - \sigma$ and $M_{\bullet} - L$ correlations. **(a)** Black hole mass, M_{\bullet} , versus stellar velocity dispersion, σ , for 65 galaxies with direct dynamical measurements of M_{\bullet} . Our sample of 32 measurements from Gültekin et al. (2009a), 16 galaxies with masses updated since 2009, 15 new galaxies with M_{\bullet} measurements, and the two galaxies reported here. For galaxies with spatially resolved stellar kinematics, σ is the luminosity-weighted average within one effective radius. **(b)** Black hole mass versus V -band bulge luminosity, L_V , for 36 early-type galaxies with direct dynamical measurements of M_{\bullet} . BCGs (defined here as the most luminous galaxy in a cluster) are plotted in green, other elliptical and S0 galaxies are plotted in red, and late-type spiral galaxies are plotted in blue. The black hole masses are measured using dynamics of masers (triangles), stars (stars), or gas (circles). Error bars represent 68% confidence intervals. For most of the maser galaxies, the error bars in M_{\bullet} are smaller than the plotted symbol. The solid black lines in **(a)** and **(b)** show the best-fitting power law for each sample. In **(a)**, we also show the best-fitting power laws for early type galaxies (dashed red line) and late-type galaxies (dotted blue line). We do not label M87 as a BCG, as NGC 4472 in the Virgo cluster is 0.2 mag brighter.

dynamics and one based on stellar dynamics all lie within 1.2 standard deviations of our revised fits to the $M_\bullet - \sigma$ and $M_\bullet - L$ relations (Dalla Bontà et al. 2009; McConnell et al. 2011a). Yet the measurement of M_\bullet in NGC 1316, the BCG of the Fornax cluster, is 3.4 standard deviations less than that predicted by our $M_\bullet - L$ relation (Nowak et al. 2008). The high scatter indicated by this collection of measurements reveals large uncertainties in the standard practice of using galactic σ or L as a proxy for the central black hole mass in giant elliptical galaxies and their predecessors.

Several BCGs within 200 Mpc of Earth are at least twice as luminous as NGC 3842, and three times as luminous as M87, which hosted the most massive black hole known before this work. In spite of their extreme luminosities, BCGs have velocity dispersions similar to those of the most massive field elliptical galaxies. Yet the most massive black holes are found predominantly in BCGs (Fig. 3.3). How galaxies are assembled and the role of gas dissipation affect the correlations (or lack thereof) among M_\bullet , σ , and L . Simulations of mergers of gas-rich disk galaxies are able to produce remnant galaxies that follow the observed $M_\bullet - \sigma$ correlation in Fig. 3a, over the intermediate mass range $M_\bullet \approx 10^7 - 10^9 M_\odot$ (Di Matteo et al. 2005; Robertson et al. 2006). By contrast, simulated mergers of elliptical galaxies with low-angular momentum progenitor orbits increase M_\bullet and L by similar numerical factors, without increasing the velocity dispersion (Boylan-Kolchin et al. 2006). Because these mergers are a likely path to forming the most massive galaxies, the $M_\bullet - \sigma$ correlation may steepen or disappear altogether at the highest galaxy masses. Massive elliptical galaxies retain residual quantities of gas even after the decline of star formation. Accretion of this gas onto the galaxies' central black holes could help increase M_\bullet and further steepen the $M_\bullet - \sigma$ and $M_\bullet - L$ relations.

3.4 Connection to High-Redshift Quasars

Black holes in excess of $10^{10} M_\odot$ are observed as quasars in the early Universe, from 1.4×10^9 to 3.3×10^9 years after the Big Bang (Vestergaard et al. 2008). The corresponding redshift range is $z = 2 - 4.5$. Throughout the last 1.0×10^{10} yr, however, these extremely massive black holes have not been accreting appreciably, and the average mass of the black holes powering quasars has decreased steadily. Quasar activity and elliptical galaxy formation are predicted to arise from similar merger-triggered processes, and there is growing evidence that present-day massive elliptical galaxies once hosted the most luminous high-redshift quasars (e.g., Hopkins et al. 2007a). Yet definitive classification of these quasars' host galaxies has remained elusive.

Our measurements of black holes with masses of around $10^{10} M_\odot$ in NGC 3842 and NGC 4889 provide circumstantial evidence that BCGs host the remnants of extremely luminous quasars. The number density of nearby BCGs ($\sim 5 \times 10^{-6} \text{ Mpc}^{-3}$) is consistent with the number density of black holes ($\sim 3 \times 10^{-7}$ to 10^{-5} Mpc^{-3}) with masses between $10^9 M_\odot$ and $10^{10} M_\odot$ predicted from the $M_\bullet - L$ relation and the luminosity function of nearby galaxies. Furthermore, both quantities agree with predictions based on the black hole masses

and duty cycles of quasars. The black hole number density predicted from the $M_{\bullet} - \sigma$ relation, however, is an order of magnitude less than the inferred quasar population Lauer et al. (2007a,c). These two predictions can be reconciled if the $M_{\bullet} - \sigma$ relation has upward curvature or a large degree of intrinsic scatter in M_{\bullet} at the high-mass end, as suggested by our new measurements. With improvements in adaptive optics instrumentation on large optical telescopes and very-long baseline interferometry at radio wavelengths, black holes are being sought and detected in increasingly exotic host galaxies. Along with our measurements of the black hole masses in NGC 3842 and NGC 4889, future measurements in other massive galaxies will quantify the cumulative growth of supermassive black holes in the Universe’s densest environments.

Acknowledgments

N.J.M., C.-P.M., K.G. and J.R.G. are supported by the National Science Foundation. C.-P.M. is supported by NASA and by the Miller Institute for Basic Research in Science, University of California, Berkeley. S.A.W. is supported by NASA through the Hubble Fellowship. Data presented here were obtained using Gemini Observatory, W.M. Keck Observatory, and McDonald Observatory. The Gemini Observatory is operated by the Association of Universities for Research in Astronomy, Inc., under a cooperative agreement with the National Science Foundation on behalf of the Gemini partnership. The W. M. Keck Observatory is operated as a scientific partnership among the California Institute of Technology, the University of California, and NASA. The McDonald Observatory is operated by the University of Texas at Austin. The instrument VIRUS-P was funded by G. and C. Mitchell. Stellar orbit models were run using the facilities at the Texas Advanced Computing Center at The University of Texas at Austin.

3.5 Appendix A: Spectroscopic Data and LOSVD Extraction

We map stellar orbital motions in NGC 3842 and NGC 4889 by measuring the LOSVD for different regions in each galaxy. Each LOSVD is determined by fitting a composite template stellar spectrum to a fully reduced spectrum of the galaxy. The LOSVDs are non-parametric probability distributions, defined at each of 15 velocity bins. We use a Maximum Penalized Likelihood technique to optimize the LOSVD value in each velocity bin while simultaneously optimizing the weights of individual template stars (Gebhardt et al. 2000b; Pinkney et al. 2003; Nowak et al. 2008).

In Table 4.2, we summarize our observations with the integral field spectrographs GMOS, OSIRIS, and VIRUS-P. Figures 3.4-3.6 illustrate a sample galaxy and template spectrum from each instrument. Our data from GMOS only cover radii within 3.8 arcseconds (1.8 kpc) of the center of NGC 3842 and NGC 4889, and by themselves cannot fully

remove the degeneracies between M_\bullet and M_\star/L . For NGC 3842, our VIRUS-P measurements cover radii out to 35.3 arcseconds (16.8 kpc) and can distinguish the enclosed stellar mass profile from the galaxy’s dark matter halo. This allows for an accurate determination of M_\star/L , such that the GMOS data can accurately constrain M_\bullet . At radii from 3.6 to 23.0 arcseconds (1.8 – 11.5 kpc) along the major axis of NGC 4889, we use Gaussian velocity profiles from Loubser et al. (2008).

Our GMOS spectra for NGC 3842 and NGC 4889 are centered on the calcium triplet absorption lines near 860 nm. A sample GMOS spectrum for each galaxy is shown in Figure 3.4, demonstrating the clean line profiles that are typical for this spectral region. Another advantage to using the calcium triplet is that kinematic measurements are not highly sensitive to the stellar template used (Barth et al. 2002).

OSIRIS data of NGC 3842 were acquired with the 0.05 arcsecond spatial scale and the broad H -band filter, which spans a large number of atomic and molecular absorption features. To measure kinematics, we fit carbon monoxide band heads at 1598, 1619, 1640, and 1661 nm, and a deep magnesium feature near 1500 nm. The most severe source of noise in our OSIRIS spectra is residual narrow-line emission from the night sky. This background emission varies rapidly and is only partially corrected by recording 15-minute sky frames in between pairs of 15-minute science exposures. Even when masked, the contaminated channels represent a non-negligible loss of spectral information. This loss must be countered by increasing the signal-to-noise ratio in the usable parts of the spectrum. To achieve adequate signal-to-noise, we bin the data to the same spatial regions as the overlapping LOSVDs from GMOS. Each of the final bins contains approximately 80 OSIRIS spatial pixels.

VIRUS-P data were acquired in low-resolution mode, which provides broad wavelength coverage. The poorest instrumental resolution over our field is 0.56 nm full width at half-maximum (FWHM), which is adequate considering that stellar velocity dispersions in NGC 3842 are typically near 250 km s^{-1} , corresponding to a resolution of approximately $0.7 \text{ nm FWHM} \times (\lambda / 360 \text{ nm})$. We fit VIRUS-P spectra with 16 template stars from the Indo-US library (Valdes et al. 2004), spanning spectral types from B9 to M3 and including stars with sub-solar and super-solar metallicities. However, some spectral regions require additional adjustments to account for metallicities and elemental abundance ratios outside the range of our template library. We do not attempt to fit the entire spectral range simultaneously, but instead follow the same fitting procedure used by Murphy et al. (2011) for VIRUS-P data of M87. Each spectrum is divided into four sub-regions, as illustrated in Figure 3.6. We independently determine the best-fit LOSVD for each sub-region and discard any sub-regions that fail to produce a believable fit. We then average the LOSVDs derived from individual spectral sub-regions.

Our stellar orbit models are axisymmetric, and so each of our final LOSVDs must represent an average over four quadrants of the galaxy. In order to preserve any rotational signal along the major axis, we invert the velocities from LOSVDs on the south side of NGC 3842 and the west side of NGC 4889. However, neither galaxy shows strong rotation. In NGC 3842, the resulting kinematics are sufficiently symmetric to average the LOSVDs from opposite sides of the galaxy. In NGC 4889, we have modeled four quadrants of the galaxy

independently.

Our stellar orbit models require an estimate of the point spread function (PSF) for each instrument at the time of spectroscopic observations. We estimate the PSF for our GMOS data for both NGC 3842 and NGC 4889 from wide-field images taken during target acquisition. Although the models discussed herein assume a 0.4-arcsecond PSF for GMOS data, we have run a small number of models with a 0.7-arcsecond PSF and have found no significant changes in our results. While observing NGC 3842, we switched from the OSIRIS spectrograph to the OSIRIS imaging camera every few hours, and observed the adaptive optics tip/tilt star. We can tolerate a large degree of uncertainty in our measured PSF, as we have re-binned OSIRIS data of NGC 3842 to spatial scales that are several times coarser than the diffraction-limited FWHM.

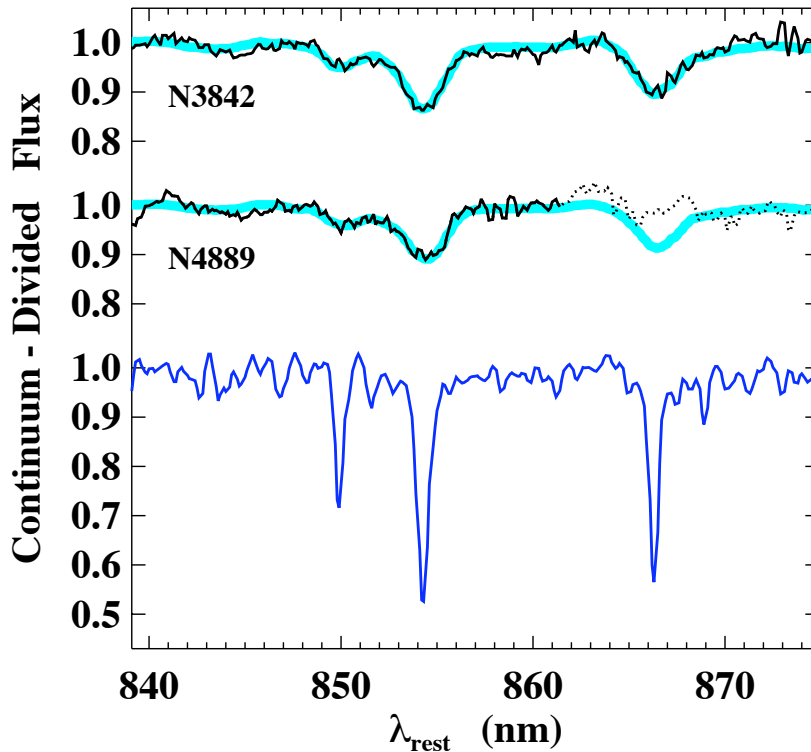


Figure 3.4: GMOS spectra of NGC 3842 and NGC 4889. Each spectrum corresponds to the center of the galaxy ($r < 0.25$ arcseconds). The upper spectrum is NGC 3842 (black), overlaid with the best-fitting, LOSVD-convolved template spectrum (thick, light blue). The middle spectrum is NGC 4889, overlaid with the best-fitting template spectrum. The dotted portion of the spectrum was excluded from the LOSVD fitting. The lower spectrum is template star HD 73710 (G9III), before convolution with the LOSVD.

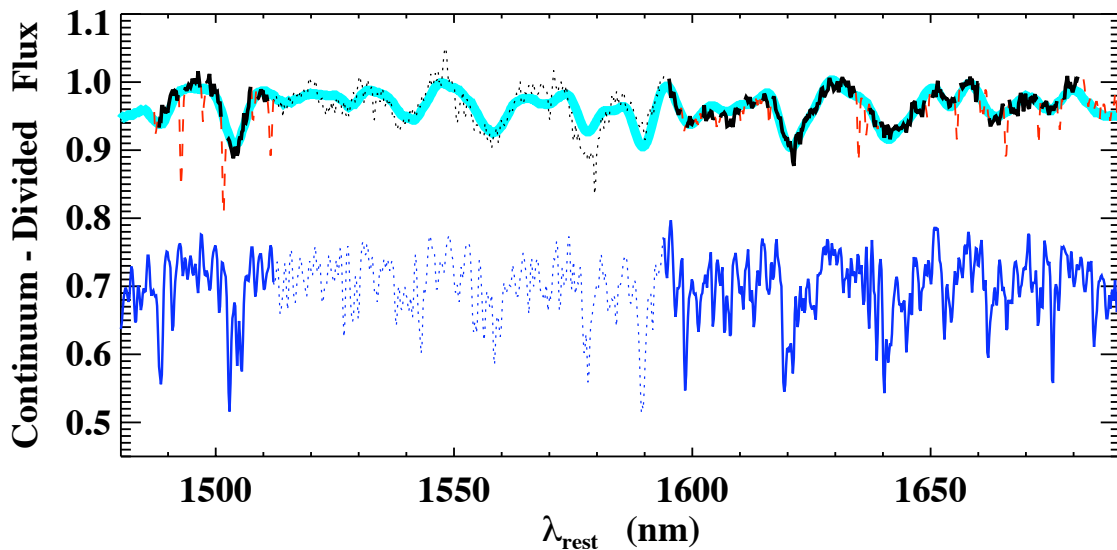


Figure 3.5: OSIRIS spectrum of the central region of NGC 3842. ($r < 0.25$ arcseconds, or 110 pc). The upper spectrum is NGC 3842 (black), overlaid with the best-fitting, LOSVD-convolved template spectrum (thick, light blue). The red dashed lines in the galaxy spectrum are residuals from imperfectly subtracted sky emission. The lower spectrum is the best-fit composite template before convolution with the LOSVD. Our observed template stars fit spectra of NGC 3842 poorly across the dotted region from 1510 to 1590 nm, and therefore this region is excluded from kinematic fitting.

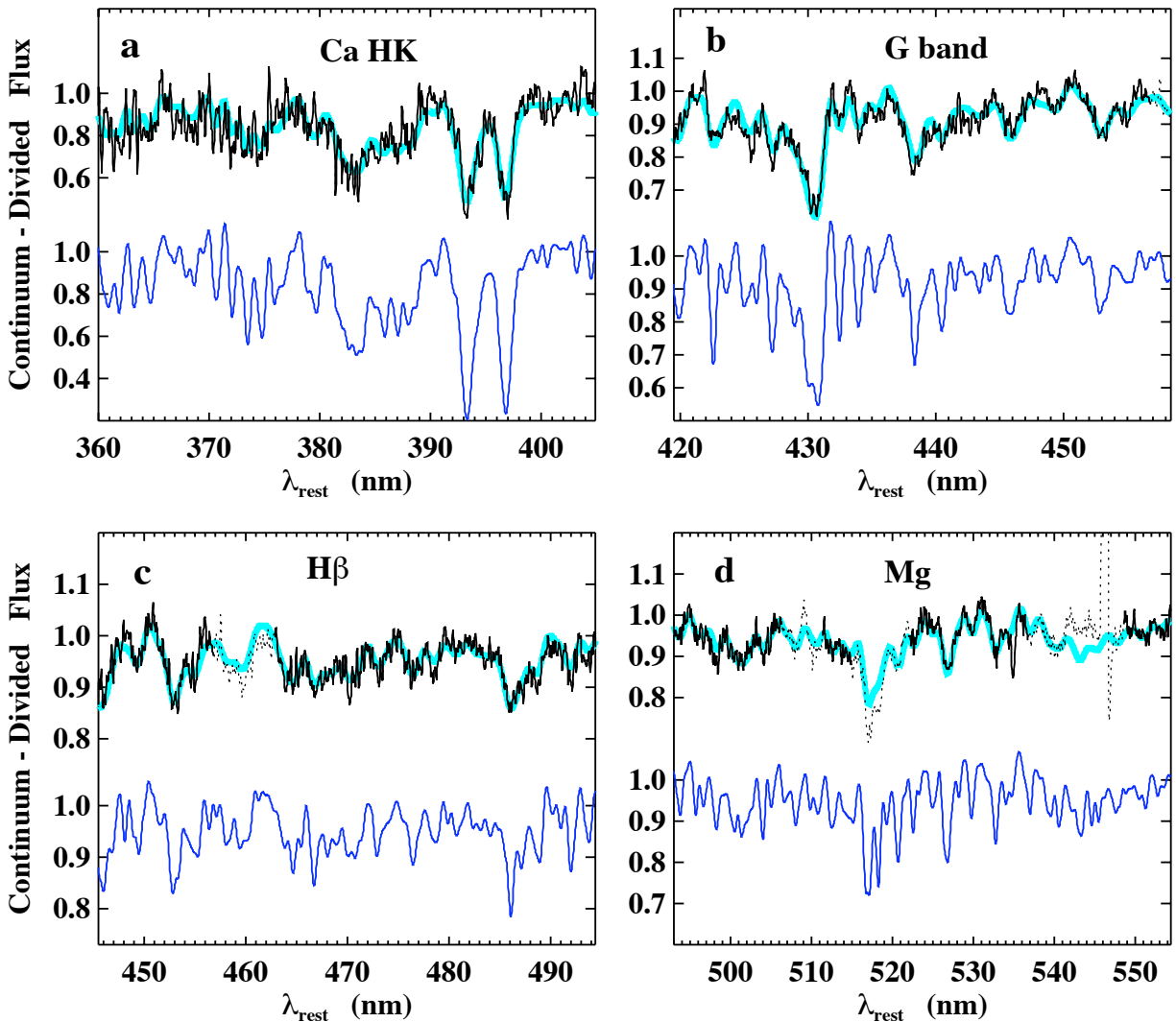


Figure 3.6: VIRUS-P spectrum of NGC 3842, corresponding to a semi-annulus with an inner radius of 17.0 arcseconds (7.7 kpc) and an outer radius of 24.5 arcseconds (11.0 kpc). The four panels contain different sub-regions of the galaxy spectrum. Each sub-region is evaluated independently for a best-fit LOSVD and best-fit composite template spectrum. The upper spectrum in each panel is NGC 3842 (black), overlaid with the best-fitting, LOSVD-convolved template spectrum (thick, light blue). Dotted portions of the galaxy spectrum have been masked from the fit. The lower spectrum in each panel is the best-fit composite template before convolution with the LOSVD.

Table 3.1: Spectroscopic observations of NGC 3842 and NGC 4889

| Galaxy | Instrument | UT Date | N_{exp} | t_{exp} (s) | λ (nm) | $\Delta\lambda$ (nm) | r_{max} (arcsec) | Δr (arcsec) | PSF FWHM (arc sec) |
|----------|------------|-----------------|------------------|-------------------------|-------------------|-------------------------|------------------------------|------------------------|-----------------------|
| NGC 3842 | GMOS | April 27, 2003 | 5 | 1200 | 755-949 | 0.25 | 3.8 | 0.2 | 0.4 |
| NGC 3842 | OSIRIS | May 8-10, 2010 | 16 | 900 | 1473-1803 | 0.72 | 0.7 | 0.05 | 0.08 |
| NGC 3842 | VIRUS-P | March 7-8, 2011 | 3 | 1200 | 358-589 | 0.52 | 35.3 | 4.1 | 2.0 |
| NGC 4889 | GMOS | March 13, 2003 | 5 | 1200 | 755-949 | 0.25 | 3.8 | 0.2 | 0.4 |

Notes: For each galaxy, we recorded N_{exp} science exposures, with an integration time per exposure of t_{exp} . The median instrumental resolution (FWHM) is $\Delta\lambda$. The maximum radius of usable data is r_{max} , defined with respect to the center of the galaxy. The instrumental spatial sampling is Δr , defined as the angular diameter of one lenslet or fiber.

3.6 Appendix B: Photometric Data

Our stellar orbit models are constrained to reproduce the observed stellar light profile of each galaxy, which requires accurate measurements of each galaxy’s surface brightness profile over a large radial range. For radii out to 10 arcseconds, we adopt high-resolution *I*-band (800 nm) surface brightness profiles, obtained with WFPC2 on the Hubble Space Telescope, and deconvolved with the instrumental PSF (Laine et al. 2003). At larger radii out to 115 arcseconds, we use *R*-band (600 nm) data obtained with the 2.1 m telescope at Kitt Peak National Observatory (KPNO). The KPNO data have a field of view of 5.2×5.2 arcminutes, which enables accurate sky subtraction. We combine the individual profiles from WFPC2 and KPNO data at overlapping radii between 5 and 10 arcseconds, accounting for the average $R - I$ color over these radii. To compute the luminosity density profile of each galaxy, we deproject the surface brightness profile while assuming spheroidal isodensity contours (Gebhardt et al. 1996).

3.7 Appendix C: Kinematic Data from Different Instruments

Stellar kinematics along the major axes of NGC 3842 and NGC 4889 were previously measured by Loubser et al. (2008), using the ISIS long-slit spectrograph on the William Herschel Telescope (WHT). The WHT measurements of NGC 3842 are in good agreement with our GMOS measurements for $r \leq 3.0$ arcseconds. The WHT data for NGC 4889 agree with our GMOS measurements on the west side of NGC 4889 and at radii between 1 and 2.4 arcseconds on the east side. However, they do not reproduce our measurement of the large central drop in stellar velocity dispersion (Figure 3.7). For a more direct comparison, we have rebinned our integral-field spectra to match the 0.4-arcsecond spatial sampling and 1.0-arcsecond slit width of the WHT data. We find that rebinning alleviates the velocity dispersion discrepancy for all but the central point ($r = 0$). Our detection of a significantly sharper decrease in velocity dispersion is consistent with the superior seeing conditions of our data (0.4 arcseconds for GMOS, versus 1.0 arcseconds for WHT). Overall, we find our kinematic measurements in NGC 3842 and NGC 4889 to be broadly consistent with the independent measurements by Loubser et al. (2008), indicating that our kinematic extraction method has low systematic errors.

For N3842, our VIRUS-P measurements are also consistent with WHT measurements, which extend along the major axis to $r = 20.8$ arcseconds. We prefer using data from VIRUS-P in our stellar orbit models because they extend to larger radii and provide full two-dimensional spatial sampling.

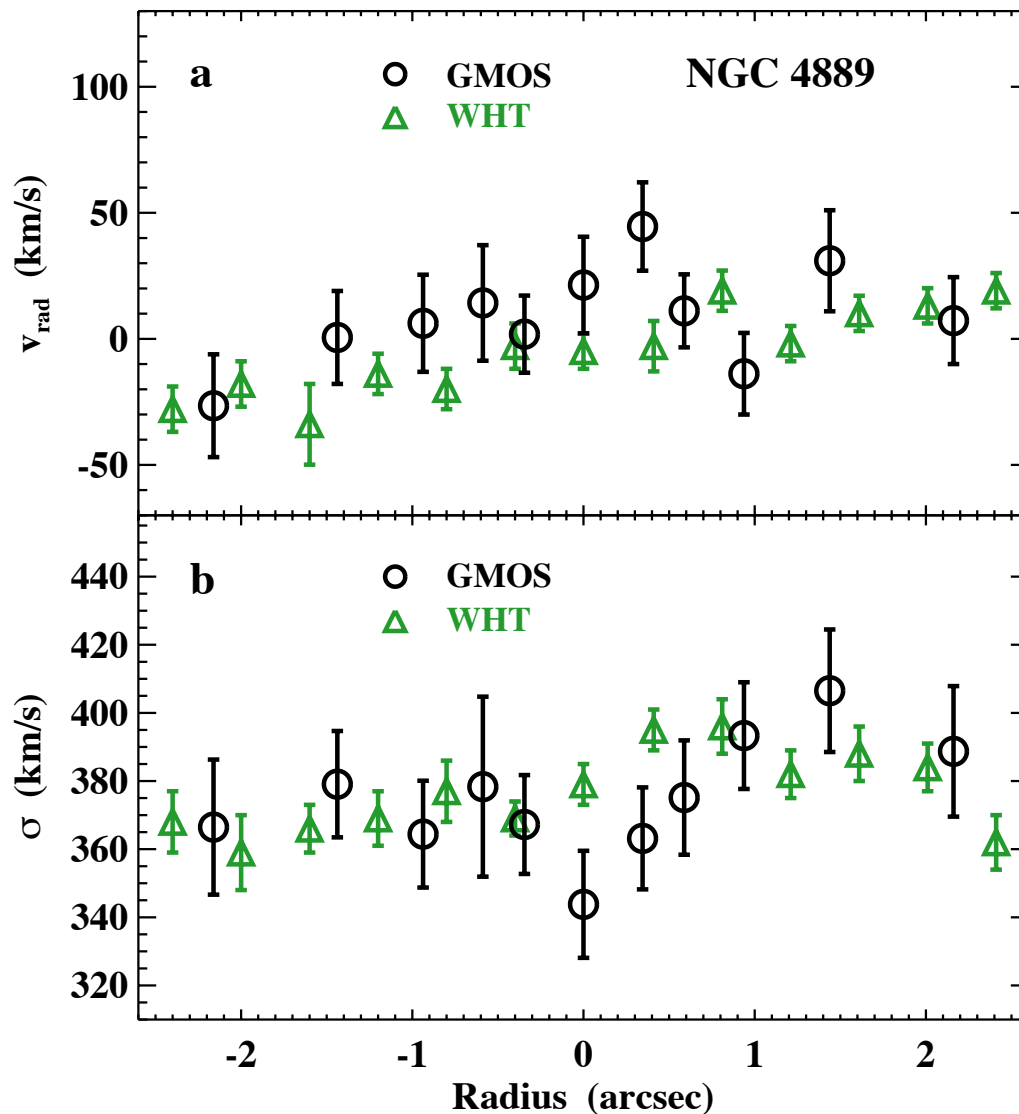


Figure 3.7: Radial velocity and dispersion in NGC 4889, from GMOS and long-slit data. (a) Radial velocity. (b) Velocity dispersion. Green triangles are measurements from Loubser et al. (2008), using the ISIS spectrograph on the William Herschel Telescope (WHT). Black circles are our measurements using the GMOS integral-field unit. Error bars represent one standard deviation. On the west side and at radii from 1.0 to 2.4 arcseconds on the east side, the GMOS and WHT measurements agree within errors. At $r < 1.0$ arcseconds on the east side, only GMOS detects a local minimum in velocity dispersion. The central feature might be unresolved in the WHT data due to worse seeing (1.0 arcseconds).

Near the center of NGC 3842, OSIRIS and GMOS provide independent measurements of stellar kinematics. We have binned data from OSIRIS and GMOS at identical spatial scales out to $r = 0.7$ arcseconds (330 pc) and have run orbit models fitting LOSVDs from OSIRIS and GMOS simultaneously (as well as VIRUS-P data at large radii). Including the OSIRIS data causes the best-fit value of M_{\bullet} to decrease by up to 23%, and the best-fit value of M_{\star}/L to increase by as much as 8%. This occurs because OSIRIS data show a less drastic increase in velocity dispersion than data from GMOS. In spite of these differences, results with and without OSIRIS data are consistent at the 68% confidence level.

Models fitting OSIRIS and GMOS data together yield higher average χ^2 values per LOSVD. This is true even if we ignore the central regions where LOSVDs from OSIRIS and GMOS are not fully consistent. Even with several template stars, the overlapping absorption features in the H-band spectral region are difficult to model, and the LOSVDs derived from OSIRIS data may have systematic errors. Consequently, we judge the models with only GMOS and VIRUS-P data to be more reliable.

3.8 Appendix D: Stellar Orbit Models and Statistical Analysis

We generate models of NGC 3842 and NGC 4889 using Schwarzschild’s method (Schwarzschild 1979), in which test particle orbits are computed in a static axisymmetric gravitational potential. We assume that each galaxy contains three mass components: stars, a central black hole, and an extended dark matter halo. The stellar mass density is assumed to follow the same profile as the observed luminosity density, with a constant stellar mass-to-light ratio, M_{\star}/L . Our modeling procedures are similar to those for NGC 6086, described in McConnell et al. (2011a).

Each orbit in the model is assigned a scalar weight, and the set of best-fit orbital weights is determined by comparing projected LOSVDs from the orbits to the observed LOSVDs for the galaxy. Each observed LOSVD spatially maps to a linear combination of bins within the model, according to the spatial boundaries of the corresponding spectrum and the PSF of the observations. A corresponding model LOSVD is computed from the projected velocity distributions of individual orbits in each spatial bin, the appropriate combination of spatial bins, and the orbital weights. The best-fit weights are determined by the method of maximum entropy (Richstone & Tremaine 1988), with the fixed constraint that the summed spatial distribution of all weighted orbits must match the observed luminosity density profile. The essential output of each model is a measurement of χ^2 , which defines the goodness of fit between our observed LOSVDs and the model LOSVDs, using the optimal combination of orbital weights. We determine the best-fit values and confidence intervals in M_{\bullet} and M_{\star}/L by evaluating the relative likelihood between models with different assumed values of M_{\bullet} and M_{\star}/L . Figure 3.8 illustrates the behavior of χ^2 with respect to M_{\bullet} and M_{\star}/L , for models with our best fitting dark matter halo.

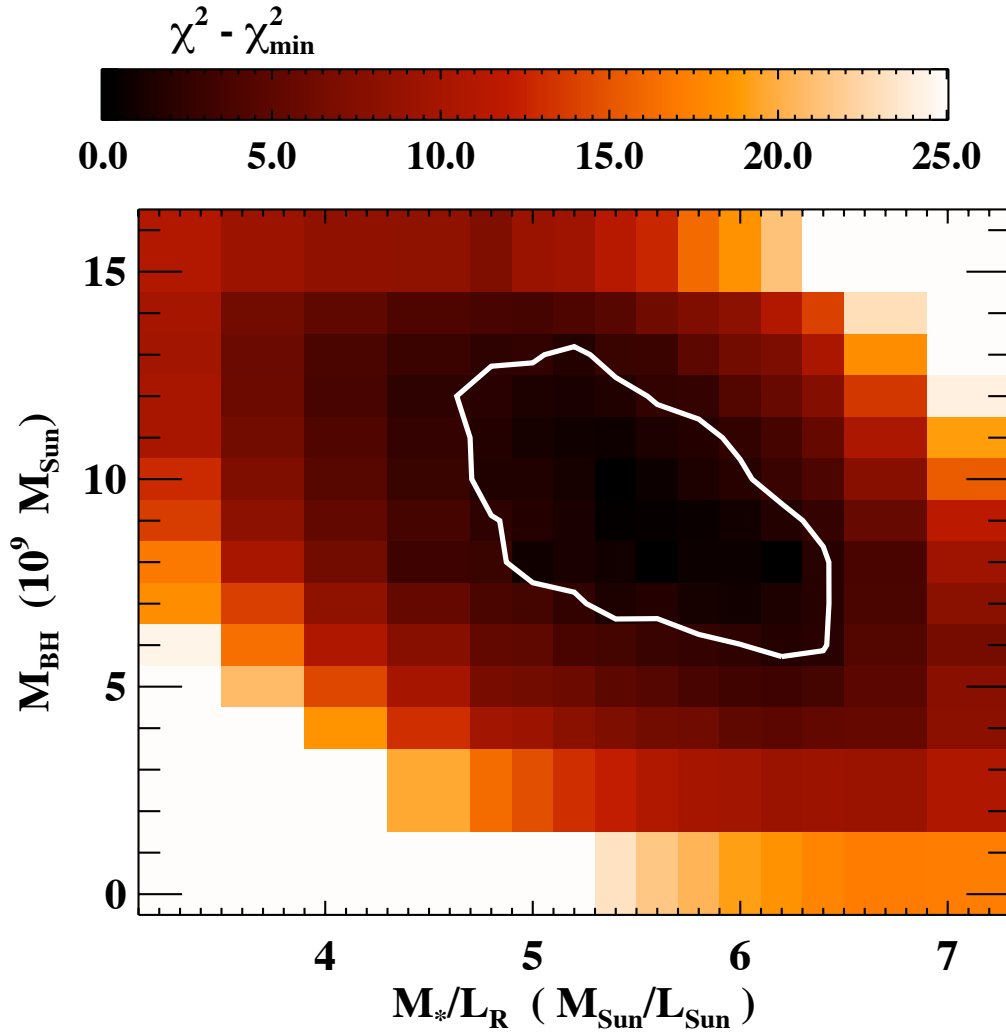


Figure 3.8: χ^2 versus M_{\bullet} and M_{\star}/L_R for stellar orbit models of NGC 3842. The models fit data from GMOS and VIRUS-P. The diagonal trend in χ^2 indicates the degeneracy between stellar mass and black hole mass near the center of NGC 3842. For two free parameters with Gaussian likelihood distributions, the 68% confidence interval is defined where $\chi^2 - \chi_{\min}^2 \leq 2.30$, illustrated by the thick white contour. We obtain 68% confidence intervals of $(7.2 - 12.7) \times 10^9 M_{\odot}$ for M_{\bullet} , and $4.4 - 5.8 M_{\odot} L_{\odot,R}^{-1}$ for M_{\star}/L_R . The median values, which we adopt as our final measurements, are $M_{\bullet} = 9.7 \times 10^9 M_{\odot}$ and $M_{\star}/L_R = 5.1 M_{\odot} L_{\odot,R}^{-1}$.

3.9 Appendix E: Models of NGC 4889

Stellar kinematics in NGC 4889 are asymmetric with respect to the major and minor axes of the galaxy. Integral-field data from GMOS reveals velocity dispersions above 410 km s^{-1} on the east side of the galaxy, while the velocity dispersion rarely exceeds 380 km s^{-1} on the west side. This asymmetry prevents NGC 4889 from being fully described by a single set of axisymmetric orbit models. In order to place upper and lower bounds on the central black hole mass, we have run four suites of models, each fitting kinematics from one projected quadrant of NGC 4889. The northeast, southeast, and northwest quadrants yield consistent black hole masses, spanning a 68% confidence interval of $M_{\bullet} = (1.0 - 3.7) \times 10^{10} M_{\odot}$. The southwest quadrant has a maximum velocity dispersion of 373 km/s and yields a 68% confidence interval of $M_{\bullet} = (0.6 - 1.7) \times 10^{10} M_{\odot}$.

We have run an additional set of models to approximate M_{\bullet} in the case of an off-center black hole. We apply a constant spatial offset of 1.4 arcseconds (700 pc) to the kinematics on the east side of the galaxy, such that the highest velocity dispersion is aligned with the center of the model gravitational potential. These models cannot be fully trusted because the kinematic and photometric data are misaligned. Still, the resulting 68% confidence interval for M_{\bullet} falls entirely within the range bracketed by the models from different quadrants. Results from individual trials are listed in Table 3.2. Figure 3.9 illustrates χ^2 versus M_{\bullet} for each series of models, after marginalizing over M_{\star}/L .

Although three-dimensional stellar velocities must increase in the vicinity of a black hole, a deficiency of radial orbits can produce a central minimum in the line-of-sight velocity dispersion, as we observe in NGC 4889. Indeed, our best-fitting models of NGC 4889 exhibit tangential bias at small radii, as shown in Figure 3.10. In contrast, models without a black hole reproduce the central drop in velocity dispersion with a nearly isotropic orbital distribution. However, these models yield a worse overall fit, indicated by higher values of χ^2 in each quadrant. Models of NGC 3842 exhibit a similar but less severe trend, consistent with the modest increase in line-of-sight velocity dispersion toward the center.

The individual quadrants of NGC 4889 represent large variations in stellar kinematics, but each quadrant still partially constrains the enclosed mass within the central few arcseconds. By adopting the most extreme range of confidence limits, $M_{\bullet} = (0.6 - 3.7) \times 10^{10} M_{\odot}$, we only exclude black holes whose gravitational influence would contradict our entire field of data. Further extensions to this confidence interval should only reflect overall systematic biases. Large systematic biases in our kinematic measurements are unlikely, as demonstrated by their agreement with independent measurements by Loubser et al. (2008). Our models of NGC 4889 assume an edge-on inclination. This is indirectly supported by the observed axis ratio of 0.7, which implies a relatively eccentric intrinsic shape even for an edge-on system. Models with a more face-on inclination might yield a systematically higher black hole mass (van den Bosch & de Zeeuw 2010). A fundamental assumption of all orbit superposition models is that the stellar motions reflect a steady-state gravitational potential, rather than transient conditions. These models could misrepresent the range of allowed black hole masses if the observed kinematics in NGC 4889 reflected a temporary phenomenon such as

an ongoing galaxy merger. NGC 4889 appears photometrically undisturbed, reducing the likelihood of such an event.

Because our adopted confidence interval places large error bars on M_\bullet in NGC 4889, this galaxy has relatively little weight in our fits to the $M_\bullet - \sigma$ and $M_\bullet - L$ relationships. A systematic error in our measurement would produce a minimal bias in the best-fit relations. Likewise, our discussion of steepening and scatter at the high-mass ends of the correlations depends upon several objects and is not highly sensitive to the measurement in NGC 4889.

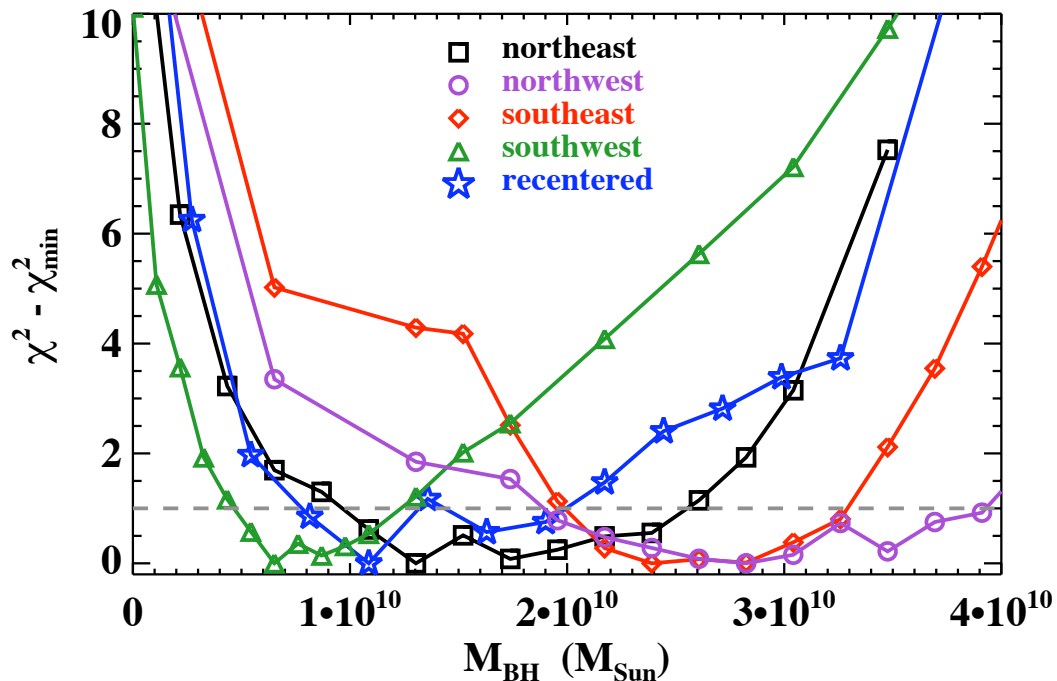


Figure 3.9: χ^2 vs. M_\bullet for NGC 4889, after marginalizing over M_\star/L . Each line with symbols represents a models constrained by different set of LOSVDs from GMOS. Black squares, purple circles, red diamonds, and green triangles each use LOSVDs from a different quadrant of the galaxy. Blue stars represent models with spatially offset LOSVDs, to match the largest velocity dispersion with the center of the gravitational potential. Considering all models, the 68% confidence interval for M_\bullet is $(0.6 - 3.7) \times 10^{10} M_\odot$.

Table 3.2: Models of NGC 4889

| Quadrant | M_{\bullet} (M_{\odot}) | $M_{\bullet,\min}$ (M_{\odot}) | $M_{\bullet,\max}$ (M_{\odot}) | M_{\star}/L_R ($M_{\odot}L_{\odot,R}^{-1}$) | $M_{\star}/L_{R,\min}$ ($M_{\odot}L_{\odot,R}^{-1}$) | $M_{\star}/L_{R,\max}$ ($M_{\odot}L_{\odot,R}^{-1}$) |
|------------|----------------------------------|---------------------------------------|---------------------------------------|----------------------------------------------------|-----------------------------------------------------------|-----------------------------------------------------------|
| northeast | 1.7×10^{10} | 1.0×10^{10} | 2.5×10^{10} | 6.1 | 4.6 | 7.3 |
| southeast | 2.6×10^{10} | 2.0×10^{10} | 3.2×10^{10} | 5.6 | 4.2 | 6.7 |
| northwest | 2.7×10^{10} | 1.6×10^{10} | 3.7×10^{10} | 5.8 | 4.4 | 7.0 |
| southwest | 9.8×10^9 | 5.5×10^9 | 1.7×10^{10} | 6.6 | 5.3 | 7.6 |
| east | 2.9×10^{10} | 2.1×10^{10} | 3.4×10^{10} | 5.4 | 4.5 | 6.4 |
| west | 1.2×10^{10} | 6.5×10^9 | 2.0×10^{10} | 6.4 | 5.2 | 7.4 |
| recentered | 1.5×10^{10} | 8.7×10^9 | 2.4×10^{10} | 6.5 | 5.4 | 7.3 |

Notes: The “east” and “west” trials used LOSVDs from spectra that were binned symmetrically over the north and south sides of the galaxy. The “recentered” trial added an artificial position offset to the LOSVDs, such that the maximum velocity dispersion was placed at the center of the gravitational potential. Columns for $M_{\bullet,\min}$, $M_{\bullet,\max}$, $M_{\star}/L_{R,\min}$, and $M_{\star}/L_{R,\max}$ represent 68% confidence limits.

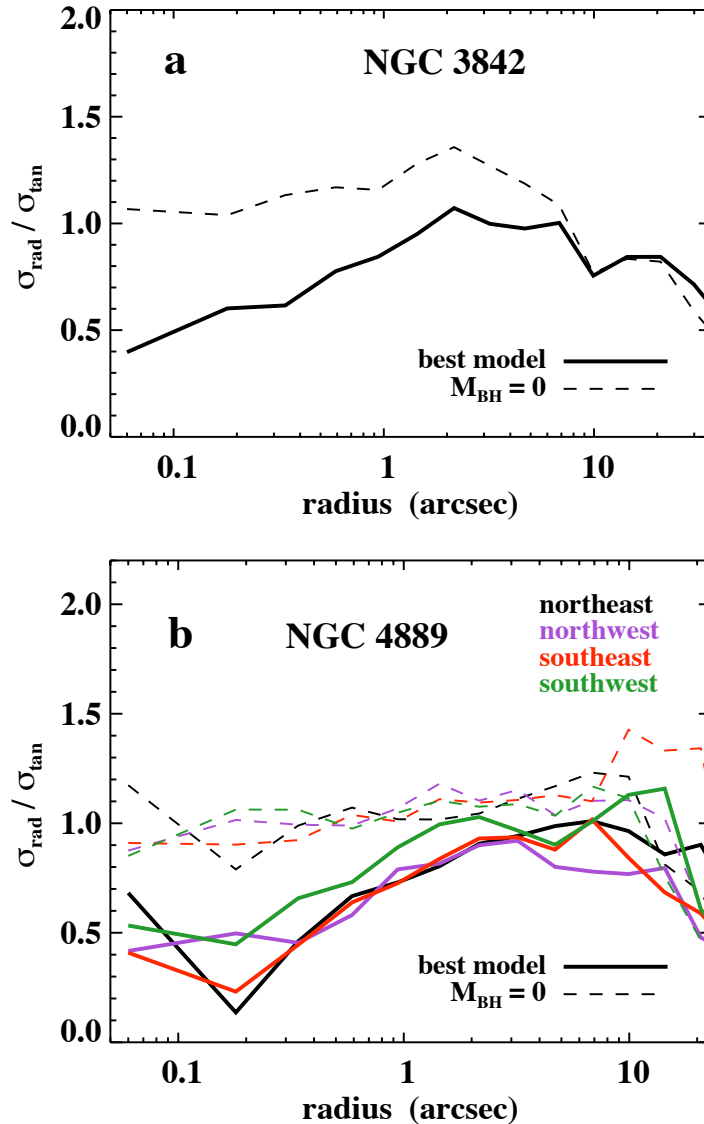


Figure 3.10: Orbital anisotropy in models of NGC 3842 and NGC 4889. Three-dimensional stellar velocities in the models are divided into radial and tangential components. The ratio of velocity dispersions, $\sigma_{\text{rad}}/\sigma_{\text{tan}}$, varies with radius and the assumed M_{\bullet} in the model. Solid lines represent the best-fitting overall models, and dashed lines represent the best-fitting models with $M_{\bullet} = 0$. (a) For NGC 3842, the best-fitting model has $M_{\bullet} = 8.5 \times 10^9 M_{\odot}$. (b) We depict models for each quadrant in NGC 4889. The best-fitting models have $M_{\bullet} = 1.3 \times 10^{10} M_{\odot}$ (northeast), $2.8 \times 10^{10} M_{\odot}$ (northwest), $2.4 \times 10^{10} M_{\odot}$ (southeast), and $6.5 \times 10^9 M_{\odot}$ (southwest). For NGC 3842 and each quadrant of NGC 4889, our kinematic data are best fit with a massive black hole and a prevalence of tangential orbits at $r < 2$ arcseconds (1 kpc). In NGC 4889, this tangential bias is responsible for the observed decrease in line-of-sight velocity dispersion near the center.

3.10 Appendix F: Power-Law Fits to the $M_{\bullet} - \sigma$ and $M_{\bullet} - L$ Relations

We revisit the $M_{\bullet} - \sigma$ and $M_{\bullet} - L$ relations by updating the sample of 49 black holes from Gültekin et al. (2009a), which was compiled from earlier studies. Including NGC 3842 and NGC 4889, we add 17 galaxies with recently measured black hole masses to the sample. The new objects include two more BCGs (Nowak et al. 2008; McConnell et al. 2011a), eight active galactic nuclei with high-precision maser-based measurements (Greene et al. 2010a; Kuo et al. 2011), and two galaxies with pseudobulges (Kormendy et al. 2011). We also include updated black hole masses for 16 other galaxies in the 2009 sample, based on stellar orbit models with dark matter halos and more thorough orbit libraries (Shen & Gebhardt 2010; van den Bosch & de Zeeuw 2010; Gebhardt et al. 2011; Schulze & Gebhardt 2011). In particular, the revised masses for M60 and M87 are twice as large as the earlier values.

Our updated sample uses the same selection criteria as Gültekin et al. (2009a); in particular, only direct dynamical measurements of M_{\bullet} are included. Gültekin et al. (2009a) estimated galaxy distances by assuming a Hubble parameter $H_0 = 70 \text{ km s}^{-1} \text{ Mpc}^{-1}$, and rescaled their sample of black hole masses accordingly ($M_{\bullet} \propto D$). We have followed this convention for NGC 3842, NGC 4889, and the rest of our sample. Our fits to $M_{\bullet}(\sigma)$ do not include upper limits. Updated models of one galaxy, NGC 2778, do not produce a significant black hole detection; after removing this object, our updated sample contains 65 black hole masses.

We define σ in the same manner as the 2009 sample. Wherever possible, we use the luminosity-weighted effective velocity dispersion, measured using spatially resolved data out to one effective radius. Gültekin et al. (2009a) found no evidence of systematic bias between this definition of σ and more ubiquitous single-aperture measurements. Nonetheless, several galaxies in Gültekin et al. (2009a) have measurements of σ that include data at very small radii, within which the central black hole directly influences the stellar velocity dispersion. This is inappropriate for studies that wish to treat M_{\bullet} and σ as fundamentally independent variables. We have therefore re-evaluated σ in three galaxies with large black hole masses and available spatially resolved kinematics, by excluding data within the black hole’s radius of influence. We use this same treatment to measure σ for NGC 3842 and NGC 4889. For M87, we adopt the updated values of M_{\bullet} and σ from Gebhardt et al. (2011). Following Gültekin et al. (2009a), we assume all measurements of σ have an uncertainty of at least 5%.

To fit the $M_{\bullet} - L$ relationship, we only consider early-type galaxies for which the stellar luminosity of the spheroidal component can be measured reliably. Including NGC 3842, we add 6 galaxies to the $M_{\bullet} - L$ sample of Gültekin et al. (2009a). We exclude NGC 2778. We also exclude NGC 3607 and NGC 4564, for which the literature contains large discrepancies in the measured luminosity (Lauer et al. 2007a; Gültekin et al. 2009a). Our final sample for fitting $M_{\bullet} - L$ contains 36 black hole masses.

Our fits to $M_{\bullet} - \sigma$ and $M_{\bullet} - L$ assume a single-index power law as the functional form of both relations, following the convention most commonly used in prior studies. Specifically,

we define the $M_\bullet - \sigma$ relationship to be $\log_{10}(M_\bullet/M_\odot) = \alpha + \beta \log_{10}(\sigma/200 \text{ km s}^{-1})$, and the $M_\bullet - L$ relationship to be $\log_{10}(M_\bullet/M_\odot) = \alpha + \beta \log_{10}(L_V/10^{11} L_\odot)$. For each relationship, we follow the method of Tremaine et al. (2002) to fit for α and β . We minimize the quantity

$$\chi^2 = \sum_{i=1}^N \frac{(M_{\bullet,i} - \alpha - \beta \sigma_i)^2}{\epsilon_0^2 + \epsilon_{M,i}^2 + \beta^2 \epsilon_{\sigma,i}^2} \quad (3.1)$$

where ϵ_σ is the measurement error in σ , ϵ_M is the measurement error in M_\bullet , and ϵ_0 is the intrinsic scatter in the $M_\bullet - \sigma$ relation. We set ϵ_0 such that χ^2 per degree of freedom is unity after minimization. The 68% confidence intervals for α and β correspond to the maximum range of α and β for which $\chi^2 - \chi_{min}^2 \leq 1$.

We list our best-fit values of α , β , and ϵ_0 for various sub-samples in Table 3.3. We list the corresponding galaxy sample in Table 3.4. Graham et al. (2011) recently compiled a sample of 64 galaxies with dynamical black hole measurements and found a power-law index of 5.13 for the $M_\bullet - \sigma$ relation, very similar to the index we report herein. However, only 52 galaxies appear in their sample as well as ours. Of the 13 galaxies that appear only in our sample, seven use precise maser-based measurements of M_\bullet (Greene et al. 2010a; Kuo et al. 2011), and three are BCGs. Additionally, 11 galaxies have received updated measurements of M_\bullet since the compilation of Graham et al. (2011), using stellar orbit models with dark matter halos and larger orbit libraries (Schulze & Gebhardt 2011).

The sample discussed above and presented in Table 3.4 is a compilation of black hole masses published before August 2011. In Chapter 5 we present a further updated sample, including black hole masses published through May 2012 and adjusted distances, velocity dispersions, and luminosities for a few host galaxies (see Table 5.1). Chapter 5 also includes updated fits to the $M_\bullet - \sigma$ and $M_\bullet - L$ relations.

 Table 3.3: Fits to $M_\bullet(\sigma)$ and $M_\bullet(L)$

| Relationship | Sample | N_{gal} | α | β | ϵ_0 |
|----------------------|------------|------------------|-----------------|-----------------|--------------|
| $M_\bullet - \sigma$ | all | 65 | 8.29 ± 0.06 | 5.12 ± 0.36 | 0.43 |
| $M_\bullet - \sigma$ | early-type | 45 | 8.38 ± 0.06 | 4.53 ± 0.40 | 0.38 |
| $M_\bullet - \sigma$ | late-type | 20 | 7.97 ± 0.22 | 4.58 ± 1.25 | 0.44 |
| $M_\bullet - \sigma$ | ML | 36 | 8.43 ± 0.07 | 4.66 ± 0.43 | 0.38 |
| $M_\bullet - L$ | ML | 36 | 9.16 ± 0.11 | 1.16 ± 0.14 | 0.50 |

Notes: The number of galaxies in each sample is N_{gal} . ML refers to the sample of early-type galaxies with reliable spheroid luminosity measurements.

Table 3.4: Galaxies with dynamical measurements of M_{\bullet} through July 2011

| Galaxy | Type | D (Mpc) | σ (km s^{-1}) | $\log L_{V,\text{sph}}$ $\log_{10}(L_{\odot})$ | M_{\bullet} (M_{\odot}) | $M_{\bullet,\text{min}}$ (M_{\odot}) | $M_{\bullet,\text{max}}$ (M_{\odot}) | Method | Ref. |
|------------------------|-----------|--------------|------------------------------------|---------------------------------------------------|----------------------------------|---------------------------------------------|---------------------------------------------|--------|-------|
| Milky Way ^a | Sbc | 0.008 | 103 ± 20 | | 4.1×10^6 | 3.5×10^6 | 4.7×10^6 | stars | 1,2,3 |
| A1836-BCG | E | 157.5 | 288 ± 14 | 11.26 | 3.9×10^9 | 3.3×10^9 | 4.3×10^9 | gas | 1,4 |
| A3565-BCG ^b | E | 54.4 | 322 ± 16 | 11.24 | 1.4×10^9 | 1.2×10^9 | 1.7×10^9 | gas | 4 |
| Circinus | Sb | 4.0 | 158 ± 18 | | 1.7×10^6 | 1.4×10^6 | 2.1×10^6 | masers | 1,5 |
| IC1459 ^c | E4 | 30.9 | 315 ± 16 | 10.96 | 2.8×10^9 | 1.6×10^9 | 3.9×10^9 | stars | 1,6 |
| N221 (M32) | E2 | 0.86 | 75 ± 3 | 8.66 | 3.1×10^6 | 2.5×10^6 | 3.7×10^6 | stars | 1,7 |
| N224 (M31) | Sb | 0.80 | 160 ± 8 | | 1.5×10^8 | 1.2×10^8 | 2.4×10^8 | stars | 1,8 |
| N524 | S0 | 23.3 | 235 ± 12 | 10.67 | 8.3×10^8 | 7.9×10^8 | 9.2×10^8 | stars | 9 |
| N821 | E4 | 25.5 | 209 ± 10 | 10.43 | 1.8×10^8 | 1.0×10^8 | 2.6×10^8 | stars | 10 |
| N1023 | SB0 | 12.1 | 205 ± 10 | 10.18 | 4.6×10^7 | 4.1×10^7 | 5.1×10^7 | stars | 1,11 |
| N1068 (M77) | SB | 15.4 | 151 ± 7 | | 8.6×10^6 | 8.3×10^6 | 8.9×10^6 | masers | 1,12 |
| N1194 ^{b,d} | SA0+ | 55.5 | 148^{+26}_{-22} | | 6.8×10^7 | 6.5×10^7 | 7.1×10^7 | masers | 13 |
| N1300 | SB(rs)bc | 20.1 | 218 ± 10 | | 7.1×10^7 | 3.6×10^7 | 1.4×10^8 | gas | 1,14 |
| N1316 | E | 18.6 | 226 ± 11 | 11.26 | 1.5×10^8 | 1.24×10^8 | 1.75×10^8 | stars | 15 |
| N1332 | S0 | 22.3 | 328 ± 16 | 10.14 | 1.45×10^9 | 1.25×10^9 | 1.65×10^9 | stars | 16 |
| N1399 ^{e,f} | E1 | 21.1 | 296 ± 15 | 10.78 | 5.1×10^8 | 4.4×10^8 | 5.8×10^8 | stars | 1,17 |
| N1399 ^{e,f} | E1 | 21.1 | 296 ± 15 | 10.78 | 1.3×10^9 | 6.4×10^8 | 1.8×10^9 | stars | 1,18 |
| N2273 ^{b,d} | SB(r)a | 26.8 | 144^{+18}_{-16} | | 7.8×10^6 | 7.4×10^6 | 8.2×10^6 | masers | 13 |
| N2549 | S0 | 12.3 | 145 ± 7 | 9.60 | 1.4×10^7 | 1.0×10^7 | 1.47×10^7 | stars | 9 |
| N2748 | Sc | 24.9 | 115 ± 5 | | 4.7×10^7 | 8.6×10^6 | 8.5×10^7 | gas | 1,14 |
| N2787 | SB0 | 7.9 | 189 ± 9 | | 4.3×10^7 | 3.8×10^7 | 4.7×10^7 | gas | 1,19 |
| N2960 ^{b,d} | Sa | 75.3 | 166^{+16}_{-15} | | 1.21×10^7 | 1.16×10^7 | 1.26×10^7 | masers | 13 |
| N3031 (M81) | Sb | 4.1 | 143 ± 7 | | 8.0×10^7 | 6.9×10^7 | 1.0×10^8 | gas | 1,20 |
| N3115 | S0 | 10.2 | 230 ± 11 | 10.40 | 9.6×10^8 | 6.7×10^8 | 1.5×10^9 | stars | 1,21 |
| N3227 | SBa | 17.0 | 133 ± 12 | | 1.5×10^7 | 7.0×10^6 | 2.0×10^7 | stars | 1,22 |
| N3245 | S0 | 22.1 | 205 ± 10 | | 2.2×10^8 | 1.7×10^8 | 2.7×10^8 | gas | 1,23 |
| N3368 ^g | SAB(rs)ab | 10.4 | 122^{+28}_{-24} | | 7.5×10^6 | 6.0×10^6 | 9.0×10^6 | stars | 24 |

Continued on next page

Table 3.4, continued

| Galaxy | Type | D (Mpc) | σ (km s^{-1}) | $\log L_{V,\text{sph}}$ $\log_{10}(L_{\odot})$ | M_{\bullet} (M_{\odot}) | $M_{\bullet,\text{min}}$ (M_{\odot}) | $M_{\bullet,\text{max}}$ (M_{\odot}) | Method | Ref. |
|----------------------------|-----------|--------------|------------------------------------|---------------------------------------------------|----------------------------------|---------------------------------------------|---------------------------------------------|--------|------|
| N3377 | E6 | 11.7 | 145 ± 7 | 9.98 | 1.9×10^8 | 9.0×10^7 | 2.9×10^8 | stars | 10 |
| N3379 (M105) ^b | E0 | 11.7 | 206 ± 10 | 10.37 | 4.6×10^8 | 3.4×10^8 | 5.7×10^8 | stars | 25 |
| N3384 | E1 | 11.7 | 143 ± 7 | 9.90 | 1.1×10^7 | 6.0×10^6 | 1.6×10^7 | stars | 10 |
| N3393 ^b | SB(rs) | 53.6 | 148 ± 10 | | 3.3×10^7 | 3.1×10^7 | 3.5×10^7 | masers | 26 |
| N3489 ^g | SAB(rs)0+ | 12.1 | 100^{+15}_{-11} | | 6.0×10^6 | 5.2×10^6 | 6.8×10^6 | stars | 24 |
| N3585 | S0 | 21.2 | 213 ± 10 | 10.65 | 3.4×10^8 | 2.8×10^8 | 4.9×10^8 | stars | 1,27 |
| N3607 ^h | E1 | 19.9 | 229 ± 11 | | 1.2×10^8 | 7.9×10^7 | 1.6×10^8 | stars | 1,27 |
| N3608 | E1 | 23.0 | 182 ± 9 | 10.35 | 4.7×10^8 | 3.7×10^8 | 5.7×10^8 | stars | 10 |
| N3842 ⁱ | E | 98.4 | 270 ± 14 | 11.20 | 9.7×10^9 | 7.2×10^9 | 1.27×10^{10} | stars | |
| N3998 | S0 | 14.9 | 305 ± 15 | | 2.4×10^8 | 6.2×10^7 | 4.5×10^8 | gas | 1,28 |
| N4026 | S0 | 15.6 | 180 ± 9 | 9.86 | 2.1×10^8 | 1.7×10^8 | 2.8×10^8 | stars | 1,27 |
| N4258 | SABbc | 7.2 | 115 ± 10 | | 3.78×10^7 | 3.77×10^7 | 3.79×10^7 | masers | 1,29 |
| N4261 | E2 | 33.4 | 315 ± 15 | 11.02 | 5.5×10^8 | 4.3×10^8 | 6.6×10^8 | gas | 1,30 |
| N4291 | E2 | 25.0 | 242 ± 12 | 10.20 | 9.2×10^8 | 6.3×10^8 | 1.21×10^9 | stars | 10 |
| N4342 | S0 | 18.0 | 225 ± 11 | | 3.6×10^8 | 2.4×10^8 | 5.6×10^8 | stars | 1,31 |
| N4374 (M84) | E1 | 17.0 | 296 ± 14 | 10.91 | 8.5×10^8 | 7.7×10^8 | 9.4×10^8 | gas | 32 |
| N4388 ^{b,d} | SA(s)b | 19.8 | 107^{+8}_{-7} | | 8.8×10^6 | 8.6×10^6 | 9.0×10^6 | masers | 13 |
| N4459 | E2 | 17.0 | 167 ± 8 | 10.36 | 7.4×10^7 | 6.0×10^7 | 8.8×10^7 | gas | 1,19 |
| N4473 | E4 | 17.0 | 190 ± 9 | 10.39 | 1.0×10^8 | 5.0×10^7 | 1.5×10^8 | stars | 10 |
| N4486 (M87) ^{b,j} | E1 | 17.0 | 324^{+28}_{-16} | 11.10 | 6.3×10^9 | 5.9×10^9 | 6.6×10^9 | stars | 33 |
| N4486A | E2 | 17.0 | 111 ± 5 | 9.41 | 1.3×10^7 | 9.0×10^6 | 1.8×10^7 | stars | 1,34 |
| N4564 ^k | S0 | 17.0 | 162 ± 8 | | 9.4×10^7 | 6.8×10^7 | 1.2×10^8 | stars | 10 |
| N4594 (M104) | Sa | 10.3 | 240 ± 12 | | 5.3×10^8 | 4.74×10^8 | 6.08×10^8 | stars | 35 |
| N4596 | SB0 | 18.0 | 136 ± 6 | | 8.4×10^7 | 5.9×10^7 | 1.2×10^8 | gas | 1,19 |
| N4649 (M60) ^{b,l} | E2 | 16.5 | 341 ± 17 | 10.99 | 4.7×10^9 | 3.7×10^9 | 5.8×10^9 | stars | 36 |
| N4697 | E6 | 12.4 | 177 ± 8 | 10.45 | 2.0×10^8 | 1.8×10^8 | 2.2×10^8 | stars | 10 |
| N4736 (M94) | Sab | 4.9 | 112 ± 6 | | 6.68×10^6 | 5.14×10^6 | 8.22×10^6 | stars | 35 |

Continued on next page

Table 3.4, continued

| Galaxy | Type | D (Mpc) | σ (km s^{-1}) | $\log L_{V,\text{sph}}$ $\log_{10}(L_{\odot})$ | M_{\bullet} (M_{\odot}) | $M_{\bullet,\text{min}}$ (M_{\odot}) | $M_{\bullet,\text{max}}$ (M_{\odot}) | Method | Ref. |
|----------------------|---------|--------------|------------------------------------|---------------------------------------------------|----------------------------------|---------------------------------------------|---------------------------------------------|--------|------|
| N4826 (M64) | Sab | 6.4 | 96 ± 5 | | 1.36×10^6 | 1.02×10^6 | 1.71×10^6 | stars | 35 |
| N4889 ^m | E | 103.2 | 347 ± 17 | 11.42 | 2.1×10^{10} | 5.5×10^9 | 3.7×10^{10} | stars | |
| N5077 | E3 | 44.9 | 222 ± 11 | 10.75 | 8.0×10^8 | 4.7×10^8 | 1.3×10^9 | gas | 1,37 |
| N5128 ^e | S0/E | 4.4 | 150 ± 7 | 10.66 | 3.0×10^8 | 2.8×10^8 | 3.4×10^8 | stars | 1,38 |
| N5128 ^e | S0/E | 4.4 | 150 ± 7 | 10.66 | 7.0×10^7 | 3.2×10^7 | 8.3×10^7 | stars | 1,39 |
| N5576 | E3 | 27.1 | 183 ± 9 | 10.44 | 1.8×10^8 | 1.4×10^8 | 2.1×10^8 | stars | 1,27 |
| N5845 | E3 | 28.7 | 234 ± 11 | 9.84 | 5.4×10^8 | 3.7×10^8 | 7.1×10^8 | stars | 10 |
| N6086 ^b | E | 139.1 | 318 ± 16 | 11.18 | 3.8×10^9 | 2.6×10^9 | 5.5×10^9 | stars | 40 |
| N6251 | E1 | 106.0 | 290 ± 14 | | 6.0×10^8 | 4.0×10^8 | 8.0×10^8 | gas | 1,41 |
| N6264 ^{b,d} | S | 145.4 | 158^{+15}_{-14} | | 3.03×10^7 | 2.99×10^7 | 3.08×10^7 | masers | 13 |
| N6323 ^{b,d} | Sab | 110.5 | 158^{+28}_{-23} | | 9.8×10^6 | 9.7×10^6 | 9.9×10^6 | masers | 13 |
| N7052 | E3 | 70.9 | 266 ± 13 | 10.87 | 4.0×10^8 | 2.4×10^8 | 6.8×10^8 | gas | 1,42 |
| N7457 | S0 | 14.0 | 67 ± 3 | 9.42 | 1.0×10^7 | 4.0×10^6 | 1.6×10^7 | stars | 10 |
| N7582 | SBab | 22.3 | 156 ± 19 | | 5.5×10^7 | 4.4×10^7 | 7.1×10^7 | gas | 1,43 |
| U3789 ^{b,d} | SA(r)ab | 48.4 | 107^{+13}_{-12} | | 1.08×10^7 | 1.03×10^7 | 1.14×10^7 | masers | 13 |

References: (1 = Gültekin et al. 2009a); (2 = Ghez et al. 2008); (3 = Gillessen et al. 2009); (4 = Dalla Bontà et al. 2009); (5 = Greenhill et al. 2003); (6 = Cappellari et al. 2002); (7 = Verolme et al. 2002); (8 = Bender et al. 2005); (9 = Krajnović et al. 2009); (10 = Schulze & Gebhardt 2011); (11 = Bower et al. 2001); (12 = Lodato & Bertin 2003); (13 = Kuo et al. 2011); (14 = Atkinson et al. 2005); (15 = Nowak et al. 2008); (16 = Rusli et al. 2011); (17 = Gebhardt et al. 2007); (18 = Houghton et al. 2006); (19 = Sarzi et al. 2001); (20 = Devereux et al. 2003); (21 = Emsellem et al. 1999); (22 = Davies et al. 2006); (23 = Barth et al. 2001); (24 = Nowak et al. 2010); (25 = van den Bosch & de Zeeuw 2010); (26 = Kondratko et al. 2008); (27 = Gültekin et al. 2009b); (28 = de Francesco et al. 2006); (29 = Herrnstein et al. 2005); (30 = Ferrarese et al. 1996); (31 = Cretton & van den Bosch 1999a); (32 = Walsh et al. 2010); (33 = Gebhardt et al. 2011); (34 = Nowak et al. 2007); (35 = Kormendy et al. 2011); (36 = Shen & Gebhardt 2010); (37 = de Francesco et al. 2008); (38 = Silge et al. 2005); (39 = Cappellari et al. 2009); (40 = McConnell et al. 2011a); (41 = Ferrarese & Ford 1999); (42 = van der Marel & van den Bosch 1998); (43 = Wold et al. 2006).

Table 3.4 Notes:

D is the distance to the galaxy, assuming $H_0 = 70 \text{ km s}^{-1} \text{ Mpc}^{-1}$. $L_{V,\text{sph}}$ is the V -band stellar luminosity of the galaxy's spheroidal component. $M_{\bullet,\text{min}}$ and $M_{\bullet,\text{max}}$ are the upper and lower bounds of the 68% confidence interval in M_{\bullet} .

^a The literature contains a large number of estimates for the velocity dispersion of our Galaxy's bulge, using different kinematic tracers at different radii. We use the radially averaged measurement of $\sigma = 103 \pm 20 \text{ km s}^{-1}$ from Tremaine et al. (2002).

^b Gültekin et al. (2009a) use the convention $H_0 = 70 \text{ km s}^{-1} \text{ Mpc}^{-1}$ for all galaxies whose distances are derived from systemic velocity measurements. To match this convention, we have adjusted the distance to several galaxies in our updated sample. All distance adjustments yield corresponding adjustments to M_{\bullet} , $M_{\bullet,\text{min}}$, and $M_{\bullet,\text{max}}$, such that $M_{\bullet} \propto D$. Our reported 68% confidence intervals for M_{\bullet} do not include uncertainties in the distance measurements.

^c We derive an effective velocity dispersion of 315 km s^{-1} for IC 1459, using spatially resolved major-axis kinematics from Cappellari et al. (2002), at radii of 0.8 - 25.1 arcseconds. For $r < 0.8$ arcseconds, stellar motions are directly influenced by the central black hole.

^d Maser-based black hole masses for several galaxies are presented in Greene et al. (2010a) and Kuo et al. (2011). We use the velocity dispersions presented in Greene et al. (2010a). For consistency with the rest of our sample, we use the black hole masses from Kuo et al. (2011), which agree with the values in Greene et al. (2010a) but do not include distance uncertainties in the overall uncertainty for M_{\bullet} . Braatz et al. (2010) provide an updated distance and black hole mass for UGC 3789, which are consistent with the values we adopt from Kuo et al. (2011).

^e Following Gültekin et al. (2009a), our sample includes two distinct measurements for NGC 1399 and also for NGC 5128. We weight each of these measurements by 50% when performing fits to $M_{\bullet}(\sigma)$ and $M_{\bullet}(L)$. In Figure 3 we only plot the more recent measurement for each galaxy.

^f We derive an effective velocity dispersion of 296 km s^{-1} for NGC 1399, using spatially resolved measurements from Graham et al. (1998) and Gebhardt et al. (2007) at radii of 0.6 - 41 arcseconds. For $r < 0.6$ arcseconds, stellar motions are directly influenced by the central black hole.

Table 3.4 Notes, continued:

^g NGC 3368 and NGC 3489 were not included in our sample until this chapter was being reviewed for publication, and so they do not contribute toward the fits reported above. For the velocity dispersions, we use the average values and outer limits of the various measurements reported by Nowak et al. (2010). Including NGC 3368 and NGC 3489, the $M_{\bullet} - \sigma$ parameters (α , β , ϵ_0) are $(8.28 \pm 0.06, 5.13 \pm 0.34, 0.42)$ for 67 galaxies, $(8.38 \pm 0.06, 4.57 \pm 0.36, 0.36)$ for 46 early-type galaxies, and $(8.00 \pm 0.21, 4.76 \pm 1.15, 0.43)$ for 21 late-type galaxies. These parameters are consistent with our reported values for the sample of 65 galaxies.

^h The literature contains two inconsistent estimates of the stellar luminosity in NGC 3607: $M_V = -21.62$ in Gültekin et al. (2009a), and $M_V = -19.88$ in Lauer et al. (2007a).

ⁱ We derive an effective velocity dispersion of 270 km s^{-1} for NGC 3842, using measurements from GMOS and VIRUS-P at radii of 1.2 - 29.8 arcseconds. For $r < 1.2$ arcseconds, stellar motions are directly influenced by the central black hole.

^j For M87, we use the updated velocity dispersion of 324 km s^{-1} from Gebhardt et al. (2011), based on measurements at radii of 2.1 - 100 arcseconds. For $r < 2.1$ arcseconds, stellar motions are directly influenced by the central black hole.

^k The literature contains two inconsistent estimates of the bulge stellar luminosity in NGC 4564: $M_V = -19.60$ in Gültekin et al. (2009a), and $M_V = -20.26$ in Lauer et al. (2007a).

^l We derive an effective velocity dispersion of 341 km s^{-1} for M60, using spatially resolved measurements from Pinkney et al. (2003) at radii of 2.2 - 44 arcseconds. For $r < 2.2$ arcseconds, stellar motions are directly influenced by the central black hole.

^m Our quoted value of M_{\bullet} for NGC 4889 is the median of the 68% confidence interval $(0.6 - 3.4) \times 10^{10} M_{\odot}$. We derive an effective velocity dispersion of 347 km s^{-1} , using kinematics from Loubser et al. (2008) at radii of 2.0 - 22.9 arcseconds. The inner cutoff of 2.0 arcseconds excludes the asymmetric velocity dispersion peak and possible stellar torus.

Chapter 4

Dynamical Measurements of Black Hole Masses in Four Brightest Cluster Galaxies at 100 Mpc

Abstract

We present stellar kinematics and orbit superposition models for the central regions of four Brightest Cluster Galaxies (BCGs), based upon integral-field spectroscopy at Gemini, Keck, and McDonald Observatories. Our integral-field data span radii from < 100 pc to tens of kiloparsecs, comparable to the effective radius of each galaxy. We report black hole masses, M_{\bullet} , of $2.1_{-1.6}^{+1.6} \times 10^{10} M_{\odot}$ for NGC 4889, $9.7_{-2.5}^{+3.0} \times 10^9 M_{\odot}$ for NGC 3842, and $1.3_{-0.4}^{+0.5} \times 10^9 M_{\odot}$ for NGC 7768, with errors representing 68% confidence limits. For NGC 2832 we report an upper limit of $M_{\bullet} < 9.0 \times 10^9 M_{\odot}$. Our models of each galaxy include a dark matter halo, and we have tested the dependence of M_{\bullet} on the model dark matter profile. Stellar orbits near the center of each galaxy are tangentially biased, on comparable spatial scales to the galaxies' photometric cores. We find possible photometric and kinematic evidence for an eccentric torus of stars in NGC 4889, with a radius of nearly 1 kpc. We compare our measurements of M_{\bullet} to the predicted black hole masses from various fits to the relations between M_{\bullet} and stellar velocity dispersion (σ), luminosity (L), or stellar mass (M_{bulge}). Still, the black holes in NGC 4889 and NGC 3842 are significantly more massive than all σ -based predictions and most L -based predictions. The black hole in NGC 7768 is consistent with a broader range of predictions. This chapter has been accepted for publication in the *Astrophysical Journal* (McConnell et al. 2012).

4.1 Introduction

For four decades, dynamical studies have provided evidence for the existence of black holes. In the most exquisite cases, the orbital motions of individual stars or megamasers place strong lower limits on the density of a central object and rule out virtually all alternatives to a black hole (e.g., Bolton 1972; Schödel et al. 2002; Ghez et al. 2005; Bender et al. 2005; Herrnstein et al. 2005). More generally, massive dark objects have been dynamically detected in a rapidly growing number of galactic nuclei and are widely assumed to be black holes (e.g., Sargent et al. 1978; Tonry 1987; for reviews and compilations see Kormendy & Richstone 1995; Gültekin et al. 2009a; McConnell et al. 2011b). The menagerie of black holes spans from stellar-mass objects to “supermassive” behemoths, whose masses, M_\bullet , can approach $10^{10} M_\odot$. Strong dynamical evidence for “intermediate-mass” black holes with $M_\bullet \sim 10^3 - 10^5 M_\odot$ is more elusive but has been recorded in a few stellar systems (Gebhardt et al. 2005; Lützgendorf et al. 2011; Jalali et al. 2012; cf. Baumgardt et al. 2003; van der Marel & Anderson 2010).

In galactic nuclei, M_\bullet appears to correlate with the stellar mass, luminosity, and velocity dispersion of the host bulge or spheroid (e.g., Dressler 1989; Kormendy & Richstone 1995; Magorrian et al. 1998; Ferrarese & Merritt 2000; Gebhardt et al. 2000a; Tremaine et al. 2002; Marconi & Hunt 2003). A frontier goal is to explore the extrema of these black hole scaling relations by directly measuring M_\bullet in low-mass galaxies and in extremely massive galaxies. Here we focus on Brightest Cluster Galaxies (BCGs), which are among the most massive galaxies in the present-day Universe. BCGs typically reside deep in the gravitational potentials of rich clusters, and their environment may provide a unique path for galaxy and black hole growth. BCGs have been observed to follow a steeper relation between luminosity (L) and velocity dispersion (σ) than less massive elliptical galaxies (e.g., Bernardi et al. 2007; Desroches et al. 2007; Lauer et al. 2007a; von der Linden et al. 2007). Bernardi et al. (2007) and Lauer et al. (2007a) have noted that the $M_\bullet - L$ relation predicts systematically more massive black holes than $M_\bullet - \sigma$ for the most massive galaxies.

To date, there are eight groups or clusters where M_\bullet has been measured dynamically in the massive central galaxy: Coma (NGC 4889; McConnell et al. 2011b), Fornax (NGC 1399; e.g. Houghton et al. 2006; Gebhardt et al. 2007), Virgo (M87; Gebhardt et al. 2011), Abell 1367 (NGC 3842; McConnell et al. 2011b), Abell 1836 (PGC 49940; Dalla Bontà et al. 2009), Abell 2162 (NGC 6086; McConnell et al. 2011a), Abell 3565 (IC 4296; Dalla Bontà et al. 2009) and the IC 1459 group (IC 1459; Cappellari et al. 2002). Only three of these systems (Coma, Abell 1367, Abell 3565) are rich clusters. In Fornax and Virgo, the central cD galaxy is not even the brightest member. The brightest galaxy in Fornax is NGC 1316, which lies near the cluster outskirts and hosts a black hole with $M_\bullet = 1.5 \times 10^8 M_\odot$ (Nowak et al. 2008). In Virgo, M49 anchors a sub-group more than 1 Mpc from the more centralized M87 and M86 sub-groups, and hosts a black hole with $M_\bullet = 1.5 \times 10^9 M_\odot$ (J. Shen et al., in prep.). In order to thoroughly explore black hole and galaxy co-evolution in different environments, we must measure M_\bullet in a larger sample of BCGs, with more examples from rich galaxy clusters. This chapter includes expanded discussion of the black

hole measurements in the BCGs of Coma and Abell 1367.

This chapter marks our continued effort to measure M_\bullet using stellar dynamics in BCGs beyond the Virgo cluster. BCGs are rare objects and typically lie at large distances, making high-resolution observations difficult. Additionally, their centers are typically fainter than less massive ellipticals, and 8- to 10-meter telescopes are required to obtain high-quality spectra at angular scales comparable to the black hole radius of influence, $r_{\text{inf}} \equiv GM_\bullet\sigma^{-2}$. For targets at distances ~ 100 Mpc and predicted black hole masses $\sim 10^9 M_\odot$ from the $M_\bullet - \sigma$ relation, adaptive optics (AO) is necessary to resolve $r_{\text{inf}} \sim 0.1''$. Under good conditions, seeing-limited observations can resolve the gravitational influence of extremely massive black holes ($M_\bullet \sim 10^{10} M_\odot$). Wide-field kinematic measurements are necessary to trace the galaxies' stellar mass profiles and dark matter halos.

We report measurements of M_\bullet and the R -band stellar mass-to-light ratio, M_\star/L_R , in four BCGs at distances of ~ 100 Mpc: NGC 4889 of the Coma cluster (Abell 1656), NGC 3842 (Abell 1367), NGC 7768 (Abell 2666), and NGC 2832 (Abell 779). We have obtained high-resolution data of the line-of-sight stellar velocities in the central regions of the four galaxies using instruments on the Gemini North and Keck Telescopes. In addition, we have used the 2.7-meter telescope at McDonald Observatory to measure stellar kinematics at large radii. At all spatial scales, we use integral-field spectrographs (IFSs) to obtain full two-dimensional spatial coverage, which places tighter constraints on stellar orbits. We determine M_\bullet and M_\star/L_R with axisymmetric orbit superposition models, which include a dark matter component in the gravitational potential. We have reported the black hole measurements of NGC 4889 and NGC 3842 in McConnell et al. (2011b), but due to space limitations, only the basic information was presented there. Here we provide a comprehensive discussion of the data analysis procedures, kinematic information, and stellar orbit modeling for all four galaxies.

The chapter is organized as follows. In Section 4.2, we describe our photometric and spectroscopic observations and data reduction procedures. In Section 4.3, we describe our procedures for extracting two-dimensional kinematics from the data obtained on three IFSs (GMOS, OSIRIS, and the Mitchell Spectrograph). The outputs of this step are non-parametric line-of-sight velocity distributions (LOSVDs) in two-dimensional spatial bins in the central regions of each galaxy. In Section 4.4, we show maps of the lowest four Gauss-Hermite moments of the LOSVDs for the four galaxies. We discuss both the two-dimensional maps and radial profiles of the kinematic moments. In Section 4.5 we summarize the stellar orbit modeling procedure. We report our measurements of M_\bullet and M_\star/L_R and describe how these measurements depend on the assumed dark matter halo profile, as well as other possible systematic biases. We also discuss the relative contributions of radial and tangential orbits in each galaxy. In Section 4.6 we summarize our results and compare our measurements of M_\bullet to predictions from the $M_\bullet - \sigma$ and $M_\bullet - L$ relations. Throughout this chapter, we assume $H_0 = 70 \text{ km s}^{-1}$, $\Omega_m = 0.27$, and $\Omega_\Lambda = 0.73$.

4.2 Observations

4.2.1 Global Galaxy Properties

We list the basic properties of each galaxy in Table 4.1. We compute co-moving distances from the average velocity of the host galaxy cluster with respect to the cosmic microwave background (CMB). We use heliocentric cluster velocities from Lauer & Postman (1994) and translate them to the CMB rest frame with the NASA/IPAC Extragalactic Database (NED). To compute the V -band luminosity, L_V , for NGC 4889, NGC 3842, and NGC 2832, we adjust the absolute magnitudes from Lauer et al. (2007a); Lauer et al. (2007b) to our assumed distances. For NGC 7768, we adopt the apparent V -band magnitude of 12.40 from the RC3 catalog (de Vaucouleurs et al. 1991) and assume a luminosity distance of 115.8 Mpc.

Galaxies with spatially resolved stellar kinematics are often placed on the $M_\bullet - \sigma$ relation using σ_{eff} , the luminosity-weighted average velocity dispersion out to one effective radius (r_{eff}). Yet when the black hole radius of influence, r_{inf} , subtends a large angle, the conventional measurement of σ_{eff} can include a direct signal from the black hole. In extreme cases, the velocity dispersion only reaches its “average” value at $r < r_{\text{inf}}$ (see, e.g., Gebhardt et al. 2011 for M87). As the $M_\bullet - \sigma$ relation is widely interpreted as an empirical correlation between independent parameters, it is important to remove the black hole’s direct influence on σ_{eff} . For our BCGs, we measure the luminosity-weighted average velocity dispersion for $r_{\text{inf}} \leq r \leq r_{\text{eff}}$:

$$\sigma_{\text{eff}}^2 \equiv \frac{\int_{r_{\text{inf}}}^{r_{\text{eff}}} (\sigma^2 + v_{\text{rad}}^2) I(r) dr}{\int_{r_{\text{inf}}}^{r_{\text{eff}}} I(r) dr}, \quad (4.1)$$

where $I(r)$ is the galaxy’s one-dimensional stellar surface brightness profile.

We compute r_{inf} and σ_{eff} from the integral-field kinematics and black hole masses presented herein; at each radius, we average v_{rad} and σ over all polar angles sampled. Because $r_{\text{inf}} \equiv GM_\bullet \sigma_{\text{eff}}^{-2}$, we compute r_{inf} and σ_{eff} iteratively; the iterations converge quickly in all cases. For NGC 2832, we only have upper limits for M_\bullet and r_{inf} , and we assume $r_{\text{inf}} = 0$. For NGC 4889 and NGC 3842, our upper integration limit is the maximum radius of our kinematic data, which corresponds to $0.4 r_{\text{eff}}$ and $0.8 r_{\text{eff}}$, respectively.

4.2.2 Photometry

We measure the stellar light profiles of each BCG with a combination of R -band ($0.6 \mu\text{m}$) and I -band ($0.8 \mu\text{m}$) photometry. For radii, r , out to $10''$ we adopt high-resolution surface brightness profiles from WFPC2 on the *Hubble Space Telescope* (*HST*) (Laine et al. 2003). At larger radii we use R -band data from Lauer, Postman & Strauss (private communication), obtained with the 2.1-m telescope at Kitt Peak National Observatory (KPNO). The KPNO data have a field-of-view (FOV) of $5.2' \times 5.2'$, which enables accurate sky subtraction. Our ground-based surface brightness profile of each galaxy extends to $115''$. We have combined the individual profiles from WFPC2 and KPNO at overlapping radii between $5''$ and $10''$,

Table 4.1: Global properties of target galaxies

| Galaxy | D (Mpc) | M_V | r_{inf} ($''$) | r_{eff} ($''$) | σ_{eff} (km s^{-1}) | PA_{maj} ($^\circ$) | b/a | i ($^\circ$) | Features |
|----------|--------------|--------|------------------------------|------------------------------|-------------------------------------------------|------------------------------------------|-------|---------------------|-------------------------------|
| (1) | (2) | (3) | (4) | (5) | (6) | (7) | (8) | (9) | (10) |
| NGC 4889 | 103.2 | -23.91 | 1.5 | 54.5 | 347 | 80 | 0.73 | 90 | |
| NGC 3842 | 98.4 | -23.21 | 1.2 | 37.8 | 270 | 5 | 0.86 | 90 | Isophotal twist at $r > 12''$ |
| NGC 7768 | 112.8 | -22.92 | 0.14 | 23.1 | 257 | 60 | 0.75 | 90 | Nuclear dust disk |
| NGC 2832 | 101.9 | -23.87 | < 0.7 | 67.4 | 334 | -21 | 0.68 | 90 | Isophotal twist at $r < 8''$ |

Notes: Column 1: galaxy. Column 2: co-moving distance, derived from cluster systemic velocity with $H_0 = 70 \text{ km s}^{-1} \text{ Mpc}^{-1}$. Column 3: absolute V -band magnitude. Column 4: black hole radius of influence, derived from our best-fit value of M_\bullet and the effective velocity dispersion in column 6. Column 5: effective radius from Lauer et al. (2007b). Column 6: effective velocity dispersion, from luminosity-weighted measurements between r_{inf} and r_{eff} . Column 7: major-axis position angle, measured from north toward east. This angle is used to define the equatorial plane of each galaxy in our stellar orbit models. Column 8: observed axis ratio. Column 9: inclination assumed for stellar orbit models. 90° corresponds to edge-on inclination. Column 10: notable photometric features.

varying the respective weights such that the WFPC2 data contribute 100% to the combined profile at $r = 5''$ and the KPNO data contribute 100% at $r = 10''$. Before stitching the profiles, we translate the WFPC2 profile to R -band using the average $R - I$ color between $5''$ and $10''$. NGC 7768 has a dust disk at $r < 0.5''$ (Grillmair et al. 1994), so we measure the innermost stellar profile with additional H -band ($1.6 \mu\text{m}$) photometry from *HST*/NICMOS (1997; PI Tonry).

We convert surface brightness to stellar luminosity density using the deprojection procedure of Gebhardt et al. (1996). In order to model each galaxy, we must define a symmetry axis. The symmetry axis in three dimensions is projected to the minor axis on the sky, and the model galaxy’s equatorial plane corresponds to the photometric major axis. Isophotal twists are evident in the outer part of NGC 3842 and the inner part of NGC 2832; in each case, we choose the major axis position angle that matches the largest range of radii covered by our kinematic data. The major axis of NGC 4889 is near 80° east of north at all radii. We summarize our photometric measurements of each galaxy in Table 4.1. The major- and minor-axis luminosity density profiles are shown in Figure 4.1.

We use R -band photometry in our stellar orbit models and therefore constrain M_\star/L_R . It is useful to derive M_\star/L_V so we can compare our results with other studies of mass-to-light ratios in early-type galaxies. To convert from R - to V -band, we use galaxy colors from Postman & Lauer (1995) and the Sloan Digital Sky Survey, with filter translations from Blanton & Roweis (2007).

4.2.3 Integral-field Spectroscopy

We measured kinematics in NGC 3842, NGC 4889, NGC 7768, and NGC 2832 using three different integral-field spectrographs (IFSs) to cover two orders of magnitude in radius. Data from GMOS-North (Allington-Smith et al. 2002; Hook et al. 2004) on the 8-m Gemini Observatory North telescope provide the most reliable measurements of the central stellar kinematics in each BCG. Additional observations with OSIRIS (Larkin et al. 2006) and the laser guide star adaptive optics (LGS-AO) system (van Dam et al. 2006; Wizinowich et al. 2006) on the 10-m W. M. Keck II telescope provide higher spatial resolution but substantially worse signal-to-noise. We measured wide-field kinematics with the George and Cynthia Mitchell Spectrograph (formerly VIRUS-P; Hill et al. 2008) on the 2.7-m Harlan J. Smith Telescope at McDonald Observatory. Our spectroscopic observations are summarized in Table 4.2.

4.2.3.1 GMOS

GMOS-N is a multi-purpose spectrograph on Gemini North. We used GMOS in IFS mode, which maps the science field and a simultaneous sky field with hexagonal lenslets. We observed the center of each BCG with the CaT filter, centered near the infrared Ca II triplet. A representative spectrum from each galaxy is shown in Figure 4.2. The GMOS

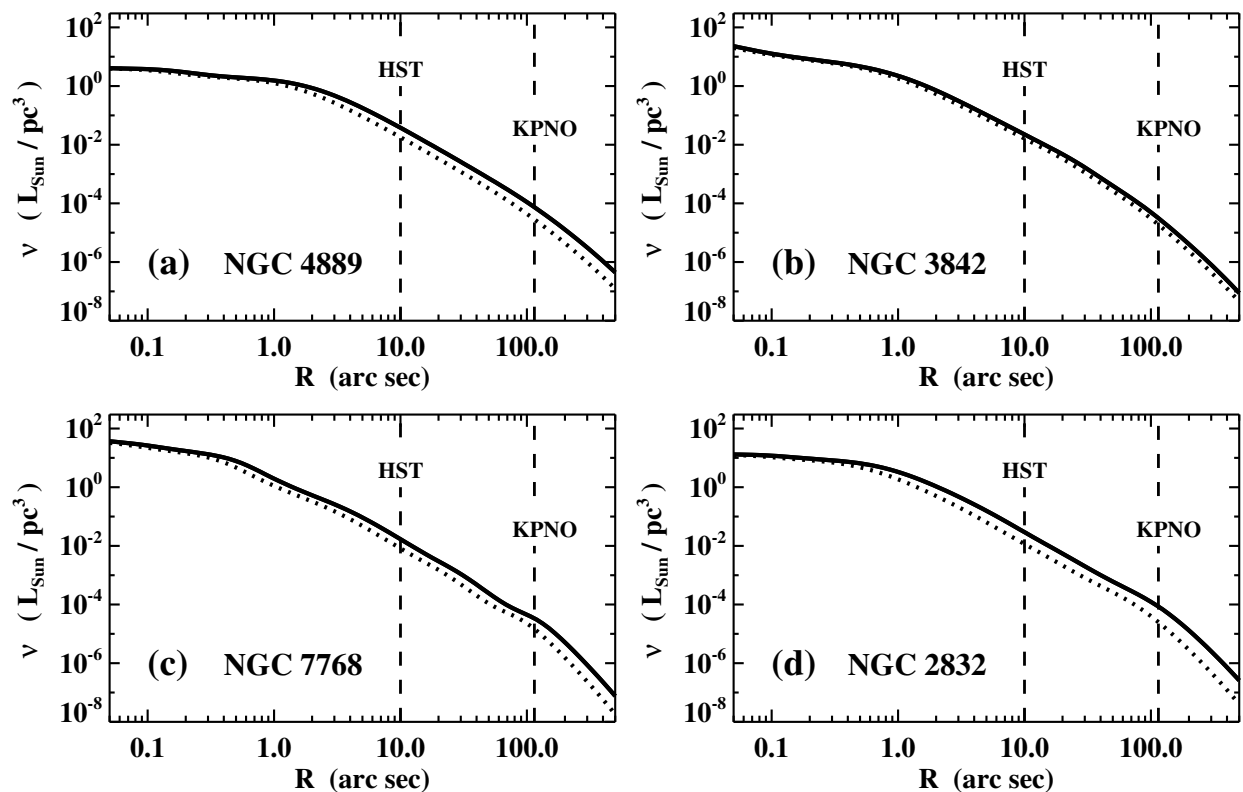


Figure 4.1: De-projected R -band stellar luminosity density versus radius along the major axis (solid line) and minor axis (dotted line) of each galaxy. The dashed vertical lines mark the outermost extents of photometric data from *HST* and KPNO. Luminosity densities beyond $115''$ are derived from a de Vaucouleurs surface brightness profile. (a) NGC 4889. (b) NGC 3842. (c) NGC 7768. (d) NGC 2832.

Table 4.2: Spectroscopic observations

| Galaxy | Instrument | Date | t_{int} (s) | λ Range (nm) | PA ($^{\circ}$) | Δx ($''$) | FWHM ($''$) |
|----------|------------|----------|-------------------------|-------------------------|----------------------|------------------------|------------------|
| (1) | (2) | (3) | (4) | (5) | (6) | (7) | (8) |
| NGC 4889 | OSIRIS | 2008 May | 9×900 | 1473 - 1803 | 135 | 0.05 | |
| NGC 4889 | OSIRIS | 2009 May | 9×900 | 1473 - 1803 | 80 | 0.05 | |
| NGC 4889 | GMOS | 2003 Mar | 5×1200 | 744 - 948 | 90 | 0.2 | 0.4 - 0.7 |
| NGC 3842 | OSIRIS | 2010 May | 9×900 | 1473 - 1803 | 10 | 0.05 | 0.06, 0.19 |
| NGC 3842 | GMOS | 2003 Apr | 5×1200 | 744 - 948 | -30 | 0.2 | 0.4 - 0.7 |
| NGC 3842 | Mitchell | 2011 Mar | 3×1200 | 358 - 588 | 0 | 4.1 | |
| NGC 7768 | OSIRIS | 2010 Sep | 14×900 | 1473-1803 | -125 | 0.05 | 0.04, 0.09 |
| NGC 7768 | Mitchell | 2011 Sep | 13×1200 | 358 - 588 | 0 | 4.1 | |
| NGC 2832 | GMOS | 2003 Mar | 4×1200 | 744 - 948 | 30 | 0.2 | 0.4 - 0.7 |
| NGC 2832 | Mitchell | 2008 Jan | 11×1200 | 354 - 584 | 0 | 4.1 | |
| NGC 2832 | Mitchell | 2008 Feb | 28×1200 | 354 - 584 | 0 | 4.1 | |

Notes: Column 1: galaxy. Column 2: instrument. OSIRIS (OH-Suppressing Infra-Red Imaging Spectrograph) was used on Keck II with LGS-AO. GMOS (Gemini Multi-Object Spectrograph) was used on Gemini North. The Mitchell Spectrograph was used on the McDonald Observatory 2.7-m telescope. Column 3: observing dates. Column 4: number of science exposures \times integration time per exposure. Column 5: observed wavelength range. Column 6: position angle of the long axis for OSIRIS and GMOS, measured from north toward east. Column 7: angular size of lenslets or fibers. Column 8: PSF FWHM at science wavelengths. For OSIRIS observations of NGC 3842 and NGC 7768, we list the FWHM values of the inner and outer PSF components.

data were reduced using version 1.4 of the Gemini IRAF software package¹.

GMOS is seeing-limited, with a lenslet scale of $0.2''$. We measure full widths at half-maximum (FWHM) of $0.4 - 0.7''$ for point sources in acquisition frames from the GMOS imager. For all stellar orbit models discussed below, we have assumed seeing of $0.4''$ FWHM for GMOS data. In a preliminary trial with NGC 3842, we obtained consistent values of M_{\bullet} and M_{\star}/L from stellar orbit models assuming $0.4''$ and $0.7''$ seeing.

4.2.3.2 OSIRIS

OSIRIS is a near-infrared (NIR), IFS built for use with the Keck AO system. We observed each BCG with the $0.05''$ lenslet scale and broad H -band filter, which covers several metal absorption lines and CO and OH vibrational bandheads at observed wavelengths of $1.47\text{-}1.80\ \mu\text{m}$. Figure 4.3 shows representative OSIRIS spectra. OSIRIS has no sky lenslets, and extended objects such as BCGs cover the entire science field. We observed each BCG with a repeated “object-sky-object,” dither sequence, such that every 900-s science frame was immediately preceded or followed by a 900-s sky frame. We observed kinematic template stars using the same filter and lenslet scale as the BCGs. Spatial variations in instrumental resolution are negligible relative to the velocity broadening in BCGs.

We used version 2.3 of the OSIRIS data reduction pipeline² to perform sky subtraction, spatial flat-fielding, spectral extraction, wavelength calibration, and spatial mosaicking of three-dimensional data cubes. We used custom routines to remove bad pixels and cosmic rays from 900-s exposures and to calibrate for telluric absorption. We estimated the AO point-spread function (PSF) by observing the LGS-AO tip/tilt star with the OSIRIS Imager. For NGC 3842 and NGC 4889, we typically measured the PSF once per half-night. For NGC 7768 we measured the PSF four times over an observing span of eight hours. The weighted average PSF for NGC 7768 has a Strehl ratio of 22% and is well-fit by an inner component with $0.04''$ FWHM and an outer component with $0.09''$ FWHM. In a similar investigation of the BCG NGC 6086, McConnell et al. (2011a) varied the AO PSF and obtained a systematic error of only $\sim 10\%$ in the final measurement of M_{\bullet} . In their investigation of M87, Gebhardt et al. (2011) measured similar values of M_{\bullet} for PSFs with different Strehl ratios.

OSIRIS data for NGC 4889 and NGC 3842 have lower quality than we initially expected. Even spectra with relatively high signal-to-noise (S/N) yield unconvincing kinematic measurements. One severe noise source is telluric OH emission, which varies faster than the 900-s exposure time and leaves large residuals even after subtracting sky frames. Although we mask the narrow residual features when measuring stellar kinematics, the missing spectral channels conceal information about the overall shapes of absorption features. Further difficulties arise from defining a continuum level among the blend of metallic and molecular absorption features in H -band. Finally, OSIRIS suffered from elevated detector temperatures throughout 2009, including the bulk of our observations of NGC 4889. Data from this

¹available from Gemini Observatory, at <http://www.gemini.edu/sciops/data-and-results/processing-software>

²available from the UCLA Infrared Laboratory, at <http://irlab.astro.ucla.edu/osiris/pipeline.html>

period exhibit increased dark noise and possible errors in spectral extraction and wavelength calibration.

Our OSIRIS data for NGC 4889 do not have sufficient quality to include in stellar orbit models. We have run stellar orbit models of NGC 3842 with and without OSIRIS data; we compare results from these models in Section 4.5.2. OSIRIS data were included in all models of NGC 7768.

4.2.3.3 Mitchell Spectrograph

The Mitchell Spectrograph, formerly named VIRUS-P, is an optical IFS on the 2.7-m telescope at McDonald Observatory. It features 246 fibers spaced evenly across a $107'' \times 107''$ field of view, with a one-third filling factor. Each fiber has a diameter of $4.1''$; this is the limiting factor in spatial resolution, rather than optical seeing.

We observed each galaxy with the low-resolution grism, which provides wavelength coverage of $\approx 360\text{-}580$ nm, including the Ca H + K region, the *G*-band region, $H\beta$, the Mg *b* region, and several Fe absorption features. The spectral resolution varies over different fibers and also with wavelength. Our observations using the low-resolution grism span instrumental resolution values of $\approx 0.45 - 0.65$ nm FWHM, with a corresponding range of $\sigma \sim 100 - 170$ km s $^{-1}$. This is sufficient to resolve the velocity profiles of BCGs ($\sigma \sim 250 - 350$ km s $^{-1}$). Because we employed the Mitchell Spectrograph for wide-field coverage rather than fine spatial resolution, we did not perform any sub-dithers to fill the gaps between fibers.

We used the Vaccine data reduction pipeline to perform bias subtraction and flat-fielding, compute the wavelength solution for each fiber, extract a spectrum for each fiber, model and subtract the sky spectrum, and reject cosmic rays. Detailed descriptions of the data reduction procedures can be found in Adams et al. (2011) and Murphy et al. (2011).

The maximum radius at which Mitchell Spectrograph data can yield robust kinematic measurements depends on the surface brightness profile of the galaxy, the background sky conditions, and the overall integration time at a given pointing. For each galaxy, we have binned numerous fibers at large radii and preserved data for which a good kinematic fit was recoverable for at least one binning scheme. Following this procedure, our outermost bins for kinematic extraction cover radii of $24.5 - 35.3''$ for NGC 3842, $18.3 - 28.5''$ for NGC 7768, and $70 - 101''$ for NGC 2832. Sample spectra from the central and outer regions of each galaxy are shown in Figure 4.4.

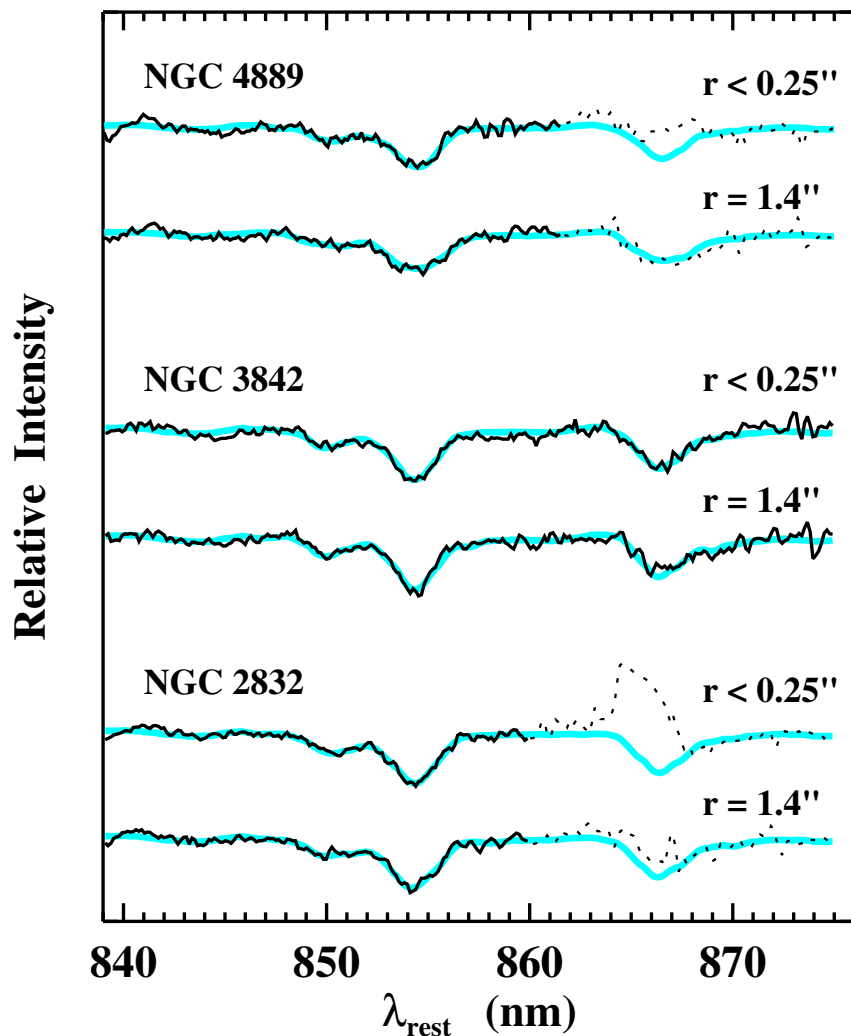


Figure 4.2: Example spectra of the calcium triplet region from the GMOS IFS. For each galaxy, the central spectrum ($r < 0.25''$) is displayed, as well as spectrum near the major axis, corresponding to an inner radius of $1.1''$ and an outer radius of $1.7''$. The major-axis spectra correspond to the east side of NGC 4889, the north side of NGC 3842, and the north side of NGC 2832. The thick cyan line for each spectrum represents the best-fitting, LOSVD-convolved stellar template. Dotted lines indicate spectral channels that were masked during fitting. Each spectrum was continuum-divided before fitting and plotting.

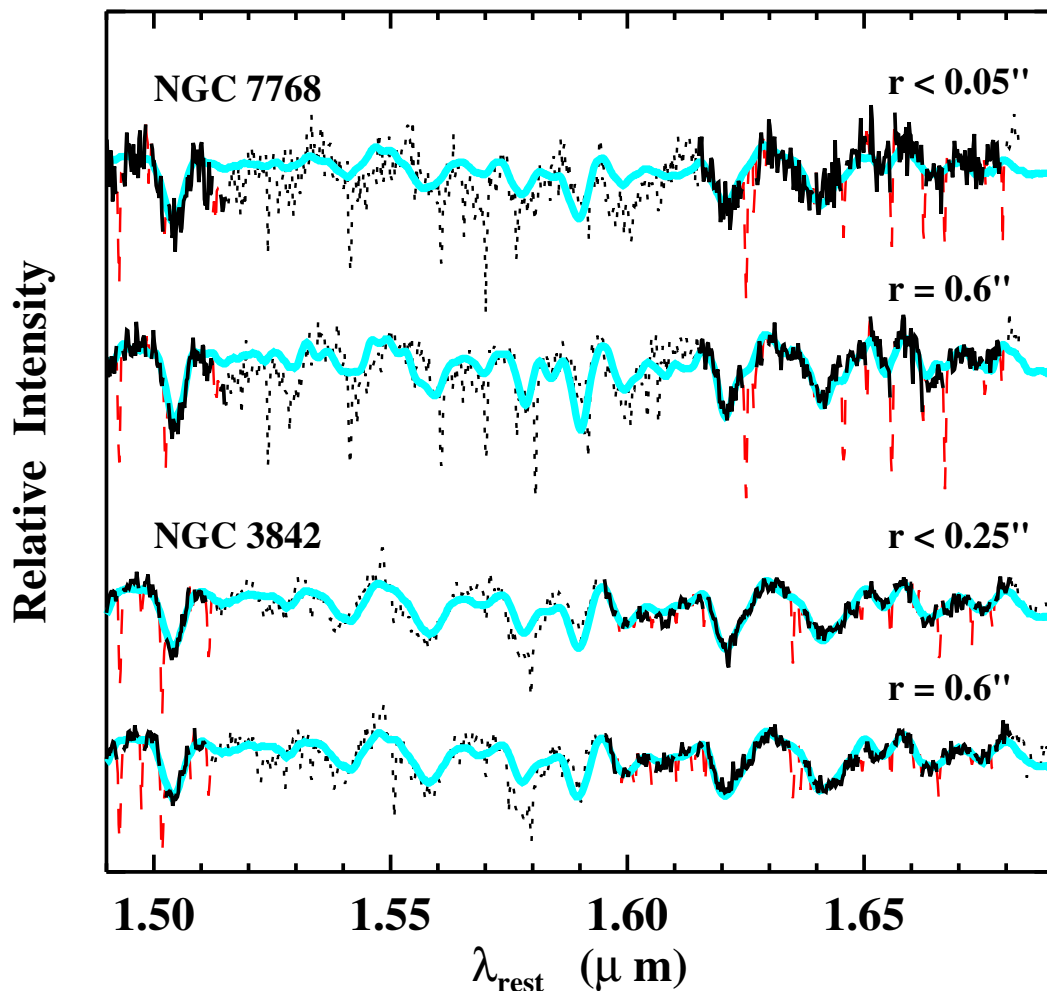


Figure 4.3: Example H -band spectra from OSIRIS. The central spectrum for NGC 7768 covers $0.1'' \times 0.1''$. The central spectrum for NGC 3842 corresponds to $r < 0.25''$. We also display an off-center spectrum for each galaxy; the corresponding spatial region is near the major axis, with an inner radius of $0.4''$ and an outer radius of $0.7''$. The major-axis spectra correspond to the east side of NGC 7768 and the north side of NGC 3842. The thick cyan line for each spectrum represents the best-fitting, LOSVD-convolved stellar template. Dotted lines indicate spectral channels that were masked during fitting, and dashed red lines indicate residual features from telluric OH, which were also masked. Each spectrum was continuum-divided before fitting and plotting. OSIRIS spectra for NGC 4889 were compromised by warm detector temperatures in 2009.

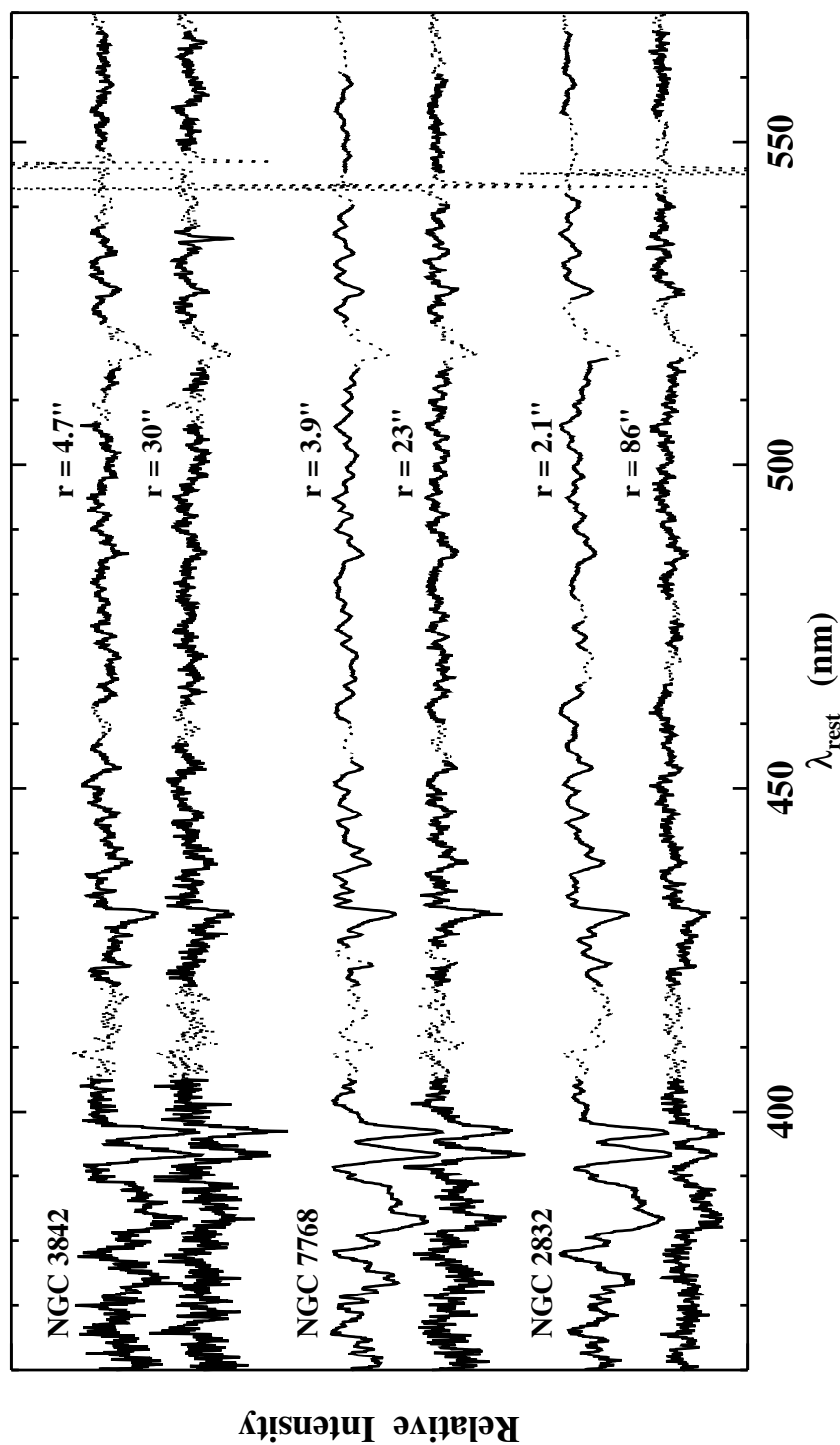


Figure 4.4: Example spectra from the Mitchell Spectrograph. For each galaxy, we display spectra corresponding to the smallest and largest radii where we employ Mitchell Spectrograph data in our stellar orbit models. The corresponding bins span $3.8 - 5.6''$ and $24.5 - 35.3''$ for NGC 3842, $3.0 - 4.8''$ and $18.3 - 28.5''$ for NGC 7768, and $1.7 - 2.5''$ and $70 - 101''$ for NGC 2832. Dotted lines indicate spectral channels that were masked during fitting. Each spectrum was continuum-divided before fitting and plotting.

4.3 Extracting Stellar Kinematics

Our dynamical models fit weighted and superposed stellar orbits to line-of-sight velocity distributions (LOSVDs) extracted from spectroscopic data. We extract LOSVDs with a Maximum Penalized Likelihood (MPL) technique, which fits an LOSVD-convolved stellar template to each galaxy spectrum. The LOSVDs are non-parametric, defined at 15 radial velocity bins in our orbit models. The MPL fitting method is described in detail in Gebhardt et al. (2000b), Pinkney et al. (2003), and Nowak et al. (2008), and adaptations for integral field data of BCGs are described in McConnell et al. (2011a).

In order to attain sufficient signal-to-noise (S/N) for effective kinematic extraction, we perform spatial binning on each data set. For GMOS data of NGC 4889, NGC 3842 and NGC 2832, our central bin combines seven hexagonal lenslets; the corresponding bin diameter is $0.55''$. For OSIRIS data of NGC 7768, we combine four square lenslets to obtain a central bin of $0.1'' \times 0.1''$. At large radii (typically $r > 15''$) we combine Mitchell Spectrograph data from multiple angular bins.

A spectral binning factor is necessary to smooth over channel-to-channel noise in some spectra. We typically use smoothing factors of 2 spectral pixels for GMOS data and 8-10 spectral pixels for OSIRIS data. Lower smoothing factors yield jagged LOSVDs. Mitchell Spectrograph spectra do not require smoothing.

The near-infrared Ca II triplet has a clearly defined continuum and yields robust kinematic measurements across a broad range of stellar templates (Dressler 1984; Barth et al. 2002). Therefore, we fit GMOS spectra with a single G9III template star. In spectra of NGC 4889 and NGC 2832, the 866 nm calcium line is contaminated by a detector artifact and is not included in our fits (see Fig. 4.2). The 850 nm and 854 nm lines are included in all fits.

For OSIRIS spectra, we optimize our LOSVD extraction by carefully choosing a subset of the many absorption features in H -band. Although we are able to perform a global equivalent width adjustment before fitting stellar templates, some of the individual metal lines exhibit further mismatch between the galaxy and template equivalent widths. Some molecular features are blended with the suspect metal lines, and others are compromised by residuals from telluric OH subtraction. The consistently reliable features for kinematic extraction are the $\nu = 3-6$, $\nu = 4-7$, and $\nu = 5-8$ bandheads of ^{12}CO , spanning the sub-region from 1.61 to 1.68 μm rest, and the Mg I absorption feature near 1.504 μm rest (see Fig. 4.3). We fit OSIRIS spectra using a set of nine template stars with spectral types from G8 to M4. Template weights are allowed to vary freely and are fit simultaneously with the LOSVD.

Mitchell Spectrograph spectra contain a multitude of absorption features, which are dominated by different stellar types and require different equivalent width adjustments. Following the procedure of Murphy et al. (2011), we divide each spectrum into five spectral sub-regions and extract LOSVDs independently for each sub-region. Our fits use a set of 16 template stars selected from the Indo-US library (Valdes et al. 2004), with spectral types from B9 to M3. We compute the instrumental resolution as a function of wavelength in each fiber and convolve the template spectra with an appropriately weighted instrumental resolution profile for each galaxy spectrum. After fitting each galaxy spectrum, we discard

sub-regions with visually unconvincing fits or severely asymmetric LOSVDs. The LOSVDs from the remaining sub-regions are averaged to produce a final representative LOSVD.

We perform Monte-Carlo trials to determine the uncertainties in the best-fit LOSVDs. In each trial, random noise is scaled to the root-mean-squared residual of the original fit and added to the galaxy spectrum before re-fitting. In each bin of the LOSVD, uncertainties are computed from the distribution of trial values. Our fitting method sometimes yields LOSVDs with noise at large positive or negative velocities. Consequently, we force our uncertainties to extend to zero power in the LOSVD wings. For Mitchell Spectrograph LOSVDs, we adopt the average uncertainty from the individual spectral sub-regions, or if greater, the $1\text{-}\sigma$ scatter in the sub-regions' LOSVD values.

4.4 Two-Dimensional Kinematics

For each galaxy, we fit a fourth-order Gauss-Hermite polynomial to each non-parametric LOSVD in order to illustrate the stellar kinematics. Below we highlight spatial trends in the Gauss-Hermite moments v_{rad} , σ , h_3 , and h_4 . To measure the Gauss-Hermite moments, the LOSVD is fit with a function $f(v)$, defined by

$$f(v) \propto \frac{1}{\sqrt{2\pi\sigma^2}} e^{-(v-v_{\text{rad}})^2/\sigma^2} \times \left[1 + h_3 H_3 \left(\frac{v - v_{\text{rad}}}{\sigma} \right) + h_4 H_4 \left(\frac{v - v_{\text{rad}}}{\sigma} \right) \right], \quad (4.2)$$

where $H_3(x) = \frac{1}{\sqrt{3}}(2x^3 - 3x)$ and $H_4(x) = \frac{1}{\sqrt{24}}(4x^4 - 12x^2 + 3)$.

4.4.1 NGC 4889

Figure 4.5 shows two-dimensional maps of v_{rad} , σ , h_3 , and h_4 , from GMOS observations of NGC 4889. Figure 4.5 also includes radial profiles of each moment in NGC 4889. The radial profiles include our GMOS data and measurements from Loubser et al. (2008), recorded with the long-slit spectrograph ISIS at the William Herschel Telescope (WHT).

The kinematic moments in NGC 4889 show several asymmetries with respect to the major and the minor axis. Asymmetries in the line-of-sight velocity dispersion, σ , likely present the greatest difficulties for accurately measuring M_{\bullet} . On the east side of the galaxy, σ peaks at $413 \pm 22 \text{ km s}^{-1}$ near the major axis and remains above 400 km s^{-1} through an extended region in the southeast quadrant. On the west side, σ exceeds 385 km s^{-1} in only a single spatial bin, reaching $406 \pm 18 \text{ km s}^{-1}$ at $0.6''$ toward the northwest. At the very center of NGC 4889, we measure $\sigma = 344 \pm 16 \text{ km s}^{-1}$. A strong deficit of radial orbits can produce the central drop in line-of-sight velocity dispersion even in the presence of a supermassive black hole; this is further discussed in Section 4.5.3. Central decreases in velocity dispersion

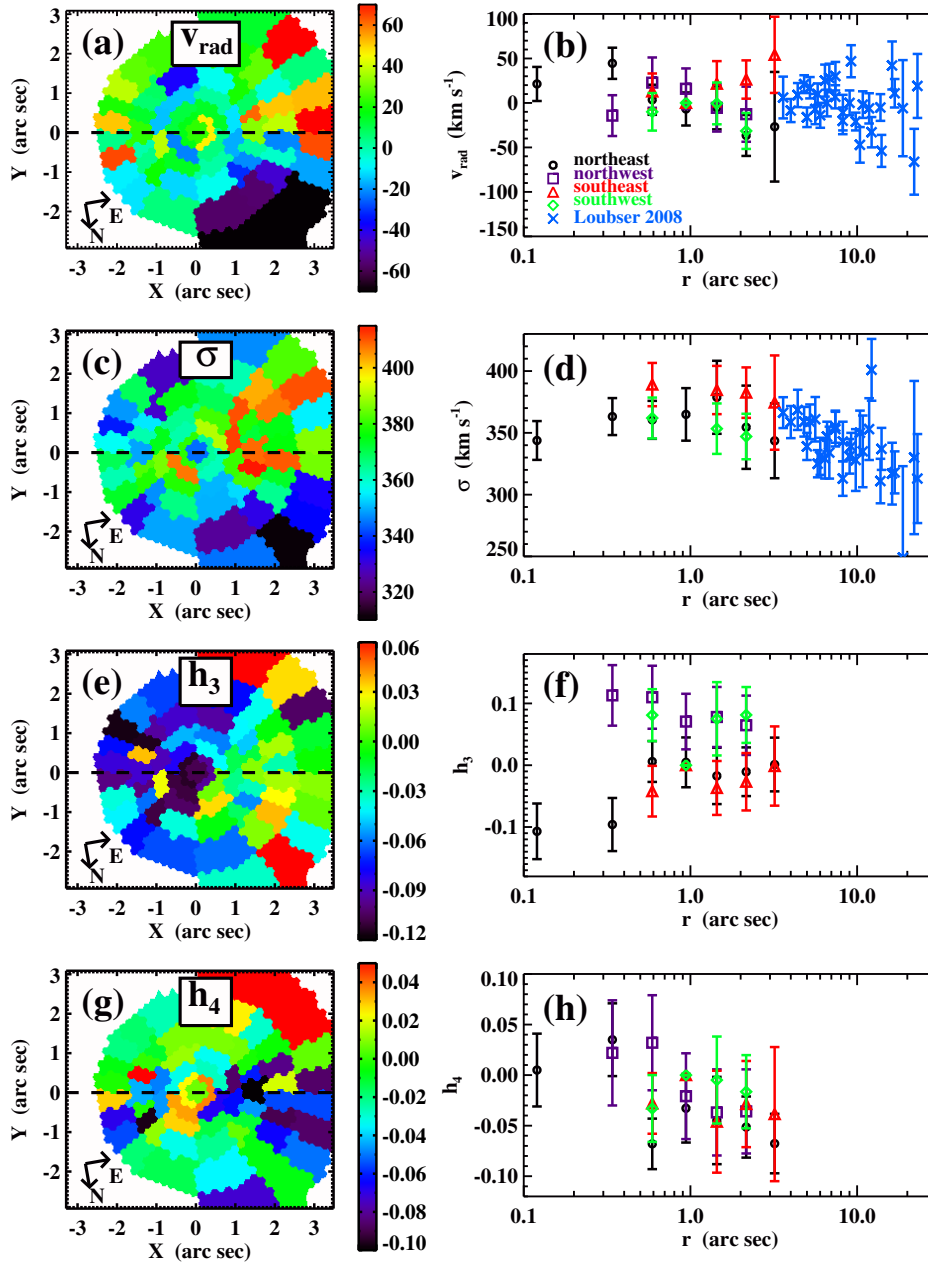


Figure 4.5: Stellar kinematics in NGC 4889. Panels (a), (c), (e), and (g) are two-dimensional maps from GMOS IFS data. The horizontal dashed line represents the photometric major axis. Panels (b), (d), (f), and (h) show kinematic moments as a function of radius, after averaging kinematic moments from different polar angles in each quadrant of NGC 4889. Panels (b) and (d) also include major-axis kinematic moments from Loubser et al. (2008). For the one-dimensional plots, the values of v_{rad} and h_3 have been inverted on the west side of the galaxy. (a) and (b): radial velocity. (c) and (d): line-of-sight velocity dispersion. (e) and (f): Gauss-Hermite moment h_3 . (g) and (h): Gauss-Hermite moment h_4 .

have been observed in several other early-type galaxies (e.g., van der Marel 1994; Pinkney et al. 2003; Houghton et al. 2006; Gebhardt et al. 2007; Nowak et al. 2008).

The h_4 moment, which describes whether an LOSVD is boxy ($h_4 < 0$) or peaky ($h_4 > 0$), varies with radius and polar angle in NGC 4889. At radii from $0.7''$ to $3.5''$, h_4 is negative near the major axis and nearly zero toward the minor axis. We have fit and subtracted a Gaussian profile from each non-parametric LOSVD and have examined the residual velocity profiles. In most of the spatial bins near the major axis, the residual profiles contain peaks near $\pm 450 \text{ km s}^{-1}$, as exemplified in Figure 4.6. An LOSVD sub-component with velocity peaks near $\pm 450 \text{ km s}^{-1}$ could correspond to a torus or thick ring of stars, including rotating and counter-rotating populations. In an eccentric ring, σ would exhibit a local maximum near periapsis.

To further investigate the hypothesis that NGC 4889 hosts a central stellar torus, we have carefully examined the inner light profile of the galaxy. We have determined a best-fit surface brightness profile by fitting concentric ellipses to a reduced and de-convolved image from *HST*/WFPC2, as in Laine et al. (2003). Subtracting the best-fit ellipses yields a two-dimensional residual image of NGC 4889, displayed in Figure 4.7. The residual image shows two peaks along the major axis, which straddle the galaxy center and contain approximately 1% of the total light at their corresponding positions. These peaks resemble a diffuse torus of stars in the equatorial plane of the galaxy, spanning radii from $1''$ to $2''$. On the east side of NGC 4889, the residual photometric peak overlaps with the velocity dispersion peak but does not extend to match the extended pattern of high σ in the southeast quadrant. Boxy LOSVDs overlap with both residual photometric peaks but also extend to radii beyond $2''$. Although NGC 4889 could host a stellar torus with a double-peaked velocity profile, the torus would only contribute $\sim 1\%$ of the total signal in the corresponding LOSVDs, too little to be fully responsible for the LOSVDs' non-Gaussianity.

The double-peaked feature in our residual image of NGC 4889 appears to be qualitatively similar to the central structure seen in a number of high-luminosity galaxies, such as NGC 4073, NGC 6876, and the BCGs NGC 910, IC 1733, and IC 4329 (Lauer et al. 2002, 2005). In these galaxies the surface brightness profile actually has a local minimum at the center. Lauer et al. (2002) have argued that such an appearance could be due to the addition of a diffuse torus to the cores of the galaxies, or could alternatively be evidence for the evacuation of stars from the center by a merging pair of supermassive black holes bound in a tight binary. In the case of NGC 4889, the torus is not strong enough to create an apparent surface brightness minimum at the center of the galaxy, and would thus be a weaker example of the phenomenon seen in the Lauer et al. (2002, 2005) galaxies. The radius of the torus in NGC 4889 is $\sim r_{\text{inf}}$. In simulations by Zier & Biermann (2001), a black hole binary with initial separation r_{inf} scours a torus of radius $\sim 3 r_{\text{inf}}$ on a timescale comparable to the hardening and coalescence of the binary.

Alternative scenarios for asymmetric kinematics include an ongoing minor merger, a surviving nucleus from a cannibalized satellite galaxy, or a chance alignment with a foreground satellite. However, none of these scenarios are consistent with the highly regular photometric contours in NGC 4889: even the 1% deviations from perfect ellipses are dis-

tributed symmetrically about the galaxy center. Another post-merger scenario is a black hole displaced from the center by gravitational wave recoil. Simulations of merger remnants with recoiling black holes suggest that even with a modest recoil velocity, a black hole can maintain an observable displacement in a gas-poor galaxy (e.g., Blecha et al. 2011; Guedes et al. 2011; Sijacki et al. 2011), and damping could be particularly weak with a shallow stellar mass profile like the core of NGC 4889. However, if a recoiling black hole affected a sufficient number of stars to displace the galaxy’s velocity dispersion peak, we would expect to observe a similarly prominent photometric disturbance, or even a cusp of stars surrounding the black hole.

Although we do not find an obvious explanation for our asymmetric velocity dispersion measurements in NGC 4889, we suggest that they arise from an asymmetric orbital structure within a largely symmetric spatial distribution of stars. In Section 4.5.3, we illustrate how tangential orbital bias in the vicinity of the black hole can produce a central minimum in the

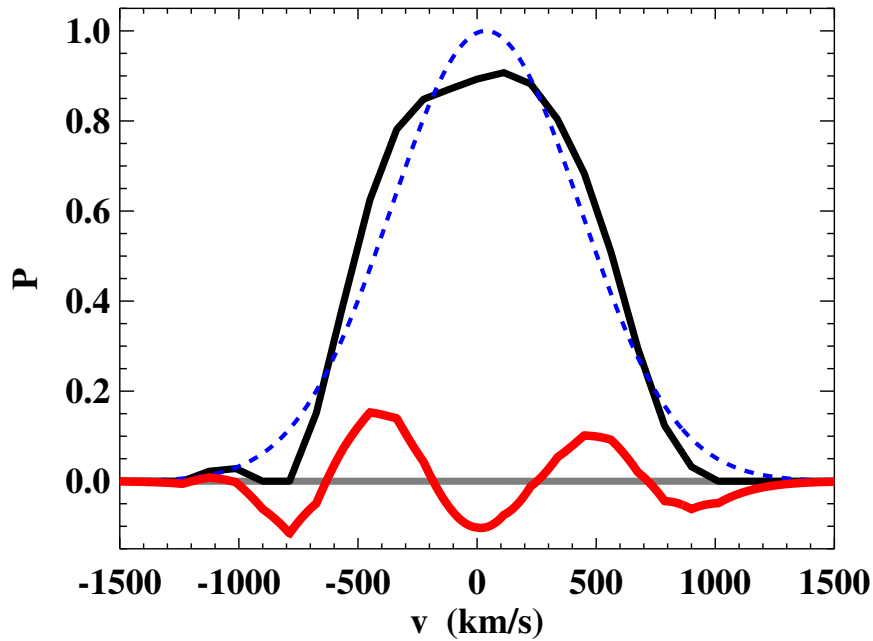


Figure 4.6: LOSVD near the velocity dispersion peak in NGC 4889, corresponding to a radius of $1.4''$ (700 pc) along the east side of the major axis. The solid black line is the non-parametric LOSVD, and the dashed blue line is the best-fit Gaussian profile. The thick red line represents the residual velocity profile after the Gaussian profile is subtracted. The residual profile includes tangential orbits centered near $\pm 450 \text{ km s}^{-1}$. Negative features in the residual profile represent an under-abundance of stars at the corresponding line-of-sight velocities.

line-of-sight velocity dispersion. A stellar torus is consistent with excess tangential orbits as well as our photometric data. However, a circular or slightly eccentric torus of stars cannot fully explain the velocity dispersion features in the southeast and northwest quadrants of NGC 4889 (see Fig. 4.5c).

4.4.2 NGC 3842

Figure 4.8 shows two-dimensional maps of the kinematic moments in NGC 3842, as measured by GMOS, as well as radial profiles of each moment as measured by GMOS and the Mitchell Spectrograph. NGC 3842 exhibits the simplest kinematics of the four BCGs. There is negligible rotation, and σ increases virtually monotonically toward the center. The maps of h_3 and h_4 are largely featureless, and h_4 is slightly negative on average. The four quadrants of NGC 3842 are similar enough to average their kinematics and model a single set of LOSVDs. The kinematics from the Mitchell Spectrograph are consistent with a

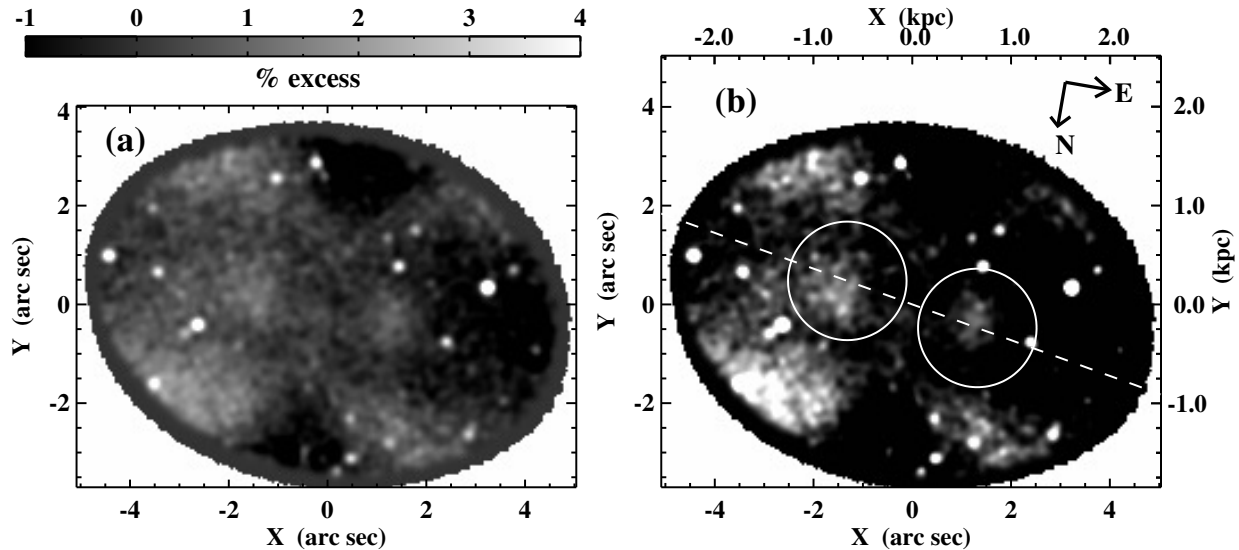


Figure 4.7: (a) Residual image of NGC 4889, after fitting elliptical isophotes to a deconvolved image from *HST*/WFPC2 (F606W). (b) Same image, with contrast adjusted to highlight the $\sim 1\%$ excess light from a possible stellar torus. The dashed white line indicates the major axis of NGC 4889. The white circles are each centered on the major axis $1.4''$ from the galaxy center. Each circle has a radius of $1.2''$. The compact bright spots in both panels are globular clusters.

continuation of the trends observed at small radii with GMOS.

4.4.3 NGC 7768

Figure 4.9 shows two-dimensional maps of the kinematic moments from OSIRIS observations of NGC 7768, and radial profiles of each moment from OSIRIS and the Mitchell Spectrograph. Unlike most BCGs, NGC 7768 exhibits a strong rotation curve along the major axis, with $|v_{\text{rad}}| \sim 100 \text{ km s}^{-1}$ at radii beyond $0.2''$. We measure $\sigma = 322 \pm 32 \text{ km s}^{-1}$ in our central OSIRIS bin, outside of which σ drops suddenly and remains near $230\text{-}260 \text{ km s}^{-1}$ over the full extent of our radial coverage. We measure h_3 to be anti-correlated with v_{rad} , particularly for OSIRIS data. This anti-correlation is common in rotating early-type galaxies (e.g., Bender et al. 1994; Krajnović et al. 2011). OSIRIS and the Mitchell Spectrograph both measure boxy LOSVDs ($h_4 < 0$).

Loubser et al. (2008) observed NGC 7768 with ISIS on WHT, measuring major-axis kinematics out to $11.4''$. At radii of $0.1\text{-}1''$, we measure a steeper radial velocity gradient and lower velocity dispersion values with OSIRIS. The differences between our measurements and those of Loubser et al. (2008) are reconciled by considering the respective spatial resolutions of the OSIRIS and WHT observations: whereas OSIRIS is nearly diffraction-limited, Loubser et al. (2008) reported $1''$ seeing at WHT. Although the poorly resolved velocity gradient artificially increases the WHT velocity dispersion measurements, the quadratic sum $v_{\text{rad}}^2 + \sigma^2$ is consistent for OSIRIS and WHT data. Only OSIRIS detects the central rise to $\sigma > 300 \text{ km s}^{-1}$.

Similarly, we attribute the low value of v_{rad} in our innermost Mitchell Spectrograph bin (Figure 4.9b) to an overlap between the corresponding fiber and the central velocity dispersion gradient. We have included this data point in stellar orbit models of NGC 7768, along with five measurements from Loubser et al. (2008) at radii between $1''$ and $3''$. This combination of data is illustrated in the radial plots in Figure 4.9. In a separate trial, we replaced the innermost LOSVD from the Mitchell Spectrograph with three additional measurements from Loubser et al. (2008), covering radii of $3.0\text{-}5.1''$. All trials yielded consistent values of M_{\bullet} and M_{\star}/L_R .

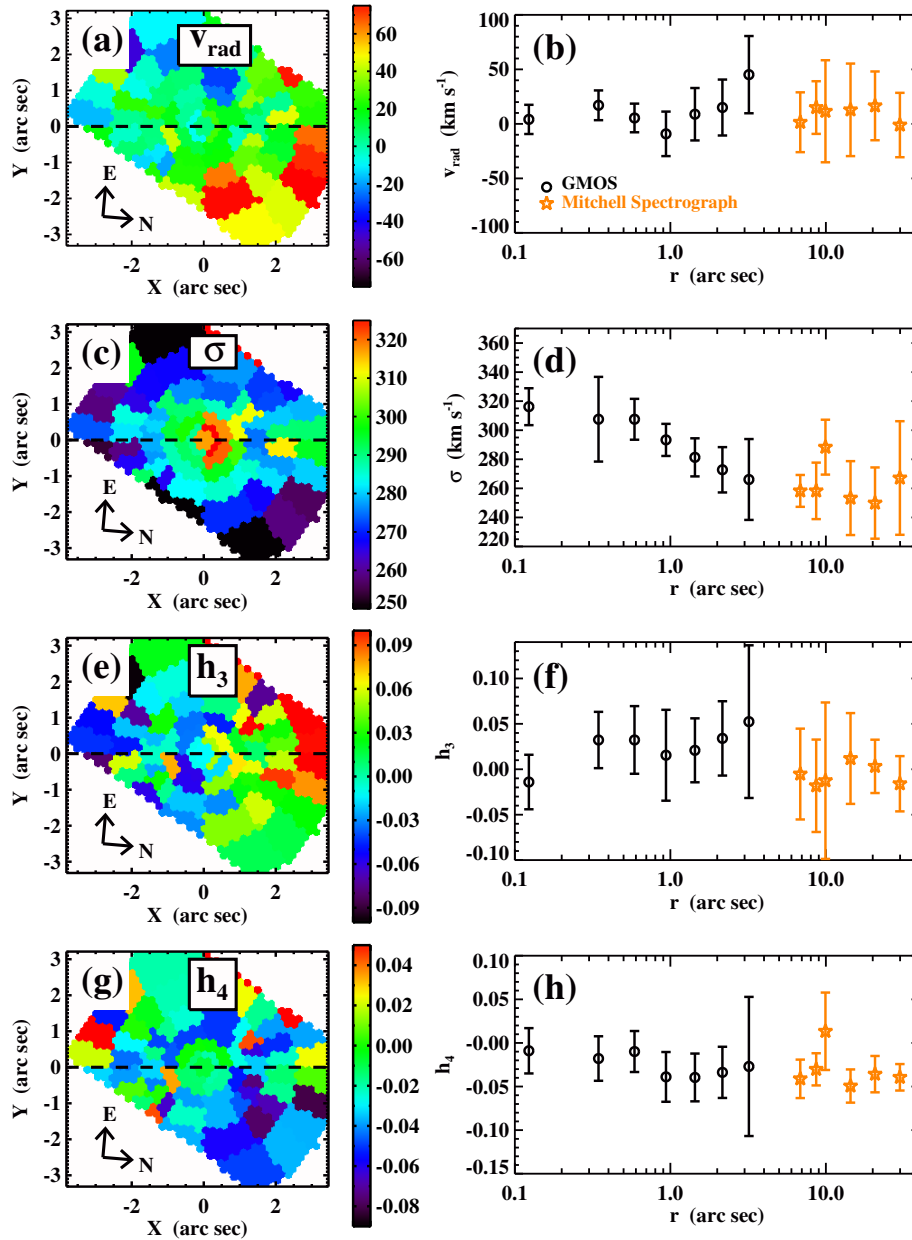


Figure 4.8: Stellar kinematics in NGC 3842. Panels (a), (c), (e), and (g) are two-dimensional maps from GMOS IFS data. The horizontal dashed line represents the photometric major axis. Panels (b), (d), (f), and (h) are radial plots, including GMOS and Mitchell Spectrograph data. In order to construct the radial plots, the kinematic moments from different quadrants and polar angles have been averaged, after inverting the values of v_{rad} and h_3 in the southeast and southwest quadrants. (a) and (b): radial velocity. (c) and (d): line-of-sight velocity dispersion. (e) and (f): Gauss-Hermite moment h_3 . (g) and (h): Gauss-Hermite moment h_4 .

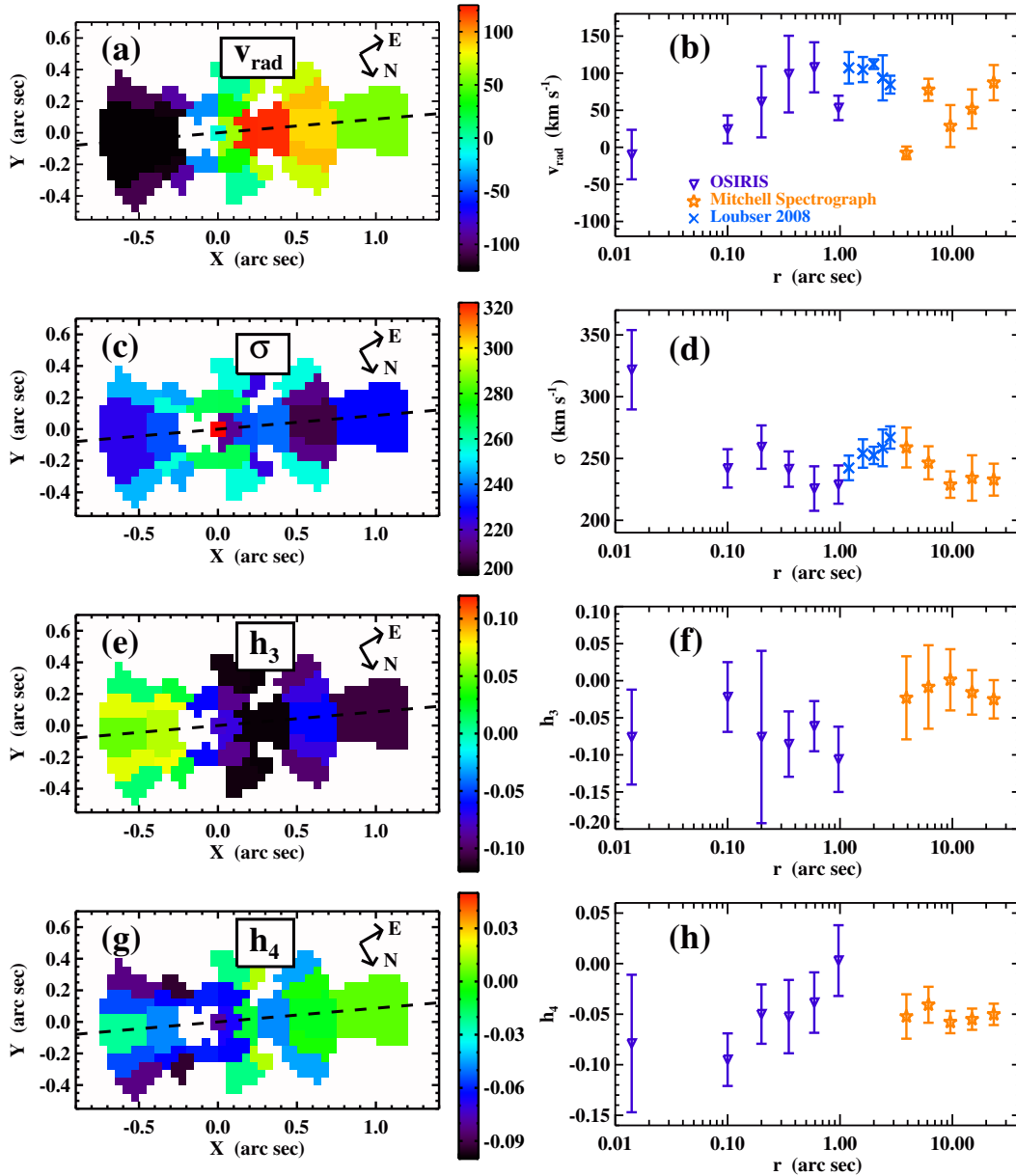


Figure 4.9: Stellar kinematics in NGC 7768. Panels (a), (c), (e), and (g) are two-dimensional maps from OSIRIS IFS data. The horizontal dashed line represents the photometric major axis. Panels (b), (d), (f), and (h) are radial plots, including OSIRIS and Mitchell Spectrograph data, plus long-slit data from Loubser et al. (2008) at radii from $1''$ to $3''$. In order to construct the radial plots, the kinematic moments from different hemispheres and polar angles have been averaged, after inverting the values of v_{rad} and h_3 on the west side of the galaxy. (a) and (b): radial velocity. (c) and (d): line-of-sight velocity dispersion. (e) and (f): Gauss-Hermite moment h_3 . (g) and (h): Gauss-Hermite moment h_4 .

4.4.4 NGC 2832

Figure 4.10 shows two-dimensional maps of the kinematic moments from GMOS observations of NGC 2832, as well as radial profiles from GMOS and the Mitchell Spectrograph. Unlike NGC 4889 and NGC 3842, which exhibit either a central or off-center local maximum in σ , our velocity dispersion map of NGC 2832 is nearly featureless, with values near 360 km s^{-1} out to $r \approx 3''$. GMOS IFS data for NGC 2832 show some evidence of rotation from north to south, although this signal is strangely absent on the east side of the galaxy. There is a similar discrepancy in our measurements of h_3 : we measure $h_3 < 0$ on the east side and $h_3 > 0$ on the west side.

Loubser et al. (2008) observed NGC 2832 with GMOS in long-slit mode, with the slit oriented 67° from the galaxy’s major axis. They detected a kinematically decoupled core, characterized by rotation out to approximately $4''$ along the slit axis. Our measurements of v_{rad} agree with the long-slit data on the west side of the galaxy, but do not follow the same trend on the east side. IFS and long-slit measurements both detect a flat velocity dispersion profile for $r \leq 3''$, with similar average values of σ . We measure significantly lower velocity dispersions with the Mitchell Spectrograph, in the range $\sim 260 - 320 \text{ km s}^{-1}$.

The majority of our Mitchell Spectrograph measurements are at $r \geq 7''$ and do not overlap with the GMOS IFS field of view. We use the long-slit data from Loubser et al. (2008) to help bridge the apparent gap between the GMOS and Mitchell Spectrograph IFS data. For radii between $4''$ and $7''$ we have averaged multiple long-slit data points from Loubser et al. (2008) and produced three LOSVDs, which we include in our stellar orbit models of NGC 2832. The corresponding values of v_{rad} and σ are included in Figures 4.10b and 4.10d.

Although measurements by Loubser et al. (2008) indicate that σ may indeed fall from $\sim 360 \text{ km s}^{-1}$ near the center of NGC 2832 to $\sim 280 \text{ km s}^{-1}$ at $r \sim 10''$, additional discrepancies point to possible systematic errors in our kinematics from GMOS and/or the Mitchell Spectrograph. Our LOSVDs from GMOS are peaky ($h_4 > 0$), whereas our LOSVDs from the Mitchell Spectrograph are boxy ($h_4 < 0$). Furthermore, the two Mitchell Spectrograph fibers nearest the galaxy center yield significantly lower velocity dispersions than GMOS IFS or long-slit data at overlapping radii. For all galaxies, we exclude the innermost Mitchell Spectrograph data from our models, so as not to dilute the more highly resolved GMOS data.

Stellar template mismatch or errant treatment of the galaxy and stellar template spectra can bias both σ and h_4 , (e.g., Rix & White 1992; van der Marel & Franx 1993; Carter et al. 1999; Emsellem et al. 2004). Although we have attempted to treat GMOS IFS and Mitchell Spectrograph data consistently for each of the three BCGs, NGC 2832 exhibits a particularly large number of internal inconsistencies. This is considered in our final assessment of stellar orbit models for NGC 2832 (Section 4.5.2).

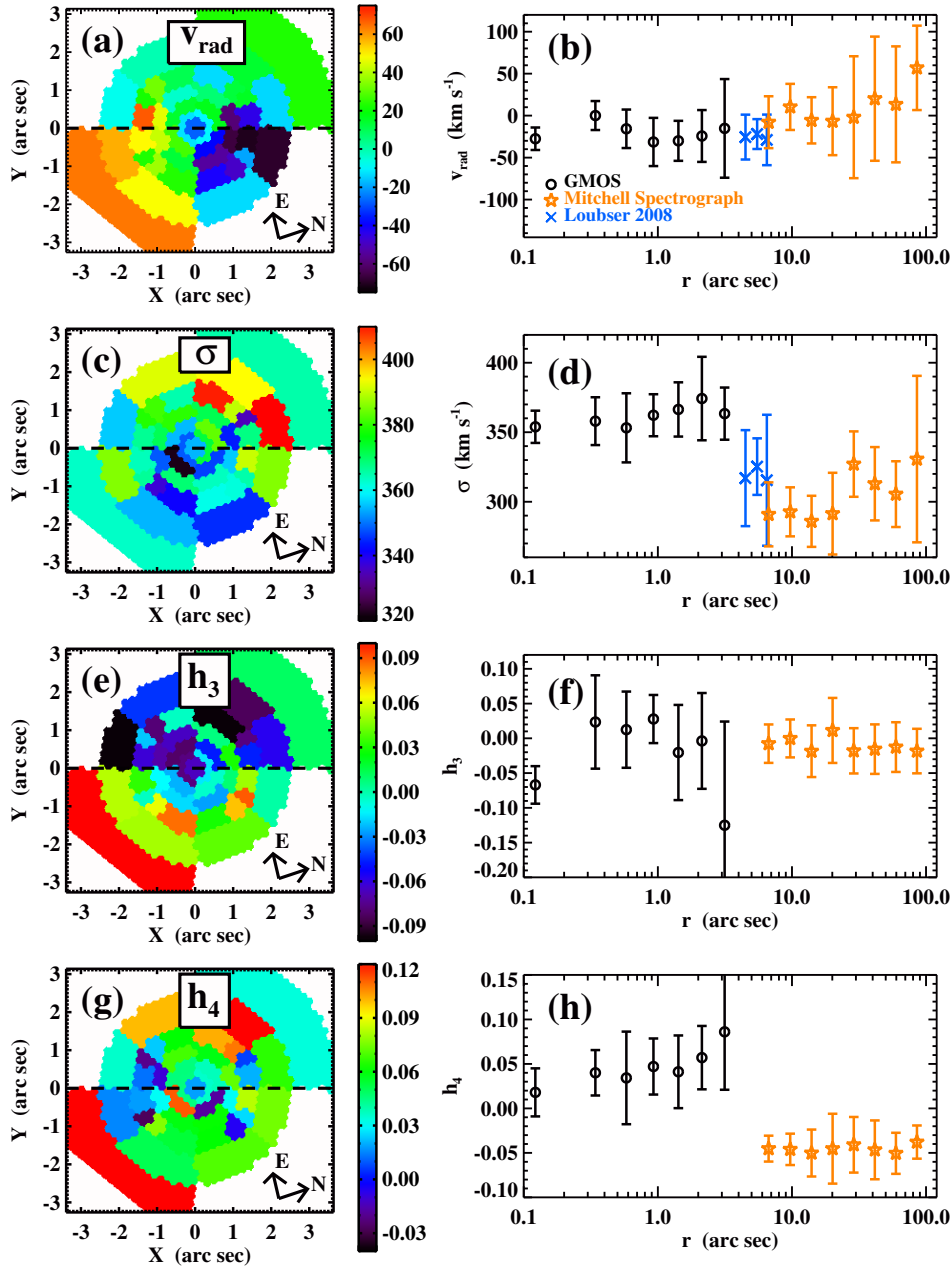


Figure 4.10: Stellar kinematics in NGC 2832. Panels (a), (c), (e), and (g) are two-dimensional maps from GMOS IFS data. The horizontal dashed line represents the photometric major axis. Panels (b), (d), (f), and (h) are radial plots, including GMOS and Mitchell Spectrograph data, plus long-slit data from Loubser et al. (2008) at radii from $4''$ to $7''$. In order to construct the radial plots, the kinematic moments from different quadrants and polar angles have been averaged, after inverting the values of v_{rad} and h_3 in the southeast and southwest quadrants. (a) and (b): radial velocity. (c) and (d): line-of-sight velocity dispersion. (e) and (f): Gauss-Hermite moment h_3 . (g) and (h): Gauss-Hermite moment h_4 .

4.5 Stellar Orbit Models and Black Hole Masses

4.5.1 Axisymmetric Orbit Models

We generate stellar orbit models of each galaxy using the static potential method introduced by Schwarzschild (1979). We use the axisymmetric modeling algorithm described in detail in Gebhardt et al. (2000b; 2003), Thomas et al. (2004; 2005), and Siopis et al. (2009). Similar models are presented in Richstone & Tremaine (1984), Rix et al. (1997), van der Marel et al. (1998), Cretton et al. (1999b), and Valluri et al. (2004).

We assume that each galaxy includes three mass components – stars, a central black hole, and an extended dark matter halo – described by the radial density profile

$$\rho(r) = \frac{M_\star}{L_R} \nu(r) + M_\bullet \delta(r) + \rho_{\text{halo}}(r), \quad (4.3)$$

where $\nu(r)$ is the observed luminosity density (see Figure 4.1). The resulting gravitational potential depends on M_\bullet , the stellar mass-to-light ratio M_\star/L (M_\star/L_R for R -band photometry), and two parameters describing the dark matter density profile $\rho_{\text{halo}}(r)$. Our models are symmetric about the z -axis (corresponding to the projected minor axis) and the equatorial plane ($z = 0$). Stellar orbits are generated by propagating test particles through the potential and computing their time-averaged velocities in each bin in a polar grid. Typical models produce $\sim 30,000$ bound orbits, including both signs of the angular momentum component L_z .

To match each observed LOSVD, we compute a model LOSVD from the projected velocities of individual orbits in the spatial region corresponding to the extracted spectrum and assumed PSF. Each orbit is assigned a scalar weight, and the orbital weights are varied to optimize the fit between the observed and model LOSVDs. The goodness of fit for each model is characterized by the χ^2 parameter:

$$\chi^2 = \sum_i \sum_j^{N_b} \frac{[\mathcal{L}_{i,\text{data}}(v_j) - \mathcal{L}_{i,\text{model}}(v_j)]^2}{\sigma_i^2(v_j)}, \quad (4.4)$$

where $\mathcal{L}_{i,\text{data}}$ and $\mathcal{L}_{i,\text{model}}$ are LOSVDs in each of the $i = 1, \dots, N_b$ spatial bins, and $\sigma_i^2(v_j)$ is the squared uncertainty in $\mathcal{L}_{i,\text{data}}$ at velocity bin v_j . The weights are constrained such that the summed spatial distribution of all weighted orbits must match the observed luminosity density profile.

For each galaxy, we have run multiple trials of orbit models. Each trial assumes a particular dark matter halo profile and fits a specific combination of kinematic data to several hundred models covering a finely sampled grid in M_\bullet and M_\star/L . The resulting confidence limits in M_\bullet and M_\star/L are computed by analyzing the distribution of χ^2 values, according to the cumulative likelihood method of McConnell et al. (2011a). Our modeling trials for the four galaxies are summarized in Tables 4.3-4.6.

High-resolution and wide-field data play complementary roles in constraining the gravitational potential of each BCG. Kinematic measurements from GMOS are sufficient to detect a black hole in NGC 4889 and NGC 3842, in part because of excellent seeing. Still, the black hole’s gravitational signature is not fully decoupled from the enclosed stellar mass, and improved measurements of M_\star/L yield tighter confidence intervals in M_\bullet . Wide-field kinematics from the Mitchell Spectrograph and long-slit instruments constrain the relative contributions of stars and dark matter and increase the accuracy and precision of M_\star/L and M_\bullet .

In principle, the orbit modeling code can accommodate any dark matter density profile. We have restricted our experiments to two functional forms: the cored logarithmic (LOG) profile (described in, e.g., McConnell et al. 2011a), or the NFW profile (Navarro et al. 1996). The free parameters in the LOG profile are the asymptotic circular speed v_c and the core radius r_c . The free parameters in the NFW profile are the concentration parameter c and the scale radius r_s . Thomas et al. (2007) used long-slit kinematics to determine the best-fitting LOG and NFW profiles for NGC 4889. Our models of NGC 4889 approximate their best-fitting LOG profile.

The literature does not provide a robust estimate of the dark matter halo profile for NGC 3842, and our kinematics from the Mitchell Spectrograph extend to only $0.9 r_{\text{eff}}$. We have tested LOG profiles with a few different values of v_c , as the total halo mass is proportional to v_c^2 . After determining the best value of v_c (350 km s^{-1} , with $r_c = 8.0 \text{ kpc}$), we tested a comparable NFW halo, scaled to enclose the same mass within the outer radius of our kinematic data. We required c and r_s to follow the relation

$$r_s^3 = \left(\frac{3 \times 10^{13} M_\odot}{200 \frac{4\pi}{3} \rho_{\text{crit}} c^3} \right) 10^{\frac{1}{0.15}(1.05 - \log_{10} c)} \quad (4.5)$$

(Rix et al. 1997; McConnell et al. 2011a), where ρ_{crit} is the present-day critical density. The resulting NFW halo has $c = 13.5$ and $r_s = 31.2 \text{ kpc}$, and fits our data to the same confidence level as the LOG profile ($\Delta\chi_{\text{min}}^2 = 0.4$). Even though the density of the NFW profile increases toward $r = 0$, the total mass near the center is dominated by stars and the supermassive black hole. We further describe our results modeling different dark matter halos in Section 4.5.2.

Our Mitchell Spectrograph kinematics extend to $1.2 r_{\text{eff}}$ for NGC 7768 and $1.5 r_{\text{eff}}$ for NGC 2832, but in both cases fail to tightly constrain the dark matter profile. In Section 4.5.2 we describe our treatment of dark matter in NGC 7768 and note that our measurement of M_\bullet is insensitive to the dark matter profile. In Section 4.5.2 we describe our dark matter models for NGC 2832 and how they affect our measurement of M_\bullet .

4.5.2 Black Hole Masses and Mass-to-Light Ratios

As in McConnell et al. (2011a), we have determined confidence intervals in M_\bullet and M_\star/L_R by running numerous models and integrating the relative likelihood function, $P \propto e^{-\frac{1}{2}(\chi^2 - \chi_{\text{min}}^2)}$. Results for individual galaxies are discussed below.

4.5.2.1 NGC 4889

In order to address the dramatic asymmetries in the stellar kinematics near the center of NGC 4889, we have independently run models to fit each observed quadrant of the galaxy, assuming the same central LOSVD ($r < 0.25''$) for all quadrants. For each quadrant, we fit IFS kinematics from GMOS and long-slit (WHT) kinematics from Loubser et al. (2008). The resulting contours in $\chi^2(M_\bullet, M_\star/L_R)$ are illustrated in Figure 4.11. There is a large degree of overlap between the two-dimensional 68% confidence regions for the northeast, southeast, and northwest quadrants, each of which contain a local maximum in σ . After marginalizing over M_\star/L_R , these three quadrants yield mutually consistent black hole mass estimates. In the southwest quadrant, σ decreases nearly monotonically with increasing r , and the marginalized 68% confidence interval $M_\bullet = (5.5 - 17.0) \times 10^9 M_\odot$ only agrees with the northeast quadrant. We wish to represent the constraints that all four quadrants impose upon the central black hole mass, and so we adopt the most extreme range of confidence limits, $M_\bullet = (5.5 - 37) \times 10^9 M_\odot$. In other words, we exclude only those models whose orbit solution is an outlier in all four quadrants. We define the best-fit black hole mass as the midpoint of the confidence interval above, such that $M_\bullet \approx (21 \pm 15) \times 10^9 M_\odot$. The stellar mass-to-light ratios from all four quadrants agree within 68% confidence limits. The extreme 68% confidence interval is $M_\star/L_R = 4.2 - 7.6 M_\odot L_{\odot,R}^{-1}$.

For a torus of stars in NGC 4889, we can estimate the total enclosed mass as $M_{\text{enc}} = rv^2/G$. We consider a characteristic velocity, v , of 450 km s^{-1} , based on the double-peaked residual features from LOSVDs near the major axis, and an average radius, r , of $1.4''$ (700 pc). These estimates yield $M_{\text{enc}} = 3.3 \times 10^{10} M_\odot$. Our stellar orbit models of NGC 4889 find M_\star/L_R in the range of $4.2 - 7.6 M_\odot L_{\odot,R}^{-1}$, corresponding to stellar masses of $(0.7 - 1.2) \times 10^{10} M_\odot$ within $1.4''$. The remaining mass of $(2.1 - 2.6) \times 10^{10} M_\odot$ lies near the middle of our adopted confidence interval for M_\bullet .

Although NGC 4889 does not show strong evidence for an off-center black hole, we wish to estimate the range of black hole masses that could reside at the location of the global maximum in σ . We have fit models to the LOSVDs from the east side of NGC 4889, spatially offset such that the center of the axisymmetric gravitational potential is aligned with the LOSVD at $r = 1.4''$ along the major axis. These models produce a 68% confidence interval $M_\bullet = (8.7 - 24) \times 10^9 M_\odot$, which falls entirely within the range spanned by the models of individual quadrants. Although these “recentered” models do not accurately reflect the spatial relationship between the stellar mass distribution and the observed kinematics, they support our overall conclusion that a black hole of at least $5.5 \times 10^9 M_\odot$ is required to produce the observed line-of-sight velocity dispersions near 400 km s^{-1} . Although the observed line-of-sight velocity dispersion decreases toward the center of NGC 4889, the best-fitting stellar orbit model for each quadrant predicts that the three-dimensional velocity dispersion σ_{3D} rises toward the black hole. A non-isotropic orbital distribution, biased toward tangential orbits, causes the projected velocity dispersion to decrease even as σ_{3D} increases. This is further discussed in Section 4.5.3 and illustrated in Figure 4.17.

Table 4.3: Axisymmetric models of NGC 4889

| Data | v_c (km s^{-1}) | r_c (kpc) | $M_h(20 \text{ kpc})$ ($10^{11} M_\odot$) | $f_{\text{DM}}(r_{\text{eff}})$ | M_\bullet ($10^9 M_\odot$) | M_*/L_R ($M_\odot L_{\odot,R}^{-1}$) | χ^2_{min} | N_{dof} |
|-----------------------|---------------------------------|----------------|------------------------------------------------|---------------------------------|-----------------------------------|---------------------------------------------|-----------------------|------------------|
| (1) | (2) | (3) | (4) | (5) | (6) | (7) | (8) | (9) |
| GMOS southwest + WHT | 425 | 8.0 | 7.21 | 0.54 | $9.8^{+7.2}_{-4.3}$ | $6.6^{+1.0}_{-1.3}$ | 176.6 | 345 |
| GMOS southeast + WHT | 425 | 8.0 | 7.21 | 0.57 | 26^{+6}_{-6} | $5.6^{+1.1}_{-1.4}$ | 137.0 | 420 |
| GMOS northwest + WHT | 425 | 8.0 | 7.21 | 0.56 | 27^{+10}_{-9} | $5.8^{+1.2}_{-1.4}$ | 170.7 | 345 |
| GMOS northeast + WHT | 425 | 8.0 | 7.21 | 0.55 | 17^{+8}_{-7} | $6.1^{+1.2}_{-1.5}$ | 119.4 | 420 |
| GMOS west + WHT | 425 | 8.0 | 7.21 | 0.54 | $12^{+8}_{-5.5}$ | $6.4^{+1.0}_{-1.2}$ | 180.4 | 330 |
| GMOS east + WHT | 425 | 8.0 | 7.21 | 0.58 | 29^{+5}_{-8} | $5.4^{+1.0}_{-0.9}$ | 217.4 | 442 |
| GMOS recentered + WHT | 425 | 8.0 | 7.21 | 0.54 | $15^{+9}_{-6.3}$ | $6.5^{+0.3}_{-1.1}$ | 239.5 | 442 |

Notes: Column 1: data sets included in trial. Column 2: circular velocity of LOG dark matter halo. Column 3: core radius of LOG dark matter halo. For NGC 4889, we have approximated the best-fitting halo from Thomas et al. (2007). Column 4: enclosed halo mass within 20 kpc. The “no dark matter” case has $v_c = 0.01 \text{ km s}^{-1}$, $r_c = 20.0 \text{ kpc}$, and $M_h \sim 200 M_\odot$. Column 5: dark matter fraction within one effective radius, assuming the best-fit values of M_\bullet and M_*/L_R . Column 6: best-fit black hole mass. Errors correspond to 68% confidence intervals. Column 7: best-fit R -band stellar mass-to-light ratio. Quoted errors correspond to 68% confidence intervals. Column 8: minimum χ^2 value for all models. Column 9: degrees of freedom in model fits to LOSVDs. Computed values include a smoothing factor of 1 degree of freedom per 2 velocity bins for non-parametric LOSVDs from GMOS.

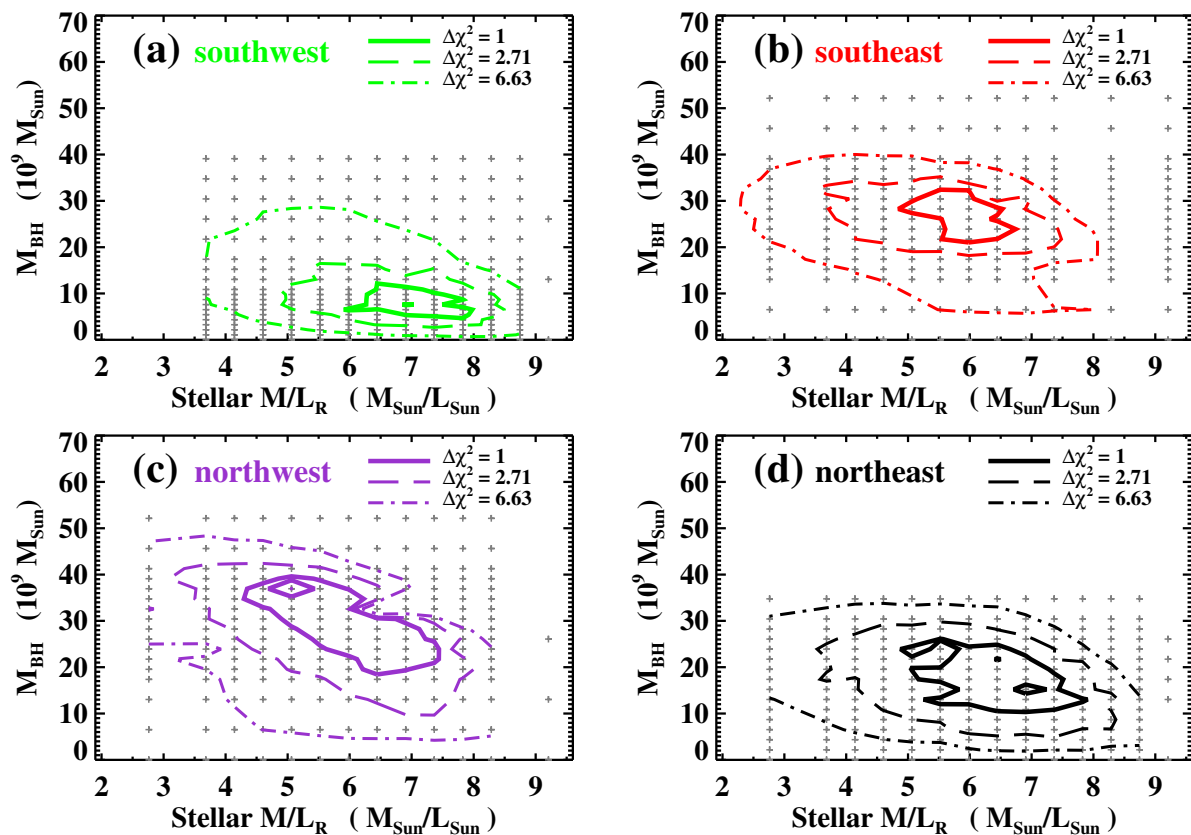


Figure 4.11: Contours of χ^2 versus M_{\star}/L_R and M_{\bullet} , for models of NGC 4889, fitting LOSVDs from the GMOS IFS and from Loubser et al. (2008). Data from each quadrant of the galaxy were fit independently, and the respective results are shown in panels (a) through (d). Contours of $\Delta\chi^2 = 1, 2.71,$ and 6.63 represent confidence levels of 68%, 90%, and 99% for one free parameter. Small crosses denote individual models.

4.5.2.2 NGC 3842

Models using our best estimate of the dark matter halo in NGC 3842 yield 68% confidence intervals of $M_\bullet = (7.2 - 12.7) \times 10^9 M_\odot$ and $M_\star/L_R = 4.4 - 5.8 M_\odot L_{\odot,R}^{-1}$. The confidence interval for M_\bullet overlaps with the confidence intervals from all other trials, even models with no dark matter. The best-fit value of M_\bullet decreases by 26% when dark matter is omitted and increases by 46% for our most massive halo. We observe a similar level of sensitivity in M_\star/L_R , where the most extreme trials yield best-fit values of 3.7 and $7.2 M_\odot L_{\odot,R}^{-1}$. Figure 4.12 illustrates the χ^2 contours for models with our best-fitting NFW profile and with no dark matter.

Before acquiring Mitchell Spectrograph data, we modeled NGC 3842 with GMOS IFS data plus major-axis kinematics from Loubser et al. (2008), measured using ISIS at WHT. The more recent Mitchell Spectrograph data yield slightly larger values of M_\bullet , but are consistent within 68% confidence limits. We prefer using the Mitchell Spectrograph data because they extend to larger radii (35.3'' versus 20.8'') and provide full two-dimensional spatial sampling.

OSIRIS and GMOS provide independent measurements of stellar kinematics in NGC 3842, for $r \leq 0.7''$. In spite of the potential for higher spatial resolution, systematic contaminants in our OSIRIS spectra force us to increase S/N by binning the data to identical spatial scales as for GMOS. We have run orbit models fitting LOSVDs from OSIRIS and

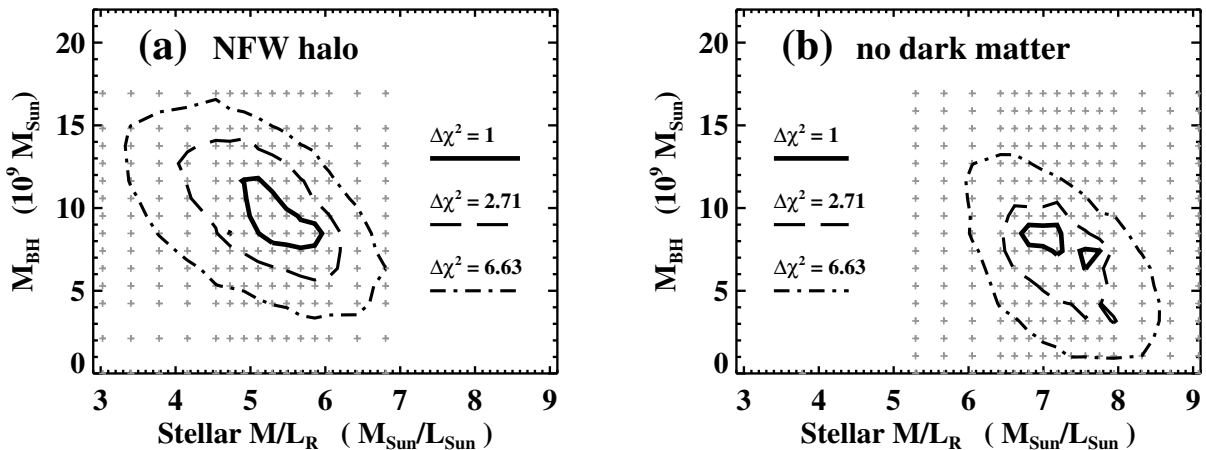


Figure 4.12: Contours of χ^2 versus M_\star/L_R and M_\bullet , for models of NGC 3842, fitting LOSVDs from GMOS and the Mitchell Spectrograph. (a) Results for our best-fitting NFW dark matter profile ($c = 13.5, r_s = 31.2$ kpc). (b) Results for models without dark matter. Contours of $\Delta\chi^2 = 1, 2.71,$ and 6.63 represent confidence levels of 68%, 90%, and 99% for one free parameter. Small crosses denote individual models.

Table 4.4: Axisymmetric models of NGC 3842

| Data | v_c (km s^{-1}) | r_c (kpc) | c | r_s (kpc) | $M_h(20 \text{ kpc})$ ($10^{11} M_\odot$) | $f_{\text{DM}}(r_{\text{eff}})$ | M_\bullet ($10^9 M_\odot$) | M_*/L_R ($M_\odot L_\odot^{-1}$) | χ^2_{min} | N_{dof} |
|-----------|---------------------------------|----------------|------|----------------|------------------------------------------------|---------------------------------|-----------------------------------|-----------------------------------------|-----------------------|------------------|
| (1) | (2) | (3) | (4) | (5) | (6) | (7) | (8) | (9) | (10) | (11) |
| G + M | 0.01 | 20.0 | | | 2×10^{-9} | 0 | $7.2^{+2.1}_{-2.9}$ | $7.2^{+0.6}_{-0.5}$ | 92.6 | 345 |
| G + M | 350 | 8.0 | | | 4.89 | 0.51 | $10.2^{+2.9}_{-2.7}$ | $5.4^{+0.6}_{-0.7}$ | 89.3 | 345 |
| G + M | | | 13.5 | 31.2 | 5.09 | 0.53 | $9.7^{+3.0}_{-2.5}$ | $5.1^{+0.7}_{-0.7}$ | 88.9 | 345 |
| G + M | 500 | 8.0 | | | 9.98 | 0.75 | $13.2^{+2.2}_{-2.2}$ | $3.7^{+0.4}_{-0.6}$ | 96.2 | 345 |
| G + O + M | 0.01 | 20.0 | | | 2×10^{-9} | 0 | $6.3^{+1.8}_{-1.9}$ | $7.1^{+0.6}_{-0.5}$ | 129.6 | 368 |
| G + O + M | 500 | 8.0 | | | 9.98 | 0.74 | $10.2^{+1.5}_{-1.5}$ | $4.0^{+0.4}_{-0.5}$ | 138.4 | 368 |
| G + WHT | 0.01 | 20.0 | | | 2×10^{-9} | 0 | $6.8^{+1.9}_{-2.6}$ | $7.3^{+0.5}_{-0.6}$ | 355.6 | 525 |
| G + WHT | 500 | 8.0 | | | 9.98 | 0.71 | $9.9^{+2.1}_{-2.2}$ | $4.8^{+0.5}_{-0.8}$ | 349.3 | 525 |

Notes: Column 1: data sets included in trial. “G” refers to GMOS, “O” refers to OSIRIS, and “M” refers to the Mitchell Spectrograph. Column 2: circular velocity of LOG dark matter halo. Column 3: core radius of LOG dark matter halo. Column 4: concentration parameter for NFW dark matter halo. Column 5: scale radius for NFW dark matter halo. Column 6: enclosed halo mass within 20 kpc. Our best-fitting halo is an NFW profile with $c = 13.5$ and $r_s = 31.2$ kpc. The equivalent LOG halo ($v_c = 350 \text{ km s}^{-1}$; $r_c = 8.0$ kpc) fits our data to the same level of confidence ($\Delta\chi^2_{\text{min}} = 0.4$). The “no dark matter” case has $v_c = 0.01 \text{ km s}^{-1}$, $r_c = 20.0$ kpc, and $M_h \sim 200 M_\odot$. Omitting dark matter from the models causes M_\bullet to decrease by 26%, consistent within errors. Column 7: dark matter fraction within one effective radius, assuming the best-fit values of M_\bullet and M_*/L_R . Column 8: best-fit black hole mass. Errors correspond to 68% confidence intervals. Column 9: best-fit R -band stellar mass-to-light ratio. Quoted errors correspond to 68% confidence intervals. Column 10: minimum χ^2 value for all models. Column 11: degrees of freedom in model fits to LOSVDs. Computed values include a smoothing factor of 1 degree of freedom per 2 velocity bins for non-parametric LOSVDs from GMOS and OSIRIS.

GMOS simultaneously (as well as Mitchell Spectrograph data at large radii). Including the OSIRIS data causes the best-fit value of M_\bullet to decrease by up to 23%, likely because OSIRIS data show a less drastic increase in σ than data from GMOS. For the best-fit models, including OSIRIS data produces higher average χ^2 values per LOSVD, even after ignoring the central regions where LOSVDs from OSIRIS and GMOS are not fully consistent. The kinematic fits to OSIRIS data may have systematic errors, resulting from imperfect sky subtraction and difficulty defining the H -band continuum. Consequently, we judge the models of NGC 3842 with only GMOS and Mitchell Spectrograph data to be the most reliable.

4.5.2.3 NGC 7768

For NGC 7768, we have combined IFU data from OSIRIS and the Mitchell Spectrograph, plus five long-slit measurements at radii of 1-3". We have run two trials with full sampling of M_\bullet and M_\star/L . One trial includes a LOG halo profile, matching our best-fitting approximation for NGC 3842 ($v_c = 350 \text{ km s}^{-1}$; $r_c = 8.0 \text{ kpc}$). The other trial does not include dark matter. The black hole masses from the two trials are in excellent agreement, and the best-fit values of M_\star/L_R agree within 68% confidence limits. The trial with no dark matter actually yields a lower value of χ^2_{\min} , albeit with marginal significance ($\Delta\chi^2_{\min} = 1.4$). Considering the lower value of χ^2_{\min} from the trial without dark matter, we formally adopt a black hole mass of $1.3^{+0.5}_{-0.4} \times 10^9 M_\odot$. The range of M_\star/L_R from both trials is 4.6-6.8 $M_\odot L_{\odot,R}^{-1}$ (68% confidence). The respective χ^2 contours are shown in Figure 4.13.

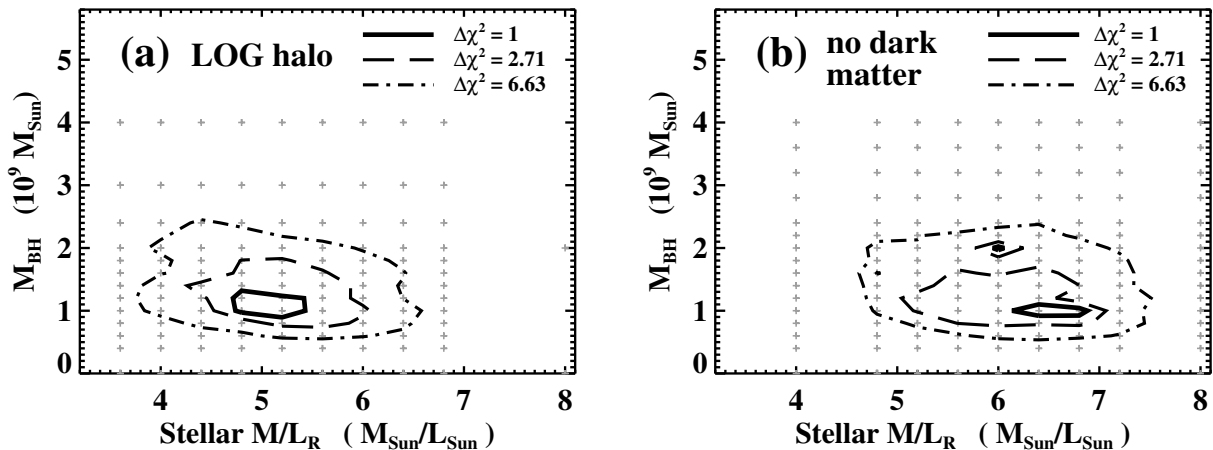


Figure 4.13: Contours of χ^2 versus M_\star/L_R and M_\bullet , for models of NGC 7768, fitting LOSVDs from OSIRIS and the Mitchell Spectrograph, plus five long-slit data points from Loubser et al. (2008). (a) Results for a LOG dark matter profile ($v_c = 350 \text{ km s}^{-1}$, $r_c = 8.0 \text{ kpc}$). (b) Results for models without dark matter. Contours of $\Delta\chi^2 = 1, 2.71, \text{ and } 6.63$ represent confidence levels of 68%, 90%, and 99% for one free parameter. Small crosses denote individual models.

Table 4.5: Axisymmetric models of NGC 7768

| Data | v_c (km s ⁻¹) | r_c (kpc) | $M_h(20 \text{ kpc})$ ($10^{11} M_\odot$) | $f_{\text{DM}}(r_{\text{eff}})$ | M_\bullet ($10^9 M_\odot$) | M_*/L_R ($M_\odot L_{\odot,R}^{-1}$) | χ_{min}^2 | N_{dof} |
|-------------------------|--------------------------------|----------------|------------------------------------------------|---------------------------------|-----------------------------------|---------------------------------------------|-----------------------|------------------|
| (1) | (2) | (3) | (4) | (5) | (6) | (7) | (8) | (9) |
| OSIRIS + Mitchell + WHT | 0.01 | 20.0 | 2×10^{-9} | 0 | $1.3^{+0.5}_{-0.4}$ | $6.1^{+0.7}_{-0.8}$ | 77.4 | 285 |
| OSIRIS + Mitchell + WHT | 350 | 8.0 | 4.89 | 0.32 | $1.2^{+0.5}_{-0.4}$ | $5.2^{+0.5}_{-0.6}$ | 78.8 | 285 |

Notes: See Table 4.3 for notes and definitions. For WHT measurements, we only include five LOSVDs, covering radii between 1'' and 3''. The LOSVDs extracted from the Mitchell Spectrograph cover five radial bins between 3.0'' and 28.5'' ($0.1 - 1.2 \times r_{\text{eff}}$). Several models with different dark matter profiles, including no dark matter and the dark matter model listed here, all have $\Delta\chi^2 < 1$. Our best-fit black hole mass for NGC 7768 is insensitive to the assumed dark matter profile, a testament to the strength of our OSIRIS data.

Given our initial trials' consistent measurements of M_\bullet and M_\star/L , we have not run finely sampled trials for additional dark matter profiles. In order to check whether any dark matter profile for NGC 7768 can fit our kinematics as well as the trial without dark matter, we have run a grid of models coarsely sampling M_\star/L , v_c , and r_c . This trial yields several models whose χ^2 values are consistent with χ_{\min}^2 for the trial without dark matter.

4.5.2.4 NGC 2832

For NGC 2832, we have combined IFU data from GMOS and the Mitchell Spectrograph, along with three long-slit measurements at radii of 4-7'', and have run full trials varying M_\bullet and M_\star/L for two dark matter halos. Figure 4.14 illustrates the χ^2 contours, and Figure 4.15 shows the likelihood distribution of M_\bullet from each trial, after marginalizing with respect to M_\star/L . Models for the less massive halo ($v_c = 350 \text{ km s}^{-1}$; $r_c = 32.0 \text{ kpc}$) yield a best-fit black hole mass of $2.9 \times 10^9 M_\odot$ and a 68% upper confidence limit of $5.2 \times 10^9 M_\odot$. However, the likelihood distribution falls slowly as M_\bullet approaches zero, and has sufficient noise between $M_\bullet = 0$ and $M_\bullet = 6.0 \times 10^9 M_\odot$ to cast doubt upon any lower limit in M_\bullet . In contrast, the more massive halo ($v_c = 560 \text{ km s}^{-1}$; $r_c = 40.0 \text{ kpc}$) yields a best-fit black hole mass of $5.9 \times 10^9 M_\odot$, and the corresponding likelihood distribution declines cleanly to both sides, producing a 68% confidence interval of $M_\bullet = (2.7 - 9.0) \times 10^9 M_\odot$. We obtain consistent results for this halo when the three long-slit data points at intermediate radii are excluded.

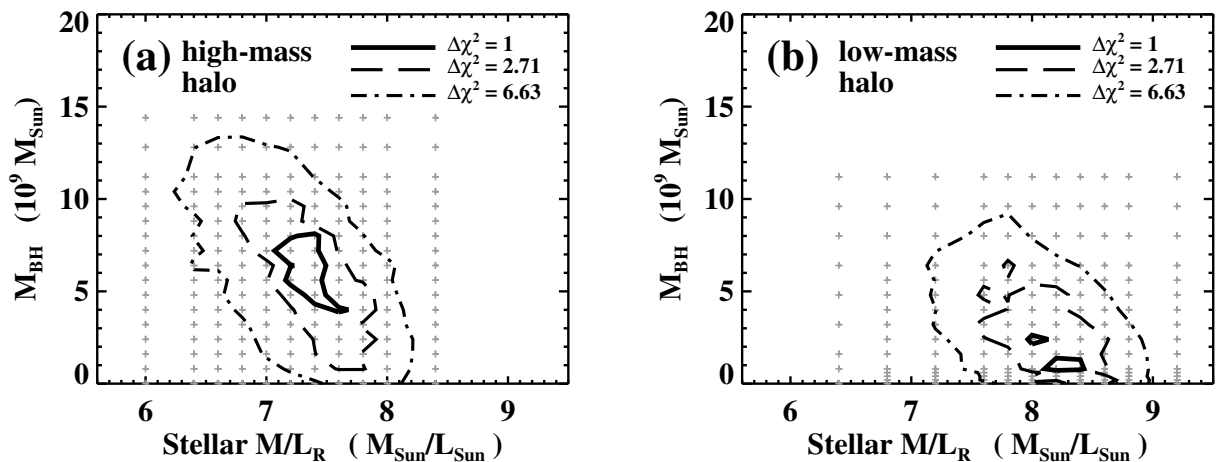


Figure 4.14: Contours of χ^2 versus M_\star/L_R and M_\bullet , for models of NGC 2832, fitting LOSVDs from GMOS and Mitchell Spectrograph IFS data, plus three long-slit data points from Loubser et al. (2008). (a) Results for a high-mass LOG dark matter profile ($v_c = 560 \text{ km s}^{-1}$, $r_c = 40.0 \text{ kpc}$). (b) Results for a lower-mass LOG profile ($v_c = 350 \text{ km s}^{-1}$, $r_c = 32.0 \text{ kpc}$). Contours of $\Delta\chi^2 = 1$, 2.71, and 6.63 represent confidence levels of 68%, 90%, and 99% for one free parameter. Small crosses denote individual models.

Table 4.6: Axisymmetric models of NGC 2832

| Data | v_c (km s ⁻¹) | r_c (kpc) | $M_h(20 \text{ kpc})$ (10 ¹¹ M _⊙) | $f_{\text{DM}}(r_{\text{eff}})$ | M_\bullet (10 ⁹ M _⊙) | M_\star/L_R (M _⊙ L _⊙ ⁻¹) | χ^2_{min} | N_{dof} |
|--------------------------|--------------------------------|----------------|-------------------------------------------------------------|---------------------------------|--------------------------------------------------|-----------------------------------------------------------------|-----------------------|------------------|
| (1) | (2) | (3) | (4) | (5) | (6) | (7) | (8) | (9) |
| GMOS IFU + GMOS slit + M | 350 | 32.0 | 1.59 | 0.28 | < 5.2 | 8.1 ^{+0.3} _{-0.5} | 129.0 | 495 |
| GMOS IFU + GMOS slit + M | 560 | 40.0 | 2.90 | 0.47 | 5.9 ^{+3.1} _{-3.2} | 7.3 ^{+0.4} _{-0.4} | 125.1 | 495 |
| GMOS IFU + M | 560 | 40.0 | 2.90 | 0.47 | 7.2 ^{+3.0} _{-3.1} | 7.2 ^{+0.3} _{-0.5} | 115.2 | 450 |

Notes: See Table 4.3 for notes and definitions. “M” refers to the Mitchell Spectrograph. For GMOS slit measurements, we only include three LOSVDs, covering radii between 4” and 7”.

When data from GMOS and the Mitchell Spectrograph are modeled simultaneously, the minimum χ^2 values for all input M_\bullet and M_\star/L significantly favor the more massive halo ($\Delta\chi^2_{\min} = 3.9$). However, there are multiple reasons to be skeptical of the corresponding confidence limits for M_\bullet . First, the sharp jump between the velocity dispersions measured with GMOS and those measured with the Mitchell Spectrograph suggests that systematic errors in the kinematic fitting could be responsible for the apparent signature of a massive black hole. Second, the best-fit stellar mass-to-light ratio of $7.3 M_\odot L_{\odot,R}^{-1}$ exceeds the upper limits for M_\star/L_R in NGC 4889 and NGC 3842. Third, the best-fit value of M_\bullet in NGC 2832 is sensitive to the dark matter halo profile, and one trial with a plausible halo fails to produce a significant black hole detection. Given the possibility of systematic errors in the kinematics, we do not find convincing evidence for a specific dark matter profile in NGC 2832. We conservatively interpret our models of NGC 2832 to provide an upper limit of $M_\bullet = 9.0 \times 10^9 M_\odot$, to 68% confidence.

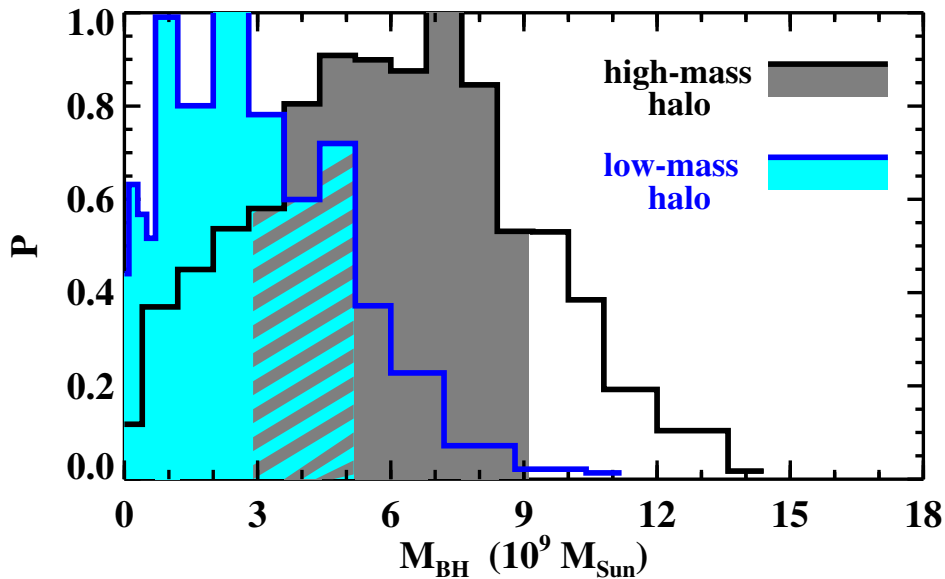


Figure 4.15: Likelihood, P , versus M_\bullet for models of NGC 2832, after marginalizing with respect to M_\star/L_R . The black line represents the trial with a high-mass LOG dark matter profile ($v_c = 560 \text{ km s}^{-1}$, $r_c = 40.0 \text{ kpc}$), and the grey shaded region represents the corresponding 68% confidence interval. The blue line and cyan shaded region represent the trial with a lower-mass LOG profile ($v_c = 350 \text{ km s}^{-1}$, $r_c = 32.0 \text{ kpc}$). The diagonally hashed region is where the two confidence intervals overlap. Both likelihood distributions have been normalized to a maximum value of 1. Considering both trials, and discrepancies between different instruments' kinematic measurements for NGC 2832, we adopt an upper limit of $M_\bullet = 9 \times 10^9 M_\odot$.

4.5.3 Tangentially Biased Orbits

In NGC 4889, NGC 3842, and NGC 7768, the supermassive black hole coincides with a deficiency of radial orbits near the galaxy center. In Figure 4.16, we plot orbital anisotropy versus radius for each BCG and compare predictions from our orbital models with the best-fit black hole mass and without a black hole. Specifically, we examine the ratio of the radial and tangential velocity dispersions in the three-dimensional models. The tangential dispersion term includes azimuthal rotation and is defined as $\sigma_{\text{tan}}^2 \equiv \frac{1}{2}(\sigma_{\theta}^2 + \sigma_{\phi}^2 + v_{\phi}^2)$, such that $\sigma_{\text{rad}}/\sigma_{\text{tan}} = 1$ for an isotropic orbit distribution.

Figure 4.16 illustrates that for NGC 4889, NGC 3842, and NGC 7768, the models with black holes predict strong tangential velocity biases toward the galactic centers (solid curves), while the models without black holes predict fairly isotropic velocity distributions with little radial dependence (dashed curves). After averaging over the four quadrants using the best-fit black hole masses, the minimum value of $\sigma_{\text{rad}}/\sigma_{\text{tan}}$ in NGC 4889 is approximately 0.3. The best models for NGC 3842 and NGC 7768 have central values of $\sigma_{\text{rad}}/\sigma_{\text{tan}} \approx 0.3 - 0.4$. This degree of tangential bias is comparable to the central values in a handful of early-type galaxies (e.g., Gebhardt et al. 2003, 2007; Shen & Gebhardt 2010). NGC 4889 and NGC 3842, however, are exceptional in terms of the size of the central regions dominated by tangential orbits. In both galaxies, this region extends to approximately $2''$, or 1 kpc. By comparison, tangential bias extends to only 50-200 pc throughout a broad sample of early-type galaxies with black hole mass measurements (Gebhardt et al. 2003; 2007; Nowak et al. 2008; Shen & Gebhardt 2010; Gebhardt et al. 2011; cf., Gültekin et al. 2009b). In NGC 7768, we measure a tangential bias for $r < 0.5''$ (270 pc) for a black hole mass of $1 \times 10^9 M_{\odot}$.

The scarcity of radial orbits at the centers of massive galaxies may be a consequence of past core-scouring by one or more pairs of in-spiraling black holes. N -body simulations of merging galaxies and black holes indicate that stars on radial orbits are more likely to interact with a binary black hole, resulting in their ejection from the galaxy center (e.g., Quinlan & Hernquist 1997; Milosavljević & Merritt 2001). Supporting this picture, Gebhardt et al. (2003) ran stellar orbit models of twelve galaxies with black holes and noted that the four core-profile galaxies had a higher degree of tangential bias than the eight power-law galaxies. Photometric data of NGC 4889 show a stellar core with a radius of 750 pc (Lauer et al. 2007a), similar to the scale on which the tangential bias appears. In the sample of 118 core-profile galaxies from Lauer et al. (2007a), only eight exhibit core radii greater of 750 pc or greater; all eight are BCGs or cD galaxies of comparable luminosity. In NGC 3842, the core radius is 310 pc, roughly one-third the size of the tangentially biased region. The surface brightness profile for NGC 7768 turns over at approximately 220 pc, similar to the size of the tangentially biased region.

It is important to note that the decrease in velocity dispersions towards the black hole, as illustrated in Figure 4.5 for NGC 4889, occurs for the observed *line-of-sight* velocity dispersions. The three-dimensional velocity dispersion σ_{3D} is not directly measurable but is predicted by our orbital models. Figure 4.17 illustrates the radial trends in σ_{3D} for models of each quadrant of NGC 4889. As expected, σ_{3D} rises toward the center of the galaxy when

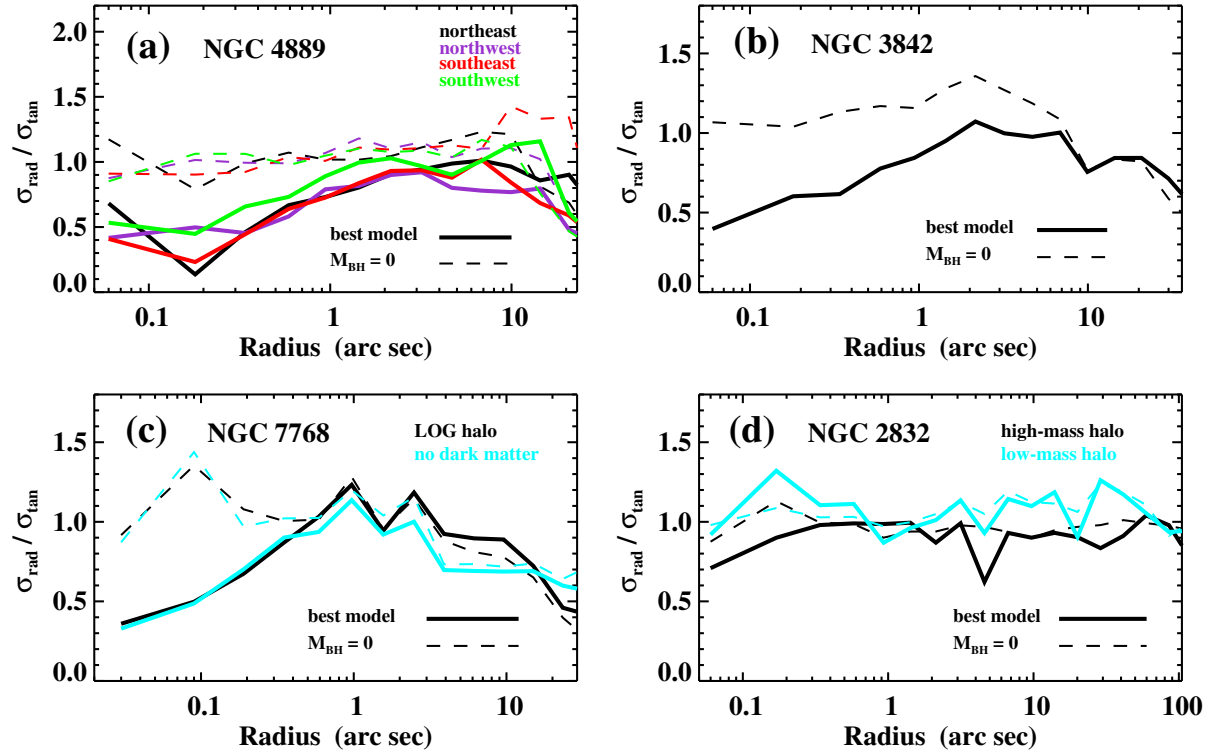


Figure 4.16: Anisotropy of model stellar orbits in each galaxy, as a function of radius. Solid lines represent the best-fitting models for each set of LOSVDs, and dashed lines represent the best-fitting models without a black hole. We define σ_{rad} and σ_{tan} such that their ratio is unity for an isotropic orbit distribution. (a) NGC 4889. Different colors represent the northeast (black; $M_{\bullet} = 1.2 \times 10^{10} M_{\odot}$), northwest (purple; $M_{\bullet} = 2.6 \times 10^{10} M_{\odot}$), southeast (red; $M_{\bullet} = 2.2 \times 10^{10} M_{\odot}$), and southwest (green; $M_{\bullet} = 6.0 \times 10^9 M_{\odot}$) quadrants. (b) NGC 3842. The best fitting model has $c = 13.5$, $r_s = 31.2$ kpc, $M_{\bullet} = 8.0 \times 10^9 M_{\odot}$. (c) NGC 7768. The best-fitting model with dark matter (black lines) has $v_c = 350 \text{ km s}^{-1}$, $r_c = 8.0$ kpc, and $M_{\bullet} = 1.0 \times 10^9 M_{\odot}$. The best-fitting model without dark matter (cyan lines) has $M_{\bullet} = 1.0 \times 10^9 M_{\odot}$. (d) NGC 2832. The best-fitting model for the high-mass dark matter halo (black lines) has $v_c = 560 \text{ km s}^{-1}$, $r_c = 40.0$ kpc, and $M_{\bullet} = 7.2 \times 10^9 M_{\odot}$. The best-fitting model for the low-mass halo (cyan lines) has $v_c = 350 \text{ km s}^{-1}$, $r_c = 32.0$ kpc, and $M_{\bullet} = 8.0 \times 10^8 M_{\odot}$.

a black hole is included in the model. Figures 4.16 and 4.17 together show that a non-isotropic orbital distribution, biased toward tangential orbits, can cause the light-of-sight velocity dispersion to decrease even as σ_{3D} increases.

Our models of NGC 4889 indicate that orbital anisotropy is responsible for the local minimum in σ at the galaxy center. In NGC 3842, the increase in σ is less pronounced than would be observed for isotropic orbits about a 10^{10} - M_{\odot} black hole. For both galaxies, models with $M_{\bullet} = 0$ have enough freedom to imitate the observed kinematics, but require a nearly isotropic orbital distribution to do so (Figure 4.16a, 4.16b). In NGC 7768, a radial bias is required to reproduce the sharp increase in σ (Figure 4.16c). Although the LOSVDs generated by models with and without black holes are qualitatively similar, the models with $M_{\bullet} = 0$ produce higher values of χ^2 in every trial.

NGC 2832 has nearly isotropic orbits at all radii, and the orbital discrepancy between models with and without a black hole is weaker than in NGC 4889 and NGC 3842. This is particularly true for models with the less massive dark matter halo, where we lack a confident black hole detection. The best-fitting model with the more massive halo has $M_{\bullet} = 7.2 \times 10^9 M_{\odot}$, and $\sigma_{\text{rad}}/\sigma_{\text{tan}}$ declines to 0.7 over the inner $0.3''$ (150 pc).

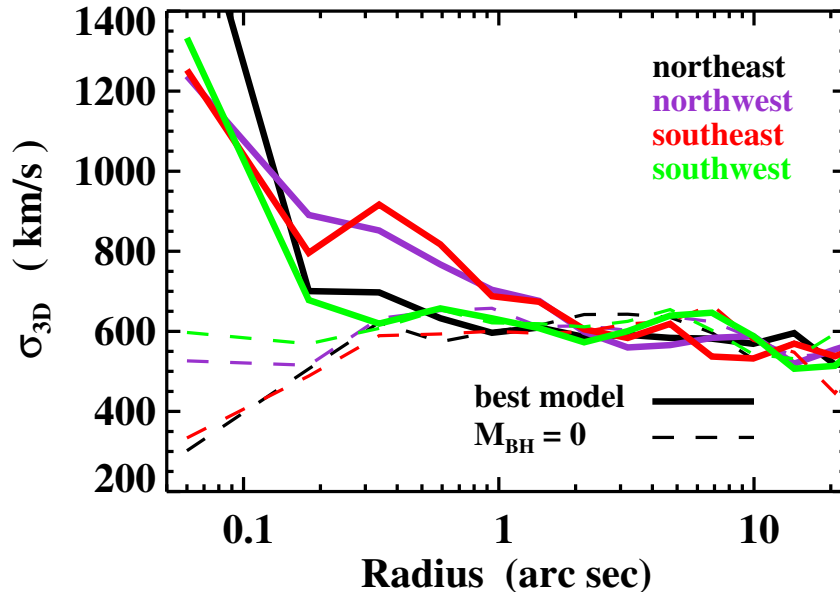


Figure 4.17: Three-dimensional velocity dispersion, σ_{3D} , as a function of radius predicted by our orbital models for NGC 4889. Solid lines represent the best-fitting model for each quadrant, and dashed lines represent the best-fitting models without a black hole. Different colors represent the northeast (black; $M_{\bullet} = 1.2 \times 10^{10} M_{\odot}$), northwest (purple; $M_{\bullet} = 2.6 \times 10^{10} M_{\odot}$), southeast (red; $M_{\bullet} = 2.2 \times 10^{10} M_{\odot}$), and southwest (green; $M_{\bullet} = 6.0 \times 10^9 M_{\odot}$) quadrants.

4.5.4 Possible Systematic Errors

The common practice for reporting errors in stellar dynamical measurements of M_\bullet and M_\star/L is to report the range of input M_\bullet and M_\star/L values that fall within a specific confidence interval for a given set of models. Yet modeling a galaxy requires explicit assumptions about its stellar content and the structure of its gravitational potential. Systematic errors from these assumptions will likely increase the overall measurement errors for M_\bullet and M_\star/L .

For each BCG, our models assume an edge-on inclination. This is indirectly supported by the observed axis ratios of 0.68-0.86, which imply relatively eccentric intrinsic shapes even for an edge-on system. Models with more face-on inclinations could yield higher black hole masses. We also model each galaxy as an oblate axisymmetric ellipsoid, in contrast to the presence of isophotal twists in NGC 3842 and NGC 2832 (Table 4.1) and circumstantial evidence that some BCGs are prolate or triaxial (Porter et al. 1991; Ryden et al. 1993; Boylan-Kolchin et al. 2006). In an early experiment with triaxial models, the best-fit black hole mass for NGC 3379 increased by a factor of two, whereas the black hole mass for M32 was unchanged from axisymmetric models (van den Bosch & de Zeeuw 2010). The increase for NGC 3379 may have arisen solely from a change in the best-fit inclination (R. C. E. van den Bosch, 2011, private communication).

Massive elliptical galaxies are known to exhibit spatial gradients in metallicity (e.g., Fisher et al. 1995; Kobayashi & Arimoto 1999; Mehlert et al. 2003; Brough et al. 2007; Greene et al. 2012), and gradients in stellar age and α -element enhancement have been reported in some cases (Fisher et al. 1995; Coccato et al. 2010).

Massive ellipticals could exhibit corresponding gradients in M_\star/L , yet our orbit models assume that M_\star/L is constant. This assumption could bias our estimates of the enclosed stellar mass at large or small radii, depending upon the steepness of the gradient and the radial sampling of our kinematic data. Preliminary single-burst stellar population modeling of M87 indicates that M_\star/L decreases by $\sim 50\%$ from $r = 0$ to $r \sim 2r_{\text{eff}}$ (G. J. Graves & J. D. Murphy, 2012, in prep). Most of our kinematics for the BCGs herein correspond to $r < r_{\text{eff}}$, and we estimate that a gradient in M_\star/L would bias our measurement of the central M_\star/L by $< 10\%$. Kinematic and photometric data probe the galaxy's total mass-to-light ratio, and models with dark matter have more flexibility to reproduce each galaxy's total mass profile. Trade-offs between dark matter and gradients in M_\star/L could mitigate potential biases in our measurements of M_\bullet . Still, our knowledge of the individual mass components in BCGs would be improved by using stellar line indices and population models to measure gradients in M_\star/L independently.

A fundamental assumption of all orbit superposition models is that the stellar motions reflect a steady-state gravitational potential. The strongly asymmetric kinematics in NGC 4889 present the possibility of an unrelaxed stellar system, although we do not witness corresponding photometric irregularities. Even with our conservative treatment of the asymmetric data, our models would be unable to assess the central black hole mass if the kinematics of NGC 4889 reflected a temporary condition.

4.6 Conclusion and Discussion

We have reported three black hole masses (NGC 4889, NGC 3842, NGC 7768) and one upper limit on M_\bullet (NGC 2832) in four of the nearby Universe’s most massive galaxies at distances of ~ 100 Mpc. As the basis for our analysis, we have presented high-resolution, two-dimensional measurements of stellar kinematics using GMOS at Gemini Observatory North and OSIRIS at Keck Observatory. For three of our galaxies, we have used wide-field stellar kinematics from the Mitchell Spectrograph at McDonald Observatory.

We have derived black hole masses from stellar kinematics using orbit superposition models. We find $M_\bullet = (2.1 \pm 1.6) \times 10^{10} M_\odot$ for NGC 4889, $M_\bullet = 9.7_{-2.5}^{+3.0} \times 10^9 M_\odot$ for NGC 3842, $M_\bullet = 1.3_{-0.4}^{+0.5} \times 10^9 M_\odot$ for NGC 7768, and $M_\bullet < 9.0 \times 10^9 M_\odot$ for NGC 2832. The orbit models also determine the stellar mass-to-light ratio M_\star/L_R , which we convert to M_\star/L_V as described in Section 4.2.2. We find $M_\star/L_R = 5.9 \pm 1.7 M_\odot L_{\odot,R}^{-1}$ ($M_\star/L_V = 7.4 \pm 2.1 M_\odot L_{\odot,V}^{-1}$) for NGC 4889, $M_\star/L_R = 5.2 \pm 0.8 M_\odot L_{\odot,R}^{-1}$ ($M_\star/L_V = 7.1 \pm 1.1 M_\odot L_{\odot,V}^{-1}$) for NGC 3842, $M_\star/L_R = 5.7 \pm 1.1 M_\odot L_{\odot,R}^{-1}$ ($M_\star/L_V = 8.8 \pm 1.7 M_\odot L_{\odot,V}^{-1}$) for NGC 7768, and $M_\star/L_R = 7.6_{-0.7}^{+0.8} M_\odot L_{\odot,R}^{-1}$ ($M_\star/L_V = 9.7 \pm 1.0 M_\odot L_{\odot,V}^{-1}$) for NGC 2832.

The orbital distributions from the best-fitting models indicate that NGC 4889 and NGC 3842 are depleted of radial orbits, out to radii of approximately 1 kpc. These extended tangential bias regions have similar sizes to the galaxies’ photometric cores, and may be linked to the extremely massive black hole ($M_\bullet \sim 10^{10} M_\odot$) in each galaxy. NGC 7768 has a black hole mass of only $\sim 10^9 M_\odot$ and a correspondingly modest tangential bias region.

Several correlations between black hole mass and scalar galaxy properties have been explored by numerous authors. Below we focus on the $M_\bullet - \sigma$ relation, the V -band $M_\bullet - L$ relation, and the relation between M_\bullet and bulge stellar mass, M_{bulge} . We estimate M_{bulge} for each BCG by multiplying L_V by M_\star/L_V .

In Figure 4.18, we compare our measured values of M_\bullet in NGC 4889, NGC 3842, and NGC 7768, and our upper limit for NGC 2832, to predicted black hole masses from the $M_\bullet - \sigma$, $M_\bullet - L_V$, and $M_\bullet - M_{\text{bulge}}$ relations. In particular, we display the σ - and L -based predictions from McConnell et al. (2011b), who use the most up-to-date sample of directly measured black hole masses. The scaling relations derived from this sample are steepened by the large black hole masses in NGC 4889 and NGC 3842, as well as upward revisions of M_\bullet in M87 and M60 (Gebhardt & Thomas 2009; Shen & Gebhardt 2010; Gebhardt et al. 2011). The $M_\bullet - \sigma$ relation is additionally steepened by the inclusion of eight late-type galaxies with maser-based measurements of M_\bullet (Kondratko et al. 2008; Greene et al. 2010a; Kuo et al. 2011). As a result, the McConnell et al. (2011b) relations predict the largest values of M_\bullet in BCGs. For comparison, we have considered a large number of reported power-law fits to earlier galaxy samples and have determined which fits yield the lowest predicted values of M_\bullet for our BCGs. These minimum predictions are also displayed in Figure 4.18, in order to illustrate the full range of investigations to date. For the $M_\bullet - M_{\text{bulge}}$ relation, we display the predicted black hole masses from Magorrian et al. (1998) and Beifiori et al. (2012), which span the full range of M_{bulge} -based predictions. Along with the M_\bullet values predicted from

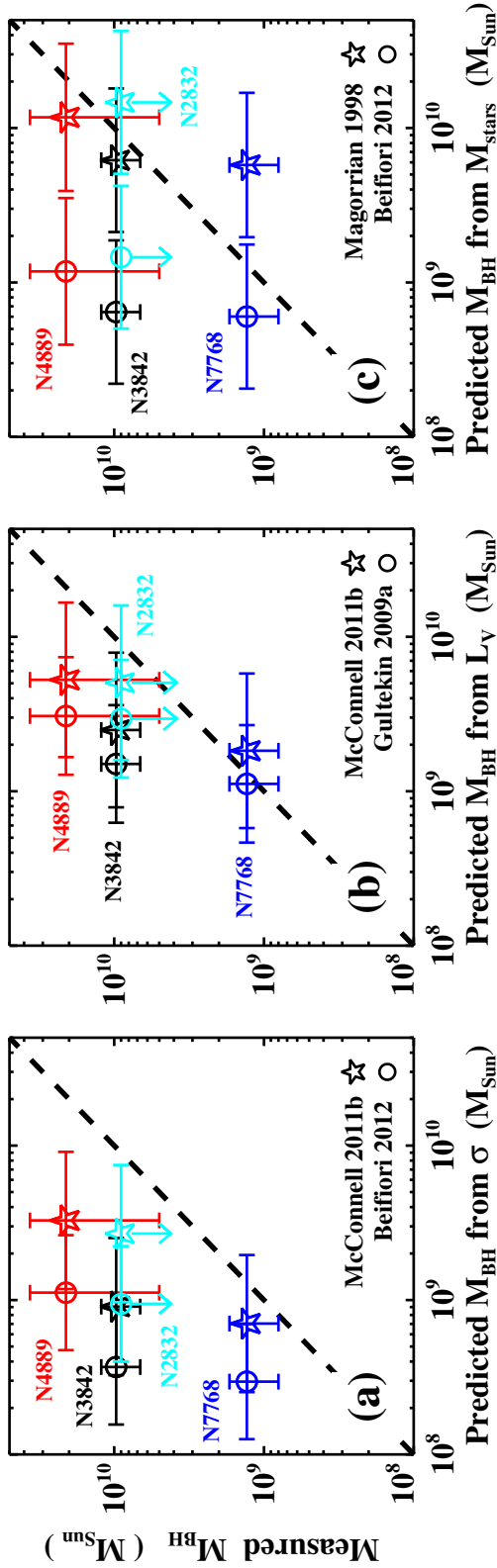


Figure 4.18: Measured black hole masses from this work versus predicted black hole masses from various scaling relations. (a) Predicted masses from the $M_{\bullet} - \sigma$ relation, $\log(M_{\bullet}) = \alpha + \beta \log(\sigma/200 \text{ km s}^{-1})$. Stars represent the relation of McConnell et al. (2011b; $\alpha = 8.29$, $\beta = 5.12$, $\epsilon_0 = 0.43$), and circles represent Beifiori et al. (2012; $\alpha = 7.99$, $\beta = 4.42$, $\epsilon_0 = 0.36$). (b) Predicted masses from the $M_{\bullet} - L_V$ relation, $\log(M_{\bullet}) = \alpha + \beta \log(L_V/10^{11} L_{\odot, V})$. Stars represent the relation of McConnell et al. (2011b; $\alpha = 9.16$, $\beta = 1.16$, $\epsilon_0 = 0.50$), and circles represent Gültekin et al. (2009; $\alpha = 8.95$, $\beta = 1.11$, $\epsilon_0 = 0.38$). (c) Predicted masses from the $M_{\bullet} - M_{\text{bulge}}$ relation, $\log(M_{\bullet}) = \alpha + \beta \log(M_{\text{bulge}}/10^{11} M_{\odot})$. Stars represent the relation of Magorrian et al. (1998; $\alpha = 8.77$, $\beta = 0.96$), and circles represent Beifiori et al. (2012; $\alpha = 7.84$, $\beta = 0.91$, $\epsilon_0 = 0.46$). The scaling relations for each panel were selected to span the widest range of predicted black hole masses. The horizontal error bars in each panel are dominated by the intrinsic scatter, ϵ_0 , in $\log(M_{\bullet})$, as estimated for each relation. Magorrian et al. (1998) do not provide an estimate of ϵ_0 with respect to M_{bulge} , so we have adopted $\epsilon_0 = 0.46$ from Beifiori et al. (2012) in panel (c). Horizontal error bars also contain a small contribution from measurement errors in σ , L_V , or M_{bulge} . Vertical error bars represent measurement errors in M_{\bullet} , as determined by our stellar orbit models.

the mean relations, we consider the intrinsic scatter, ϵ_0 , in $\log(M_\bullet)$ at fixed σ , L_V , or M_{bulge} . The horizontal error bars in Figure 4.18 essentially illustrate ϵ_0 ; measurement errors in σ , L_V , and M_{bulge} have much smaller effects on the predicted black hole masses.

The left panel of Figure 4.18 indicates that our measurements of M_\bullet in NGC 4889, NGC 3842, and NGC 7768 are all greater than the predicted values from various fits to the $M_\bullet - \sigma$ relation. For NGC 4889 and NGC 3842, the discrepancy exceeds the intrinsic scatter in M_\bullet , regardless of which fit to $M_\bullet - \sigma$ we select. For NGC 7768, M_\bullet exceeds the mean $M_\bullet - \sigma$ relations from Gültekin et al. (2009a), Graham et al. (2011) and Beifiori et al. (2012) by more than the corresponding estimates of ϵ_0 , but is consistent with the power-law fit and ϵ_0 estimate from McConnell et al. (2011b).

The predicted black hole masses from $M_\bullet - L_V$, indicated in the middle panel of Figure 4.18, are uniformly more massive than the σ -based predictions. Our large measurement errors for M_\bullet in NGC 4889, combined with estimates of ϵ_0 , yield agreement between the measured black hole mass and the $M_\bullet - L_V$ relation of McConnell et al. (2011b). However, the black hole in NGC 3842 is significantly more massive than predicted by any version of the $M_\bullet - L_V$ relation. For NGC 7768, our measurement of M_\bullet agrees with all versions of the $M_\bullet - L_V$ relation.

The right panel of Figure 4.18 shows that the $M_\bullet - M_{\text{bulge}}$ relation offers the widest range of predicted black hole masses from the literature. Only the historical relation from Magorrian et al. (1998) is consistent with the measured black hole masses of both NGC 4889 and NGC 3842. More recent estimates of $M_\bullet - M_{\text{bulge}}$ by Sani et al. (2011) and Beifiori et al. (2012), however, predict black hole masses an order of magnitude lower and are consistent with our measurement in NGC 7768.

Our upper limit for M_\bullet in NGC 2832 is consistent with the full range of predicted black hole masses from σ , L_V , and M_{bulge} .

There has been recent dispute over the existence of a fundamental correlation between M_\bullet and the Virial mass or circular velocity of the host galaxy’s dark matter halo (e.g., Ferrarese 2002; Kormendy & Bender 2011; Volonteri et al. 2011; also Beifiori et al. 2012 and references therein). We can compare NGC 4889 and NGC 3842 to this correlation by using v_c from their best-fitting LOG dark matter halos, or by computing the Virial mass of the best-fitting NFW halo for NGC 3842 ($M_{200} = 8.5 \times 10^{12} M_\odot$). Using either metric, we find that the black holes in NGC 4889 and NGC 3842 are several times more massive than those in galaxies with comparable dark matter halos.

The present-day black hole mass function is a testable prediction of galaxy evolution and feedback models. In particular, different models make divergent predictions for the number density of black holes with $M_\bullet \sim 10^9 - 10^{10} M_\odot$ (see, e.g., Kelly & Merloni 2012, and references therein). Our measurements of $M_\bullet \sim 10^{10} M_\odot$ in NGC 4889 and NGC 3842, plus the $6.3 \times 10^9 M_\odot$ black hole in M87 (Gebhardt et al. 2011) and the $4.7 \times 10^9 M_\odot$ black hole in M60 (Shen & Gebhardt 2010), place a lower limit of four galaxies with $M_\bullet > 10^{9.5} M_\odot$ within a local volume $\sim 10^6 \text{ Mpc}^3$. This is slightly higher than the space density predicted from models of proportional black hole and spheroid growth in major mergers (e.g., Hopkins et al. 2008). Several other BCGs lie within 100 Mpc, and the discovery of more black

holes with $M_{\bullet} > 10^{9.5} M_{\odot}$ could approach the predicted space density from models by Shen (2009), in which all quasars follow a universal light curve and the most massive black holes accrete gas until redshifts ~ 1 . Natarajan & Treister (2009) have predicted the black hole mass function from the X-ray luminosity function of active galactic nuclei (AGN). Our lower limit is consistent with their prediction using the original luminosity function from Ueda et al. (2003) but does not support their hypothesis of a truncated luminosity function for AGN with $M_{\bullet} > 10^9$. Models by Yoo et al. (2007) find that black hole-black hole mergers can increase M_{\bullet} by factors ~ 2 in galaxy clusters, with the largest black holes reaching $(1 - 1.5) \times 10^{10} M_{\odot}$. Black hole mergers also dominate the growth of the largest black holes in recent models by Fanidakis et al. (2011), but their prescriptions for quasar-mode (near-Eddington) and radio-mode (low-Eddington) accretion predict relatively low space densities for black holes with $M_{\bullet} > 10^9 M_{\odot}$.

The steep $L - \sigma$ relation for BCGs may arise from extreme size evolution, either via low-angular momentum mergers (e.g., Boylan-Kolchin et al. 2005; Boylan-Kolchin et al. 2006) or via cannibalism of numerous low-density systems (e.g., Ostriker & Tremaine 1975; Ostriker & Hausman 1977; Hopkins et al. 2010; Oser et al. 2010). In both scenarios, size evolution is driven by gas-poor or “dry” processes. Dry major mergers should preserve any initial relation between M_{\bullet} and stellar mass. For black hole growth to mirror stellar mass growth in the cannibalism scenario, the devoured satellites must indeed contain central black holes, and dynamical friction must deliver them efficiently to the center of the BCG. The forms of the $M_{\bullet} - \sigma$, $M_{\bullet} - L$, and $M_{\bullet} - M_{\text{bulge}}$ relations for BCGs could provide additional insight to their progenitors and growth mechanisms.

Our BCGs are not the only systems that have been observed to deviate from the black hole scaling relations. The $M_{\bullet} - \sigma$, $M_{\bullet} - L$, and $M_{\bullet} - M_{\text{bulge}}$ relations each have outliers that span a variety of galaxy masses and environments (e.g., Nowak et al. 2008; Greene et al. 2010a; Nowak et al. 2010; Reines et al. 2011; Bogdán et al. 2012b). In fact, some merging models predict that the most massive galaxies will exhibit smaller deviations from the mean black hole scaling relations, as a consequence of experiencing greater numbers of hierarchical mergers (Peng 2007; Volonteri & Natarajan 2009; Jahnke & Macciò 2011). In this scenario, black hole growth and galaxy growth need not be coupled through direct feedback processes. On the other hand, systematic offsets for M_{\bullet} in BCGs could point to unique evolutionary processes near cluster centers. A larger sample of BCGs with measured M_{\bullet} is necessary to distinguish between systematic trends and random scatter.

We aim to use high-resolution and wide-field kinematic data of several more galaxies to explore the high-mass slopes of the empirical correlations between galaxies and supermassive black holes, and to quantify the total and intrinsic scatter in M_{\bullet} for massive galaxies in different environments. This investigation and future studies are important tests for the hypothesis of universal scaling relations between black holes and their host galaxies, and for galaxy evolution models using different modes and timescales for black hole accretion.

Acknowledgments

We thank Jenny Greene, Remco van den Bosch, and Jonelle Walsh for helpful discussions during this investigation, and our referee for highlighting a number of complementary investigations. NJM thanks Anne-Marie Weijmans for instrument training at McDonald Observatory. This work was supported by NSF AST-1009663. Support for C.-P.M. is provided in part by the Miller Institute for Basic Research in Science, University of California, Berkeley. KG acknowledges support from NSF-0908639. The W. M. Keck Observatory is operated as a scientific partnership among the California Institute of Technology, the University of California, and the National Aeronautics and Space Administration. The Observatory was made possible by the generous financial support of the W. M. Keck Foundation. The Gemini Observatory is operated by the Association of Universities for Research in Astronomy, Inc., under a cooperative agreement with the NSF on behalf of the Gemini partnership: the National Science Foundation (United States), the Science and Technology Facilities Council (United Kingdom), the National Research Council (Canada), CONICYT (Chile), the Australian Research Council (Australia), Ministério da Ciência e Tecnologia (Brazil) and Ministerio de Ciencia, Tecnología e Innovación Productiva (Argentina). GMOS data were obtained under Program GN-2003A-Q-11. We thank the Cynthia and George Mitchell Foundation for funding the Mitchell Spectrograph, formerly known as VIRUS-P. Stellar orbit models were run on supercomputers at the Texas Advanced Computing Center (TACC). In addition, we wish to acknowledge the significant cultural role and reverence that the summit of Mauna Kea has always had within the indigenous Hawaiian community. We are most fortunate to have the opportunity to conduct observations from this mountain.

Chapter 5

Revisiting the Black Hole Scaling Relations

Abstract

Dynamical measurements of black hole masses (M_{\bullet}) in nearby galaxies are accumulating rapidly, and data from the past three years have potential to deliver new insights to the empirical scaling relations between black holes and their host galaxies. Here we highlight an updated compilation of 65 galaxies and black holes, and investigate the relations between M_{\bullet} and stellar velocity dispersion (σ), V -band luminosity (L), and bulge mass (M_{bulge}), for different galaxy subsamples. For the $M_{\bullet} - \sigma$ relation, we find discrepancies in the best-fit intercept for early-type versus late-type galaxies, and for core-profile versus power-law-profile galaxies; at fixed σ , these subsamples' predictions for M_{\bullet} vary by factors ~ 2 . We also find that high- σ galaxies follow a steeper $M_{\bullet} - \sigma$ relation than low- σ galaxies, for cutoff values near $\sigma \sim 150 - 200 \text{ km s}^{-1}$. Our $M_{\bullet} - L$ and $M_{\bullet} - M_{\text{bulge}}$ relations bear closer resemblance to the results from older compilations, and core and power-law galaxies yield similar L - and M_{bulge} -based predictions for M_{\bullet} . Various models of black hole growth and galaxy merging predict that the intrinsic scatter in $\log(M_{\bullet})$ will vary as a function of σ or galaxy mass. Using the current data set, we find no evidence that scatter varies systematically with σ , and weak evidence for increased scatter in galaxies with $L < 10^{10} L_{\odot}$ or $M_{\text{bulge}} < 10^{10.5} M_{\odot}$.

5.1 Introduction

Empirical correlations between the masses, M_{\bullet} , of supermassive black holes and different properties of their host galaxies have proliferated in the past decade. Power-law fits to these correlations provide efficient means to estimate M_{\bullet} in large samples of galaxies, or in individual objects with insufficient data to measure M_{\bullet} from the dynamics of stars, gas, or masers. Still, the black hole scaling relations are not universal tools. Their predictive

abilities for a given scientific case can be improved by using the most relevant sample of measured black hole masses and host galaxy properties.

Correlations between black hole masses and numerous properties of their host galaxies have been explored in the literature. These include scaling relations between M_{\bullet} and stellar velocity dispersion (e.g., Ferrarese & Merritt 2000; Gebhardt et al. 2000a; Merritt & Ferrarese 2001; Tremaine et al. 2002; Wyithe 2006a,b; Hu 2008; Graham et al. 2011; Gültekin et al. 2009a; Schulze & Gebhardt 2011; McConnell et al. 2011b; Beifiori et al. 2012), and between M_{\bullet} and the stellar mass of the bulge (e.g., Magorrian et al. 1998; Marconi & Hunt 2003; Häring & Rix 2004; Hu 2009; Sani et al. 2011; Beifiori et al. 2012). Various scaling relations between M_{\bullet} and the photometric properties of the bulge have also been examined: bulge optical luminosity (e.g., Kormendy & Richstone 1995; Kormendy & Gebhardt 2001; Gültekin et al. 2009a; Schulze & Gebhardt 2011; McConnell et al. 2011b; Beifiori et al. 2012), bulge near-infrared luminosity (e.g., Marconi & Hunt 2003; McLure & Dunlop 2002, 2004; Graham 2007; Hu 2009; Sani et al. 2011), total luminosity (e.g., Kormendy & Gebhardt 2001; Kormendy et al. 2011; Beifiori et al. 2012), and bulge concentration or Sérsic index (e.g., Graham et al. 2001; Graham & Driver 2007; Beifiori et al. 2012). On a larger scale, correlations between M_{\bullet} and the circular velocity or dynamical mass of the dark matter halo have been reported as well as disputed (e.g., Ferrarese 2002; Baes et al. 2003; Zasov et al. 2005; Kormendy & Bender 2011; Volonteri et al. 2011; Beifiori et al. 2012). More recently, M_{\bullet} have been found to correlate with the number and total mass of globular clusters in the host galaxy (e.g., Burkert & Tremaine 2010; Harris & Harris 2011; Sadoun & Colin 2012). In core-profile galaxies, Lauer et al. (2007a) and Kormendy & Bender (2009) have explored correlations between M_{\bullet} and the core radius, or the total “light deficit” of the core relative to a Sérsic profile.

New kinematic data and modeling efforts have substantially revised and expanded the various samples used in all of the studies above. In this chapter, we take advantage of these recent developments and present an updated compilation of 65 black holes and their host galaxies. Multiple collaborations have put forth considerable and commendable efforts to assemble measurements of black holes and host galaxies from myriad sources. Still, the sample of galaxies with directly measured M_{\bullet} is growing rapidly enough for the empirical scaling relations to evolve significantly over only a few years. Our sample is a significant update from two recent compilations by Gültekin et al. (2009a) and Graham et al. (2011). Compared with the 49 objects in Gültekin et al. (2009a), 18 black holes in our present sample are new measurements, and 18 masses are updated values from better data and/or more sophisticated modeling. Compared with the 64 objects in Graham et al. (2011) (an update of Graham 2008), 28 of our black hole masses are new or updates. Some of the most significant updates in our sample are galaxies with extremely high M_{\bullet} (Shen & Gebhardt 2010; Gebhardt et al. 2011; McConnell et al. 2011a,b; McConnell et al. 2012) and galaxies with some of the smallest observed central black holes (Greene et al. 2010a; Nowak et al. 2010; Kormendy et al. 2011; Kuo et al. 2011). The Gültekin et al. (2009a) and Graham (2008) samples differ by only a few galaxies, based on the authors’ respective judgments about which dynamical measurements are reliable.

We investigate how M_{\bullet} scales with stellar velocity dispersion (σ), V -band bulge luminosity (L), and bulge mass (M_{bulge}). We focus on these correlations because we have high confidence in the measured values of σ and L for galaxies with dynamical measurements of M_{\bullet} . Dynamical studies of individual galaxies connect L to M_{bulge} . As we report below, our new compilation results in different scaling relations from the recent study by Beifiori et al. (2012), who combined the old sample of 49 black holes from Gültekin et al. (2009a) with a larger sample of upper limits on M_{\bullet} from Beifiori et al. (2009). In particular, we find a steeper power law for the $M_{\bullet} - \sigma$ and $M_{\bullet} - L$ relations.

Another important measurable quantity is the intrinsic or cosmic scatter in M_{\bullet} for fixed galaxy properties. Quantifying the scatter in M_{\bullet} is useful for identifying the tightest correlations from which to predict M_{\bullet} and for testing different scenarios of galaxy and black hole growth. In particular, models of stochastic black hole and galaxy growth via hierarchical merging predict decreasing scatter in M_{\bullet} as galaxy mass increases (e.g., Peng 2007; Jahnke & Macciò 2011).

Here we attempt to quantify the scaling relations for different subsamples of galaxies with dynamically measured black hole masses. In particular, we examine different cuts in σ , L , and M_{bulge} , as well as cuts based on galaxies' morphologies and surface brightness profiles.

In Section 5.2, we summarize a compilation of 65 black hole mass measurements and an updated compilation of 34 bulge masses from dynamical studies. In Section 5.3, we present our fits to the $M_{\bullet} - \sigma$, $M_{\bullet} - L$, and $M_{\bullet} - M_{\text{bulge}}$ relations and highlight subsamples that yield significant variations in the best-fit power laws. In Section 5.4, we discuss scatter in M_{\bullet} and attempt to quantify its behavior as a function of σ , L , and M_{bulge} . In Section 5.5, we discuss how our analysis of galaxy subsamples may be beneficial for various applications of the black hole scaling relations.

5.2 An Updated Black Hole and Galaxy Sample

We have updated our previous compilation of 67 dynamical black hole measurements, presented in the supplementary materials to McConnell et al. (2011b). The current sample includes one new measurement of M_{\bullet} (McConnell et al. 2012) and two updated black hole masses (Jardel et al. 2011; Walsh et al. 2012). For NGC 5128, we have adopted the value $M_{\bullet} = (5.3 \pm 1.2) \times 10^7 M_{\odot}$ (at a distance of 3.5 Mpc), by combining the $1-\sigma$ confidence intervals from Neumayer et al. (2007) and Cappellari et al. (2009).

We have removed three galaxies whose original measurements have exceptional complications. Lodato & Bertin (2003) measured non-Keplerian maser velocities in NGC 1068 and estimated M_{\bullet} by modeling a self-gravitating disk. Still, other physical processes might reproduce the observed maser motions. Atkinson et al. (2005) reported a measurement of M_{\bullet} in NGC 2748 but noted that heavy extinction could corrupt their attempt to locate the center of the nuclear gas disk. Gebhardt et al. (2003) justified classifying the central point source of NGC 7457 as an active galactic nucleus, but their arguments permit the central mass to be shared by an accreting black hole and a nuclear star cluster. Our final sample

contains 65 galaxies, which are listed in Table 5.1.

For the $M_{\bullet} - \sigma$ relation, we have also considered upper limits for M_{\bullet} in 89 galaxies from Beifiori et al. (2012), plus 3 new upper limits (Schulze & Gebhardt 2011; Gültekin et al. 2011b; McConnell et al. 2012). Five additional galaxies in the Beifiori et al. (2012) upper limit sample have recently obtained secure measurements of M_{\bullet} and are included in our 65-galaxy sample. Including upper limits results in a lower normalization (intercept) for the $M_{\bullet} - \sigma$ relation, but does not significantly alter the relative trends between different galaxy subsamples.

In our investigation of the $M_{\bullet} - \sigma$ correlation below, we will consider two different definitions of σ . Both definitions use spatially resolved kinematics $\sigma(r)$ and $v(r)$, integrated out to one effective radius (r_{eff}):

$$\sigma^2 \equiv \frac{\int_{r_{\text{min}}}^{r_{\text{eff}}} [\sigma^2(r) + v^2(r)] I(r) dr}{\int_{r_{\text{min}}}^{r_{\text{eff}}} I(r) dr}, \quad (5.1)$$

where $I(r)$ is the galaxy's one-dimensional stellar surface brightness profile. In Gültekin et al. (2009a) and most other studies, the lower integration limit r_{min} is set to zero and sampled at the smallest scale allowed by the data. This definition of σ , however, includes signal from within the black hole radius of influence, $r_{\text{inf}} \equiv GM_{\bullet}\sigma^{-2}$. In some galaxies, particularly the most massive ellipticals, σ decreases substantially when spatially resolved data within r_{inf} are excluded. Setting $r_{\text{min}} = r_{\text{inf}}$ produces an alternative definition of σ , which emphasizes the global structure of the galaxy and is less sensitive to angular resolution. We have set $r_{\text{min}} = r_{\text{inf}}$ for nine galaxies whose kinematics within r_{inf} are notably different from kinematics at larger radii. These galaxies are listed in Table 5.2. All nine galaxies are massive ($\sigma \geq 230 \text{ km s}^{-1}$ using either definition).

For the $M_{\bullet} - M_{\text{bulge}}$ relation, we have compiled the bulge stellar masses for 34 galaxies. Among them, 15 bulge masses are taken from Häring & Rix (2004), who used spherical Jeans models to fit stellar kinematics. For 21 more galaxies, we have multiplied the V -band luminosity in Table 5.1 with the bulge mass-to-light ratio (M/L) derived from kinematics and dynamical modeling of stars or gas (see Table 5.1 for references). Where necessary, M/L is converted to V -band using galaxy colors. The values of M_{bulge} are scaled to reflect the assumed distances in Table 5.1.

Most of the dynamical models behind our compiled values of M_{bulge} have assumed that mass follows light. This assumption can be appropriate in the inner regions of galaxies, where dark matter does not contribute significantly to the total enclosed mass. However, several investigations include kinematic measurements out to large radii. Furthermore, some galaxies exhibit contradictions between the dynamical estimates of M/L and estimates of M/L from stellar population synthesis models (e.g., Cappellari et al. 2006; Conroy & van Dokkum 2012). For this reason, we have adopted a conservative approach and assigned a minimum error of 0.24 dex to each value of M_{bulge} , corresponding to the interval $0.5M_{\text{bulge}} - 1.5M_{\text{bulge}}$. To test how well our M_{bulge} values represent the stellar mass of each galaxy, we have also fit the $M_{\bullet} - M_{\text{bulge}}$ relation using a sample of 16 galaxies for which M_{bulge} was computed from

Table 5.1: Galaxies with dynamical measurements of M_{\bullet} through May 2012

| Galaxy | M_{\bullet} (+, -) (M_{\odot}) | Ref. | σ (km s^{-1}) | $\log L_V$ | M_{bulge} (M_{\odot}) | Ref. | r_{inf} (arcsec) | Morph. | D (Mpc) | Method |
|------------------------|-----------------------------------------|------|------------------------------------|--------------|---------------------------------------|------|------------------------------|---------|--------------|--------|
| Milky Way ^a | 4.1 (0.6,0.6) e6 | 1,2 | 103 ± 20 | | | | 43.0 | S | 0.008 | stars |
| A1836-BCG | 3.9 (0.4,0.6) e9 | 3 | 288 ± 14 | 11.26 ± 0.06 | | | 0.27 | E (C) | 157.5 | gas |
| A3565-BCG | 1.4 (0.3,0.2) e9 | 3 | 322 ± 16 | 11.24 ± 0.06 | | | 0.22 | E (C) | 54.4 | gas |
| Circinus | 1.7 (0.4,0.3) e6 | 4 | 158 ± 18 | | | | 0.02 | S | 4.0 | masers |
| IC 1459 | 2.8 (1.1,1.2) e9 | 5 | 315 ± 16 | 10.96 ± 0.06 | 3.09e11 | 45 | 0.81 | E (C) | 30.9 | stars |
| N221 (M32) | 3.1 (0.6,0.6) e6 | 6 | 75 ± 3 | 8.66 ± 0.02 | 8.32e8 | 45 | 0.57 | E (I) | 0.86 | stars |
| N224 (M31) | 1.5 (0.9,0.3) e8 | 7 | 160 ± 8 | | 3.98e10 | 45 | 6.5 | S | 0.80 | stars |
| N524 | 8.3 (0.9,0.4) e8 | 8 | 235 ± 12 | 10.60 ± 0.04 | | | 0.57 | S0 (C) | 23.3 | stars |
| N821 | 1.8 (0.8,0.8) e8 | 9 | 209 ± 10 | 10.43 ± 0.05 | 2.09e11 | 9 | 0.14 | E (I) | 25.5 | stars |
| N1023 | 4.6 (0.5,0.5) e7 | 10 | 205 ± 10 | 10.18 ± 0.11 | 8.32e10 | 45 | 0.08 | S0 (pl) | 12.1 | stars |
| N1194 ^b | 6.8 (0.3,0.3) e7 | 11 | 148 ⁺²⁶ ₋₂₂ | | | | 0.05 | S0 | 55.5 | masers |
| N1300 | 7.1 (3.4,1.8) e7 | 12 | 218 ± 10 | | | | 0.07 | S (pl) | 20.1 | gas |
| N1316 | 1.5 (0.25,0.26) e8 | 13 | 226 ± 11 | 11.09 ± 0.05 | | | 0.14 | E (I) | 18.6 | stars |
| N1332 | 1.45 (0.2,0.2) e9 | 14 | 328 ± 16 | 10.14 ± 0.05 | | | 0.54 | S0 (pl) | 22.3 | stars |
| N1399 ^c | 5.1 (0.7,0.7) e8 | 15 | 296 ± 15 | 10.78 ± 0.04 | 3.98e11 | 46 | 0.25 | E (C) | 21.1 | stars |
| N1399 ^c | 1.3 (0.5,0.66) e9 | 16 | 296 ± 15 | 10.78 ± 0.04 | 3.98e11 | 46 | 0.63 | E (C) | 21.1 | stars |
| N2273 ^b | 7.8 (0.4,0.4) e6 | 11 | 144 ⁺¹⁸ ₋₁₅ | | | | 0.01 | S | 26.8 | masers |
| N2549 | 1.4 (0.07,0.4) e7 | 8 | 145 ± 7 | 9.53 ± 0.04 | 1.95e10 | 8 | 0.05 | S0 (pl) | 12.3 | stars |
| N2787 | 4.3 (0.4,0.5) e7 | 17 | 189 ± 9 | | | | 0.14 | S0 (pl) | 7.9 | gas |
| N2960 ^b | 1.21 (0.05,0.05) e7 | 11 | 166 ⁺¹⁶ ₋₁₅ | | | | 0.01 | S | 75.3 | masers |
| N3031 (M81) | 8.0 (2.0,1.1) e7 | 18 | 143 ± 7 | | | | 0.85 | S | 4.1 | gas |
| N3115 | 9.6 (5.4,2.9) e8 | 19 | 230 ± 11 | 10.40 ± 0.02 | 1.70e11 | 45 | 1.6 | S0 (pl) | 10.2 | stars |
| N3227 | 1.5 (0.5,0.8) e7 | 20 | 133 ± 12 | | | | 0.04 | S | 17.0 | stars |
| N3245 | 2.2 (0.5,0.5) e8 | 21 | 205 ± 10 | | 7.24e10 | 45 | 0.21 | S0 (pl) | 22.1 | gas |
| N3368 | 7.5 (1.5,1.5) e6 | 22 | 122 ⁺²⁸ ₋₂₄ | | | | 0.04 | S | 10.4 | stars |
| N3377 | 1.9 (1.0,1.0) e8 | 9 | 145 ± 7 | 9.98 ± 0.04 | 2.51e10 | 9 | 0.69 | E (pl) | 11.7 | stars |
| N3379 (M105) | 4.6 (1.1,1.2) e8 | 23 | 206 ± 10 | 10.37 ± 0.01 | 7.59e10 | 45 | 0.83 | E (C) | 11.7 | stars |

Continued on next page

Table 5.1, continued

| Galaxy | M_{\bullet} (+, -) (M_{\odot}) | Ref. | σ (km s^{-1}) | $\log L_V$ | M_{bulge} (M_{\odot}) | Ref. | r_{inf} (arcsec) | Morph. | D (Mpc) | Method |
|--------------------|-----------------------------------------|------|------------------------------------|------------------|---------------------------------------|------|------------------------------|---------|--------------|--------|
| N3384 | 1.1 (0.5,0.5) e7 | 9 | 143 ± 7 | 9.90 ± 0.09 | $1.91e10$ | 9 | 0.04 | S0 (pl) | 11.7 | stars |
| N3393 | 3.3 (0.2,0.2) e7 | 24 | 148 ± 10 | | | | 0.03 | S | 53.6 | masers |
| N3489 | 6.0 (0.8,0.8) e6 | 22 | 100^{+15}_{-11} | | | | 0.04 | S0 | 12.1 | stars |
| N3585 | 3.4 (1.5,0.6) e8 | 25 | 213 ± 10 | 10.65 ± 0.08 | $1.51e11$ | 25 | 0.31 | S0 (I) | 21.2 | stars |
| N3607 ^d | 1.2 (0.4,0.41) e8 | 25 | 229 ± 11 | | | | 0.10 | E (C) | 19.9 | stars |
| N3608 | 4.7 (1.0,1.0) e8 | 9 | 182 ± 9 | 10.35 ± 0.04 | $7.76e10$ | 9 | 0.55 | E (C) | 23.0 | stars |
| N3842 | 9.7 (3.0,2.5) e9 | 26 | 270 ± 14 | 11.20 ± 0.05 | $1.55e12$ | 44 | 1.2 | E (C) | 98.4 | stars |
| N3998 | 8.8 (0.7,0.7) e8 | 27 | 272 ± 14 | 9.95 ± 0.04 | | | 0.71 | S0 (pl) | 14.9 | stars |
| N4026 | 2.1 (0.7,0.4) e8 | 25 | 180 ± 9 | 9.86 ± 0.08 | $3.24e10$ | 25 | 0.37 | S0 (pl) | 15.6 | stars |
| N4258 | 3.78 (0.01,0.01) e7 | 28 | 115 ± 10 | | | | 0.35 | S | 7.2 | masers |
| N4261 | 5.5 (1.1,1.2) e8 | 29 | 315 ± 15 | 11.02 ± 0.02 | $8.51e11$ | 45 | 0.15 | E (C) | 33.4 | gas |
| N4291 | 9.2 (2.9,2.9) e8 | 9 | 242 ± 12 | 10.20 ± 0.05 | $9.55e10$ | 9 | 0.56 | E (C) | 25.0 | stars |
| N4342 ^e | 4.6 (2.6,1.5) e8 | 30 | 255 ± 11 | | $1.82e10$ | 45 | 0.35 | S0 (pl) | 23.0 | stars |
| N4374 (M84) | 8.5 (0.9,0.8) e8 | 31 | 296 ± 14 | 10.91 ± 0.02 | $3.31e11$ | 45 | 0.51 | E (C) | 17.0 | gas |
| N4388 ^b | 8.8 (0.2,0.2) e6 | 11 | 107^{+8} | | | | 0.03 | S | 19.8 | masers |
| N4459 | 7.4 (1.4,1.4) e7 | 17 | 167 ± 8 | 10.36 ± 0.02 | | | 0.14 | E (pl) | 17.0 | gas |
| N4473 | 1.0 (0.5,0.5) e8 | 9 | 190 ± 9 | 10.39 ± 0.02 | $1.82e11$ | 9 | 0.15 | E (C) | 17.0 | stars |
| N4486 (M87) | 6.3 (0.3,0.4) e9 | 32 | 324^{+28}_{-16} | 11.10 ± 0.02 | $1.35e12$ | 47 | 3.1 | E (C) | 17.0 | stars |
| N4486A | 1.3 (0.5,0.48) e7 | 33 | 111 ± 5 | 9.41 ± 0.02 | | | 0.06 | E (pl) | 17.0 | stars |
| N4564 ^f | 9.4 (2.6,2.6) e7 | 9 | 162 ± 8 | | $5.01e10$ | 45 | 0.19 | S0 (pl) | 17.0 | stars |
| N4594 (M104) | 6.9 (0.5,0.4) e8 | 34 | 230^{+62}_{-12} | 10.80 ± 0.06 | $3.63e11$ | 45 | 1.1 | S | 10.3 | stars |
| N4596 | 8.4 (3.6,2.5) e7 | 17 | 136 ± 6 | | | | 0.22 | S0 (pl) | 18.0 | gas |
| N4649 (M60) | 4.7 (1.1,1.0) e9 | 35 | 341 ± 17 | 10.99 ± 0.02 | $7.76e11$ | 35 | 2.2 | E (C) | 16.5 | stars |
| N4697 | 2.0 (0.2,0.2) e8 | 9 | 177 ± 8 | 10.45 ± 0.04 | $1.26e11$ | 9 | 0.46 | E (pl) | 12.4 | stars |
| N4736 (M94) | 6.68 (1.54,1.54) e6 | 36 | 112 ± 6 | 9.75 ± 0.04 | | | 0.10 | S | 4.9 | stars |
| N4826 (M64) | 1.36 (0.35,0.34) e6 | 36 | 96 ± 5 | 9.52 ± 0.04 | | | 0.02 | S | 6.4 | stars |

Continued on next page

Table 5.1, continued

| Galaxy | M_{\bullet} (+, -) (M_{\odot}) | Ref. | σ (km s^{-1}) | $\log L_V$ | M_{bulge} (M_{\odot}) | Ref. | r_{inf} (arcsec) | Morph. | D (Mpc) | Method |
|--------------------|-----------------------------------------|-------|------------------------------------|------------------|---------------------------------------|------|------------------------------|----------|--------------|--------|
| N4889 | 2.1 (1.6,1.55) e10 | 26 | 347 ± 17 | 11.48 ± 0.05 | $1.74\text{e}12$ | 46 | 1.5 | E (C) | 103.2 | stars |
| N5077 | 8.0 (5.0,3.3) e8 | 37 | 222 ± 11 | 10.75 ± 0.05 | $3.63\text{e}11$ | 37 | 0.32 | E (C) | 44.9 | gas |
| N5128 | 5.3 (1.2,1.2) e7 | 38,39 | 150 ± 7 | 10.46 ± 0.03 | | | 0.60 | S0/E (C) | 3.5 | stars |
| N5576 | 1.8 (0.3,0.4) e8 | 25 | 183 ± 9 | 10.44 ± 0.05 | $1.02\text{e}11$ | 25 | 0.18 | E (C) | 27.1 | stars |
| N5845 | 5.4 (1.7,1.7) e8 | 9 | 234 ± 11 | 9.84 ± 0.05 | $3.72\text{e}10$ | 9 | 0.31 | E (pl) | 28.7 | stars |
| N6086 | 3.8 (1.7,1.2) e9 | 40 | 318 ± 16 | 11.23 ± 0.05 | $1.41\text{e}12$ | 40 | 0.24 | E (C) | 139.1 | stars |
| N6251 | 6.0 (2.0,2.0) e8 | 41 | 290 ± 14 | | $5.62\text{e}11$ | 45 | 0.06 | E (pl) | 106.0 | gas |
| N6264 ^b | 3.03 (0.05,0.04) e7 | 11 | 158^{+16}_{-14} | | | | 0.01 | S | 145.4 | masers |
| N6323 ^b | 9.8 (0.1,0.1) e6 | 11 | 158^{+28}_{-23} | | | | 0.003 | S | 110.5 | masers |
| N7052 | 4.0 (2.8,1.6) e8 | 42 | 266 ± 13 | 10.92 ± 0.04 | $3.47\text{e}11$ | 45 | 0.07 | E (C) | 70.9 | gas |
| N7582 | 5.5 (1.6,1.1) e7 | 43 | 156 ± 19 | | | | 0.09 | S | 22.3 | gas |
| N7768 | 1.3 (0.5,0.4) e9 | 44 | 257 ± 13 | 11.09 ± 0.05 | $1.15\text{e}12$ | 44 | 0.14 | E (C) | 112.8 | stars |
| U3789 ^b | 1.08 (0.06,0.05) e7 | 11 | 107^{+13}_{-12} | | | | 0.02 | S | 48.4 | masers |

References: (1 = Ghez et al. 2008) ; (2 = Gillessen et al. 2009) ; (3 = Dalla Bontà et al. 2009) ; (4 = Greenhill et al. 2003) ; (5 = Cappellari et al. 2002) ; (6 = Verolme et al. 2002) ; (7 = Bender et al. 2005) ; (8 = Krajnović et al. 2009) ; (9 = Schulze & Gebhardt 2011) ; (10 = Bower et al. 2001) ; (11 = Kuo et al. 2011) ; (12 = Atkinson et al. 2005) ; (13 = Nowak et al. 2008) ; (14 = Rusli et al. 2011) ; (15 = Gebhardt et al. 2007) ; (16 = Houghton et al. 2006) ; (17 = Sarzi et al. 2001) ; (18 = Devereux et al. 2003) ; (19 = Emsellem et al. 1999) ; (20 = Davies et al. 2006) ; (21 = Barth et al. 2001) ; (22 = Nowak et al. 2010) ; (23 = van den Bosch & de Zeeuw 2010) ; (24 = Kondratko et al. 2008) ; (25 = Gültekin et al. 2009b) ; (26 = McConnell et al. 2011b) ; (27 = Walsh et al. 2012) ; (28 = Herrnstein et al. 2005) ; (29 = Ferrarese et al. 1996) ; (30 = Cretton & van den Bosch 1999a) ; (31 = Walsh et al. 2010) ; (32 = Gebhardt et al. 2011) ; (33 = Nowak et al. 2007) ; (34 = Jarrel et al. 2011) ; (35 = Shen & Gebhardt 2010) ; (36 = Kormendy et al. 2011) ; (37 = de Francesco et al. 2008) ; (38 = Neumayer et al. 2007) ; (39 = Cappellari et al. 2009) ; (40 = McConnell et al. 2011a) ; (41 = Ferrarese & Ford 1999) ; (42 = van der Marel & van den Bosch 1998) ; (43 = Wold et al. 2006) ; (44 = McConnell et al. 2012) ; (45 = Häring & Rix 2004) ; (46 = Magorrian et al. 1998) ; (47 = Gebhardt & Thomas 2009).

Table 5.1 Notes:

Bulge luminosity L_V and bulge mass M_{bulge} are in solar units. Quoted errors (+, -) for M_{\bullet} are 68% confidence intervals. We assume 0.24 dex uncertainty for all M_{bulge} values. Morphologies include designations for power-law (pl), core (C), and intermediate (I) surface brightness profiles.

^a The literature contains a large number of estimates for the velocity dispersion of our Galaxy’s bulge, using different kinematic tracers at different radii. We use the radially averaged measurement of $\sigma = 103 \pm 20 \text{ km s}^{-1}$ from Tremaine et al. (2002).

^b Maser-based black hole masses for several galaxies are presented in Greene et al. (2010a) and Kuo et al. (2011). We use the velocity dispersions presented in Greene et al. (2010a). For consistency with the rest of our sample, we use the black hole masses from Kuo et al. (2011), which agree with the values in Greene et al. (2010a) but do not include distance uncertainties in the overall uncertainty for M_{\bullet} . Braatz et al. (2010) provide an updated distance and black hole mass for UGC 3789, which are consistent with the values we adopt from Kuo et al. (2011).

^c Following Gültekin et al. (2009a), our sample includes two distinct measurements for NGC 1399. We weight each of these measurements by 50% when performing fits to the black hole scaling relations.

^d The literature contains two inconsistent estimates of the V -band luminosity of NGC 3607: $M_V = -21.62$ in Gültekin et al. (2009a), and $M_V = -19.88$ in Lauer et al. (2007a)

^e For NGC 4342, we have rescaled M_{bulge} and M_{\bullet} to the updated distance of 23 Mpc by Bogdán et al. (2012a).

^f The literature contains two inconsistent estimates of the V -band bulge luminosity of NGC 4564: $M_V = -19.60$ in Gültekin et al. (2009a), and $M_V = -20.26$ in Lauer et al. (2007a).

the stellar mass-to-light ratio, M_*/L . Our fits using the dynamical M_{bulge} and stellar M_{bulge} samples are fully consistent.

5.3 Subsamples and Power-law Fits

We consider black hole scaling relations for different subsamples of galaxies. Our power law fit to each subsample is defined in log space by an intercept α and slope β :

$$\log_{10}(M_{\bullet}) = \alpha + \beta \log_{10} X, \quad (5.2)$$

where $X = \sigma/200 \text{ km s}^{-1}$, $L/10^{11} L_{\odot}$, or $M_{\text{bulge}}/10^{11} M_{\odot}$ for the three scaling relations. We use the MPFITEXY procedure by Williams et al. (2010), which considers measurement errors in two variables and includes an intrinsic scatter term in $\log(M_{\bullet})$. For samples including upper limits on M_{\bullet} , we use the BIVAR EM algorithm in the ASURV software package by Lavalley et al. (1992), which implements the methods presented in Isobe et al. (1986). We have chosen these fitting algorithms because they are publicly available¹. Other procedures should yield consistent fits, as discussed in Section 5.3.3 below.

¹The IDL source code of MPFITEXY is available at <http://purl.org/mike/mpfitexy>. ASURV is available at <http://www2.astro.psu.edu/statcodes/asurv>.

Table 5.2: Galaxies with multiple definitions of σ

| Galaxy | Ref. | r_{inf} (arcsec) | σ ($0 - r_{\text{eff}}$) (km s^{-1}) | σ ($r_{\text{inf}} - r_{\text{eff}}$) (km s^{-1}) |
|----------|------|------------------------------|-------------------------------------------------------------|--------------------------------------------------------------------------|
| IC 1459 | 1 | 0.8 | 340 | 315 |
| NGC 1399 | 2,3 | 0.6 | 337 | 296 |
| NGC 3842 | 4 | 1.2 | 275 | 270 |
| NGC 3998 | 5 | 0.7 | 286 | 272 |
| NGC 4486 | 6 | 2.1 | 375 | 324 |
| NGC 4594 | 7 | 1.2 | 240 | 230 |
| NGC 4649 | 8 | 2.2 | 385 | 341 |
| NGC 4889 | 4 | 1.5 | 360 | 347 |
| NGC 7768 | 4 | 0.14 | 265 | 257 |

Notes: References for kinematic data used to derive r_{inf} are: (1 = Cappellari et al. 2002) ; (2 = Graham et al. 1998) ; (3 = Gebhardt et al. 2007) ; (4 = McConnell et al. 2012) ; (5 = Walsh et al. 2012) ; (6 = Gebhardt et al. 2011) ; (7 = Jardel et al. 2011) ; (8 = Pinkney et al. 2003).

5.3.1 $M_{\bullet} - \sigma$

Our fits to $M_{\bullet}(\sigma)$ for various galaxy subsamples are summarized in Table 5.3. Our entire sample of 65 galaxies yields an intercept $\alpha = 8.29 \pm 0.05$ and slope $\beta = 5.48 \pm 0.34$. When upper limits are added, the sample of 157 galaxies yields $\alpha = 8.09 \pm 0.05$ and $\beta = 5.29 \pm 0.30$. The reduced intercept is a natural consequence of considering upper limits, while the slightly shallower slope is consistent within errors.

Fitting early- and late-type galaxies separately yields slightly shallower slopes ($\beta \approx 5.0$), but the late-type galaxies have a significantly lower intercept; at fixed σ , our fits predict $M_{\bullet, \text{early}} \sim 2 M_{\bullet, \text{late}}$. Because most of the late-type bulges have low σ , the split in intercepts is consistent with a steeper total sample. Figure 5.1a shows the $M_{\bullet} - \sigma$ correlation for early-versus late-type galaxies.

We obtain different fits when the early-type galaxies are classified by the slopes of their inner surface brightness profiles, $\gamma = -d \log I / d \log r$. Faber et al. (1997) and Lauer et al. (2007b) distinguished “power-law” galaxies with $\gamma > 0.5$ from “core” galaxies with $\gamma < 0.3$. Core galaxies tend to be more massive than power-law galaxies, and there is some evidence that M_{\bullet} correlates with properties of the inner stellar core (Lauer et al. 2007a; Kormendy & Bender 2009). In our fits to $M_{\bullet}(\sigma)$, core galaxies have a steeper slope and higher intercept than power-law galaxies: $\beta \approx 5.1$ versus 4.4, and $\alpha \approx 8.4$ versus 8.2. At high σ ($\sim 300 \text{ km s}^{-1}$), our fits predict $M_{\bullet, \text{core}} \sim 2 M_{\bullet, \text{pow}}$. Figure 5.1b shows the $M_{\bullet} - \sigma$ correlation for core versus power-law galaxies.

5.3.2 $M_{\bullet} - L$ and $M_{\bullet} - M_{\text{bulge}}$

Tables 5.4 and 5.5 contain our fits to $M_{\bullet}(L)$ and $M_{\bullet}(M_{\text{bulge}})$. We have fit 40 galaxies with reliable V -band luminosities and measure an $M_{\bullet}(L)$ slope of 1.24 ± 0.15 . For 34 with dynamically measured bulge masses, we measure an $M_{\bullet}(M_{\text{bulge}})$ slope of 1.07 ± 0.12 . Our $M_{\bullet} - L$ and $M_{\bullet} - M_{\text{bulge}}$ samples are dominated by early-type galaxies; removing the few late-type galaxies has a negligible effect on the fits. The $M_{\bullet} - L$ and $M_{\bullet} - M_{\text{bulge}}$ relations do not show significant differences between core and power-law galaxies, as shown in Figures 5.1d and 5.1f.

We have also experimented with dividing the galaxies into low- σ and high- σ subsamples, separated by a cutoff value σ_{cut} . Figure 5.2 illustrates the best-fit power-law parameters as σ_{cut} is varied. Although we find no significant discrepancies, the high- σ galaxies consistently exhibit a steeper $M_{\bullet} - \sigma$ slope ($\beta \sim 6$).

We have also tried fitting $M_{\bullet}(\sigma)$ for subsamples defined by cuts in L and M_{bulge} . Some of the high- L and high- M_{bulge} subsamples exhibit a steep $M_{\bullet} - \sigma$ slope, but with large uncertainties. Two examples are listed in Table 5.3.

We consider the two different definitions of σ discussed in Section 5.2. Excluding data within r_{inf} has the overall effect of decreasing σ and increasing the slope of the $M_{\bullet} - \sigma$ relation. Fits to the low- σ subsamples are unaffected. For $r_{\text{min}} = r_{\text{inf}}$, the high- σ subsample yields $\beta \sim 5$ -6 for all values of σ_{cut} (Figure 5.2). For the conventional definition with $r_{\text{min}} = 0$,

Table 5.3: Power-law fits to $M_{\bullet}(\sigma)$

| Sample | N_{gal} | α | β | ϵ_0 |
|---------------------------------------------------------------|------------------|-----------------|-----------------|--------------|
| All galaxies | 65 | 8.29 ± 0.05 | 5.48 ± 0.34 | 0.38 |
| All + upper limits | 157 | 8.09 ± 0.05 | 5.29 ± 0.30 | |
| All galaxies ($0-r_{\text{eff}}$) | 65 | 8.26 ± 0.05 | 5.29 ± 0.32 | 0.38 |
| G09 ($0-r_{\text{eff}}$) | 49 | 8.19 ± 0.06 | 4.12 ± 0.38 | 0.39 |
| Early-type | 46 | 8.35 ± 0.06 | 5.01 ± 0.38 | 0.33 |
| Late-type | 19 | 8.05 ± 0.22 | 5.02 ± 1.18 | 0.46 |
| Power-law | 19 | 8.22 ± 0.09 | 4.43 ± 0.75 | 0.35 |
| Core | 22 | 8.44 ± 0.13 | 5.08 ± 0.88 | 0.37 |
| Core ($0-r_{\text{eff}}$) | 22 | 8.45 ± 0.13 | 4.56 ± 0.78 | 0.37 |
| $\sigma \leq 150 \text{ km s}^{-1}$ | 20 | 8.34 ± 0.24 | 5.30 ± 1.04 | 0.32 |
| $\sigma > 150 \text{ km s}^{-1}$ | 45 | 8.20 ± 0.08 | 6.37 ± 0.62 | 0.40 |
| $\sigma \leq 200 \text{ km s}^{-1}$ | 34 | 8.29 ± 0.15 | 5.42 ± 0.84 | 0.42 |
| $\sigma > 200 \text{ km s}^{-1}$ | 31 | 8.17 ± 0.14 | 6.37 ± 1.00 | 0.35 |
| $\sigma > 200 \text{ km s}^{-1}$ ($0-r_{\text{eff}}$) | 31 | 8.22 ± 0.13 | 5.54 ± 0.87 | 0.35 |
| $L \leq 10^{11} L_{\odot}$ | 31 | 8.33 ± 0.06 | 5.19 ± 0.38 | 0.29 |
| $L > 10^{11} L_{\odot}$ | 9 | 8.14 ± 0.59 | 7.31 ± 3.40 | 0.52 |
| $L > 10^{11} L_{\odot}$ ($0-r_{\text{eff}}$) | 9 | 8.19 ± 0.52 | 6.56 ± 2.79 | 0.50 |
| $M_{\text{bulge}} \leq 10^{11} M_{\odot}$ | 14 | 8.38 ± 0.12 | 4.84 ± 0.87 | 0.38 |
| $M_{\text{bulge}} > 10^{11} M_{\odot}$ | 20 | 8.40 ± 0.14 | 5.19 ± 0.98 | 0.35 |
| $M_{\text{bulge}} > 10^{11} M_{\odot}$ ($0-r_{\text{eff}}$) | 20 | 8.41 ± 0.14 | 4.62 ± 0.85 | 0.34 |

Notes: $\log(M_{\bullet}) = \alpha + \beta \log(\sigma/200 \text{ km s}^{-1})$, with intrinsic scatter ϵ_0 in $\log(M_{\bullet})$. Subsamples designated ($0-r_{\text{eff}}$) define σ using kinematic data over the interval $0 < r < r_{\text{eff}}$. For all other subsamples, we define σ using data over the interval $r_{\text{inf}} < r < r_{\text{eff}}$. “G09” refers to the sample of Gültekin et al. (2009a). Figure 5.2 illustrates N_{gal} , α , β , and ϵ_0 for additional cuts in σ . For other cuts in L or M_{bulge} , α and β are consistent with our fit to $M_{\bullet}(\sigma)$ for all galaxies.

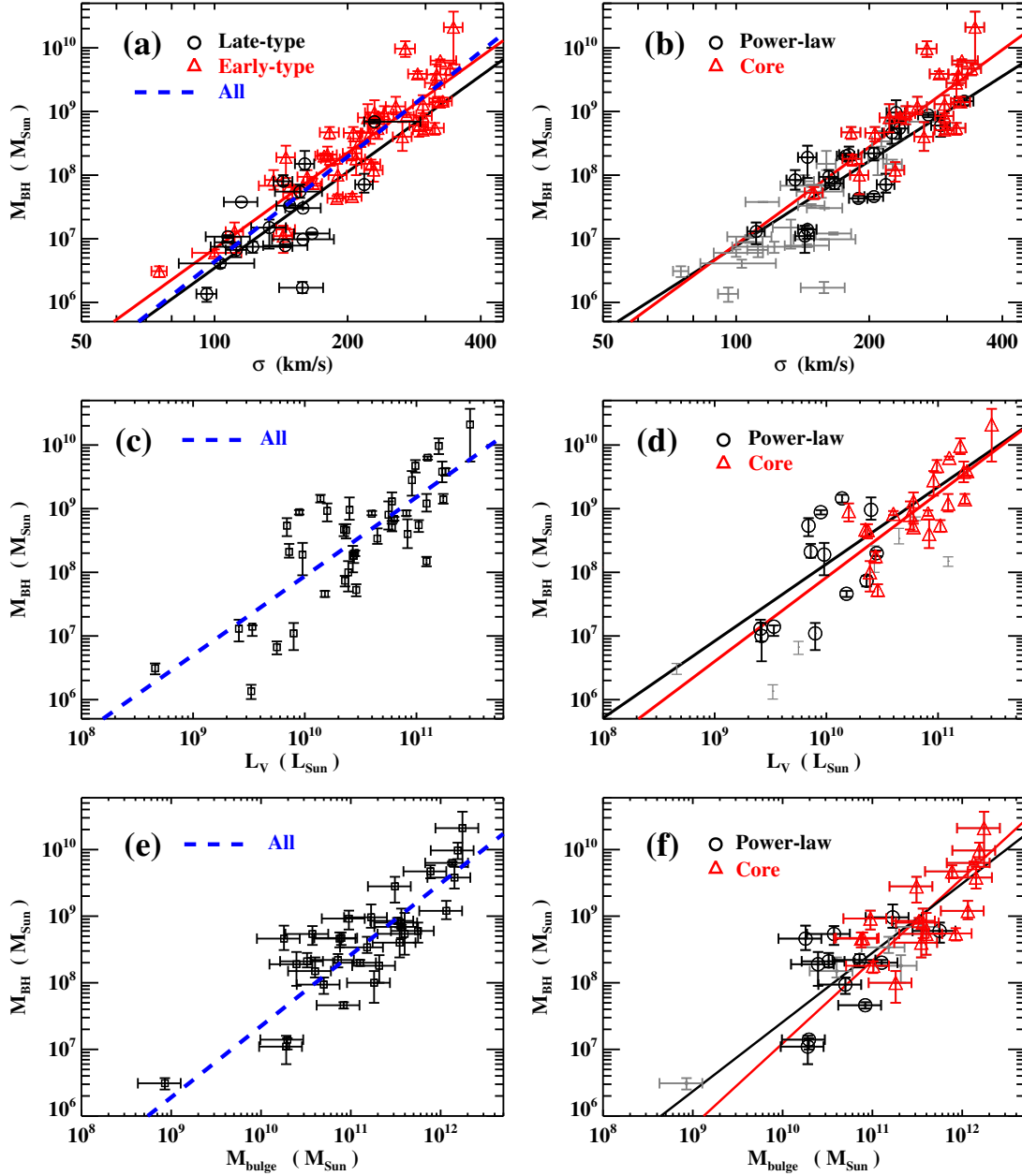


Figure 5.1: Three black hole scaling relations. (a) $M_{\bullet} - \sigma$ relation, with separate fits for early- and late-type galaxies. The blue dashed line represents the power-law fit to the entire 65-galaxy sample. (b) $M_{\bullet} - \sigma$ relation, with separate fits for core and power-law galaxies. For (a) and (b) we define σ using kinematic data over the interval $r_{\text{inf}} < r < r_{\text{eff}}$. (c) $M_{\bullet} - L$ relation, including the power-law fit to the full sample of 40 galaxies with V -band bulge luminosities. (d) $M_{\bullet} - L$ relation, fitting core and power-law galaxies separately. (e) $M_{\bullet} - M_{\text{bulge}}$ relation, including the power-law fit to the full sample of 34 galaxies with dynamical bulge masses. (f) $M_{\bullet} - M_{\text{bulge}}$ relation, fitting core and power-law galaxies separately.

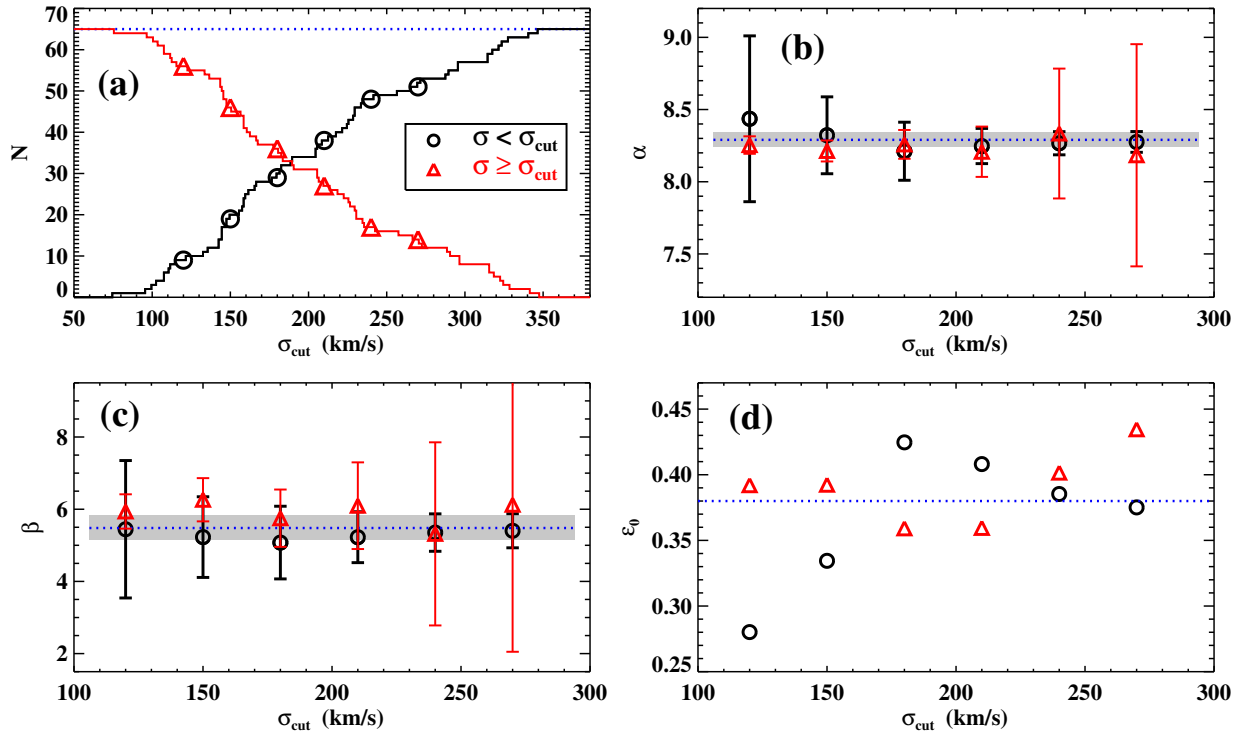


Figure 5.2: Power-law fits to $M_*(\sigma)$, using different cuts in σ . Each fit has the form $\log(M_*) = \alpha + \beta \log(\sigma/200 \text{ km s}^{-1})$. (a) Cumulative distribution of galaxies with $\sigma < \sigma_{\text{cut}}$ (black circles) and $\sigma \geq \sigma_{\text{cut}}$ (red triangles). (b) Power-law coefficient α , for $\sigma < \sigma_{\text{cut}}$ and $\sigma \geq \sigma_{\text{cut}}$. (c) Power-law index β . (d) Intrinsic scatter ϵ_0 in $\log(M_*)$. For the above fits and sample cuts, σ is defined using kinematic data over the interval $r_{\text{inf}} < r < r_{\text{eff}}$. The blue dashed lines and grey shaded regions represent the parameters and uncertainties of the power-law fit to the 65-galaxy sample.

β decreases steadily in the high- σ subsample as σ_{cut} increases. Our choice for defining σ has a negligible effect on our measurements of the intrinsic scatter in $\log(M_{\bullet})$.

Our $M_{\bullet} - L$ and $M_{\bullet} - M_{\text{bulge}}$ samples both appear to have a central knot, where black holes with $10^8 M_{\odot} < M_{\bullet} < 10^9 M_{\odot}$ show relatively weak correlation with L or M_{bulge} (see Figures 5.1c and 5.1e). This makes it difficult to interpret the fits to high- L and low- L (or high- M_{bulge} and low- M_{bulge}) subsamples. We find tentative evidence that the most luminous and massive galaxies ($L \sim 10^{11} L_{\odot}$; $M_{\text{bulge}} > 10^{11.5} M_{\odot}$) have steeper slopes in $M_{\bullet}(L)$ and $M_{\bullet}(M_{\text{bulge}})$, as exemplified in Tables 5.4 and 5.5. Both samples are sparsely populated at the low- M_{\bullet} end.

5.3.3 Comparison to Previous Studies

The slope of the $M_{\bullet} - \sigma$ relation reported in prior studies has wavered between ~ 4 (e.g., Gebhardt et al. 2000a; Tremaine et al. 2002; Gültekin et al. 2009a; Beifiori et al. 2012) and ~ 5 (e.g., Ferrarese & Merritt 2000; Merritt & Ferrarese 2001; Graham et al. 2011). Our best-fit slope for the global $M_{\bullet} - \sigma$ relation falls at the steep end of this distribution, while various subsamples exhibit a wider range of slopes ($\beta \approx 4.4$ to $\beta \approx 7.3$). Our fit to early-type galaxies is significantly steeper than the early-type fit by Gültekin et al. (2009a): $\beta = 5.01 \pm 0.38$ versus $\beta = 3.86 \pm 0.38$. Our fit to late-type galaxies is slightly steeper than Gültekin et al. (2009a): $\beta \approx 5.0$ versus $\beta \approx 4.6$.

Our $M_{\bullet} - L$ and $M_{\bullet} - M_{\text{bulge}}$ slopes are consistent with a number of previous investigations (e.g., Marconi & Hunt 2003; Häring & Rix 2004; McLure & Dunlop 2004; Gültekin et al. 2009a; Schulze & Gebhardt 2011), including multiple bandpasses for L . However, they are steeper than the recent fits by Sani et al. (2011; M_{bulge} and 3.6 μm luminosity) and Beifiori et al. (2012; i -band luminosity).

Recently, Graham (2012) examined the $M_{\bullet} - \sigma$ and $M_{\bullet} - M_{\text{bulge}}$ relations with separate fits to core and non-core galaxies, based on the galaxy sample of Häring & Rix (2004) and updated black hole masses from Graham et al. (2011). He found non-core galaxies to follow a very steep $M_{\bullet} - M_{\text{bulge}}$ relation ($\beta \sim 2$), and found virtually no discrepancy in the $M_{\bullet} - \sigma$ relations for core versus non-core galaxies. Our relative trends for core and power-law galaxies oppose his results. This is likely due to differences in the galaxy samples. Our sample of core galaxies includes two Brightest Cluster Galaxies with new measurements of $M_{\bullet} \sim 10^{10} M_{\odot}$ (McConnell et al. 2011b) and seven galaxies where we have excluded the black hole's influence in our definition of σ . Both updates contribute to our detection of a steeper and more massive $M_{\bullet} - \sigma$ relation for core galaxies (although we still find a significantly higher intercept when we adopt the original σ values). Our photometric classification of galaxies also differs from Graham (2012). In particular, we classify the high- M_{bulge} object NGC 6251 as a power-law galaxy, based on the surface brightness profile of Ferrarese & Ford (1999). Excluding NGC 6251, we measure $\beta \approx 1.7$ for power-law galaxies on the $M_{\bullet} - M_{\text{bulge}}$ relation.

Several least-squares estimators have been used by various authors to fit the black hole

Table 5.4: Power-law fits to $M_{\bullet}(L)$

| Sample | N_{gal} | α | β | ϵ_0 |
|---------------------------------------------|------------------|-----------------|-----------------|--------------|
| All galaxies | 40 | 9.18 ± 0.12 | 1.24 ± 0.15 | 0.55 |
| G09 | 32 | 9.01 ± 0.10 | 1.17 ± 0.12 | 0.36 |
| Power-law | 12 | 9.34 ± 0.66 | 1.21 ± 0.63 | 0.67 |
| Core | 21 | 9.24 ± 0.10 | 1.32 ± 0.27 | 0.40 |
| $L \leq 10^{11} L_{\odot}$ | 31 | 9.21 ± 0.18 | 1.26 ± 0.20 | 0.56 |
| $L > 10^{11} L_{\odot}$ | 9 | 8.67 ± 0.30 | 3.83 ± 1.48 | 0.47 |
| $M_{\text{bulge}} \leq 10^{11.5} M_{\odot}$ | 17 | 9.21 ± 0.23 | 1.16 ± 0.23 | 0.46 |
| $M_{\text{bulge}} > 10^{11.5} M_{\odot}$ | 12 | 9.22 ± 0.10 | 2.34 ± 0.59 | 0.30 |

Notes: $\log(M_{\bullet}) = \alpha + \beta \log(L/10^{11} L_{\odot})$, with intrinsic scatter ϵ_0 in $\log(M_{\bullet})$. Luminosities are in V -band. ‘‘G09’’ refers to the sample of Gültekin et al. (2009a).

Table 5.5: Power-law fits to $M_{\bullet}(M_{\text{bulge}})$

| Sample | N_{gal} | α | β | ϵ_0 |
|---------------------------------------------|------------------|-----------------|-----------------|--------------|
| Dynamical masses | 34 | 8.42 ± 0.08 | 1.07 ± 0.12 | 0.33 |
| Stellar masses | 16 | 8.49 ± 0.12 | 1.26 ± 0.16 | 0.31 |
| Power-law | 12 | 8.45 ± 0.20 | 1.04 ± 0.42 | 0.50 |
| Core | 17 | 8.33 ± 0.19 | 1.24 ± 0.26 | 0.28 |
| $L \leq 10^{10.5} L_{\odot}$ | 15 | 8.44 ± 0.15 | 1.08 ± 0.25 | 0.43 |
| $L > 10^{10.5} L_{\odot}$ | 14 | 7.55 ± 0.50 | 2.10 ± 0.60 | N/A |
| $M_{\text{bulge}} \leq 10^{11.5} M_{\odot}$ | 21 | 8.52 ± 0.12 | 1.15 ± 0.22 | 0.39 |
| $M_{\text{bulge}} > 10^{11.5} M_{\odot}$ | 13 | 7.07 ± 0.78 | 2.49 ± 0.86 | N/A |

Notes: $\log(M_{\bullet}) = \alpha + \beta \log(M_{\text{bulge}}/10^{11} M_{\odot})$, with intrinsic scatter ϵ_0 in $\log(M_{\bullet})$. All fits except for the ‘‘stellar masses’’ line use the sample of bulges with dynamical masses. For sufficiently steep slopes ($\beta \approx 2$), the measurement error terms for M_{\bullet} and M_{bulge} permit $\chi_{\nu}^2 \leq 1$ with no intrinsic scatter term.

scaling relations. Tremaine et al. (2002) and Gültekin et al. (2009a) have compared multiple methods, which yield consistent fits in nearly every reported case. We have applied the FITEXY method to the original $M_\bullet(\sigma)$ sample of Gültekin et al. (2009a) (Table 5.3, not including upper limits), and find $\alpha = 8.19 \pm 0.06$ and $\beta = 4.12 \pm 0.38$, consistent with their best-fit values $\alpha = 8.19 \pm 0.06$ and $\beta = 3.95 \pm 0.42$. Gültekin et al. (2009a) have introduced a maximum-likelihood treatment for secure measurements plus upper limits; their procedure accounts for measurement errors (with various options for the error distribution and intrinsic scatter distribution) and for the possibility that $M_\bullet = 0$ in galaxies with a reported upper limit. Our fits including upper limits employ the ASURV BIVAR EM procedure, which does not consider measurement errors. Nonetheless, this procedure yields a consistent fit to the Gültekin et al. (2009a) sample of 49 galaxies plus 18 upper limits: $\alpha = 8.11 \pm 0.06$ and $\beta = 4.19 \pm 0.36$ with ASURV, versus $\alpha = 8.12 \pm 0.08$ and $\beta = 4.24 \pm 0.41$ from Gültekin et al. (2009a). Beifiori et al. (2012) have also used the FITEXY and ASURV procedures; our fit to their $M_\bullet(\sigma)$ sample yields identical parameters: $\alpha = 8.19 \pm 0.07$ and $\beta = 4.17 \pm 0.32$ (FITEXY, no upper limits) and $\alpha = 7.99 \pm 0.06$ and $\beta = 4.42 \pm 0.30$ (ASURV, including upper limits).

5.4 Scatter in $\log(M_\bullet)$

For a given black hole scaling relation, deviations between the measured values of M_\bullet and the mean power-law relation are conventionally interpreted as a combination of measurement errors and intrinsic scatter. We assume the scatter in M_\bullet to be log normal, and define the intrinsic scatter term ϵ_0 such that

$$\chi^2 = \sum_i \frac{[\log(M_{\bullet,i}) - \alpha - \beta x_i]^2}{\epsilon_0^2 + \epsilon_{M,i}^2 + \beta^2 \epsilon_{x,i}^2}, \quad (5.3)$$

where $x = \log_{10}(\sigma/200 \text{ km s}^{-1})$ for the $M_\bullet - \sigma$ relation, $x = \log_{10}(L/10^{11} L_\odot)$ for the $M_\bullet - L$ relation, and

$x = \log_{10}(M_{\text{bulge}}/10^{11} M_\odot)$ for the $M_\bullet - M_{\text{bulge}}$ relation. Here, ϵ_M is the $1-\sigma$ error in $\log(M_\bullet)$, and ϵ_x is the $1-\sigma$ error in x . For a given sample and power-law fit, we adopt the value of ϵ_0 for which $\chi_\nu^2 = 1$ ($\chi^2 = N_{\text{dof}}$). Gültekin et al. (2009a) tested several forms of intrinsic scatter in M_\bullet and found log normal scatter to be an appropriate description.

Figure 5.3 illustrates how ϵ_0 varies across each of the $M_\bullet - \sigma$, $M_\bullet - L$, and $M_\bullet - M_{\text{bulge}}$ relations. For each relation, we have constructed four bins containing equal numbers of galaxies and have computed ϵ_0 in each bin. The same values of α and β are used for all bins, representing the global fit to the appropriate scaling relation.

Figure 5.3 does not show any systematic trends with respect to σ , although ϵ_0 varies from bin to bin. For the $M_\bullet - L$ and $M_\bullet - M_{\text{bulge}}$ relations, we find possible evidence that galaxies with low spheroid luminosities ($L \lesssim 10^{10} L_\odot$) and masses ($M_{\text{bulge}} \lesssim 10^{10.5} M_\odot$) exhibit increased scatter in M_\bullet . These galaxies, however, only comprise a quarter of our respective $M_\bullet(L)$ and $M_\bullet(M_{\text{bulge}})$ samples. More measurements in the range $M_{\text{bulge}} \sim 10^8 -$

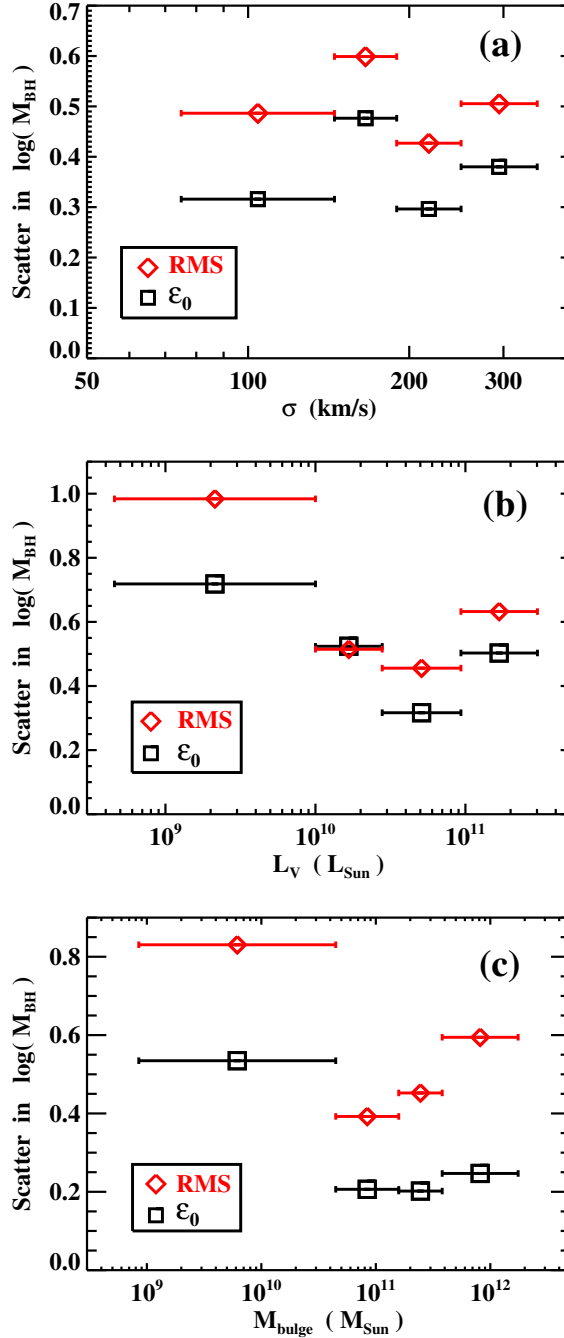


Figure 5.3: Scatter in $\log(M_\bullet)$ for different intervals in σ , L , and M_{bulge} . For each interval, ϵ_0 is the intrinsic scatter required to obtain $\chi^2 = N_{\text{gal}}$ between the subsample of galaxies and the global power law. RMS is the root-mean-squared scatter in $\log(M_\bullet)$ for each interval. (a) Scatter with respect to the $M_\bullet - \sigma$ relation, $\log(M_\bullet) = 8.29 + 5.20 \log(\sigma/200 \text{ km s}^{-1})$. (b) Scatter with respect to the $M_\bullet - L$ relation, $\log(M_\bullet) = 9.18 + 1.24 \log(L/10^{11} L_\odot)$. (c) Scatter with respect to the $M_\bullet - M_{\text{bulge}}$ relation, $\log(M_\bullet) = 8.42 + 1.07 \log(M_{\text{bulge}}/10^{11} M_\odot)$.

$10^{10} M_{\odot}$ are needed to reveal whether intrinsic scatter in M_{\bullet} varies systematically across an extended range of bulge luminosities or masses.

The ϵ_0 term provides a reliable assessment of intrinsic scatter only if random measurement errors are small: measurements with large uncertainties can yield $\chi^2_{\nu} \leq 1$ with no intrinsic scatter term. The root-mean-squared scatter (RMS) in $\log(M_{\bullet})$ is a more basic estimate, with no explicit dependence on measurement errors. Figure 5.3 shows that RMS varies with σ , L , and M_{bulge} in a similar manner to ϵ_0 . The qualitative agreement between the behavior of ϵ_0 and RMS suggests that variations in measurement errors are not responsible for the apparent trends (or lack thereof) in ϵ_0 . We have tested alternative bin sizes and boundaries for each relation, and find similar trends to those displayed in Figure 5.3.

Fitting the full galaxy sample for each scaling relation, we measure $\epsilon_0 = 0.41$ for $M_{\bullet}(\sigma)$, $\epsilon_0 = 0.55$ for $M_{\bullet}(L)$, and $\epsilon_0 = 0.33$ for $M_{\bullet}(M_{\text{bulge}})$. While it is tempting to conclude that M_{bulge} is the superior predictor of M_{\bullet} , the relative errors in M_{bulge} , σ , and L demand a more cautious interpretation. As noted in Section 5.2, we have assumed that all M_{bulge} values have an error of at least 0.24 dex. We have repeated our fits to $M_{\bullet}(M_{\text{bulge}})$ with a minimum error of only 0.09 dex. Fitting the full M_{bulge} sample with this reduced error in M_{bulge} , we obtain a larger intrinsic scatter ($\epsilon_0 = 0.39$) as expected from equation 5.3, while the slope and intercept of the fit remain unchanged. Similarly, our measurements of ϵ_0 for the $M_{\bullet} - \sigma$ and $M_{\bullet} - L$ relations depend in part upon the assumed errors in σ ($\geq 5\%$, following Gültekin et al. (2009a)) and L (typically < 0.05 dex). In light of these precautions, we find no strong evidence favoring $M_{\bullet}(\sigma)$, $M_{\bullet}(L)$, or $M_{\bullet}(M_{\text{bulge}})$ as the fundamental correlation. This opposes the conclusion by Beifiori et al. (2012) that the $M_{\bullet} - \sigma$ relation is intrinsically tighter than other black hole scaling relations.

5.5 Discussion

Specifying the black hole scaling relations for different galaxy types will benefit several lines of investigation. Refined scaling relations can be combined with large surveys of host galaxy properties to estimate more precisely the present-day mass function of black holes. The mass function represents the integrated growth of supermassive black holes and can be compared with quasar surveys to gain insight to the light curves and duty cycles of quasars (e.g., Small & Blandford 1992; Hopkins et al. 2006). Comparisons between cosmological simulations and the empirical black hole mass function can constrain the requisite conditions for forming the first massive black hole seeds and the subsequent roles of quasar-mode accretion, radio-mode accretion, and binary black hole merging toward black hole growth (e.g., Yoo et al. 2007; Volonteri et al. 2008; Natarajan & Treister 2009; Shen 2009; Fanidakis et al. 2011). One challenge for measuring the black hole mass function is predicting M_{\bullet} in the most luminous galaxies, which do not exhibit comparably high σ (Bernardi et al. 2007; Lauer et al. 2007a). Here we have found that the $M_{\bullet} - \sigma$ relation for core galaxies predicts larger M_{\bullet} than the global relation and agrees more closely with L -based predictions.

The scaling relations themselves are often used to constrain numerical simulations of

galaxies, which may track individual events such as galaxy mergers (e.g., Di Matteo et al. 2005; Hopkins et al. 2007b), or galaxy and black hole growth over cosmological timescales (e.g., Kauffmann & Haehnelt 2000; Bower et al. 2006; Croton et al. 2006; Malbon et al. 2007; Volonteri & Natarajan 2009). Reproducing the black hole scaling relations in their global power-law forms is no longer a pioneering challenge for simulations, but new details may be required to obtain distinct scaling relations for galaxies of different sizes or morphologies. On the observational side, updated scaling relations can be used to estimate M_\bullet more accurately in individual galaxies. This can improve our knowledge of Eddington rates and spectral energy distributions for accreting black holes, as well as time and distance scales for tidal disruption events. Finally, the $M_\bullet - \sigma$ relation for quiescent black holes has been used to normalize the black hole masses obtained from reverberation mapping studies of active galaxies (Onken et al. 2004; Woo et al. 2010). This important calibration could be improved by addressing morphology biases in the reverberation mapping samples and the $M_\bullet - \sigma$ relations for different galaxy types.

At fixed σ , core galaxies are typically more luminous than power-law galaxies (Lauer et al. 2007a; Hopkins et al. 2009a), and we find that M_\bullet follows L and M_{bulge} substantially more tightly in core galaxies (see Tables 5.4 and 5.5). Correspondingly, we measure a steeper slope and greater intercept for the core galaxy $M_\bullet - \sigma$ relation, relative to power-law galaxies. This may reflect a greater contribution from gas-poor (“dry”) mergers toward the overall growth of core galaxies. A galaxy accreting satellites (with $M_\bullet > 0$ in the satellites) can grow in both L and M_\bullet without increasing σ , especially if little gas is available to increase the central mass concentration (e.g., Hopkins et al. 2009b; Oser et al. 2012). Major mergers without gas can also preserve σ under certain orbital configurations (Boylan-Kolchin et al. 2005; Boylan-Kolchin et al. 2006). Cores are believed to form from three-body interactions between stars and an inspiraling binary black hole (e.g., Ebisuzaki et al. 1991; Milosavljević & Merritt 2001), and should be more prominent in systems with little gas to drive the black holes quickly toward coalescence or to replenish the central stellar population (Hopkins et al. 2009a). Successive dry mergers could tighten the $M_\bullet - L$ and $M_\bullet - M_{\text{bulge}}$ relations in bulge-dominated galaxies, as larger numbers of mergers drive these systems toward the average $M_\bullet/M_{\text{bulge}}$ ratio (e.g., Peng 2007). We therefore argue that core galaxies exemplify the tendency of dry galaxy mergers to increase M_\bullet , L , and M_{bulge} relative to σ .

Our attempt to measure scatter in M_\bullet for different intervals in σ , L , and M_{bulge} serves as another test for simulations of black hole and galaxy growth. We have used the current set of observational data to measure roughly constant scatter in M_\bullet for $\sigma > 100 \text{ km s}^{-1}$, but observations thus far are insufficient to probe the $30 - 100 \text{ km s}^{-1}$ range, where scatter in M_\bullet could identify the initial formation mechanism for massive black holes (Volonteri et al. 2008; Volonteri & Natarajan 2009). Simulations of hierarchical mergers in Λ CDM cosmology predict that scatter in M_\bullet should decline steadily with increasing stellar mass (M_\star), even when M_\bullet and M_\star are initially uncorrelated (Malbon et al. 2007; Peng 2007; Hirschmann et al. 2010; Jahnke & Macciò 2011). For instance, semi-analytic models by Malbon et al. (2007) predict that black holes with present-day masses $> 10^8 M_\odot$ have gained most of their mass via black hole-black hole mergers, yielding extremely low scatter ($\epsilon_0 \sim 0.1$) at the upper end

of the $M_{\bullet} - M_{\text{bulge}}$ relation. More recent models by Jahnke & Macciò (2011) employ fully decoupled prescriptions for star formation and black hole growth, and attain a more realistic amount of scatter on average. Yet these models still exhibit decreasing scatter as M_{bulge} increases from $\sim 10^9 M_{\odot}$ to $\sim 10^{11.5} M_{\odot}$. In comparison, we observe nearly constant scatter from $M_{\text{bulge}} \sim 10^{10.5} M_{\odot}$ to $M_{\text{bulge}} \sim 10^{12} M_{\odot}$, beyond the highest bulge masses produced in the Jahnke & Macciò (2011) models.

Finally, we note that investigations using the $M_{\bullet} - \sigma$ correlation should consider the definition of σ : i.e., whether it is measured from an inner radius of zero or r_{inf} . We find that both definitions yield similar amounts of scatter in the $M_{\bullet} - \sigma$ relation (Table 5.3), and so neither has a clear advantage for predicting M_{\bullet} . Excluding data within r_{inf} corresponds more closely to cases where r_{inf} is unresolved, such as seeing-limited galaxy surveys, high-redshift observations, or numerical simulations with limited spatial resolution. From a theoretical perspective, the evolutionary origin of an $M_{\bullet} - \sigma$ relation and the immediate effects of gravity may warrant separate consideration. On the other hand, the total gravitational potential of a galaxy includes its black hole.

Our investigation of how redefining σ alters the $M_{\bullet} - \sigma$ relation has only considered nine galaxies for which data within r_{inf} contribute prominently to the spatially integrated velocity dispersion. A full investigation would require more galaxies with published values of $\sigma(r)$ and $v(r)$. At present, the full sample of M_{\bullet} and σ measurements comprises a rather heterogeneous selection of kinematic data. Rather than arguing for a definitive protocol, we wish to call attention to the nuances of interpreting the $M_{\bullet} - \sigma$ relation and encourage future investigators to consider their options carefully.

Dynamical measurements of M_{\bullet} require substantial observational resources and careful analysis, and are often published individually. Our exploration of scatter in M_{\bullet} for the most luminous and massive galaxies is greatly aided by the updated measurement of M_{\bullet} in M87 (Gebhardt et al. 2011) and new measurements in five Brightest Cluster Galaxies (Nowak et al. 2008; McConnell et al. 2011a,b; McConnell et al. 2012). New maser-based measurements by Greene et al. (2010a) and Kuo et al. (2011) have made important contributions to the sample of low- and intermediate-mass galaxies. Yet the cascade of individual measurements has begun to outpace the periodic updates to the galaxy samples fueling the empirical black hole scaling relations. More reliable comparisons and better insight can be achieved if all researchers have easy access to a frequently updated sample of black hole masses and host galaxy properties. We aim to support this effort with an online sample.

Acknowledgments

This work is supported in part by NSF AST-1009663. We thank Karl Gebhardt, Tod Lauer, and collaborators for useful discussions about the black hole scaling relations. We thank Michael Reed for help with the data table and website.

Chapter 6

Conclusions and Future Work

New measurements of black hole masses (M_{\bullet}) in nearby galaxies continue to modify our understanding of the connections between black hole growth and galaxy growth, and our expectations for M_{\bullet} across a broad range of galaxy types. With the measurements presented herein, we have nearly doubled the number of Brightest Cluster Galaxies (BCGs) with securely measured M_{\bullet} , from five objects in the compilation of Gültekin et al. (2009a) to nine objects today. Our work has been complemented by several new measurements of M_{\bullet} in low-mass galaxies (e.g., Greene et al. 2010a; Kuo et al. 2011). As a result of these efforts, the black hole scaling relations look quite different than they did ten years ago, or even three years ago (Gültekin et al. 2009a). In particular, M_{\bullet} was once reported to form a very tight correlation with stellar velocity dispersion (Ferrarese & Merritt 2000; Gebhardt et al. 2000a), possibly dictated by a universal co-evolutionary mechanism for galaxies and black holes. Yet several of the recent measurements at high and low galaxy masses are outliers from the early scaling relations, and it is now apparent that this idea was overly simplistic. A variety of physical processes must contribute to the black hole scaling relations and their intrinsic scatter.

Environmental effects could be an important source of scatter in the black hole scaling relations, particularly for the enormous galaxies residing at the centers of galaxy clusters. Do BCGs exhibit a different range of black hole masses from galaxies in less dense cosmic environments? Although it is virtually impossible to assemble a sample of nearby field galaxies with comparable luminosities to BCGs, we can examine luminous cD galaxies anchoring galaxy groups, poor clusters, and rich clusters, and residing in cluster outskirts. The clusters themselves can be classified by their thermal X-ray properties, which trace the overall mass of the cluster dark matter halo, and the likelihood of “cooling flows” of condensing intracluster gas (e.g., Fabian 1994). Cooling flows may provide an additional food source for galaxies and black holes. A larger and more diverse sample of M_{\bullet} in BCGs and central group galaxies will provide a clearer picture of black hole growth in extreme cosmic environments.

Our survey of stellar kinematics at the centers of BCGs is ongoing, and we are optimistic that the results presented here will merely be the tip of the iceberg. We have obtained adaptive optics data for three additional BCGs, and several nights have been awarded for a

seeing-limited survey of BCGs and other massive ellipticals, using the twin GMOS instruments on the Gemini North and Gemini South telescopes (Hook et al. 2004; Allington-Smith et al. 2002). In the next two semesters, we will observe 15 galaxies with the GMOS integral field units. Their stellar kinematics and black hole masses will be measured using the methods described in this dissertation.

Integral-field spectroscopy of galaxy nuclei can reveal far more than the central black hole masses. Our survey is building an exciting dataset for exploring kinematic substructures, spatial gradients in stellar populations, and links between galaxies' photometric cores and central orbital distributions. Each of these avenues of investigation could provide additional insights to the processes that build and reshape the Universe's most massive galaxies.

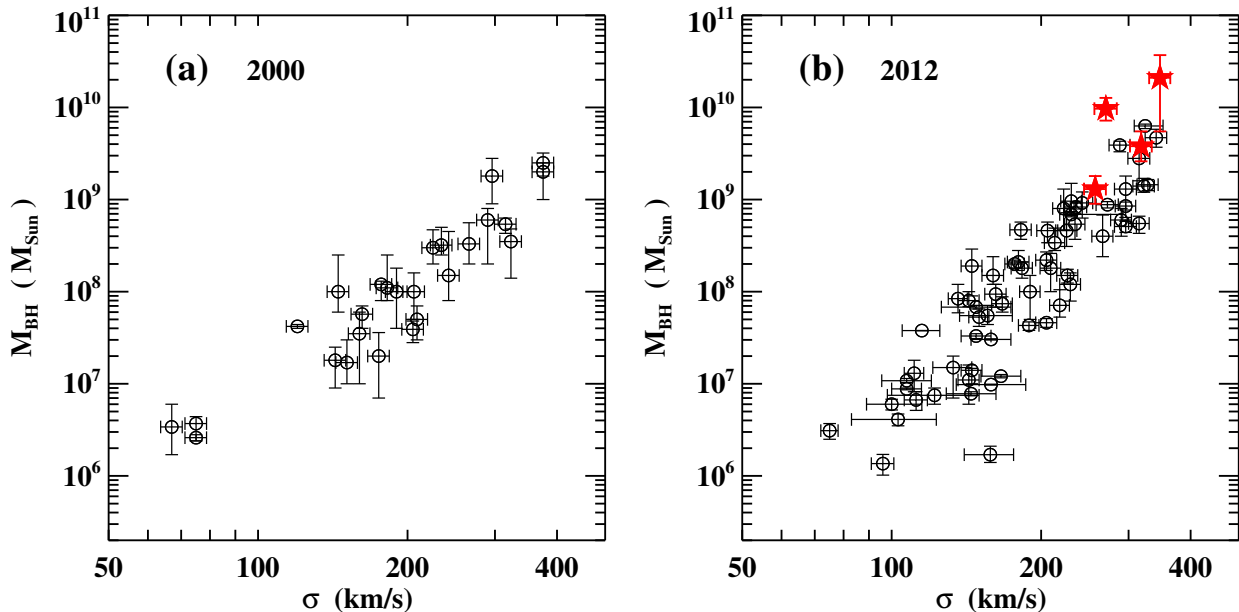


Figure 6.1: Empirical correlation between black hole mass (M_{\bullet}) and stellar velocity dispersion (σ). Panel (a) illustrates the correlation presented by Gebhardt et al. (2000a), based on data from 26 galaxies. Ferrarese & Merritt (2000) presented a similar correlation for 12 galaxies. Panel (b) illustrates our present compilation of 65 galaxies. The red stars represent NGC 6086, NGC 3842, NGC 4889, and NGC 7768, whose black hole mass measurements are presented herein. Measurements and revisions over the past 12 years have increased the apparent scatter in the $M_{\bullet} - \sigma$ relation.

Bibliography

- Abell, G. O., Corwin, Jr., H. G., & Olowin, R. P. 1989, *ApJS*, 70, 1
- Adams, J. J., Blanc, G. A., Hill, G. J., et al. 2011, *ApJS*, 192, 5
- Allington-Smith, J., Murray, G., Content, R., et al. 2002, *PASP*, 114, 892
- Atkinson, J. W., Collett, J. L., Marconi, A., et al. 2005, *MNRAS*, 359, 504
- Baes, M., Buyle, P., Hau, G. K. T., & Dejonghe, H. 2003, *MNRAS*, 341, L44
- Barnes, J. E. 1992, *ApJ*, 393, 484
- Barnes, J. E., & Hernquist, L. 1996, *ApJ*, 471, 115
- Barth, A. J., Ho, L. C., & Sargent, W. L. W. 2002, *AJ*, 124, 2607
- Barth, A. J., Sarzi, M., Rix, H.-W., et al. 2001, *ApJ*, 555, 685
- Baumgardt, H., Makino, J., Hut, P., McMillan, S., & Portegies Zwart, S. 2003, *ApJ*, 589, L25
- Bechtold, J., Siemiginowska, A., Shields, J., et al. 2003, *ApJ*, 588, 119
- Begelman, M. C., Volonteri, M., & Rees, M. J. 2006, *MNRAS*, 370, 289
- Beifiori, A., Courteau, S., Corsini, E. M., & Zhu, Y. 2012, *MNRAS*, 419, 2497
- Beifiori, A., Sarzi, M., Corsini, E. M., et al. 2009, *ApJ*, 692, 856
- Bell, E. F., Naab, T., McIntosh, D. H., et al. 2006, *ApJ*, 640, 241
- Bell, E. F., van der Wel, A., Papovich, C., et al. 2012, *ApJ*, 753, 167
- Bender, R., Saglia, R. P., & Gerhard, O. E. 1994, *MNRAS*, 269, 785
- Bender, R., Kormendy, J., Bower, G., et al. 2005, *ApJ*, 631, 280
- Bennert, V. N., Auger, M. W., Treu, T., Woo, J.-H., & Malkan, M. A. 2011, *ApJ*, 742, 107
- Bernardi, M., Hyde, J. B., Sheth, R. K., Miller, C. J., & Nichol, R. C. 2007, *AJ*, 133, 1741
- Binney, J., & Tabor, G. 1995, *MNRAS*, 276, 663
- Blanton, M. R., & Roweis, S. 2007, *AJ*, 133, 734
- Blecha, L., Cox, T. J., Loeb, A., & Hernquist, L. 2011, *MNRAS*, 412, 2154
- Bogdán, Á., Forman, W. R., Kraft, R. P., et al. 2012a, *ApJ*, 755, 25
- Bogdán, Á., Forman, W. R., Zhuravleva, I., et al. 2012b, *ApJ*, 753, 140
- Bolton, C. T. 1972, *Nature*, 235, 271
- Bond, J. R., Arnett, W. D., & Carr, B. J. 1984, *ApJ*, 280, 825
- Bower, G. A., Green, R. F., Bender, R., et al. 2001, *ApJ*, 550, 75
- Bower, R. G., Benson, A. J., Malbon, R., et al. 2006, *MNRAS*, 370, 645
- Boylan-Kolchin, M., Ma, C.-P., & Quataert, E. 2005, *MNRAS*, 362, 184
- Boylan-Kolchin, M., Ma, C.-P., & Quataert, E. 2006, *MNRAS*, 369, 1081

- Braatz, J. A., Reid, M. J., Humphreys, E. M. L., et al. 2010, *ApJ*, 718, 657
- Bromm, V., & Yoshida, N. 2011, *ARAA*, 49, 373
- Brooks, A. M., Governato, F., Quinn, T., Brook, C. B., & Wadsley, J. 2009, *ApJ*, 694, 396
- Brough, S., Proctor, R., Forbes, D. A., et al. 2007, *MNRAS*, 378, 1507
- Bruce, V. A., Dunlop, J. S., Cirasuolo, M., et al. 2012, arXiv 1206.4322
- Bundy, K., Ellis, R. S., Conselice, C. J., et al. 2006, *ApJ*, 651, 120
- Burke, C., Collins, C. A., Stott, J. P., & Hilton, M. 2012, arXiv 1206.4735
- Burkert, A., Naab, T., Johansson, P. H., & Jesseit, R. 2008, *ApJ*, 685, 897
- Burkert, A., & Tremaine, S. 2010, *ApJ*, 720, 516
- Cappellari, M., Neumayer, N., Reunanen, J., et al. 2009, *MNRAS*, 394, 660
- Cappellari, M., Verolme, E. K., van der Marel, R. P., et al. 2002, *ApJ*, 578, 787
- Cappellari, M., Bacon, R., Bureau, M., et al. 2006, *MNRAS*, 366, 1126
- Carter, D., Bridges, T. J., & Hau, G. K. T. 1999, *MNRAS*, 307, 131
- Carter, D., & Metcalfe, N. 1980, *MNRAS*, 191, 325
- Churazov, E., Sunyaev, R., Forman, W., & Böhringer, H. 2002, *MNRAS*, 332, 729
- Ciotti, L., & Ostriker, J. P. 2007, *ApJ*, 665, 1038
- Cisternas, M., Jahnke, K., Inskip, K. J., et al. 2011, *ApJ*, 726, 57
- Cocato, L., Gerhard, O., & Arnaboldi, M. 2010, *MNRAS*, 407, L26
- Colpi, M., Mayer, L., & Governato, F. 1999, *ApJ*, 525, 720
- Conroy, C., & van Dokkum, P. 2012, arXiv 1205.6473
- Cowan, G. 1998, *Statistical Data Analysis* (Oxford: Clarendon Press)
- Cowie, L. L., Songaila, A., Hu, E. M., & Cohen, J. G. 1996, *AJ*, 112, 839
- Cox, T. J., Dutta, S. N., Di Matteo, T., et al. 2006, *ApJ*, 650, 791
- Cretton, N., de Zeeuw, P. T., van der Marel, R. P., & Rix, H.-W. 1999b, *ApJS*, 124, 383
- Cretton, N., & van den Bosch, F. C. 1999a, *ApJ*, 514, 704
- Croton, D. J., Springel, V., White, S. D. M., et al. 2006, *MNRAS*, 365, 11
- Dalla Bontà, E., Ferrarese, L., Corsini, E. M., et al. 2009, *ApJ*, 690, 537
- Davies, R. I., Thomas, J., Genzel, R., et al. 2006, *ApJ*, 646, 754
- de Francesco, G., Capetti, A., & Marconi, A. 2006, *A&A*, 460, 439
- . 2008, *A&A*, 479, 355
- De Lucia, G., & Blaizot, J. 2007, *MNRAS*, 375, 2
- de Vaucouleurs, G., de Vaucouleurs, A., Corwin, Jr., H. G., et al. 1991, *Third Reference Catalogue of Bright Galaxies* (Berlin: Springer-Verlag)
- Debuhr, J., Quataert, E., Ma, C.-P., & Hopkins, P. 2010, *MNRAS*, 406, L55
- Dekel, A., & Birnboim, Y. 2006, *MNRAS*, 368, 2
- Desroches, L.-B., Quataert, E., Ma, C.-P., & West, A. A. 2007, *MNRAS*, 377, 402
- Devereux, N., Ford, H., Tsvetanov, Z., & Jacoby, G. 2003, *AJ*, 125, 1226
- Di Matteo, T., Springel, V., & Hernquist, L. 2005, *Nature*, 433, 604
- Djorgovski, S., & Davis, M. 1987, *ApJ*, 313, 59
- Dressler, A. 1984, *ApJ*, 286, 97
- Dressler, A. 1989, in *IAU Symposium, Vol. 134, Active Galactic Nuclei*, ed. D. E. Osterbrock & J. S. Miller, 217

- Dressler, A., Oemler, Jr., A., Couch, W. J., et al. 1997, *ApJ*, 490, 577
- Dubinski, J. 1998, *ApJ*, 502, 141
- Ebisuzaki, T., Makino, J., & Okumura, S. K. 1991, *Nature*, 354, 212
- Emsellem, E., Dejonghe, H., & Bacon, R. 1999, *MNRAS*, 303, 495
- Emsellem, E., Cappellari, M., Peletier, R. F., et al. 2004, *MNRAS*, 352, 721
- Faber, S. M., Tremaine, S., Ajhar, E. A., et al. 1997, *AJ*, 114, 1771
- Fabian, A. C. 1994, *ARAA*, 32, 277
- Fabian, A. C., Sanders, J. S., Taylor, G. B., et al. 2006, *MNRAS*, 366, 417
- Fakhouri, O., & Ma, C.-P. 2008, *MNRAS*, 386, 577
- . 2009, *MNRAS*, 394, 1825
- Fan, X., Narayanan, V. K., Lupton, R. H., et al. 2001, *AJ*, 122, 2833
- Fanidakis, N., Baugh, C. M., Benson, A. J., et al. 2011, *MNRAS*, 410, 53
- Ferrarese, L. 2002, *ApJ*, 578, 90
- Ferrarese, L., & Ford, H. C. 1999, *ApJ*, 515, 583
- Ferrarese, L., Ford, H. C., & Jaffe, W. 1996, *ApJ*, 470, 444
- Ferrarese, L., & Merritt, D. 2000, *ApJ*, 539, L9
- Fine, S., Croom, S. M., Bland-Hawthorn, J., et al. 2010, *MNRAS*, 409, 591
- Fisher, D., Franx, M., & Illingworth, G. 1995, *ApJ*, 448, 119
- Förster Schreiber, N. M., Genzel, R., Bouché, N., et al. 2009, *ApJ*, 706, 1364
- Fryer, C. L., Woosley, S. E., & Heger, A. 2001, *ApJ*, 550, 372
- Gabor, J. M., Davé, R., Oppenheimer, B. D., & Finlator, K. 2011, *MNRAS*, 417, 2676
- Gebhardt, K., Adams, J. J., Richstone, D. O., et al. 2011, *ApJ*, 729, 119
- Gebhardt, K., Rich, R. M., & Ho, L. C. 2005, *ApJ*, 634, 1093
- Gebhardt, K., & Thomas, J. 2009, *ApJ*, 700, 1690
- Gebhardt, K., Richstone, D., Ajhar, E. A., et al. 1996, *AJ*, 112, 105
- Gebhardt, K., Bender, R., Bower, G., et al. 2000a, *ApJ*, 539, L13
- Gebhardt, K., Richstone, D., Kormendy, J., et al. 2000b, *AJ*, 119, 1157
- Gebhardt, K., Richstone, D., Tremaine, S., et al. 2003, *ApJ*, 583, 92
- Gebhardt, K., Lauer, T. R., Pinkney, J., et al. 2007, *ApJ*, 671, 1321
- Genel, S., Bouché, N., Naab, T., Sternberg, A., & Genzel, R. 2010, *ApJ*, 719, 229
- Ghez, A. M., Salim, S., Hornstein, S. D., et al. 2005, *ApJ*, 620, 744
- Ghez, A. M., Salim, S., Weinberg, N. N., et al. 2008, *ApJ*, 689, 1044
- Gillessen, S., Eisenhauer, F., Trippe, S., et al. 2009, *ApJ*, 692, 1075
- Gonzalez, A. H., Zabludoff, A. I., & Zaritsky, D. 2005, *ApJ*, 618, 195
- Graham, A. W. 2007, *MNRAS*, 379, 711
- . 2008, *PASA*, 25, 167
- . 2012, *ApJ*, 746, 113
- Graham, A. W., Colless, M. M., Busarello, G., Zaggia, S., & Longo, G. 1998, *A&AS*, 133, 325
- Graham, A. W., & Driver, S. P. 2007, *ApJ*, 655, 77
- Graham, A. W., Erwin, P., Caon, N., & Trujillo, I. 2001, *ApJ*, 563, L11
- Graham, A. W., Onken, C. A., Athanassoula, E., & Combes, F. 2011, *MNRAS*, 412, 2211

- Graves, G. J., & Faber, S. M. 2010, *ApJ*, 717, 803
- Greene, J. E., Murphy, J. D., Comerford, J. M., Gebhardt, K., & Adams, J. J. 2012, *ApJ*, 750, 32
- Greene, J. E., Peng, C. Y., Kim, M., et al. 2010a, *ApJ*, 721, 26
- Greene, J. E., Hood, C. E., Barth, A. J., et al. 2010b, *ApJ*, 723, 409
- Greenhill, L. J., Booth, R. S., Ellingsen, S. P., et al. 2003, *ApJ*, 590, 162
- Grillmair, C. J., Faber, S. M., Lauer, T. R., et al. 1994, *AJ*, 108, 102
- Guedes, J., Madau, P., Mayer, L., & Callegari, S. 2011, *ApJ*, 729, 125
- Gültekin, K., Richstone, D. O., Gebhardt, K., et al. 2011b, *ApJ*, 741, 38
- Gültekin, K., Tremaine, S., Loeb, A., & Richstone, D. O. 2011a, *ApJ*, 738, 17
- Gültekin, K., Richstone, D. O., Gebhardt, K., et al. 2009a, *ApJ*, 698, 198
- . 2009b, *ApJ*, 695, 1577
- Håring, N., & Rix, H.-W. 2004, *ApJ*, 604, L89
- Harris, G. L. H., & Harris, W. E. 2011, *MNRAS*, 410, 2347
- Hernquist, L. 1989, *Nature*, 340, 687
- Hernquist, L., Spergel, D. N., & Heyl, J. S. 1993, *ApJ*, 416, 415
- Herrnstein, J. R., Moran, J. M., Greenhill, L. J., & Trotter, A. S. 2005, *ApJ*, 629, 719
- Hill, G. J., MacQueen, P. J., Smith, M. P., et al. 2008, in *Society of Photo-Optical Instrumentation Engineers (SPIE) Conference Series*, Vol. 7014
- Hilz, M., Naab, T., & Ostriker, J. P. 2012, arXiv 1206.5004
- Hirschmann, M., Khochfar, S., Burkert, A., et al. 2010, *MNRAS*, 407, 1016
- Hook, I. M., Jørgensen, I., Allington-Smith, J. R., et al. 2004, *PASP*, 116, 425
- Hopkins, P. F., Bundy, K., Hernquist, L., & Ellis, R. S. 2007a, *ApJ*, 659, 976
- Hopkins, P. F., Bundy, K., Hernquist, L., Wuyts, S., & Cox, T. J. 2010, *MNRAS*, 401, 1099
- Hopkins, P. F., Bundy, K., Murray, N., et al. 2009b, *MNRAS*, 398, 898
- Hopkins, P. F., Hernquist, L., Cox, T. J., et al. 2006, *ApJS*, 163, 1
- Hopkins, P. F., Hernquist, L., Cox, T. J., Keres, D., & Wuyts, S. 2009c, *ApJ*, 691, 1424
- Hopkins, P. F., Hernquist, L., Cox, T. J., & Kereš, D. 2008, *ApJS*, 175, 356
- Hopkins, P. F., Hernquist, L., Cox, T. J., Robertson, B., & Krause, E. 2007b, *ApJ*, 669, 45
- Hopkins, P. F., Lauer, T. R., Cox, T. J., Hernquist, L., & Kormendy, J. 2009a, *ApJS*, 181, 486
- Hopkins, P. F., & Quataert, E. 2010a, *MNRAS*, 405, L41
- . 2010b, *MNRAS*, 407, 1529
- Houghton, R. C. W., Magorrian, J., Sarzi, M., et al. 2006, *MNRAS*, 367, 2
- Hu, J. 2008, *MNRAS*, 386, 2242
- . 2009, arXiv 0908.2028
- Isobe, T., Feigelson, E. D., & Nelson, P. I. 1986, *ApJ*, 306, 490
- Jahnke, K., & Macciò, A. V. 2011, *ApJ*, 734, 92
- Jalali, B., Baumgardt, H., Kissler-Patig, M., et al. 2012, *A&A*, 538, A19
- Jardel, J. R., Gebhardt, K., Shen, J., et al. 2011, *ApJ*, 739, 21
- Jørgensen, I., Franx, M., & Kjaergaard, P. 1996, *MNRAS*, 280, 167
- Kaspi, S., Smith, P. S., Netzer, H., et al. 2000, *ApJ*, 533, 631

- Kauffmann, G., & Haehnelt, M. 2000, *MNRAS*, 311, 576
- Kelly, B. C., & Merloni, A. 2012, *Advances in Astronomy*, 970858
- Kereš, D., Katz, N., Weinberg, D. H., & Davé, R. 2005, *MNRAS*, 363, 2
- Khochfar, S., & Silk, J. 2006, *ApJ*, 648, L21
- Kobayashi, C., & Arimoto, N. 1999, *ApJ*, 527, 573
- Kondratko, P. T., Greenhill, L. J., & Moran, J. M. 2008, *ApJ*, 678, 87
- Kormendy, J., & Bender, R. 2009, *ApJ*, 691, L142
- . 2011, *Nature*, 469, 377
- Kormendy, J., Bender, R., & Cornell, M. E. 2011, *Nature*, 469, 374
- Kormendy, J., & Gebhardt, K. 2001, in *American Institute of Physics Conference Series*, Vol. 586, 20th Texas Symposium on relativistic astrophysics, ed. J. C. Wheeler & H. Martel, 363–381
- Kormendy, J., & Richstone, D. 1995, *ARAA*, 33, 581
- Koushiappas, S. M., Bullock, J. S., & Dekel, A. 2004, *MNRAS*, 354, 292
- Krajnović, D., McDermid, R. M., Cappellari, M., & Davies, R. L. 2009, *MNRAS*, 399, 1839
- Krajnović, D., Emsellem, E., Cappellari, M., et al. 2011, *MNRAS*, 414, 2923
- Kuo, C. Y., Braatz, J. A., Condon, J. J., et al. 2011, *ApJ*, 727, 20
- Laine, S., van der Marel, R. P., Lauer, T. R., et al. 2003, *AJ*, 125, 478
- Larkin, J., Barczys, M., Krabbe, A., et al. 2006, in *Society of Photo-Optical Instrumentation Engineers (SPIE) Conference Series*, Vol. 6269
- Lauer, T. R., & Postman, M. 1994, *ApJ*, 425, 418
- Lauer, T. R., Tremaine, S., Richstone, D., & Faber, S. M. 2007c, *ApJ*, 670, 249
- Lauer, T. R., Gebhardt, K., Richstone, D., et al. 2002, *AJ*, 124, 1975
- Lauer, T. R., Faber, S. M., Gebhardt, K., et al. 2005, *AJ*, 129, 2138
- Lauer, T. R., Faber, S. M., Richstone, D., et al. 2007a, *ApJ*, 662, 808
- Lauer, T. R., Gebhardt, K., Faber, S. M., et al. 2007b, *ApJ*, 664, 226
- Lavalley, M. P., Isobe, T., & Feigelson, E. D. 1992, in *Bulletin of the American Astronomical Society*, Vol. 24, *Bulletin of the American Astronomical Society*, 839–840
- Ledlow, M. J., & Owen, F. N. 1995, *AJ*, 109, 853
- Lodato, G., & Bertin, G. 2003, *A&A*, 398, 517
- Lodato, G., & Natarajan, P. 2006, *MNRAS*, 371, 1813
- Loubser, S. I., Sánchez-Blázquez, P., Sansom, A. E., & Soechting, I. K. 2009, *MNRAS*, 398, 133
- Loubser, S. I., Sansom, A. E., Sánchez-Blázquez, P., Soechting, I. K., & Bromage, G. E. 2008, *MNRAS*, 391, 1009
- Lucy, L. B. 1974, *AJ*, 79, 745
- Lützgendorf, N., Kissler-Patig, M., Noyola, E., et al. 2011, *A&A*, 533, A36
- Macchetto, F., Marconi, A., Axon, D. J., et al. 1997, *ApJ*, 489, 579
- Madau, P., & Rees, M. J. 2001, *ApJ*, 551, L27
- Magorrian, J., Tremaine, S., Richstone, D., et al. 1998, *AJ*, 115, 2285
- Malbon, R. K., Baugh, C. M., Frenk, C. S., & Lacey, C. G. 2007, *MNRAS*, 382, 1394
- Marcolini, A., Brighenti, F., & D’Ercole, A. 2003, *MNRAS*, 345, 1329

- Marconi, A., Axon, D. J., Maiolino, R., et al. 2008, *ApJ*, 678, 693
- Marconi, A., & Hunt, L. K. 2003, *ApJ*, 589, L21
- Martig, M., Bournaud, F., Teyssier, R., & Dekel, A. 2009, *ApJ*, 707, 250
- McConnell, N. J., Ma, C.-P., Gebhardt, K., et al. 2011b, *Nature*, 480, 215
- McConnell, N. J., Ma, C.-P., Graham, J. R., et al. 2011a, *ApJ*, 728, 100
- McConnell, N. J., Ma, C.-P., Murphy, J. D., et al. 2012, arXiv 1203.1620
- McLure, R. J., & Dunlop, J. S. 2002, *MNRAS*, 331, 795
- . 2004, *MNRAS*, 352, 1390
- McLure, R. J., & Jarvis, M. J. 2002, *MNRAS*, 337, 109
- McLure, R. J., Jarvis, M. J., Targett, T. A., Dunlop, J. S., & Best, P. N. 2006, *MNRAS*, 368, 1395
- Mehlert, D., Thomas, D., Saglia, R. P., Bender, R., & Wegner, G. 2003, *A&A*, 407, 423
- Merloni, A., Bongiorno, A., Bolzonella, M., et al. 2010, *ApJ*, 708, 137
- Merritt, D. 1985, *ApJ*, 289, 18
- Merritt, D., & Ferrarese, L. 2001, *ApJ*, 547, 140
- Mihos, J. C., & Hernquist, L. 1996, *ApJ*, 464, 641
- Milosavljević, M., & Merritt, D. 2001, *ApJ*, 563, 34
- Mo, H. J., Mao, S., & White, S. D. M. 1998, *MNRAS*, 295, 319
- Mortlock, D. J., Warren, S. J., Venemans, B. P., et al. 2011, *Nature*, 474, 616
- Murphy, J. D., Gebhardt, K., & Adams, J. J. 2011, *ApJ*, 729, 129
- Natarajan, P., & Treister, E. 2009, *MNRAS*, 393, 838
- Navarro, J. F., Frenk, C. S., & White, S. D. M. 1996, *ApJ*, 462, 563
- Netzer, H. 2003, *ApJ*, 583, L5
- Netzer, H., Lira, P., Trakhtenbrot, B., Shemmer, O., & Cury, I. 2007, *ApJ*, 671, 1256
- Neumayer, N., Cappellari, M., Reunanen, J., et al. 2007, *ApJ*, 671, 1329
- Nowak, N., Saglia, R. P., Thomas, J., et al. 2008, *MNRAS*, 391, 1629
- Nowak, N., Saglia, R. P., Thomas, J., et al. 2007, *MNRAS*, 379, 909
- Nowak, N., Thomas, J., Erwin, P., et al. 2010, *MNRAS*, 403, 646
- Oegerle, W. R., & Hill, J. M. 2001, *AJ*, 122, 2858
- Oegerle, W. R., & Hoessel, J. G. 1991, *ApJ*, 375, 15
- Onken, C. A., Ferrarese, L., Merritt, D., et al. 2004, *ApJ*, 615, 645
- Oser, L., Naab, T., Ostriker, J. P., & Johansson, P. H. 2012, *ApJ*, 744, 63
- Oser, L., Ostriker, J. P., Naab, T., Johansson, P. H., & Burkert, A. 2010, *ApJ*, 725, 2312
- Ostriker, J. P., & Hausman, M. A. 1977, *ApJ*, 217, L125
- Ostriker, J. P., & Tremaine, S. D. 1975, *ApJ*, 202, L113
- Peng, C. Y. 2007, *ApJ*, 671, 1098
- Peng, C. Y., Impey, C. D., Ho, L. C., Barton, E. J., & Rix, H.-W. 2006a, *ApJ*, 640, 114
- Peng, C. Y., Impey, C. D., Rix, H.-W., et al. 2006b, *ApJ*, 649, 616
- Pinkney, J., Gebhardt, K., Bender, R., et al. 2003, *ApJ*, 596, 903
- Porter, A. C., Schneider, D. P., & Hoessel, J. G. 1991, *AJ*, 101, 1561
- Postman, M., & Lauer, T. R. 1995, *ApJ*, 440, 28
- Quinlan, G. D., & Hernquist, L. 1997, *New Astronomy*, 2, 533

- Reines, A. E., Sivakoff, G. R., Johnson, K. E., & Brogan, C. L. 2011, *Nature*, 470, 66
- Richardson, W. H. 1972, *Journal of the Optical Society of America (1917-1983)*, 62, 55
- Richstone, D. O., & Tremaine, S. 1984, *ApJ*, 286, 27
- . 1988, *ApJ*, 327, 82
- Rix, H.-W., de Zeeuw, P. T., Cretton, N., van der Marel, R. P., & Carollo, C. M. 1997, *ApJ*, 488, 702
- Rix, H.-W., & White, S. D. M. 1992, *MNRAS*, 254, 389
- Robertson, B., Hernquist, L., Cox, T. J., et al. 2006, *ApJ*, 641, 90
- Rusli, S. P., Thomas, J., Erwin, P., et al. 2011, *MNRAS*, 410, 1223
- Ruszkowski, M., & Springel, V. 2009, *ApJ*, 696, 1094
- Ryden, B. S., Lauer, T. R., & Postman, M. 1993, *ApJ*, 410, 515
- Sadoun, R., & Colin, J. 2012, *arXiv 1204.0144*
- Sanders, D. B., Soifer, B. T., Elias, J. H., et al. 1988, *ApJ*, 325, 74
- Sani, E., Marconi, A., Hunt, L. K., & Risaliti, G. 2011, *MNRAS*, 413, 1479
- Sargent, W. L. W., Young, P. J., Lynds, C. R., et al. 1978, *ApJ*, 221, 731
- Sarzi, M., Rix, H.-W., Shields, J. C., et al. 2001, *ApJ*, 550, 65
- Sastry, G. N. 1968, *PASP*, 80, 252
- Schawinski, K., Treister, E., Urry, C. M., et al. 2011, *ApJ*, 727, L31
- Schödel, R., Ott, T., Genzel, R., et al. 2002, *Nature*, 419, 694
- Schulze, A., & Gebhardt, K. 2011, *ApJ*, 729, 21
- Schwarzschild, M. 1979, *ApJ*, 232, 236
- Shapiro, K. L., Cappellari, M., de Zeeuw, T., et al. 2006, *MNRAS*, 370, 559
- Shapiro, K. L., Genzel, R., Förster Schreiber, N. M., et al. 2008, *ApJ*, 682, 231
- Shemmer, O., Netzer, H., Maiolino, R., et al. 2004, *ApJ*, 614, 547
- Shen, J., & Gebhardt, K. 2010, *ApJ*, 711, 484
- Shen, Y. 2009, *ApJ*, 704, 89
- Shen, Y., Greene, J. E., Strauss, M. A., Richards, G. T., & Schneider, D. P. 2008, *ApJ*, 680, 169
- Sijacki, D., Springel, V., & Haehnelt, M. G. 2011, *MNRAS*, 414, 3656
- Silge, J. D., & Gebhardt, K. 2003, *AJ*, 125, 2809
- Silge, J. D., Gebhardt, K., Bergmann, M., & Richstone, D. 2005, *AJ*, 130, 406
- Silk, J., & Rees, M. J. 1998, *A&A*, 331, L1
- Siopis, C., Gebhardt, K., Lauer, T. R., et al. 2009, *ApJ*, 693, 946
- Small, T. A., & Blandford, R. D. 1992, *MNRAS*, 259, 725
- Smith, A. J., Loveday, J., & Cross, N. J. G. 2009, *MNRAS*, 397, 868
- Sofue, Y. 1994, *ApJ*, 423, 207
- Somerville, R. S., Hopkins, P. F., Cox, T. J., Robertson, B. E., & Hernquist, L. 2008, *MNRAS*, 391, 481
- Springel, V., Di Matteo, T., & Hernquist, L. 2005, *ApJ*, 620, L79
- Thomas, J., Saglia, R. P., Bender, R., et al. 2005, *MNRAS*, 360, 1355
- . 2007, *MNRAS*, 382, 657
- . 2004, *MNRAS*, 353, 391

- Tonry, J. L. 1987, *ApJ*, 322, 632
- Toomre, A. 1977, in *Evolution of Galaxies and Stellar Populations*, ed. B. M. Tinsley & R. B. G. Larson, D. Campbell, 401
- Tremaine, S. 1990, in *International Conference on Dynamics and Interactions of Galaxies*, ed. R. Wielen, 394–405
- Tremaine, S., Gebhardt, K., Bender, R., et al. 2002, *ApJ*, 574, 740
- Trujillo, I., Förster Schreiber, N. M., Rudnick, G., et al. 2006, *ApJ*, 650, 18
- Ueda, Y., Akiyama, M., Ohta, K., & Miyaji, T. 2003, *ApJ*, 598, 886
- Valdes, F., Gupta, R., Rose, J. A., Singh, H. P., & Bell, D. J. 2004, *ApJS*, 152, 251
- Valluri, M., Merritt, D., & Emsellem, E. 2004, *ApJ*, 602, 66
- van Dam, M. A., Bouchez, A. H., Le Mignant, D., et al. 2006, *PASP*, 118, 310
- van den Bergh, S. 2009, *ApJ*, 702, 1502
- van den Bosch, R. C. E., & de Zeeuw, P. T. 2010, *MNRAS*, 401, 1770
- van den Bosch, R. C. E., van de Ven, G., Verolme, E. K., Cappellari, M., & de Zeeuw, P. T. 2008, *MNRAS*, 385, 647
- van der Marel, R. P. 1994, *MNRAS*, 270, 271
- van der Marel, R. P., & Anderson, J. 2010, *ApJ*, 710, 1063
- van der Marel, R. P., Cretton, N., de Zeeuw, P. T., & Rix, H.-W. 1998, *ApJ*, 493, 613
- van der Marel, R. P., & Franx, M. 1993, *ApJ*, 407, 525
- van der Marel, R. P., & van den Bosch, F. C. 1998, *AJ*, 116, 2220
- van Dokkum, P. G. 2005, *AJ*, 130, 2647
- van Dokkum, P. G., Whitaker, K. E., Brammer, G., et al. 2010, *ApJ*, 709, 1018
- Verolme, E. K., Cappellari, M., Copin, Y., et al. 2002, *MNRAS*, 335, 517
- Vestergaard, M. 2004, *ApJ*, 601, 676
- Vestergaard, M., Fan, X., Tremonti, C. A., Osmer, P. S., & Richards, G. T. 2008, *ApJ*, 674, L1
- Vestergaard, M., & Peterson, B. M. 2006, *ApJ*, 641, 689
- Volonteri, M., Lodato, G., & Natarajan, P. 2008, *MNRAS*, 383, 1079
- Volonteri, M., & Natarajan, P. 2009, *MNRAS*, 400, 1911
- Volonteri, M., Natarajan, P., & Gültekin, K. 2011, *ApJ*, 737, 50
- von der Linden, A., Best, P. N., Kauffmann, G., & White, S. D. M. 2007, *MNRAS*, 379, 867
- Walsh, J. L., Barth, A. J., & Sarzi, M. 2010, *ApJ*, 721, 762
- Walsh, J. L., van den Bosch, R. C. E., Barth, A. J., & Sarzi, M. 2012, *ApJ*, 753, 79
- White, S. D. M., & Rees, M. J. 1978, *MNRAS*, 183, 341
- Williams, M. J., Bureau, M., & Cappellari, M. 2010, *MNRAS*, 409, 1330
- Wizinowich, P. L., Le Mignant, D., Bouchez, A. H., et al. 2006, *PASP*, 118, 297
- Wold, M., Lacy, M., Käuffl, H. U., & Siebenmorgen, R. 2006, *A&A*, 460, 449
- Woo, J.-H., Treu, T., Barth, A. J., et al. 2010, *ApJ*, 716, 269
- Wyithe, J. S. B. 2006a, *MNRAS*, 365, 1082
- . 2006b, *MNRAS*, 371, 1536
- Yoo, J., Miralda-Escudé, J., Weinberg, D. H., Zheng, Z., & Morgan, C. W. 2007, *ApJ*, 667, 813

-
- Zabludoff, A. I., Geller, M. J., Huchra, J. P., & Ramella, M. 1993, *AJ*, 106, 1301
- Zasov, A. V., Petrochenko, L. N., & Cherepashchuk, A. M. 2005, *Astronomy Reports*, 49, 362
- Zier, C., & Biermann, P. L. 2001, *A&A*, 377, 23